Crashworthiness Optimization of Ultralight Metal Structures

by

Weigang Chen

B.S., Naval Architecture, Shanghai Jiao Tong University, 1992
M.S., Mechanical Engineering, Massachusetts Institute of Technology, 2000
M.S., Ocean Engineering, Massachusetts Institute of Technology, 2000

Submitted to the Department of Ocean Engineering
in Partial Fulfillment of the Requirements for the Degree of
Doctor of Philosophy in Applied Mechanics
at the
MASSACHUSETTS INSTITUTE OF TECHNOLOGY
February 2001

Author..... .....
Weigang Chen
January 26, 2001

Certified by... .....
Tomasz Wierzbicki
Professor of Applied Mechanics
Thesis Supervisor

Accepted by.. .....
Nicholas M. Patrikalakis
Kawasaki Professor of Engineering
Chairman, Department Committee on Graduate Students

Dynamic Stiffness and Transfer Matrix Analysis of Marine Riser Vibration

by

Yongming Cheng

Submitted to the Department of Ocean Engineering
on January 24, 2001, in partial fulfillment of the
requirements for the degree of
Doctor of Philosophy

Abstract

This dissertation extends the use of the dynamic stiffness and transfer matrix methods in marine riser vibration. Marine risers possess a predominant chain topology. The transfer matrix method is appropriate for the analysis of such structures. Wave transmission and reflection matrices are formulated in terms of transfer-matrix elements. The delta-matrix method is introduced to deal with numerical problems associated with very long beams and high frequencies. The general internal relationships between the transfer matrix and dynamic stiffness methods are derived and applied to the problem of a non-uniform beam with discontinuities. An implicit transfer matrix of a general non-uniform beam is derived.

The vibration analysis of non-uniform marine risers is addressed by combining the procedure of the dynamic stiffness method with the WKB theory. The WKB-based dynamic stiffness matrix is derived and the frequency-dependent shape function is expressed implicitly. The Wittrick-Williams algorithm is extended to the analysis of a general non-uniform marine riser, allowing automatic computation of natural frequencies. Marine riser models with complex boundary conditions are analyzed. The WKB-based dynamic stiffness method is improved and applied to a non-uniform beam system with discontinuities. A dynamic stiffness library is created.

Dynamic vibration absorbers and wave-absorbing terminations are investigated as a means of suppressing vibration. The optimal tuning of multiple absorbers to a non-uniform beam system under varying tension is investigated. The properties of wave-absorbing terminations of a beam system are derived.

The vibration of two concentric cylinders coupled by the annulus fluid and by periodic centralizers is modeled. The effects of coupling factors on vibration are numerically evaluated. It is shown that a properly designed inner tubular member may be used to damp the flow-induced vibration of the outer cylinder.

Thesis Supervisor: J. Kim Vandiver
Title: Professor of Ocean Engineering

Acknowledgment

First, I would like to express my deepest appreciation to my advisor, Professor Tomasz Wierzbicki, for his continuous guidance, support and encouragement during the three and half years of my study at MIT. I would also like to thank Professor Franz-Josef Ulm, Professor Nicholas Patrikalakis, and Dr. Christopher Magee, for serving in my dissertation committee and for their inspiring comments and discussions.

I am very grateful to Dr. Tony Warren and Dr. Dubravko Nardini for giving me the opportunity to work as a summer intern at Alcan International, Banbury Laboratory in England, where all the specimens used in this thesis were manufactured and some preliminary tests were conducted. Thanks are also extended to Mr. Stephen Rudolph and Mr. Jim Tansley for their assistance in preparing specimens and conducting tests.

My appreciation goes out to my colleagues at the Impact and Crashworthiness Laboratory. In this intellectually enlightening and friendly work environment, I have the opportunity to work together with many brilliant staff members and fellow students. In particular, I would like to thank Dr. Mulalo Doyoyo for proof-reading the manuscript, and for his valuable comments and discussions. Thanks are also due to Mr. Heung-Soo Kim for his technical assistance on computer system.

I gratefully acknowledge all the members of the Joint MIT/Industry Ultralight Consortium for their financial support of this research.

Last, but not the least, I would like to thank my wife Zhenrong for her encouragement and patience during this study.

Contents

List of Figures

List of Tables

Chapter 1

Introduction

1.1 Motivation

The term "crashworthiness" evolved around 1950s and was first associated with aviation safety [1]. It refers to the capacity of a vehicle or component to provide occupant protection during potentially survivable collisions. A crashworthy design should be able to dissipate in a controlled manner the kinetic energy of the impact, and to retain a survival space for occupants and to attenuate the forces and accelerations experienced by the occupants. Because of the very demanding requirement of crash, it is plausible that the crush criteria will dominate the structural design of a vehicle body. Well designed crashworthy structures will, as a rule, meet the general stiffness criteria set by other requirements such as NVH (Noise, Vibration and Harshness) [1].

The most important challenge for today's automotive engineers is to design vehicles that are not only structural safe, but also light, fuel efficient and environmentally friendly. The quest for reduction of vehicle weight without jeopardizing structure's crash performance has led to investigating structural materials other than steel, such as, aluminum, composite, magnesium, etc. Among others, aluminum appears to be the most attractive material due to its low specific weight, recycling potential and excellent corrosion resistance. Aluminum space frame and extruded aluminum components have been used in the automotive industry (for example, Audi A8 and Audi

Al2). It was proved that excellent crash performance as well as other performance parameters can be achieved by aluminum structures while satisfying weight saving targets.

In order to achieve the weight reduction without compromising the vehicle crashworthiness, structural stiffening methods have also been investigated. Thornton et al. [2, 3] proposed a method to reinforce thin-walled components by filling the empty space with polyurethane foam. They found that the filling may be of benefit on a weight effectiveness basis only for thin-walled sections made from high density, low strength material, e.g. mild steel. However, when the wall thickness of a section is reduced below a certain limit, the range of useful wall thickness for which foam reinforcement is weight effective tends to be of no practical use. These conclusions were substantially verified by a later study by Lampinen and Jeryan [4] who developed regression models to predict the load capacity and axial collapse of polyurethane foam-filled sections.

Recent advances in cost-effective process for the production of ultralight ($\leq$ 20% of solid aluminum) cellular materials, such as aluminum foams and aluminum honeycombs, has cleared the way for using these materials as reinforcement to existing thin-walled structural members. The motivation for using the ultralight metal core is to increase the rigidity of the thin-walled members and therefore increase the energy absorption while minimizing additional weight penalty. Santosa and Wierzbicki [5, 6, 7, 8, 9, 10, 11] carried out extensive numerical studies on the crash behavior of thin-walled prismatic structural members with ultralight filler subjected to axial compression, bending and torsional loadings. It was found in their studies that superior weight efficiency can be achieved for thin-walled members filled with the ultralight metal core. Seizberger et al. [12, 13] conducted experimental study on the axial crushing of steel columns filled with aluminum foam. They reported that considerable weight efficiency improvements with respect to energy absorption were obtained by foam filling. Comprehensive experimental studies on the effect of filling thin-walled square and circular aluminum extrusions with aluminum foam were carried out by Hanssen et al. [14, 15, 16]. They concluded that foam-filled extrusions are advantageous over empty ones in terms of least weight where high levels of energy absorption are required.

In the present research, extensive theoretical, numerical and experimental studies

are carried out on the axial crushing, bending collapse and torsional deformation of thin-walled structures filled with ultralight metal core material (aluminum foam or honeycomb). A clear physical understanding of the crush mechanics of such ultralight structures is achieved. The strengthening effects of the filling are revealed and quantitatively assessed. With this fundamental work, the optimization problem of ultralight structures for minimum weight is formulated and a methodology is developed, which combines the above results with numerical optimization techniques, to determine among all feasible options an optimum design of structural geometry and material properties for the minimum weight while satisfying the requirements of structural integrity and crashworthiness.

1.2 Research Objective

The objective of the present research is to study the crushing behavior of two new types of structural components, i.e., aluminum foam-filled thin-walled members and aluminum honeycomb-filled members, and then to optimize such components with crashworthiness constraints.

A number of new contributions are generated from this research

- An analytical solution for mean crushing force of multi-cell sections is developed, based on the *Superfolding Element* theory. Closed-form solutions are derived to predict the mean crushing forces of foam-filled multi-cell sections.
- Technologies of manufacturing foam-filled closed-hat profiles and joint techniques are investigated.
- Axial crushing tests are conducted on foam-filled hat profiles to study their collapse behavior, energy absorption and weight efficiency.
- Experiments of bending up to 150^o on filled beams are performed. Numerical simulations of bending collapse are also carried out. The strengthening effects of filling are quantitatively assessed based on the results of numerical and physical experiments.

- Theoretical models of torsional crushing of empty and filled thin-walled prismatic tubes are developed. Solutions are validated by numerical simulations and physical testing. The strengthening effects of foam filling are quantified.
- A new methodology of design optimization of ultralight structures for minimum weight with crashworthiness constraints is developed.

1.3 Overview of the Thesis

The present thesis is organized into seven chapters and a bibliography of cited references.

In *Chapter 2*, two types of ultralight cellular solid materials (aluminum foam and honeycomb) used as core materials in ultralight structures are discussed. The production process and the mechanical behavior of these two materials are addressed. The yield criteria of the materials present in literature are reviewed, and the simple maximum principal stress yield model employed in the numerical simulations in the present research is discussed. Finally, the ultralight structural components studied in this thesis are briefly introduced, and they are aluminum foam or honeycomb filled extrusions, aluminum foam-filled hat profiles, and double-walled sandwich components.

Chapter 3 investigates the axial crushing behavior of empty and foam-filled double-cell and triple-cell extrusions and foam-filled hat profiles. Based on the *Superfolding Element* theory, an analytical solution for the mean crushing force of multi-cell sections is derived, and the solution is compared with numerical predictions. Numerical studies are then carried out in the second part of this chapter on the axial crushing of foam-filled multi-cell columns. With the numerical results of filled columns and analytical solutions for non-filled columns, closed-form solutions are derived to predict the mean crushing strength of the foam-filled double-cell and triple-cell sections. The relative merits in energy absorption of multi-cell and foam-filled sections are discussed.

In the third part of *Chapter 3*, experimental study is conducted on the axial crushing behavior of aluminum foam-filled hat profiles. A total of 34 specimens are tested,

which are of three different section types, i.e., single-hat, double-hat, double-hat with a center flange. Various processes of fitting foam into hat sections and joint techniques are investigated. The experiments revealed important features of axial crushing behavior of empty and foam-filled hat profiles. Joint techniques should be the point of concern. The spot-welding and weld-bond schemes, which appear sufficiently strong for empty members, are not strong enough for foam-filled members. Finally, the relative merit of foam-filled members compared to non-filled ones are quantified by performance tests.

The first part of *Chapter 4* presents the experimental results of aluminum foam-filled hat profiles undergoing bending collapse. Quasi-static bending tests are carried out on empty and foam-filled single and double-hat beams. A new experimental approach is applied so that the specimens can undergo large bending angles up to 150^o. Salient features of the deep bending behavior of empty and filled hat members are revealed in the experiments.

The strengthening effects of the foam and honeycomb fillings on the plastic resistance of thin-walled beams in bending collapse mode are then studied numerically in *Chapter 4*. The increase in bending resistance resulting from filling is quantified, and closed-form expressions are derived based on the analytical solutions, experimental data and numerical results. The densities of the cellular solid fillers considered in the study are up to 20% relative density, which is of practical interest.

Torsional crushing behavior of empty and foam-filled thin-walled tubes are discussed in *Chapter 5*. An analysis by applying the principle of virtual velocities to kinematically admissible displacement fields is conducted to predict the torsional behavior of thin-walled tubes with large plastic deformations. Three successive deformation phases, namely pre-buckling, cross-section buckling, and collapse-spreading phase, are identified. The analytical model is then extended to the cases of thin-walled rectangular and hexagonal tubes. Numerical simulations are carried out and the results are compared with the analytical solutions.

Of particular interest in crashworthiness application is the effect of the lightweight metal filler on the resistance and energy absorption of a structural member. The torsional collapse behavior and plastic resistance of thin-walled tubes filled with aluminum foam are investigated theoretically and numerically in the second part of

Chapter 5. It is found that the presence of the filler acting as elastic-plastic foundation to the skin changes the sectional buckling mode into higher ones, and hence increases the torsional resistance. The upper and lower bounds on the torsional resistance of filled tubes are established approximately. Numerical simulations are carried out. The torsional resistance elevation due to filling is quantitatively assessed, and closed-form expressions are derived based on the analytical solutions and numerical results. Finally, results of torsional experiments on empty and foam-filled square tubes are presented. Results are used to validate the theoretical and numerical solutions.

The fundamental work discussed in previous chapters is of great importance in achieving a clear physical understanding of the crush mechanics of ultralight structures. The strengthening effects of the core material under various loading conditions are investigated and quantified. In particular, closed-form solutions are developed based on numerical simulations, physical experiments and theoretical considerations. This forms the basis of an optimization methodology proposed in *Chapter 6.* The methodology combines the numerical optimization techniques with the above results in the crush mechanics of ultralight structures. The optimization formulations are constructed on a component level for the minimum weight with the constraints of crashworthiness and elastic bending stiffness. Design optimization of various sections are carried out using the proposed methodology to decide the most weight-efficient design for crash energy management in axial crushing, bending collapse and torsional crushing loadings. It is shown that the proposed methodology is suitable for the early-stage component design with very little computational effort.

Finally, a summary of the results is presented in *Chapter 7.* Recommendations for future research are suggested.

Chapter 2

Ultralight Core Materials and Ultralight Structures

2.1 Introduction

Highly porous metallic materials with a cellular structure have many attractive characteristics, including low density, good acoustic and thermal resistance, and high compressive strength-to-weight ratios. Therefore they have great potentials for use in structural applications, such as reinforcement to hollow thin-walled structures, cores for sandwich panels, and devices for absorbing impact energy. Reviews of the research on the mechanical and physical properties of cellular materials are given by Gibson and Ashby [17], Santosa [5], and Doyoyo and Wierzbicki [18].

Two typical cellular solid materials are aluminum foams and aluminum honeycombs. Aluminum foams are made of a network of three-dimensional cells, while honeycombs are composed of an array of parallel, prismatic cells. When subjected to a compressive load greater than their maximum strength, deformation occurs by progressive crushing of individual cells through the thickness of the foams and honeycombs. This deformation characteristics gives the materials the capacity to undergo very large compressive strains. Typically, the compressive stress-strain curve of aluminum foam shows an elastic regime, followed by a long plastic collapse plateau regime, truncated

by a regime of densification where the stress rises steeply. The elastic regime in foam materials is a function of bending stiffness of cell walls and edges (Christensen [19]). The collapse regime is associated with the development of plastic hinges formed in these members, until cell walls begin to touch and the foam densifies (Thornton and Magee [20, 21]). Likewise, the compressive stress-strain curve of aluminum honeycomb shows three regimes: elastic, plastic and densification regimes. The elastic stage is associated with axial compression of cell walls in out-of-plane loading and bending of cell walls in in-plane-loading. Beyond a critical strain, the cells collapse by plastic buckling (McFarland [22] and Wierzbicki [23]), and plastic deformation continues until cell walls begin to touch. As the cells close up, the honeycomb densifies and the slope of the stress-strain curve increases rapidly.

The manufacturing process, the mechanical properties and plasticity models of aluminum foams and honeycombs are summarized in the following.

2.2 Aluminum Foam

Metallic foams have been around since the 1950s. However, because of the high cost and unsatisfactory quality, no industrial applications were found for those early foams. Recent advances in cost-effective process for the production of high quality aluminum foam has cleared the way for using this material in many applications, such as reinforcement to thin-walled structures, cores for sandwich panels, and other energy absorption applications.

2.2.1 Production Process of Aluminum Foam

The techniques of manufacturing aluminum foam fall into three main categories, namely, melt route process, powder route process, and deposition techniques (Markaki [24] and Santosa [5]).

Melt Route Process

While the techniques in this category vary, they basically involve melting the metal

and introducing the gas either by direct injection or by foaming agent decomposing. The Cymat, Hydro, and Mepura foams are produced by injecting and mixing gas into a vat of molten aluminum alloy and ceramic particles (typically SiC or Al_2O_3). The volume fraction of ceramic particles in the mix is between 0.05 and 0.15; the size of the particles is between $1\mu m$ to 20 μm (Prakash et al. [25]). The injected air causes bubbles to rise to the surface of the melt, form a liquid foam which is stabilized by the presence of the ceramic particles on the gas-liquid interface of the cell walls. The average size of the bubbles is between 3mm and 30mm and can be controlled by the gas injection rate. The stabilized liquid foam is mechanically conveyed off the surface of the melt and allowed to cool below the solidus temperature of the alloy. This method allows for the semi-continuous production of foam panels.

The Alporas foam, on the other hand, is produced by adding 0.2 to 8 weight percentage calcium and 1 to 3 weight percentage titanium hydride powder to molten aluminum, which is then mixed with an impeller in a special casting chamber (Akiyama et al. [26]). The calcium acts to increase the viscosity of the melt, while the titanium hydride powder dissociates into titanium metal and gaseous hydrogen. The bubbles formed by the gaseous hydrogen cause the melt to expand into a liquid foam. During the expansion, the casting chamber maintains a constant chamber pressure, resulting in a homogeneous cell structure in the liquid foam. Once the foam expands to the desired volume, it is then cooled below the solidus temperature of the melt to form a solid foam casting. Foams with average cell size between 2mm and 10mm can be produced by this method.

Figure 2.1 shows the aluminum foam (Hydro) produced by the melt route process.

The advantage of the melt route techniques is that the manufacturing cost is relatively low, while the disadvantage is that the size and distribution of the pores can only be controlled to a limited extent.

Powder Route Process

Powder route techniques avoid the handling of molten metals by using a powdered mixture of a metal or alloy and a foaming agent. IFAM foam is produced by this technique. The foam agent is usually 0.4 to 0.8 weight percentage depending on the desired foam density. The powder blend is then compacted by extrusion to be-

come foamable semi-finished product in which the foaming agent is homogeneously distributed within a dense, virtually non-porous metallic matrix. The semi-finished product is then processed into pieces of the desired size and shape by rolling and cutting. Upon heating the foamable material to temperature within the range of the melting point, the foam agent releases gas in a controlled way, so that the metal transforms into semi-solid, foamy mass which expands slowly into a highly porous cellular solid with a closed-pore structure. The density of the metal foam is controlled by adjusting the content of the foaming agent and varying the heating condition.

Figure 2.1 shows the aluminum foam (IFAM) produced by the powder route process.

Powder metallurgy allows greater control over foam macrostructure and can be used to produce foams with complex shapes and inside hollow thin-walled structures. However, powder route techniques are inevitably more expensive than the melt route.

Deposition Techniques

Deposition techniques are based on the deposition of a metal onto a polymeric substrate which is then removed by thermal decomposition. The foam produced by this technique are with uniform cell structures, but the high cost limits their application.

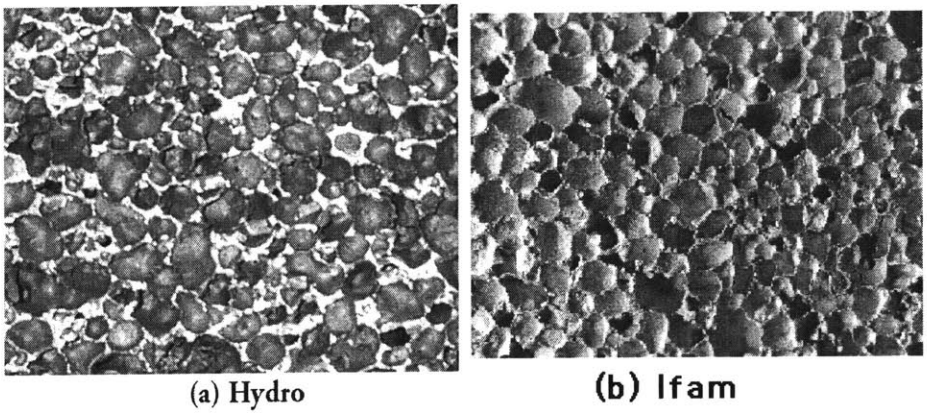

Figure 2.1: Aluminum foam (a) Hydro (b) IFAM

2.2.2 Mechanical Behavior of Aluminum Foam

The mechanical properties of aluminum foam depend on both the cell structure of the foam and the properties of the base material. A typical compressive stress-strain curve of aluminum foam may be approximated by three regimes: linear elasticity at small strains, a long plateau stress region, and a final densification region where stress rises steeply, see Fig.2.2

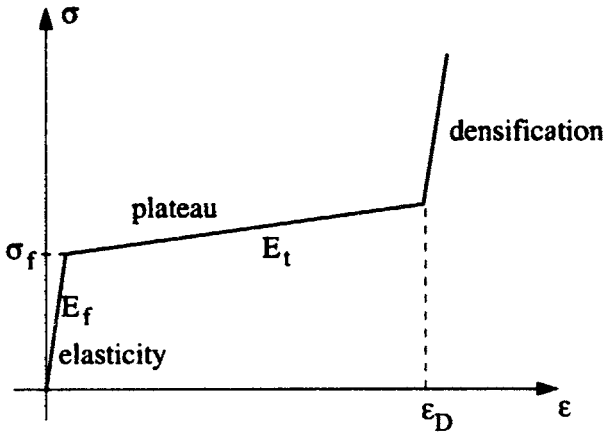

Figure 2.2: Compressive stress-strain curve of aluminum foam

The mechanical properties of aluminum foam for various relative densities can be given as follows

$$E_f = E_s \left(\frac{\rho_f}{\rho_s}\right)^2 \tag{2.1}$$

$$E_t = 0.02E_f \tag{2.2}$$

$$G_f = E_f \tag{2.3}$$

$$\sigma_f = \sigma_{0f} \left(\frac{\rho_f}{\rho_s}\right)^{3/2} \tag{2.4}$$

$$\tau_f = 0.5\sigma_{0f} \left(\frac{\rho_f}{\rho_s}\right)^{3/2} \tag{2.5}$$

$$\epsilon_D = 1 - 1.4\frac{\rho_f}{\rho_s} \tag{2.6}$$

where E_s, σ_{0f}, ρ_s are the Young's modulus, plastic flow stress, and mass density of the skeleton material of the foam, respectively. The plastic collapse stress σ_f in Eq.(2.4) was given among others by Santosa and Wierzbicki [27], while the expressions for Young's modulus E_f, shear modulus G_f and densification strain ϵ_D were developed by Gibson and Ashby [17]. Based on experimental data, the plastic shear strength τ_f is usually a fraction of the plastic collapse stress, $\tau_f = (0.5 \backsim 0.8)\sigma_f$. The coefficient was assumed to be 0.5 in Eq.(2.5) for simplicity. The expression for the tangent modulus E_t describing the strain hardening of the foam at the plastic stress plateau was proposed by Santosa and Wierzbicki [27] and Hanssen [28].

The tensile stress-strain response of aluminum foam differs from a compressive one. A typical tensile stress-strain curve is illustrated schematically in Fig.2.3. Unlike in compressive loading where the material can undergo large macroscopic strains (> 60%), the aluminum foam in tension tends to fail in a brittle fashion at a relatively small strain (around 10%), and cracks start propagating after stress reaches a peak and until it ruptures.

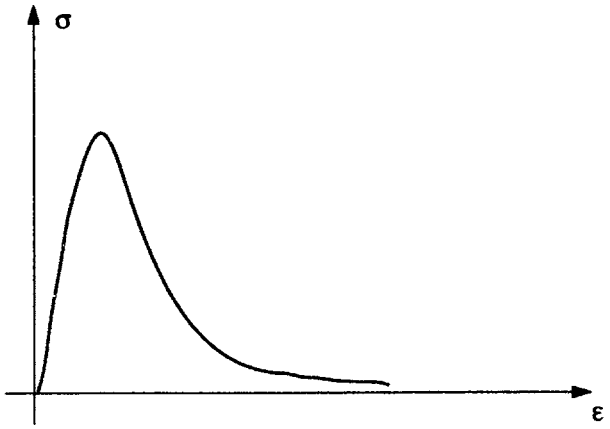

Figure 2.3: Tensile stress-strain curve of aluminum foam

Harte et al. [29] found that the uniaxial tensile yield strength is approximately equal to the uniaxial compressive yield strength for some commercial foams. However, a recent experimental study carried out by Doyoyo and Wierzbicki [30] showed that for anisotropic foams the tensile strength is about one-third of the compressive strength for the aluminum foam they tested. Sugimura et al. [31] reported that certain metal foams exhibit a higher yield point in tension than in compression. The wide scattering results suggest that more studies are needed to achieve a clear picture.

Many investigators have focused on the development of physical models of failure of cellular solids under multi-axial stresses. A few of such models are described below. Gibson et al. [32] used an analysis of an idealized cubic unit cell to develop a yield surface of the form

$$\pm\frac{\sigma_e}{\sigma_f} + 0.81(\frac{\rho_f}{\rho_s})(\frac{\sigma_m}{\sigma_f})^2 = 1 \tag{2.7}$$

where σ_f is the magnitude of the uniaxial compressive collapse stress; ρ_f/ρ_s is the relative density of the foam compared to the solid aluminum; σ_e and σ_m are the Von Mises effective stress and mean stress defined in terms of the stress tensor as

$$\sigma_m = \frac{1}{3}\sigma_{kk} \tag{2.8}$$

$$\sigma_e = \sqrt{\frac{3}{2}s_{ij}s_{ij}} \tag{2.9}$$

$$s_{ij} = \sigma_{ij} - \sigma_m\delta_{ij} \tag{2.10}$$

In the principal stress space (σ_1, σ_2, σ_3), the above yield surface is an ellipsoid sitting on the hydrostatic axis, see Fig.2.4(c). In biaxial loading, the yield surface is a skewed ellipse, see Fig.2.5(dotted line). This model, however, does not account for the difference in tensile and compressive strengths of foams which is a characteristic of compressible materials.

The well-known Drucker-Prager yield criterion [33] has also been used for porous materials such as soils

$$f = \sigma_e + \nu\sigma_m - d \tag{2.11}$$

where ν and d are constants which can be determined by uniaxial tensile and compressive tests. The Drucker-Prager yield surface is a cone sitting on the hydrostatic axis in the principal stress space, see Fig.2.4(b).

Miller [34] improved the Gibson's model by incorporating the Drucker-Prager model to account for the unequal tensile and compressive strengths in metal foams. Three adjustable parameters were introduced in his model to fit the yield surface to the experimental data. The yield surface takes the form

$$f = \sigma_e + \nu\sigma_m + \frac{\alpha}{d}\sigma_m^2 - d \tag{2.12}$$

where ν, α and d are material parameters to be determined from experimental data of uniaxial tensile and compressive yield strength, and the plastic Poisson's ratio.

Deshpande and Fleck [35] suggested a self-similar yield model based on axisymmetric loading tests on isotropic foams. The yielding would occur when the equivalent stress $\hat{\sigma}$ attains the yield value Y (uniaxial yield strength in tension and compression)

$$\Phi = \hat{\sigma} - Y \leq 0 \tag{2.13}$$

where the stress function $\hat{\sigma}$ is defined by

$$\hat{\sigma}^2 = \frac{1}{1 + (\frac{\beta}{3})^2}(\sigma_e^2 + \beta^2\sigma_m^2) \tag{2.14}$$

This criterion produces a yield surface of elliptical shape in (σ_m, σ_e) space, with an aspect ratio determined by the parameter β. The value of β can be established by measuring the plastic Poisson's ratio ν^p

$$\beta = 3(\frac{0.5 - \nu^p}{1 + \nu^p})^{\frac{1}{2}} \tag{2.15}$$

In the principal stress space, this yield surface is of ellipsoid shape similar to those described above (Fig.2.4(c). With $\beta^2 = 4.5$, i.e., the plastic Poisson's ratio $\nu^p = 0$ (which is close to the case of aluminum foam), the yield surface in the biaxial loading condition is a circle with radius being the value of σ_y, see Fig.2.5(dashed line).

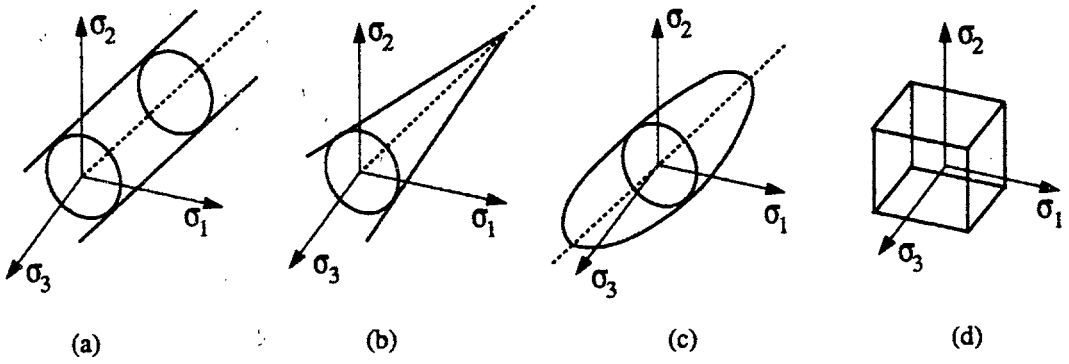

Figure 2.4: Yield surfaces. (a)Von Mises model (b)Drucker-Prager model (c)Modified Drucker-Prager model (d) Maximum principal stress criterion

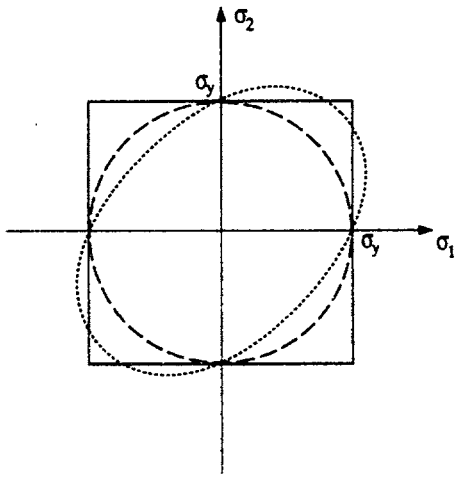

Figure 2.5: Yield surfaces in biaxial loading. Solid line:the maximum principal stress yielding model. Dotted line: Gibson's model. Dashed line: Deshpande & Fleck model

The models described above are for isotropic ductile foams, whereas many foams tend to develop anisotropy under large plastic deformations. Gioux et al. [36] suggested that anisotropy can be accounted for in the above yield models by using normalized values of the equivalent and mean stresses

$$\hat{\sigma}_e = \sqrt{\frac{1}{2}\left[\left(\frac{\sigma_1}{\sigma_{pl1}} - \frac{\sigma_2}{\sigma_{pl2}}\right)^2 + \left(\frac{\sigma_2}{\sigma_{pl2}} - \frac{\sigma_3}{\sigma_{pl3}}\right)^2 + \left(\frac{\sigma_3}{\sigma_{pl3}} - \frac{\sigma_1}{\sigma_{pl1}}\right)^2\right]} \tag{2.16}$$

and

$$\hat{\sigma}_m = \frac{1}{3}\left(\frac{\sigma_1}{\sigma_{pl1}} + \frac{\sigma_2}{\sigma_{pl2}} + \frac{\sigma_3}{\sigma_{pl3}}\right) \tag{2.17}$$

where $\sigma_{pl1}, \sigma_{pl2}$ and σ_{pl3} are the uni-axial strengths in the X_1, X_2 and X_3 directions.

Recently, Doyoyo and Wierzbicki [37] conducted combined normal and shear loading tests on aluminum foam and honeycomb specimens. The tests were carried out on a modified Arcan apparatus with a butterfly cellular solid specimen rigidly connected at the center (see Fig.2.6). Their preliminary tests showed that, under the biaxial state of stress, the foam tested exhibited a brittle fracture envelop determined by three different models in the principal stress space. The fracture occurred at the maximum principal stress in one regime, and when either the normalized difference or sum of the principal stresses reached a critical value in the other stress regimes.

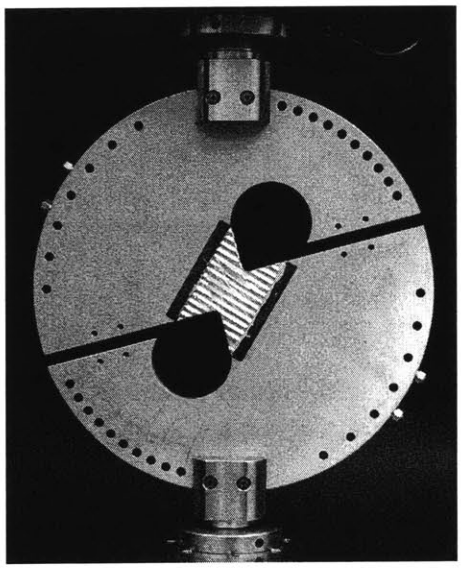

Figure 2.6: The Arcan apparatus with a butterfly cellular solid specimen at the center (Doyoyo and Wierzbicki [37])

Although the yield prediction method has been advanced by the above investigations, a lack of multi-axial experimental data and the scattering of the available data made it difficult to establish a general yield surface applicable for aluminum foams from different manufacturer and of various densities. Furthermore, in most of the theories discussed above, only the initial yield surface has been addressed, which is not

sufficient for the applications such as energy absorption structure design, where an understanding of the post-yield behavior is essential.

In the numerical analysis carried out in this thesis, we shall use a simple maximum principal stress criterion for aluminum foam material (Shaw and Sata [38], Santosa [5]). In this yield model, no interactions between components of the stress tensor is incorporated. On the other hand, the model describes adequately the hardening and locking. Also the anisotropic properties of the foam can be easily incorporated in the constitutive description. As shown in Fig.2.4(d), the yield surface is a cube in the principal stress space, while in biaxial loading, it is a square (Fig.2.5, solid line).

This simple uncoupled yielding model is relatively easy to implement in numerical analysis, and is available in some finite element code such as PAM-CRASH and LS-DYNA. This model was employed in the analysis of foam-filled structures undergoing compression, bending and torsion, and good agreements were shown between the simulation and experimental data [7, 39, 40, 41]. The mechanical properties described in Eq.(2.1) $\backsim$ Eq.(2.6) are specified in numerical analysis in three normal directions and three shear directions, see Fig.2.7.

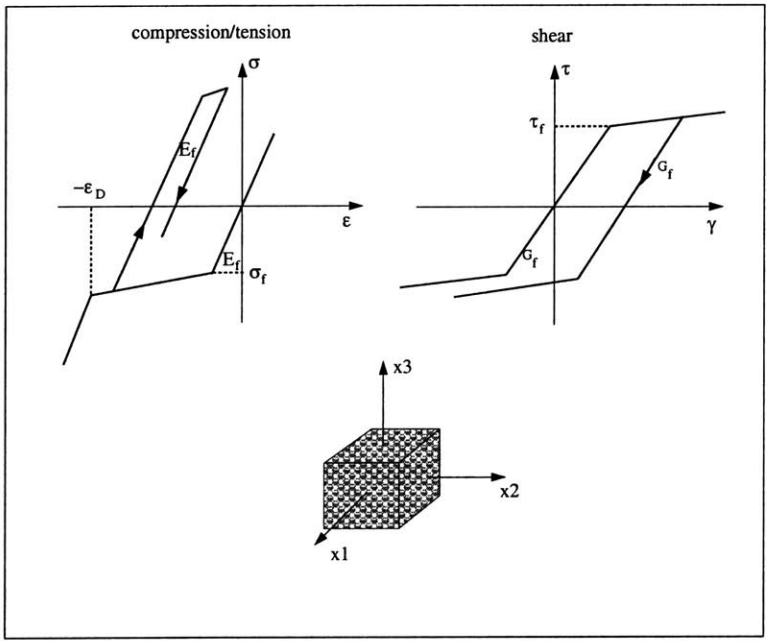

Figure 2.7: Material model for the aluminum foam used in numerical simulation

Bao et al. [42] performed a comparative study on indentation response of aluminum foam using the above uncoupled yielding model in PAM-CRASH and the Deshpande & Fleck model implemented in ABAQUS. They found that the uncoupled model generally agrees well with the experiments in punch force, while the Deshpande & Fleck model underpredicted the punch force response.

The strain rate compressive behavior of two aluminum alloy foams (Alulight and Duocel) was investigated by Deshpande and Fleck [43] using the split Hopkinson pressure bar and direct impact tests. It was found that for both foams tested, the mode of collapse is qualitatively the same under quasi-static and dynamic ($\dot{\epsilon} < 5000s^{-}1$) loadings. The micro-inertia and shock wave propagation do not significantly affect the properties of metallic foams for the range of impact velocities employed. The effect of strain rate on the dynamic strength of the cell wall material is smaller than the scatter band in strength of the foams. The stress elevation due to compression of the trapped air is less than 1.5% of the static strength. It was concluded that the dynamic behavior of these foams is very similar to their quasi-static behavior, and the plateau stress is almost insensitive to strain rate, for strain rate up to 5000 s^{-1} (impact velocity 50 m/s).

This is consistent with what Hanssen et al. [16] found in their experimental study on static and dynamic axial crushing of square aluminum extrusions filled with aluminum foam. They found that the introduction of foam filler in general reduces the "energy ratio" (the ratio between dynamic and static mean loads) compared to non-filled extrusions. This behavior can be explained by considering two factors: (1) the foam filler increases the absolute force level of the componens (2) aluminum foam shows little loading rate dependency in their velocity range (up to 25 m/s).

2.3 Aluminum Honeycomb

Structural honeycomb revolutionized the aerospace industry 40 years ago, making aircraft lighter, stronger and faster. The automotive industry has also recognized the potential of honeycomb material to help it meet the increasing need for improved safety, reduced emission, improved fuel consumption, lower weight and demanding cost reductions. Much effort has been directed towards the research on the mechanical

behavior of aluminum honeycomb. We shall give in the following a brief introduction on the production process, mechanical behavior and the material modeling of the aluminum honeycomb.

2.3.1 Production Process of Aluminum Honeycomb

Honeycomb is made primarily by the expansion method. The corrugated process is most common for high density honeycomb materials (Hexcel [44]).

Expansion Process

The aluminum honeycomb fabrication process by the expansion method begins with the stacking of aluminum sheets on which adhesive node lines have been printed. (see Fig.2.8). The adhesive lines are then cured to form a HOBE (HOneycomb Before Expansion) block. The HOBE block itself may be expanded after curing to give an expanded block. Slices of the expanded block may then be cut to the desired T dimension. Alternatively, HOBE slices can be cut from the HOBE block to the appropriate T dimension and subsequently expanded. Slices can be expanded to regular hexagons, underexpanded to 6-sided diamonds, and overexpanded to nearly rectangular cells. The expanded sheets are trimmed to the desired L dimension (ribbon direction) and W dimension (transverse to the ribbon).

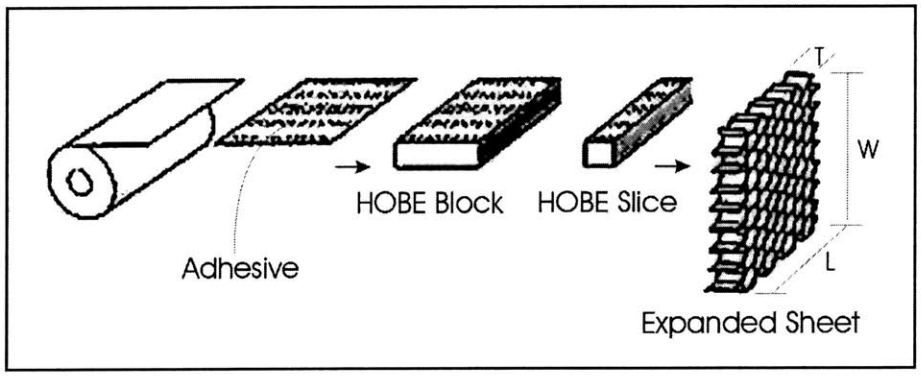

Figure 2.8: Expansion process of aluminum honeycomb production(Hexcel [44])

Corrugated Process

The corrugated process of honeycomb manufacture is normally used to produce products in the higher density range. In this process, adhesive is applied to the corrugated nodes, the corrugated sheets are stacked into blocks, the node adhesive cured, and sheets are cut from these blocks to the required core thickness, see Fig.2.9.

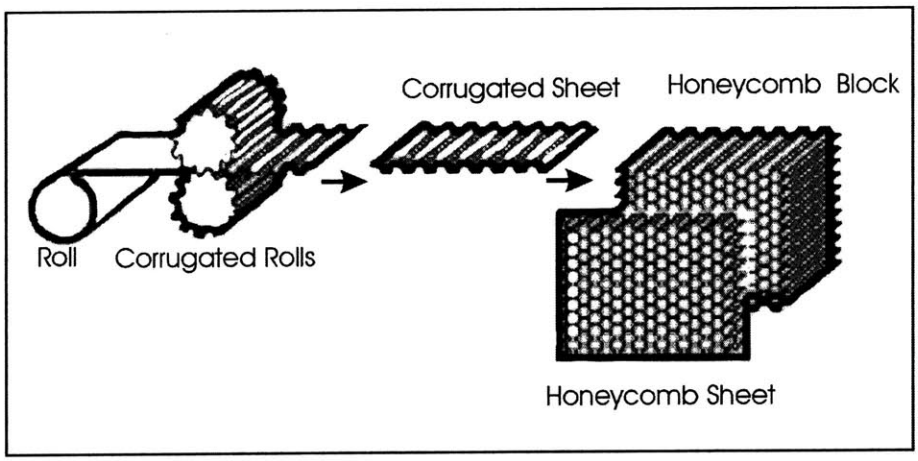

Figure 2.9: Corrugated process of aluminum honeycomb production(Hexcel [44])

2.3.2 Mechanical Behavior of Aluminum Honeycomb

The strength and stiffness of honeycomb are higher when loaded along the cell axis (out-of-plane loading, T direction in Fig.2.11) than when loaded perpendicular to the cell axis (in-plane loading, L and W directions in Fig.2.11). Much effort has been made to study the mechanical behavior of aluminum honeycomb. McFarland [22] was the first to analyze the axial crushing resistance of the aluminum honeycomb used in the Apollo space program (in fact, honeycomb was the first material from the earth to touch the moon). This early work was followed by Wierzbicki [23]. The progressive folding of hexagonal honeycomb in the T direction was analyzed by using his *Superfolding Element* method, and the crushing strength of honeycomb was given

as a function of its relative density

$$\sigma_h = 3.22\sigma_0 \left(\frac{\rho_h}{\rho_s}\right)^{\frac{5}{3}} \tag{2.18}$$

where σ_0 is the flow stress of the cell wall material; ρ_h is the apparent mass density of the honeycomb; ρ_s is the mass density of the cell wall material.

The theoretical prediction appears to be in good agreement with the experimental data [45].

Figure 2.10 shows a typical uniaxial compressive stress-strain curve of aluminum honeycomb. As can be seen, elastic, collapse plateau and densification regimes can be clearly identified.

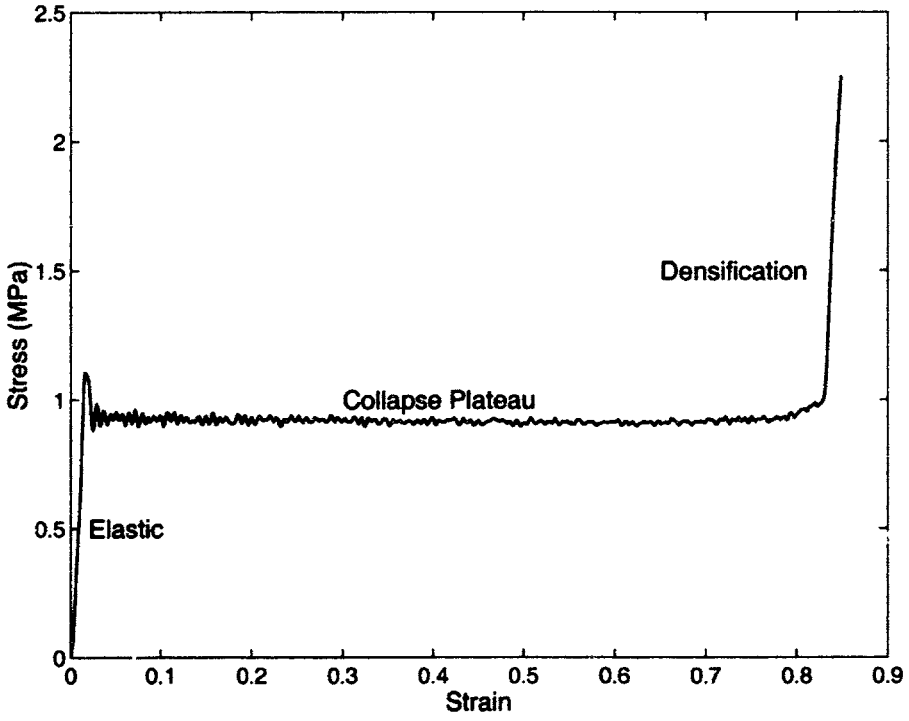

Figure 2.10: Compressive stress-strain curve for Hexcel Aluminum honeycomb

Very little theoretical or experimental work was found in the literature on the failure properties of aluminum honeycomb under combined normal and shear stress load-

ing [46]. Recently, Doyoyo and Wierzbicki [37] proposed a test fixture, an Arcan apparatus with a butterfly cellular solids at the center (see Fig.2.6), to measure failure envelops of aluminum foam and honeycomb under biaxial loading. It was found in their preliminary tests that the honeycomb collapsed plastically under biaxial loading, developing collapse lines oriented at directions parallel to the maximum principal stress. The plastic yield surface of the honeycomb is elliptic in the space of the second principal invariant of the stress deviator (J_2) and the first principal stress invariant (I_1).

Similar to the case of aluminum foam, the maximum principal stress yield model (Santosa [5]) is employed for aluminum honeycomb in the numerical analysis conducted in this thesis. The mechanical properties of aluminum honeycomb, which include the elastic moduli (E_h, G_h) and plastic collapse stresses (σ_h, τ_h) are smeared in three orthogonal directions of T, L, and W as shown in Fig.2.11. The mechanical properties in each direction are defined in Table 2.1. The out-of-plane direction T is considered as the *strong axis*, while the in-plane direction L and W are *weak axis*. No interaction between components of the stress tensor is incorporated in the yield condition.

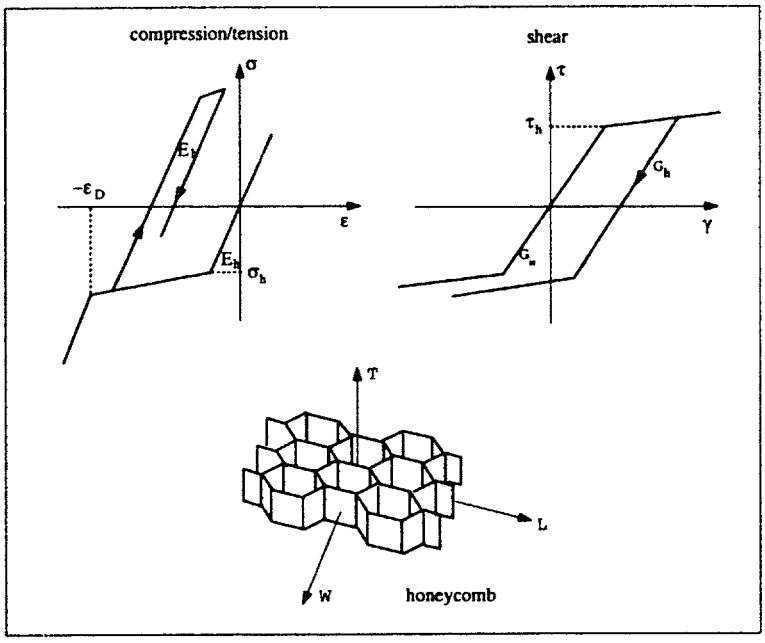

Figure 2.11: The material modeling of aluminum honeycomb in the numerical analysis

Table 2.1: The mechanical properties of aluminum honeycomb

Properties	Normal T	Normal L or W
E_h	$E_s\frac{\rho_h}{\rho_s}$	$1.49E_s\frac{\rho_h}{\rho_s}$
G_h	$0.5E_s\frac{\rho_h}{\rho_s}$	$0.37E_s(\frac{\rho_h}{\rho_s})^3$
σ_h	$3.22\sigma_{0h}(\frac{\rho_h}{\rho_s})^{5/3}$	$0.5\sigma_{0h}(\frac{\rho_h}{\rho_s})^2$
τ_h	$1.61\sigma_{0h}(\frac{\rho_h}{\rho_s})^{5/3}$	$0.22\sigma_{0h}(\frac{\rho_h}{\rho_s})^2$
ϵ_D	$1-1.4\frac{\rho_h}{\rho_s}$	

The in-plane and out-of-plane expressions of Young's modulus E_h, shear modulus G_h, plastic collapse stress σ_h, plastic shear stress τ_h and densification strain ϵ_D for various relative densities listed in Table 2.1 are given by Gibson and Ashby [17]. The expression of σ_h in T direction was given by Wierzbicki [23]. The plastic shear stress τ_h in the T direction is tentatively assumed to be a half of the plastic shear stress σ_h. Parameters E_s, σ_0, and ρ_s are respectively the Young's modulus, the flow stress, and the mass density of the cell wall material. Note that the expressions given above were derived for a low relative density range $\frac{\rho_h}{\rho_s} < 0.3$.

Regarding the dynamic properties, previous studies [47, 48, 49] found an increase of between 20 and 70% in the dynamic crush strength at impact velocities of the order of 30 m/s compared with the corresponding quasi-static value. These findings are inconsistent with an apparent insensitivity of the foam to the strain rate.

2.4 Ultralight Metal Structures

The ultralight metal structures studied in this thesis are based on the innovative ideas of ultralight structural components, which consist of aluminum sheets, extrusions, honeycombs, foams and sandwich panels. They will be assembled into ultralight structures using a variety of operations, including press break forming, stamping, hydroforming, flanging, foaming, and various methods of joining (Wierzbicki [50]).

Aluminum extrusions are the most probable candidate for ultralight space-frame applications because they can be welded. A considerable weight advantage of extrusions

can be achieved by placing aluminum foam or honeycomb inside tubes, see Fig.2.12. The crush behavior and design optimization of aluminum foam or honeycomb filled extrusions will be studied intensively in the course of the current thesis work.

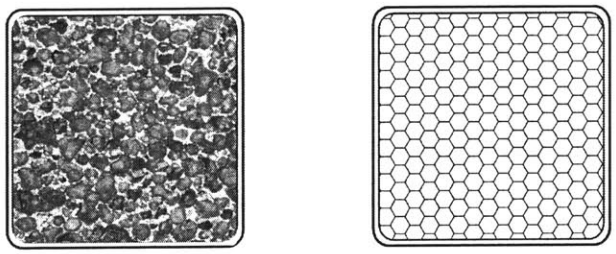

(a) (b)

Figure 2.12: Aluminum foam and aluminum honeycomb filled extrusions

Another ultralight structural component considered in this thesis is the reinforced cross-sections of spot-welded channel (single or double) beams with an insertion of pre-casted foams (see Fig.2.13). The foam element of a desired geometry is provided by foam manufacturer as a semi-finished product. This element will be fit inside two channel profiles before spot-welding. This technique is especially attractive for local reinforcing A and B pillars and longitudinal rails [50]. The manufacturing process and the crush behavior of such foam-filled hat profiles will be investigated experimentally in this thesis. Design optimization for minimum weight will also be carried out.

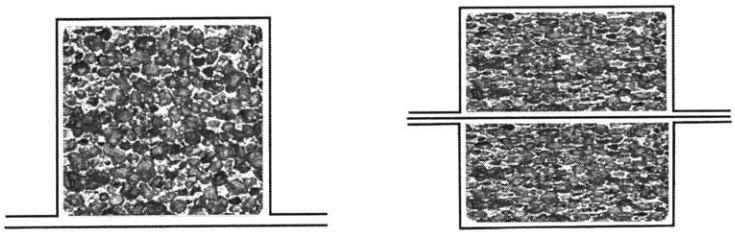

(a) (b)

Figure 2.13: Aluminum foam-filled single-hat and double-hat profiles

Double-walled sandwich component (see Fig.2.14) are recognized as a very weight-efficient structural member is crash energy management (Santosa [5], Barrera et al. [51], Mohr and Meyer [52]). The double-walled sandwich components can be made

of extrusions and ultralight cores by hydroforming, or made of commercially available sandwich panels (thin skins are separated by, and bonded to, ultralight cores) by edge bending or press break forming [50]. Weight optimization of double-walled sandwich members with stiffness and energy absorption constraints will be addressed in this thesis.

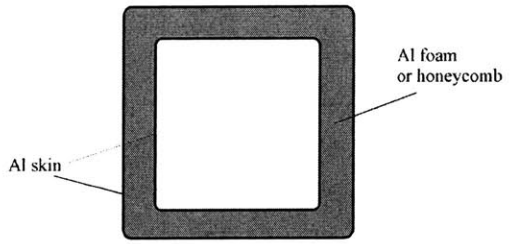

Figure 2.14: Double-walled sandwich components

Chapter 3

Axial Crushing of Ultralight Structures

Over the past twenty years, enormous efforts have been made in the academia and industry to understand the mechanisms of structural collapse in axial crushing of thin-walled metal tubes. The axial progressive folding deformation of the tubes is known to be an efficient energy absorbing mechanism. It is recognized that the number of "angle" elements on a tube's cross-section decides, to a large extent, on the efficiency of the energy absorption [53, 54]. It is therefore desirable to design thin-walled sheet metal profiles or extrusions with internal webs for weight-efficient energy absorption. The axial crushing of single-cell, double-cell and triple-cell aluminum extrusions is studied analytically and numerically in this chapter. Based on the *Superfolding Element* theory [53, 54], an analytical solution for mean crushing force of multi-cell sections is developed. Numerical simulations using a non-linear explicit finite element code are then conducted. The numerical results are compared to the analytical solutions.

In the second part of this chapter, the axial crushing of aluminum foam-filled multi-cell columns is addressed. The applications of cellular solids such as aluminum foam and honeycomb as reinforcement to thin-walled structures, and as cores for sandwich panels, have received increasing interest in recent years. Aluminum foam is of particular interest because of its mass efficiency, its attractive mechanical prop-

erties, and the recent development of cost-effective production process. Extensive studies have been carried out by a number of authors on the axial crushing behavior of foam-filled columns [12, 13, 14, 15, 16, 10, 39], and it was revealed that the crushing resistance and energy absorption of thin-walled columns are improved dramatically by filling them with aluminum foam. This is due to the interaction between the tube wall and the foam core which changes the local buckling mode of the tube wall. Seizberger et al. [12, 13] conducted experimental studies on the axial crushing of steel columns filled with aluminum foam. Various cross-sections were considered in their studies, including square, hexagonal, octagonal and bitubal arrangements of these cross-sections (two concentrically oriented profiles with aluminum foam in between). They reported that considerable mass efficiency improvements with respect to energy absorption were obtained by foam filling, particularly the bitubal arrangements. Comprehensive experimental studies on the effect of filling thin-walled square and circular aluminum extrusions with aluminum foam were carried out by Hanssen et al. [14, 15, 16]. Santosa et al. [10, 39] conducted numerical investigations on the effect of foam-filling undergoing axial crushing. Aluminum foam filling was found to be preferable to thickening the column wall in terms of specific energy absorption. Based on their numerical simulations, a simple closed-form solution was developed to calculate the mean crushing force of foam-filled square sections. It was found that the increase of mean crushing force of a filled column has a linear dependency on the foam compressive resistance and cross-sectional area.

Numerical analyses are carried out in this chapter to simulate the axial crushing of double-cell and triple-cell extrusions filled with aluminum foam. Based on the numerical results and the analytical solutions to non-filled sections, closed-form solutions are derived to calculate the mean crushing force of foam-filled multi-cell sections.

In the third part of this chapter, an experimental study is conducted on the axial crushing behavior of aluminum foam-filled hat profiles. Closed-hat sections are commonly used in automobile structures. Experimental, numerical and theoretical studies have been initiated to investigate the crash behavior of empty closed-hat members [55, 56, 57, 58, 59, 60]. McGregor et al. [55] presented the experimental results for the performance of aluminum structural components with various closed-hat sections subjected to axial and bending loading. It has been demonstrated in their work that it is possible to obtain weight saving of around 45% of aluminum automotive

structures in comparison with an equivalent mild steel structure while still meeting the required structural performance in terms of crashworthiness and other structural performance criteria. However, no extensive experimental data regarding axial crushing and bending collapse of aluminum closed-hat sections with aluminum foam filler appears to have been published in the open literature.

A total of 46 specimens were tested in this experimental program, 34 of which were of length 350mm and tested in axial crushing mode. The remaining specimens were of length 675mm and were tested in bending collapse mode, which will be discussed in the next chapter. Three different cross-sections are considered which are single-hat, double-hat and double-hat with a center plate. The sheet metal is aluminum alloy HS5754 with 2.0mm gauge. The foam is CYMAT Al-SiC foam with apparent mass density of 0.27 g/cm^3.

3.1 Single-cell and Multi-cell Thin-walled Extrusions

The *Superfold Element* theory [53, 54] on the crushing mechanics of thin-walled structures is reviewed first. Then theoretical solutions to the mean crushing force of multi-cell columns undergoing axial crushing is derived based on this theory. Numerical analyses using the explicit finite element code PAM-CRASH are then carried out, and the results are compared to the theoretical solutions

3.1.1 *Superfolding Element* Theory

The *Superfolding Element* theory on the crushing mechanics of thin-walled structures was developed by Wierzbicki and Abramowicz [53, 54] to describe the crushing behavior of a class of thin-walled structures. The physical problem considered in the theory was two intersected plates subjected to axial compression. The initial geometry of the compressed element was defined by the height $2H$, total width b, wall thickness t, and the angle $2\psi_0$ between two adjacent plates. The current geometry was described by the crushing distance δ. See Fig.3.1.

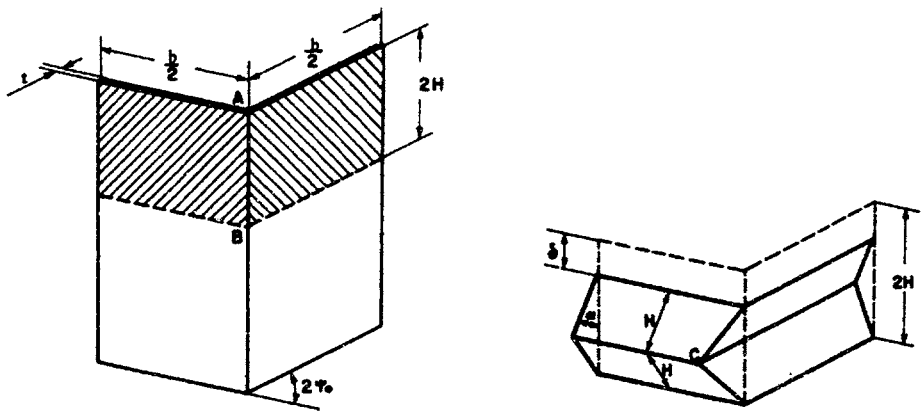

Figure 3.1: The geometry of the *Superfolding Element.* Left: initial geometry. Right: global geometry of the basic folding mechanism

The following assumptions were made in the derivation:
(i) The structure consists initially of planar surface element.
(ii) The material is regarded as rigid-perfectly plastic with a constant value of flow stress σ_0.
(iii) The length of the local buckling wave $2H$ remains constant during the formation of each buckle or fold.
(iv) The constraints imposed on the crushing process by the boundary and symmetry conditions are forcing the fold lines to move through the material.

A basic folding mechanism was then constructed based on the above assumptions and the kinematic continuity conditions. Figure 3.2 shows the proposed basic folding mechanism, which is a one-degree-of-freedom system and consists of four trapezoidal elements, a section of two horizontal cylindrical surfaces, two inclined conical surfaces, and a section of a toroidal surface.

The equilibrium of the system was expressed via the principle of virtual velocities

$$P\dot{\delta} = \dot{E}_{int} \tag{3.1}$$

The product $P\dot{\delta}$ represents the rate of work of external force where the relative velocity of the uniformly shortened upper and lower edges of the basic folding mechanism is

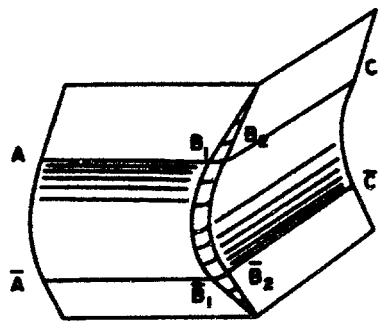

Figure 3.2: Basic folding mechanism in *Superfolding Element* theory

denoted by $\dot{\delta}$ while P is the instantaneous force. The rate of energy $\dot{E}_{int}$ dissipated in the crushing process results from the continuous and discontinuous velocity fields (horizontal and inclined hinge lines)

$$\dot{E}_{int} = \int_S (M^{\alpha\beta}\dot{\kappa}_{\alpha\beta} + N^{\alpha\beta}\dot{\lambda}_{\alpha\beta})ds + \int_L M_0\dot{\theta}dl \tag{3.2}$$

where $\dot{\kappa}_{\alpha\beta}$ and $\dot{\lambda}_{\alpha\beta}$ are respectively the rate of curvature and the rate of extension in the continuous deformation field; $M^{\alpha\beta}$ and $N^{\alpha\beta}$ are respectively stress couples and stress resultant; $M_0 = \frac{1}{4}\sigma_0 t^2$, the fully plastic bending moment.

Since the basic folding mechanism is a one-degree-of-freedom system, the equilibrium equation Eq.(3.1) can be integrated over the whole deformation process (distance $2H$), which gives the balance of total energies

$$2P_m H = E_1 + E_2 + E_3 \tag{3.3}$$

where P_m is the mean crushing force; E_1 is the energy dissipated in the continuous deformation field; E_2 and E_3 are respectively the energy dissipated on the horizontal hinge lines and on the inclined hinge lines. E_1, E_2 and E_3 can be calculated from the geometry of the basic folding mechanism.

From Eq.(3.3), a general form of the formula for P_m can be obtained (for details, see

reference [53])

$$\frac{P_m}{M_0} = A_1\frac{r}{t} + A_2\frac{b}{H} + A_3\frac{H}{r} \tag{3.4}$$

where the numerical values of the coefficients A_1, A_2 and A_3 are known and depend on the type of problem. The wall thickness is denoted by t and r is the smaller radius of the toroidal surface.

It was postulated in the derivation that the collapse mechanism, which activates and persists in the course of the crushing process, leads to the least possible amount of the mean crushing force. The unknown parameters can thus be determined from the set of equations

$$\frac{\partial P_m}{\partial H} = 0, \qquad \frac{\partial P_m}{\partial r} = 0 \tag{3.5}$$

which results in an expression for the mean crushing force

$$\frac{P_m}{M_0} = 3\sqrt[3]{A_1A_2A_3}\sqrt[3]{b/t} \tag{3.6}$$

and the half folding wavelength

$$H = \sqrt[3]{A_2^2/(A_1A_3)}\sqrt[3]{b^2t} \tag{3.7}$$

The result shows that two thirds of the plastic energy is always dissipated through inextensional deformations at stationary and moving plastic hinge lines. The extensional deformation, confined to the small fraction of the total area of the shell, are responsible for the remaining one-third of the dissipated energy.

For a square box column with with b and wall thickness t, the theory gives the mean crushing force,

$$P_m = 9.56\sigma_0 t^{\frac{5}{3}} b^{\frac{1}{3}} \tag{3.8}$$

The above formula was revised by the same authors [54] taking the effect crushing distance into account

$$P_m = 13.06\sigma_0 t^{\frac{5}{3}} b^{\frac{1}{3}} \tag{3.9}$$

For a material with power law hardening, the flow stress σ_0 can be approximated by an energy equivalent stress [39]

$$\sigma_0 = \sqrt{\frac{\sigma_y \sigma_u}{1+n}} \tag{3.10}$$

where σ_y and σ_u denote the yield strength and the ultimate strength of the material, respectively; n is the exponent of the power law.

3.1.2 Simplified *Superfolding Element* Theory for Multi-cell Sections

In order to apply the *Superfolding Element* theory to the multi-cell sections (such as double-cell and triple-cell, see Fig.3.3), a simplified approach is used in the following derivation. In this approach, instead of constructing a kinematically admissible model consisting of trapezoidal, toroidal and cylindrical surfaces with moving hinge lines as described above, the basic folding element proposed hereby only consists of three extensional triangular elements and three stationary hinge lines [61]. See Fig.3.4 for the global geometry of the basic folding mechanism, and Fig.3.5 for extensional elements and bending hinge lines on the basic folding mechanism.

Figure 3.4 shows one contributing flange with width c (which is a half of the sectional width b on a single-cell section), thickness t, length $2H$ (folding wavelength), and flow stress σ_0. After deformation, three membrane elements (one in extension and two in compression) are developed near the corner line (Fig.3.5(a)), and three horizontal stationary hinge lines are developed on the flange with rotation angles θ, 2θ and θ

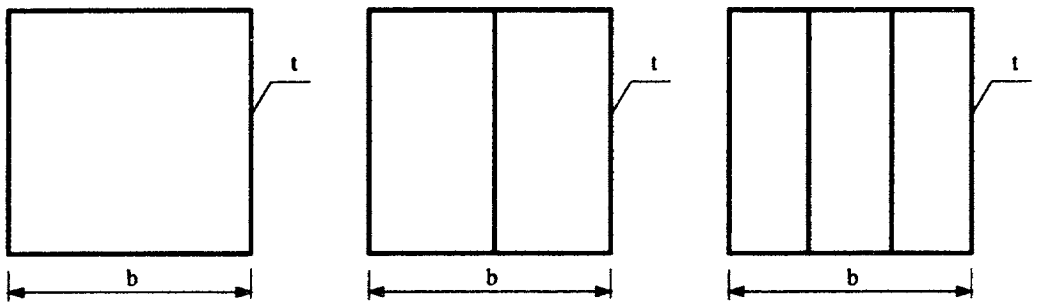

Figure 3.3: Single-cell, double-cell and triple-cell cross-sections

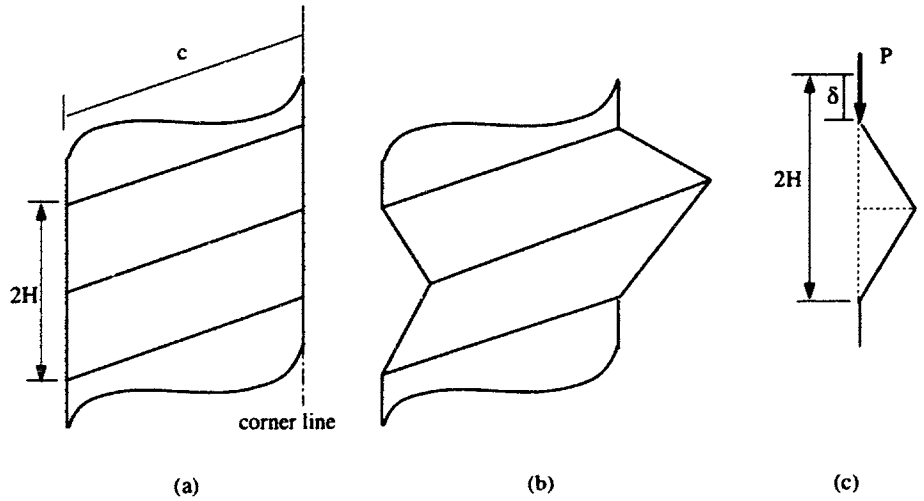

Figure 3.4: The global geometry of the basic folding mechanism. (a) Before deformation. (b) After deformation. (c) Side view

respectively (Fig.3.5(b)). The equilibrium of the system can be stated by the principle of virtual velocities

$$P\dot{\delta} = \dot{E}_b + \dot{E}_m \tag{3.11}$$

where P denotes the instantaneous crushing force; $\dot{\delta}$ is the axial displacement rate; $\dot{E}_b$ and $\dot{E}_m$ are respectively the energy dissipation rate in bending and membrane deformation.

By integrating Eq.(3.11) for one wavelength in the process of progressive folding, the

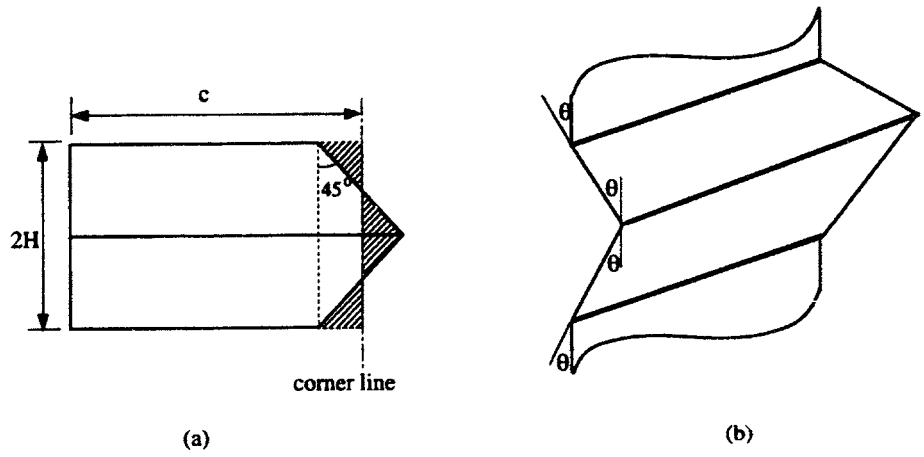

Figure 3.5: Extensional elements and bending hinge lines

equilibrium can be restated as

$$P_m 2H = E_b + E_m \tag{3.12}$$

In the above equation, P_m denotes the mean crushing force. The membrane energy E_m dissipated during one wavelength crushing can be evaluated by integrating the extensional and compressional area (shaded area in Fig.3.5(a))

$$E_m = \int_S \sigma_0 t ds = \frac{1}{2}\sigma_0 t H^2 = 2M_0 \frac{H^2}{t} \tag{3.13}$$

where $M_0 = \frac{1}{4}\sigma_0 t^2$, the fully plastic bending moment of the flange plate.

The bending energy E_b can be calculated by summing up the energy dissipation at three stationary hinge lines

$$E_b = \sum_{i=1}^{3} M_0 \theta_i c_i \tag{3.14}$$

where θ_i is the rotation angle at each hinge line. For simplicity, it is assumed that the flange is completely flattened after the axial displacement of $2H$, see Fig.3.6.

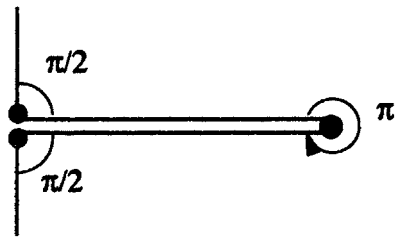

● plastic hinge line

Figure 3.6: A simplified model of post-deformation geometry

It can be seen therefore that the rotation angles at three hinge lines are respectively $\frac{\pi}{2}$, π and $\frac{\pi}{2}$. On employing Eq.(3.14), E_b can be obtained

$$E_b = 2\pi M_0 c \tag{3.15}$$

With Eq.(3.12), Eq.(3.13) and Eq.(3.15), the mean crushing force P_m can then be obtained

$$\frac{P_m}{M_0} = \left(\frac{H}{t} + \pi\frac{c}{H}\right) \tag{3.16}$$

However, in a real structure, the flange can never be completely crushed as in Fig.3.6. The available crush distance for one wavelength is actually less than $2H$. Wierzbicki and Abramowicz [53, 54] found that the effective crush distance is about 70%$\backsim$ 75% of the wavelength. This value is taken as 0.75 in the following derivation for simplicity. Eq.(3.16) should then be modified taking the effective crush distance into account

$$\frac{P_m}{M_0} = \frac{4}{3}\left(\frac{H}{t} + \pi\frac{c}{H}\right) \tag{3.17}$$

Now lets consider a multi-cell section which consists of N number of contributing flanges (for example, $N = 14$ for double-cell and $N = 20$ for triple-cell). Assume

the wall thickness is constant over the cross-section, the mean crushing force of the multi-cell section can be calculated by summing up all the contributing flanges

$$\frac{P_m}{M_0} = \frac{4}{3}\sum_{i=1}^{N}\left(\frac{H}{t} + \pi\frac{c}{H}\right) = \frac{4}{3}\left(\frac{NH}{t} + \frac{\pi l}{H}\right) \tag{3.18}$$

where l is the total length of the walls (and internal webs) of the cross-section.

The wavelength H can be determined by the stationary condition of the mean crushing force

$$\frac{\partial P_m}{\partial H} = 0 \tag{3.19}$$

which leads to

$$H = \sqrt{\frac{\pi l t}{N}} \tag{3.20}$$

Substituting Eq.(3.20) into Eq.(3.18) results in the final expression of the mean crushing force for a multi-cell section

$$P_m = \frac{2}{3}\sigma_0 t\sqrt{\pi N A} \tag{3.21}$$

where A is the (material) area of the cross-section.

Take, for instance, a double-cell section with width b. The number of contributing flanges is $N = 14$, and the material area $A = 5bt$. Eq.(3.21) can then be rewritten for the double-cell section

$$P_m^{II} = 9.89\sigma_0 b^{\frac{1}{2}} t^{\frac{3}{2}} \tag{3.22}$$

Similarly, for triple-cell section ($N = 20$, $A = 6bt$), the mean crushing force is

$$P_m^{III} = 12.94\sigma_0 b^{\frac{1}{2}} t^{\frac{3}{2}} \tag{3.23}$$

It should be noted that the above theory is derived for a rigid perfectly plastic material with a constant flow stress σ_0. For a material with power law hardening $\sigma = \sigma_u(\frac{\epsilon}{\epsilon_u})^n$, the flow stress σ_0 can be approximated by an average stress over the strain range $0 < \epsilon < \epsilon_u$ (see Fig.3.7).

$$\sigma_0 = \frac{1}{\epsilon_u}\int_0^{\epsilon_u} \sigma d\epsilon = \frac{\sigma_u}{1+n} \tag{3.24}$$

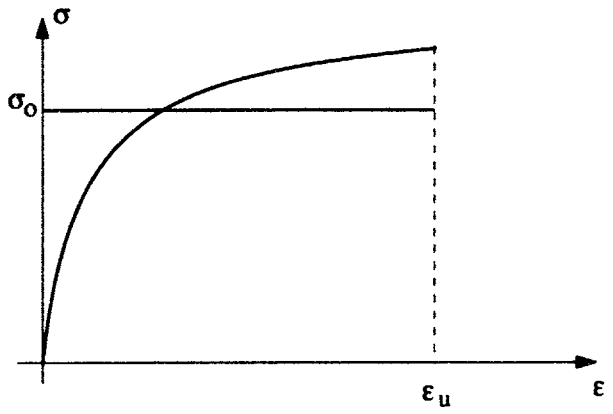

Figure 3.7: Energy equivalent flow stress

3.1.3 Numerical Simulations of Multi-cell Sections

Quasi-static finite element analyses are carried out using the explicit code PAM-CRASH to simulate the axial crushing of single-cell, double-cell and triple-cell columns. Numerical results are then compared to the theoretical solutions derived above.

3.1.3.1 Finite Element Modeling

The single-cell, double-cell and triple-cell columns (see Fig.3.3) with sectional width b = 80mm and column length L = 400mm were considered in the analyses. The wall thickness for each cross-section was varying in the range of 1mm $\backsim$ 3mm. The column walls were modeled using the Belytschko-Tsay 4-node shell elements with three integration points through the thickness and one integration point in the element plane. One end of the column was simply supported, while the other end was pushed in the axial direction by a rigid wall. A single surface contact algorithm was used in the simulation to account for the contact between lobes during deformation.

In order to initiate a stable and progressive crushing, triggers with a magnitude of 5mm were introduced in the models. The positions of the triggers were guided by the theoretical predictions of the buckling and folding wavelength: a half folding wavelength H down from the pushed end of the columns, where H was calculated by Eq.(3.7) for single-cell and Eq.(3.20) for multi-cell columns. The shape of the triggers are illustrated in Fig.3.8.

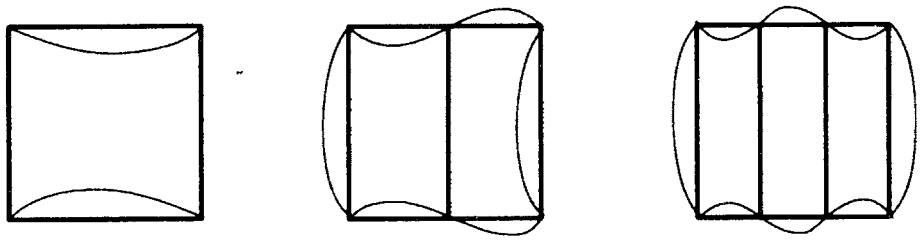

Figure 3.8: Triggers introduced in the finite element models

The column wall material was aluminum extrusion AA6061 T4, with Young's modulus E = 70GPa, Poisson's ratio ν = 0.28, yield strength σ_y = 110.3MPa, ultimate strength σ_u = 213.0MPa, and elongation 19%. The tensile stress-strain curve is shown in Fig.3.9. It can be well fitted by a power law expression with n = 0.2. The constitutive behavior of the thin shell element was based on an elastic-plastic material model with Von Mises isotropic plasticity algorithm with piecewise linear plastic hardening.

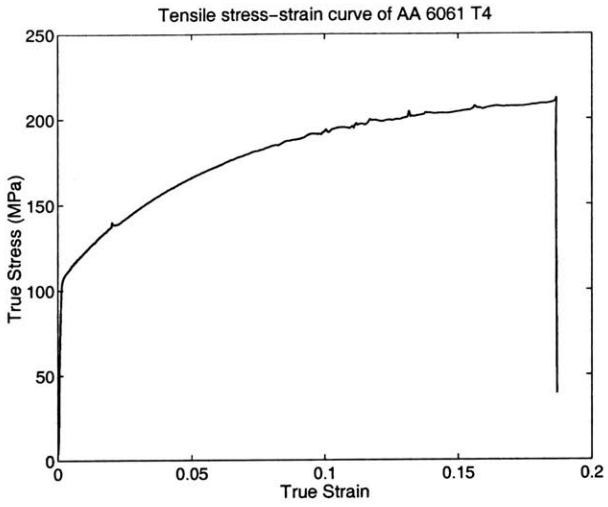

Figure 3.9: Tensile stress-strain curve of AA6061 T4

3.1.3.2 Numerical Results

The specimens were crushed axially in simulations with a final displacement equal to 75% of the initial length. Fig.3.10 shows examples of deformed meshes of single-cell (t = 3.0mm), double-cell (t = 2.0mm) and triple-cell (t = 1.67mm) columns. The three columns thus have the same mass with these values of thickness. The corresponding crushing force responses are shown in Fig.3.11.

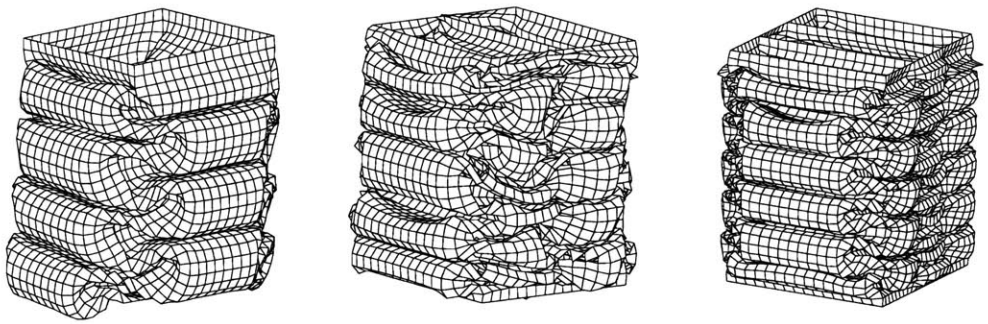

Figure 3.10: Deformation patterns of single-cell, double-cell and triple-cell columns

As can be seen, all three columns developed stable and progressive folding deformation patterns. The crushing forces fluctuate around mean values before they rise steeply

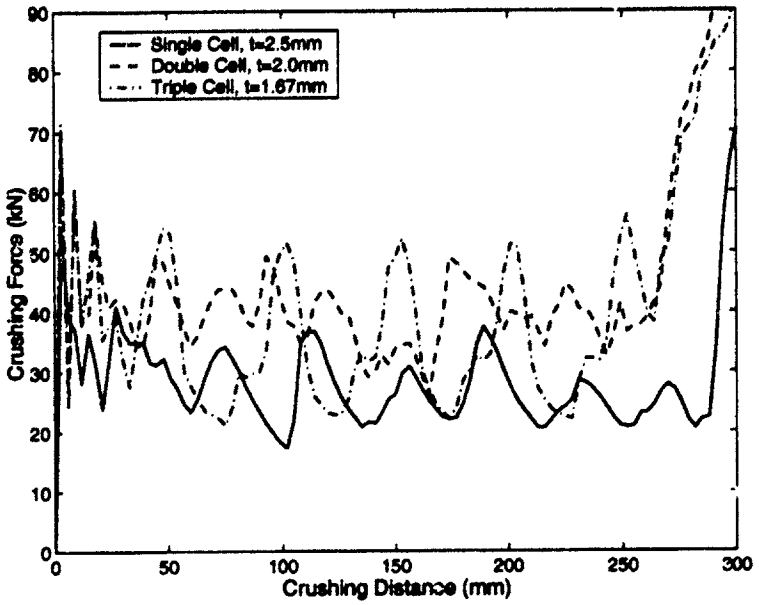

Figure 3.11: Crushing force responses of single-cell, double-cell and triple-cell columns

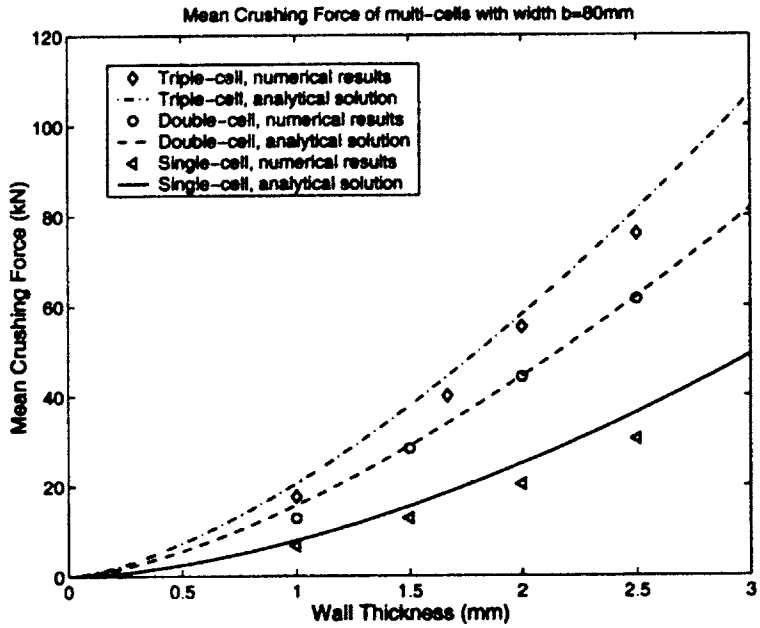

Figure 3.12: Mean crushing forces predicted by theoretical solutions and by numerical simulations

when the deformation capacity is exhausted at the effective stroke length. While the exact definition of the effective stroke length on the force-displacement curve is somehow not unique, the theoretical prediction by Wierzbicki and Abramowicz [53, 54] giving the stroke efficiency of 0.70∽0.75 (stroke efficiency is defined as the ratio between the effective stroke length to the initial length of the column) agrees very well with the numerical predictions. The mean crushing force P_m is defined by

$$P_m = \frac{1}{s_e}\int_0^{s_e} P(s)ds \tag{3.25}$$

where s_e is the effective stroke length, and is taken as $0.73l$ in the following calculation.

The mean crushing forces of single-cell, double-cell and triple-cell columns with various wall thicknesses were calculated, and the results are shown in Fig.3.12. The theoretical solutions (Eq.(3.9), Eq.(3.22) and Eq.(3.23)) are shown in the same figure for comparison. One can see that in the case of empty columns the theoretical solutions compared very well with the numerical predictions.

3.2 Foam-filled Extrusions

In order to achieve higher weight efficiency in energy absorption, the lightweight cellular materials such as aluminum foam was utilized to fill the thin-walled structures. Significant increases in the crushing resistance and energy absorption were obtained from the direct compressive strength of the foam and from the interaction between the foam and the column wall. The foam filler functions as an elastic-plastic foundation to the column wall, and accordingly reduces the folding wavelength and thus increases the crushing resistance. In this section, the crushing resistances of foam-filled single-cell and multi-cell columns were studied by dimensional analysis and by numerical simulations. The mean crushing force elevation due to the foam filling for such cross-sections were quantified thereafter.

3.2.1 Foam-filled Single-cell Sections

Based on the results of numerical simulations, Santosa and Wierzbicki [10] assumed that the mean crushing force of a foam-filled square column (P_{mf}) takes an additive form of the mean crushing force of a non-filled column (P_m) and a force elevation due to the foam filling (ΔP_m), that is

$$P_{mf} = P_m + \Delta P_m \tag{3.26}$$

where the force elevation ΔP_m is a function of the materials and geometries of the column and the foam filler

$$\Delta P_m = f(\sigma_0, \sigma_f, b, t) \tag{3.27}$$

where σ_0 and σ_f are respectively the flow stress of the column wall material and the compressive strength of the foam; b and t are respectively the sectional width and the wall thickness.

Now let us inspect the dimensions of these quantities in the standard LMT-base dimension system. ΔP_m is the dependent quantity, and σ_0, σ_f, b, t are the complete

set of independent variables. In the chosen base dimension system, the dimension functions read

$$[\Delta P_m] = MLT^{-2}; \quad [\sigma_0] = [\sigma_f] = ML^{-1}T^{-2}; \quad [b] = [t] = L \tag{3.28}$$

By simple inspection, we can choose two dimensionally independent quantities, σ_f and b. The sought dimensionless form of Eq.(3.27) is straightforwardly obtained by applying Vaschy-Buckingham Theorem (or Pi-Theorem) (e.g. Ulm [62])

$$\frac{\Delta P_m}{\sigma_f b^2} = F\left(\frac{\sigma_0}{\sigma_f}, \frac{b}{t}\right) \tag{3.29}$$

Hassen et al. [39] conducted experiments on foam-filled columns with a wide range of width-to-thickness ratio, $28 \leq \frac{b}{t} \leq 80$ (which is a practical range of many thin-walled structures applications), and with three different column material, AA6060 T4, AA6082 T4 and mild steel Rst37, and with a wide range of foam strength $0.3 \leq \sigma_f \leq 12.5MPa$. They found that the non-dimensionalized force elevation $\frac{\Delta P_m}{\sigma_f b^2}$ shows very weak dependences on the quantities $\frac{\sigma_0}{\sigma_f}$ and $\frac{b}{t}$ in the interested range (see Fig.3.13). Based on this observation, Eq.(3.29) was further simplified

$$\frac{\Delta P_m}{\sigma_f b^2} = C \tag{3.30}$$

The constant C was determined by fitting the experimental and numerical simulation data, and was found to be 1.8. Therefore, the mean crushing force of the foam-filled single-cell sections reads

$$P_{mf} = P_m + 1.8b^2\sigma_f \tag{3.31}$$

where P_{mf} is the mean crushing force of the filled section; P_m denotes the mean crushing force of the corresponding non-filled section and is given in Eq.(3.9); b is the sectional width; σ_f is the compressive strength of the foam material.

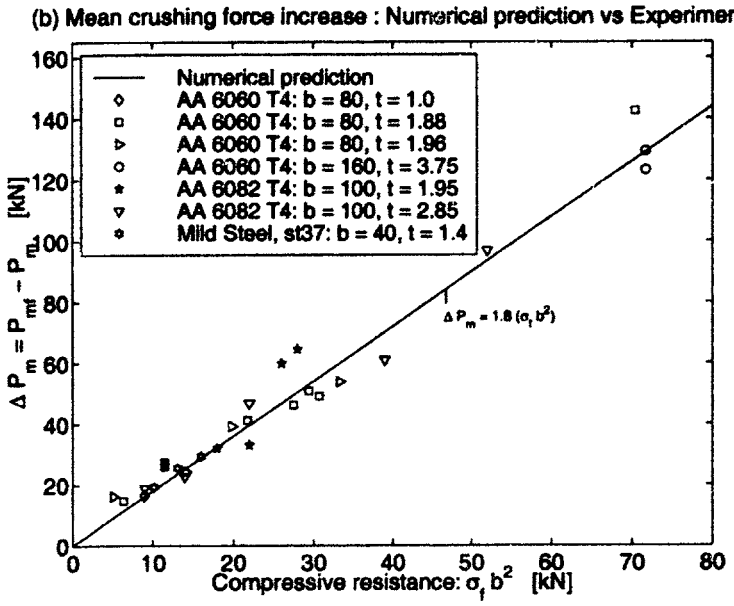

Figure 3.13: Mean crushing force elevation due to foam filling:experiments and prediction (Santosa et al. [39])

The above equation can be interpreted that the increase in the mean crushing force of the foam-filled section is due to the direct compressive resistance of the foam ($b^2\sigma_f$) plus the foam-wall interaction effect $0.8b^2\sigma_f$ which accounts for 80% of the direct compressive resistance of the foam. The proposed solution is within 8% of the experimental data for wide range of column geometries, materials and foam strength [39].

3.2.2 Foam-filled Multi-cell Sections

Using the same argument as above, the mean crushing force elevation of double-cell and triple-cells due to foam filling are assumed to have a linear dependence on the foam strength and the cross-sectional area of the column. The proportionality constant are to be determined by the following numerical analyses.

3.2.2.1 Finite Element Modeling

The double-cell and triple-cell columns with sectional width $b = 80$mm were considered in the analyses (see Fig.3.14). The wall thickness of the double-cell column was 2.0mm, while the wall thickness of the triple-cell was 1.67mm (so that two empty columns have the same weight). The column walls were modeled with Belytschko-Tsay 4-node shell elements, while the aluminum foam filler was modeled with 8-node solid elements. The interaction between the foam filler and the column wall was simulated with a surface-surface sliding contact. A single surface contact algorithm was used to account for the contact between the lobes of the walls. The axial crushing process was simulated quasi-statically by a moving rigid wall pushing one end of the column while the other end was simply supported. The same type of triggers as illustrated in Fig.3.8 were introduced in the finite element models.

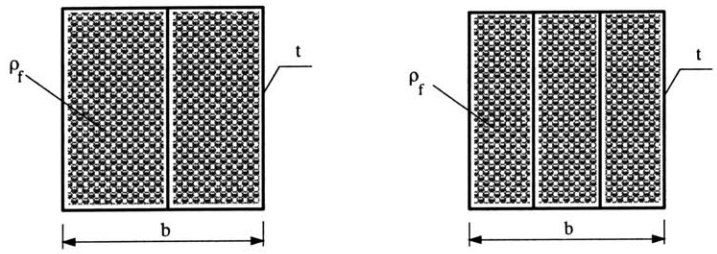

Figure 3.14: Foam-filled double-cell and triple-cell sections

The column wall material was aluminum extrusion AA6061 T4. Its mechanical properties and tensile stress-strain curve were provided in the previous section. The mechanical behavior of aluminum foam is characterized by elastic modulus E_f, plastic collapse stress σ_f, shear modulus G_f, plastic shear strength τ_f, and densification strain ϵ_D, see Fig.2.7. These parameters strongly depend on the aluminum foam density ρ_f, and they were described in Chapter 2 via Eq.(2.1)$\backsim$ Eq.(2.6). The maximum principal stress yielding model, as discussed in Chapter 2, was applied in the calculation for aluminum foam.

The CYMAT Al-SiC foam was used in the present analysis, with the plastic flow stress of the base material $\sigma_{0f} = 98.3$MPa, and Young's modulus $E_f = 70$GPa.

3.2.2.2 Numerical Results

Numerical simulations were carried out for the double-cell and triple-cell columns filled with aluminum foam with relative density in the range of 2.5∽20%. Fig.3.15 shows examples of deformed meshes of columns filled with 10% relative density foam.

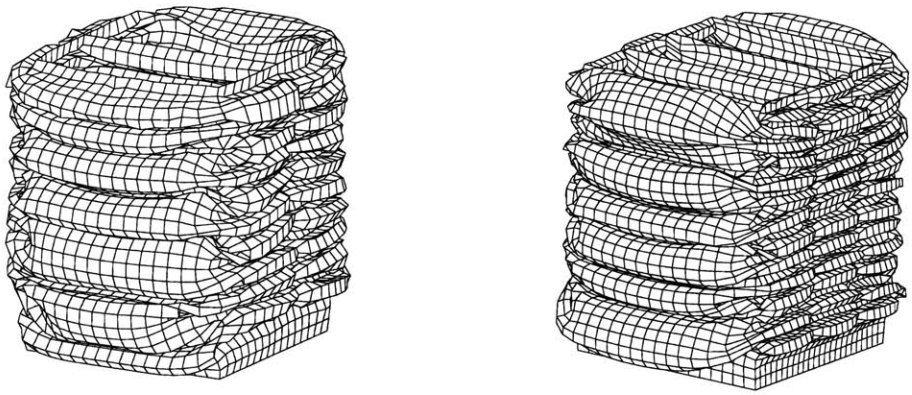

Figure 3.15: Deformation patterns of column walls of double-cell and triple-cell filled with 10% relative density foam

One can see that the columns deformed in a stable and progressive folding patterns. Compared to the non-filled columns (Fig.3.10), the filled ones exhibit smaller folding wavelength. The number of 13 lobes were developed on the filled double cell, while only 10 lobes were developed on the non-filled one. For the triple cell, 12 lobes were developed on the non-filled one, while much more lobes appeared on the triple-side of the filled one. On the other hand, the extensional folding mode (all lobes moving outward) is evident in the filled columns, while for non-filled columns the folding mode is mainly inextensional one where the individual lobes around the circumference of the column alternatively move inward and outward. Due to the foam filling, the crushing resistances are substantially elevated, as can be seen in Fig.3.16 for double-cell columns and in Fig.3.17 for triple-cell columns.

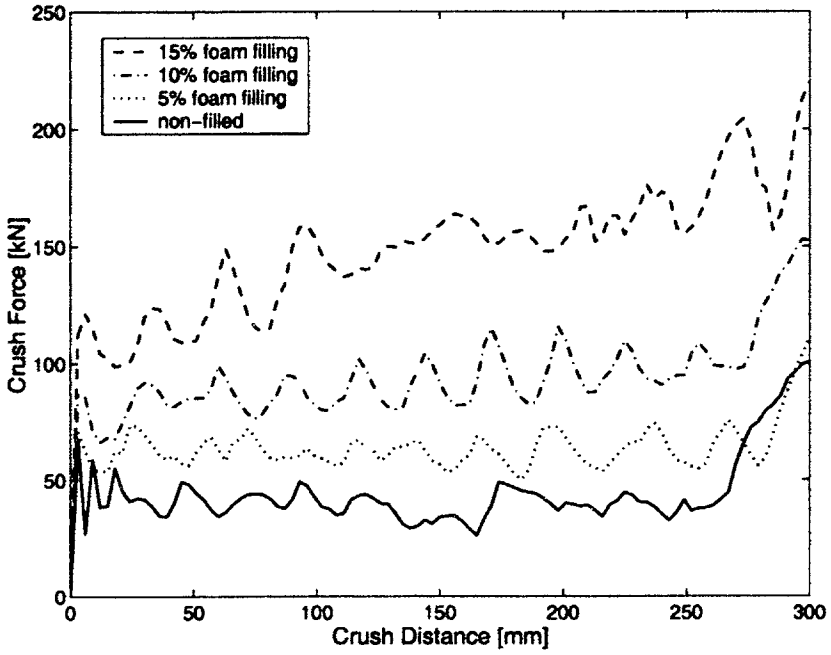

Figure 3.16: Crushing force responses of foam-filled double-cell columns

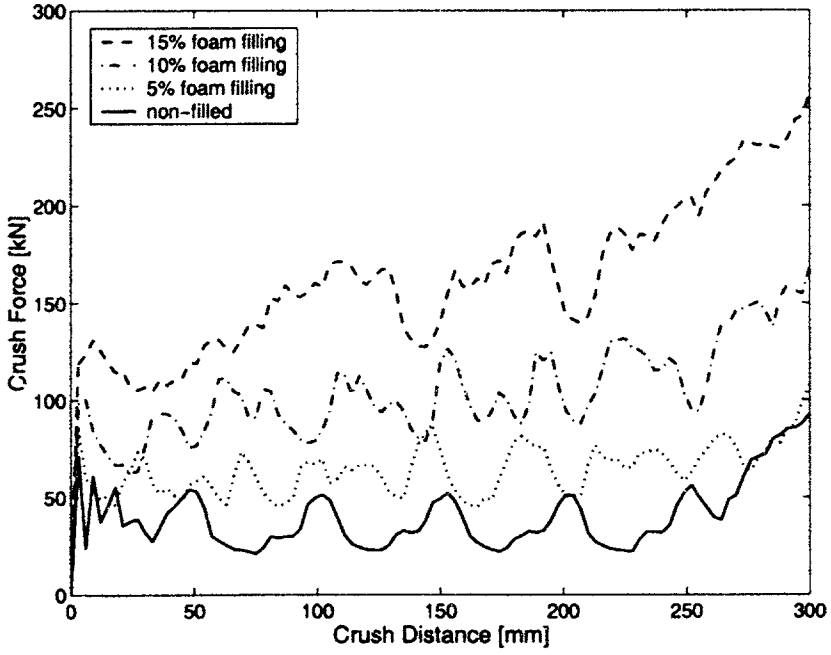

Figure 3.17: Crushing force responses of foam-filled triple-cell columns

3.2.2.3 Mean Crushing Force Prediction

The mean crushing forces up to the effective stroke length were calculated for the columns filled with various foams with relative densities in the range of 2.5∽ 20%. As can be seen in Fig.3.16 and Fig.3.17, the effective stroke length (at which the crushing force rises steeply) varies slightly for different densities of foam filling. It is therefore assumed in the mean crushing force calculation that the stroke efficiency is 0.73 for all filled columns considered in the present study, which is the same as that of non-filled ones. Using the same argument as in the case of single-cell sections that the increase of the mean crushing strength due to the foam filler depends linearly on the foam crushing strength (σ_f) and the cross-sectional area (b^2), the proportionality constants for double-cell and triple-cell sections are found to be 2.4 and 2.8 respectively, based on the numerical results obtained in the present study. Therefore, the mean crushing force of foam-filled double-cell section can be predicted by

$$P_{mf}^{II} = P_m^{II} + 2.4b^2\sigma_f \tag{3.32}$$

where P_m^{II} is the mean crushing force for a non-filled double-cell section and is given in Eq.(3.22).

Similarly, the mean crushing force of the foam-filled triple-cell section can be predicted by

$$P_{mf}^{III} = P_m^{III} + 2.8b^2\sigma_f \tag{3.33}$$

where P_m^{III} is the mean crushing force of a non-filled triple-cell section and is given in Eq.(3.23).

The above equations should be compared with Eq.(3.31) for a foam-filled single-cell column where the proportionality parameter equals 1.8. Eq.(3.32) and Eq.(3.33) can be interpreted that the elevation of the mean crushing resistance of the foam-filled section is due to the direct compressive resistance of the foam plus the foam-wall interaction effect which accounts for respectively 140% and 180% of the direct contribution of the foam for double-cell and triple-cell sections. The resulting solutions

of $\Delta P_m = P_{mf} - P_m$ as functions of foam strength are plotted in Fig.3.18 together with the numerical solutions for double cell and in Fig.3.19 for triple cell. It can be seen that the analytical curve compares very well with the finite element predictions.

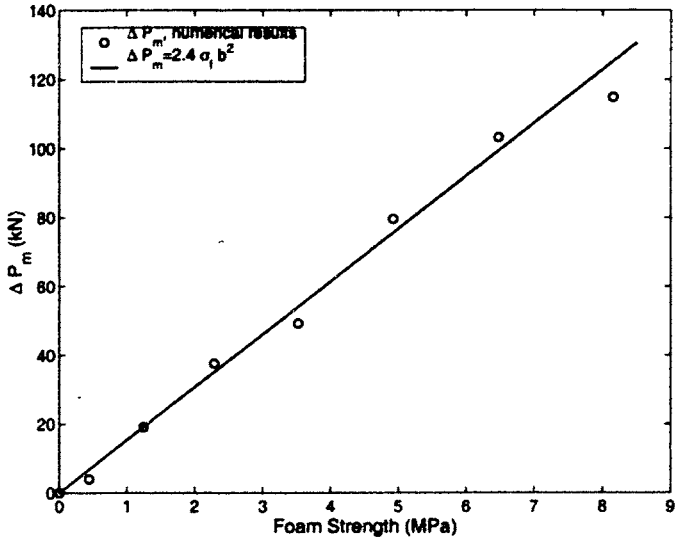

Figure 3.18: The increase of mean crushing strength due to foam filling for double cell

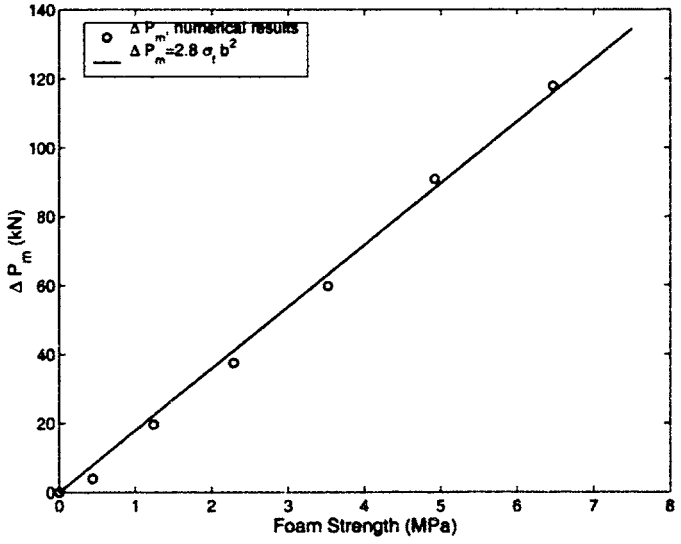

Figure 3.19: The increase of mean crushing strength due to foam filling for triple cell

3.2.3 Discussions

The axial crushing of hollow multi-cell columns were addressed in this section. Based on the *Superfolding Element* theory, an analytical solution for the mean crushing force of multi-cell sections was derived, and the solution was compared very well with the numerical predictions.

Numerical studies were also carried out on the axial crushing of foam-filled double-cell and triple-cell columns. Based upon the numerical results of filled columns and the analytical solutions for non-filled columns, closed-form expressions were derived to calculate the mean crushing strength of the foam-filled double-cell and triple-cell sections. It was found that the interaction effects between the foam core and the columns wall contribute to the total crushing resistance by the amounts equal to 140% and 180% of the direct foam resistance for double cell and triple cell, respectively.

The energy absorption En during the axial crushing up to the effective stroke length can be calculated using the expressions of the mean crushing force

$$E_n = P_m L S_E \tag{3.34}$$

where P_m is the mean crushing force; L denotes the length of the column; S_E is the stroke efficiency;

The energy absorbed is often divided by the weight of the structure to give a Specific Engery Absorption (SEA), and this quantity is widely used to judge the relative effectiveness of various energy absorbing devices and structures [3]. The specific energy absorption of foam-filled columns can be calculated

$$SEA = \frac{E_n}{m_c + m_f} \tag{3.35}$$

where m_c is the mass of the column wall and m_f is the mass of the foam filler. $m_f = 0$ for non-filled columns;

Take, for instance, columns with sectional width b = 80mm, column length L = $400mm$, and wall thickness t = 1mm. To achieve higher energy absorption, one

approach is to increase the wall thickness (up to 5mm) of the non-filled single-cell, double-cell and triple-cell sections. The other approach is to keep the wall thickness constant but increase the weight by filling the columns with aluminum foams (relative density up to 15%). Take stroke efficiency $S_E = 0.73$ in the calculation. The resulting SEAs are plotted in Fig.3.20

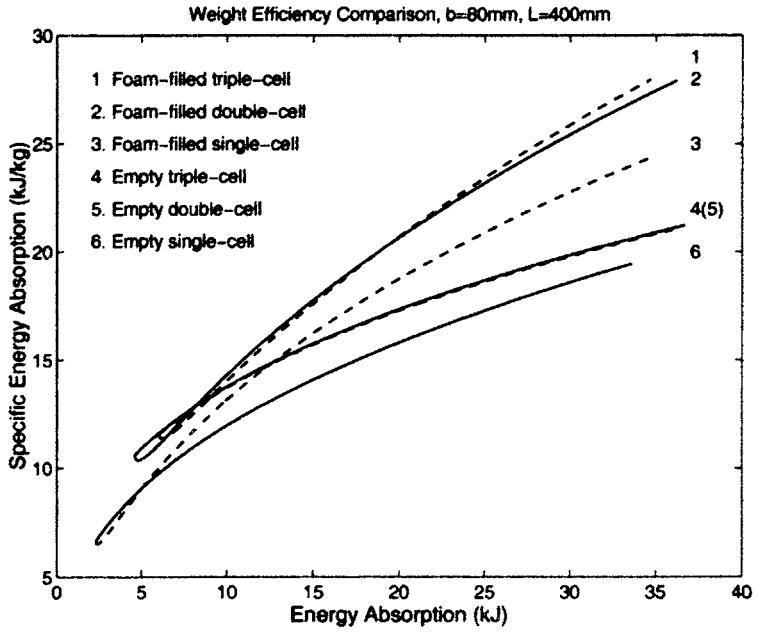

Figure 3.20: Specific energy absorptions of various types of columns

A few observations can be made based upon the SEA plot.

- The foam-filled sections generally exhibit higher specific energy absorption values and thus higher weight-efficiency in energy absorption. The gain in SEA of filled columns is about 30% for single cell and about 40% for double cell and triple cell relative to empty columns.
- The gain in SEA of the double cell and the triple cell is about 15% compared to the single cell.
- The triple cell is no better than the double cell in terms of SEA, either filled or non-filled.

- At very low energy absorption level, all the sections considered show comparable SEAs.

It should be noted that the above comparisons are based on one fixed sectional width (b = 80mm) and a same starting wall thickness (t = 1mm). In other words, the resulting SEAs are by no means optimized. According to the optimization study, which will be addressed in Chapter 6 of this thesis, the gain in SEA for foam-filled members can be as high as 300% if the sectional width, wall thickness and foam density are optimized. Besides, the wall thickness of the non-filled section in the above calculation is allowed to be increased up to 5mm. This must be limited in practical design by manufacturing consideration and fracture controlling, which will result in a much lower specific energy absorption for non-filled sections.

3.3 Foam-filled Sheet Profiles

An experimental study was carried out on aluminum sheet profiles filled with aluminum foam and subjected to axial crushing loading. The objective of the undertaken experimental program is to:

(i) study the various process of fitting aluminum foam into hat section, suitable for high volume production;

(ii) study the various joint techniques for foam-filled thin-walled hat members, including spot-welding, welding-bonding and riveting;

(iii) quantify the relative merit of foam-filled members compared to empty ones by performance tests on axial crushing

A total of 34 specimens were tested. Three different sections were considered which are single-hat, double-hat and double-hat with a center plate. All the specimens were of length 350mm. The sheet metal was aluminum alloy HS5754 with 2.0mm gauge. The CYMAT Al-SiC foam with a mass density of 0.27 g/cm^3 was used.

3.3.1 Experimental Details

3.3.1.1 "Standard" Hat Section

A "Standard" hat section in this experiment is considered as an open-hat section of 50mm x50mm, 2.0mm gauge and 21 mm flange (Fig.3.21).

This open hat section was first fitted with aluminum foam and then assembled with closing plate or center plate by various joint techniques to form three different types of closed hat sections, i.e., single hat, double hat, and double hat with a center plate. The geometry of sections is illustrated in Fig.3.22, Fig.3.23 and Fig.3.24.

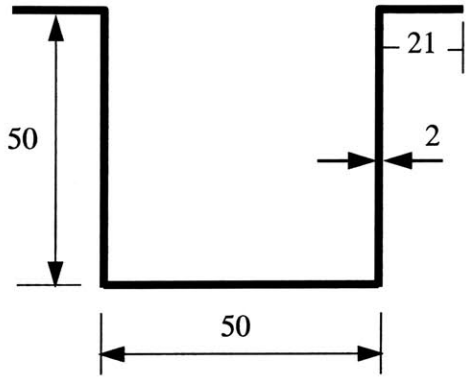

Figure 3.21: A "Standard" open hat section

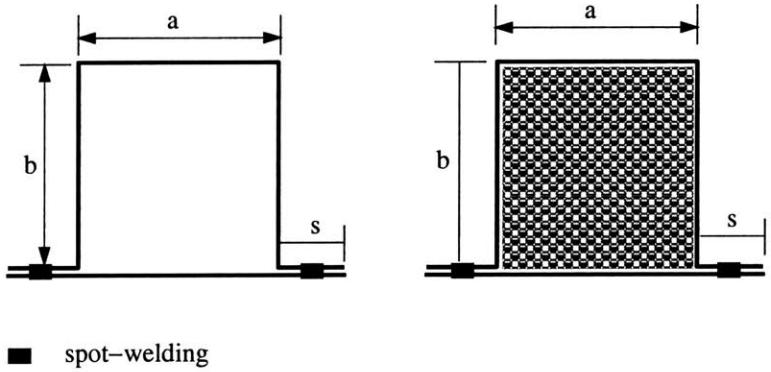

Figure 3.22: Geometry of a single-hat section (empty and foam-filled)

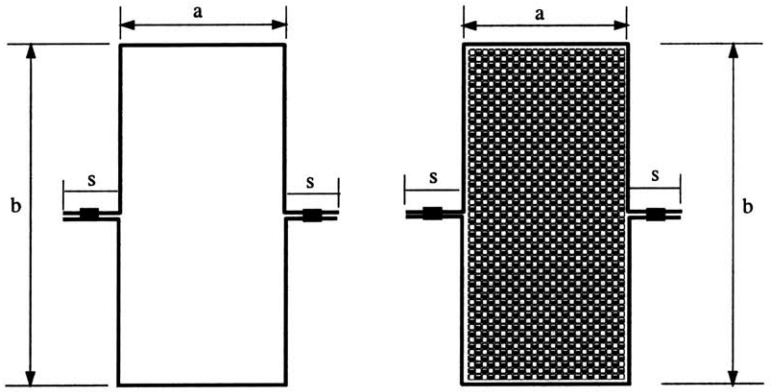

Figure 3.23: Geometry of a double-hat section (empty and foam-filled)

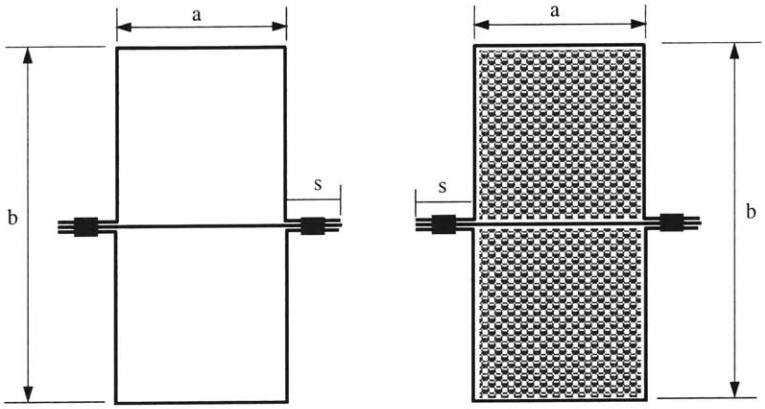

Figure 3.24: Geometry of a double-hat with center flange section (empty and foam-filled)

3.3.1.2 Foam-fitting

The aluminum foam blocks were fitted into the open hat channel by three different methods.

Precise Fitting

The inner dimensions of a few open hat channels were measured carefully. The foam blocks were cut from a foam panel by machine saw. They were then sized accurately by milling machine to fit into the open channel. Fig.3.25 shows precisely fitted sections.

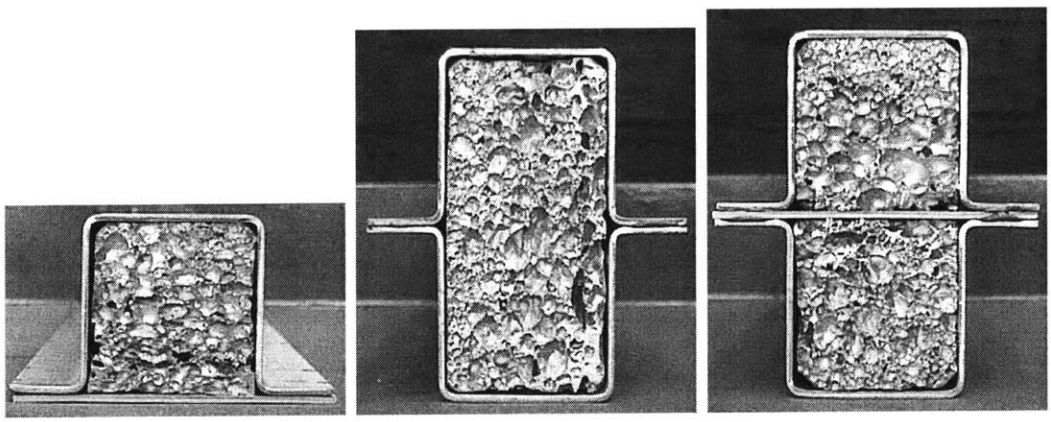

Figure 3.25: Precisely fitted sections

This fitting method does not require special processing during fitting other than cutting the foam with some prescribed tolerances. However, the foam blocks have to be machined carefully by milling machine, which is time-consuming and expensive. Worse yet, special care is needed during machining because the foam cell comprises Silicon carbide particles. It is evident that this fitting method is not suitable for mass production of foam-filled structural members. Pre-casting method successfully developed by other research centers seems to be more suitable.

Pre-compression Fitting

The second fitting method studied in this project was pre-compression fitting. The foam blocks were cut by machine saw into the sizes slightly larger (1%-2%) than the average inner dimensions of the open channels. They were then pressed into the channels by a compression jig (testing machine in the experiment). In order to prevent the channels opening up during fitting, a special foam-fitting jig was designed (Fig.3.26) to provide lateral confinement.

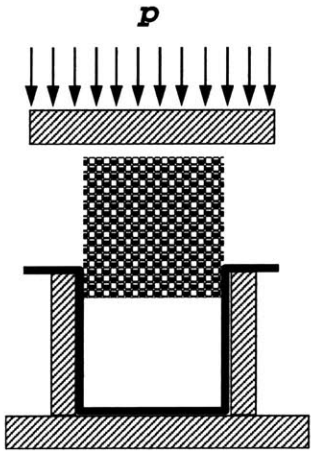

Figure 3.26: Illustration of pre-compression fitting

The width of the jig is adjustable for taking out the fitted channel after the fitting. The channel opened-up slightly and a small slant angle around 1^o was observed at each of the bottom corners (Fig.3.27). Three pre-compression fitted sections are shown in Fig.3.28.

The pressure associated with the fitting operation is quite small. No noticeable crush

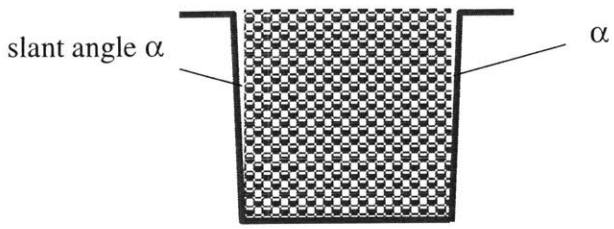

Figure 3.27: Illustration of pre-compression fitted open hat with small slant angles

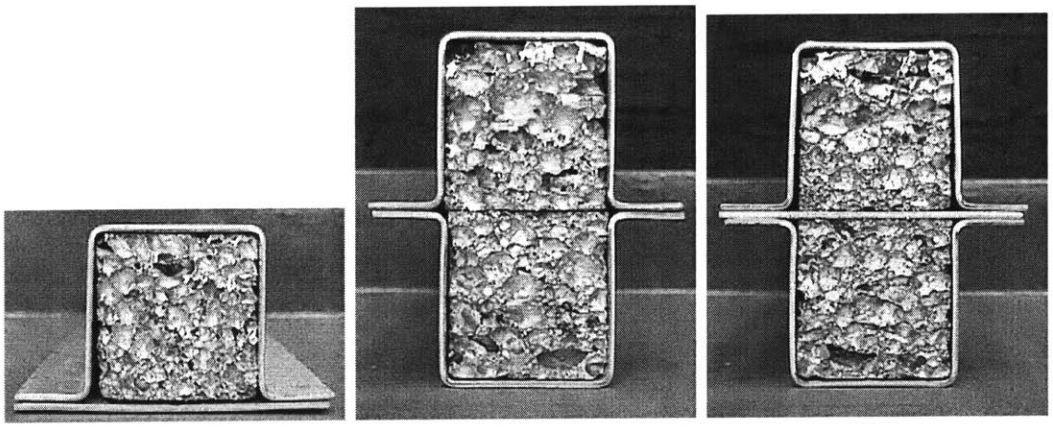

Figure 3.28: Pre-compression fitted sections

of the foam was observed. This fitting process does not require accurate machining of the foam block. The operation needed for the processing is simple. It could be developed as an appropriate way for high volume production.

Adhesive-bond Fitting

The third alternative for foam fitting is to bond the under-sized foam blocks to the sheet aluminum by adhesive. The gap between the sheet skin and the foam was set around 2-3 mm, which was filled with adhesive (Fig.3.29). Three bond fitting sections are shown in Fig.3.30.

The adhesive used in the experiment is XD4600. The fitted hat members needed to be cured by heating up to 180^oC for 40 minutes for adhesive treatment. This fitting method could also be a choice in mass production.

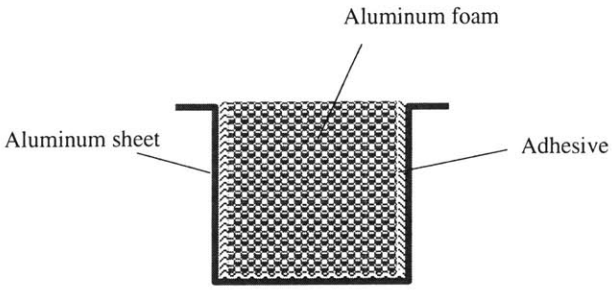

Figure 3.29: Illustration of adhesive bond fitting

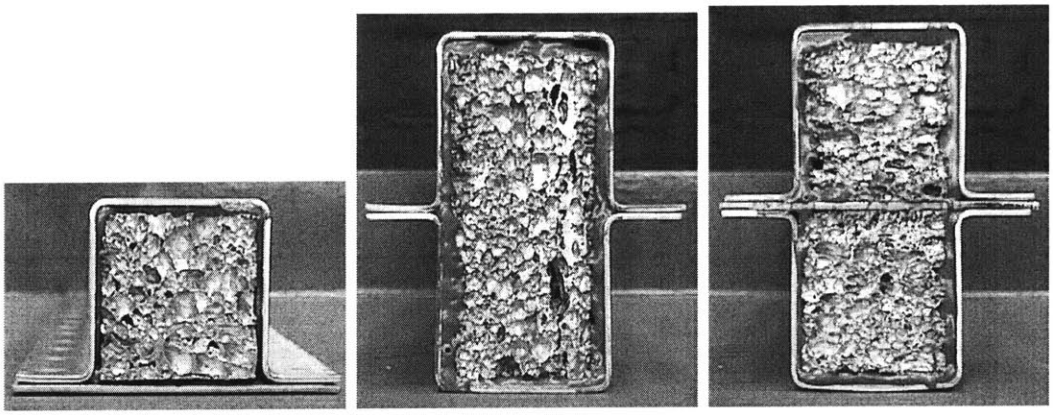

Figure 3.30: Adhesive bond fitted sectioned

3.3.1.3 Joining Techniques

The foam-fitted hat members were assembled with closing plate or center plate by spot-welding, welding-bonding and/or riveting. In this experiment, the pitch of spot-weld was set to be 25 mm for spot-welding only, and 75 mm for welding-bonding. Riveting were later added at critical locations in axially crushed specimens to strengthen the joint and prevent premature joint failure.

The strength of one spot-weld is 4.27kN (minimum average) in shear (data provided by Alcan International, Banbury Laboratory). No strength data for peel and tension is available at this moment.

3.3.1.4 Material Properties

1. Aluminum Sheet

The aluminum sheet used in the tests is HS5754, which is a high strength variant of AA5754. Fig.3.31 shows typical tensile stress-strain curves of this alloy, obtained from specimens cut from longitudinal, 45-degree and transverse directions. The mechanical properties are listed in Table 3.1.

Table 3.1: Mechanical properties of aluminum alloy HS5754

	0.2% Proof stress (MPa)	Ultimate stress (MPa)	Young's modulus(MPa)	Poisson's ratio	Elongation (%)
Longitudinal	110	244	70,00	0.33	22.3
45 degree	106	234	70,000	0.33	26.2
Transverse	108	234	70,000	0.33	24.3

2. Aluminum Foam

The aluminum foam used in the testing was manufactured and provided by CYMAT. The foam density is 0.27 g/cm^3. Fig.3.32 shows typical stress-strain curves for a cube of aluminum foam obtained from quasi-static uni-axial compression crush tests

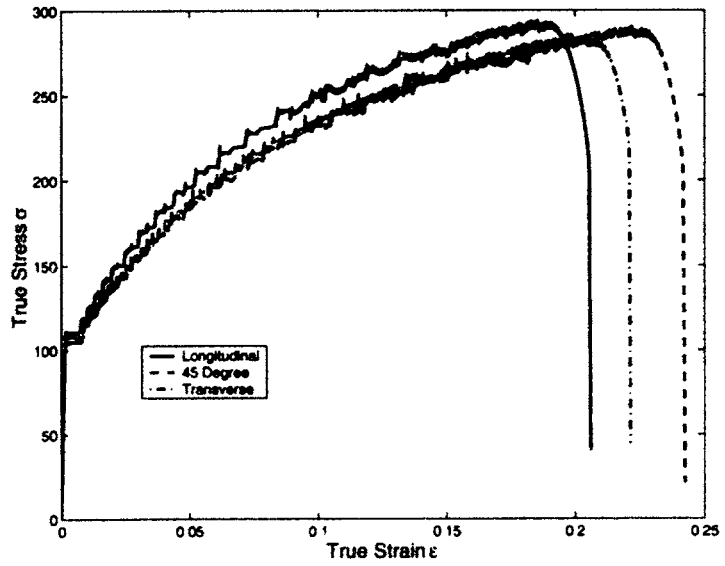

Figure 3.31: Typical tensile stress-strain curves of aluminum alloy HS5754, 2.0mm gauge

in three different directions. The directions are defined as: l: longitudinal direction of the foam panel; t: thickness direction of the foam panel; w: width direction of the foam panel. One can see, the foam shows certain anisotropy, which is associated with its manufacturing process. The foam core was fitted into the hat member with its l direction aligning with the axial direction of the column and its t direction aligning with the width direction of the hat section.

3. Adhesive

The adhesive applied in bonding foam to the aluminum sheet and in weld-bond joint is Adhesive XD4600. The tensile properties are listed in Table 3.2 and typical tensile stress-strain curves are shown in Fig.3.33.

Table 3.2: Mechanical properties of adhesive XD4600

Adhesive	Young's Modulus (MPa)	Poisson's ratio	Proportionality limit	Ultimate strength (MPa)	Strain at (%)
XD4600	2954	0.35	33.6	63.0	5.6

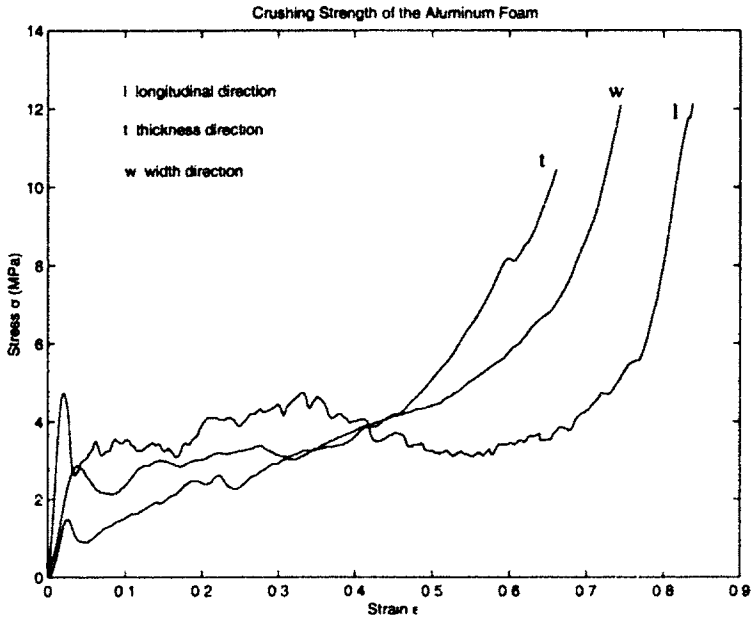

Figure 3.32: Stress-strain curve of aluminum foam in uni-axial crushing

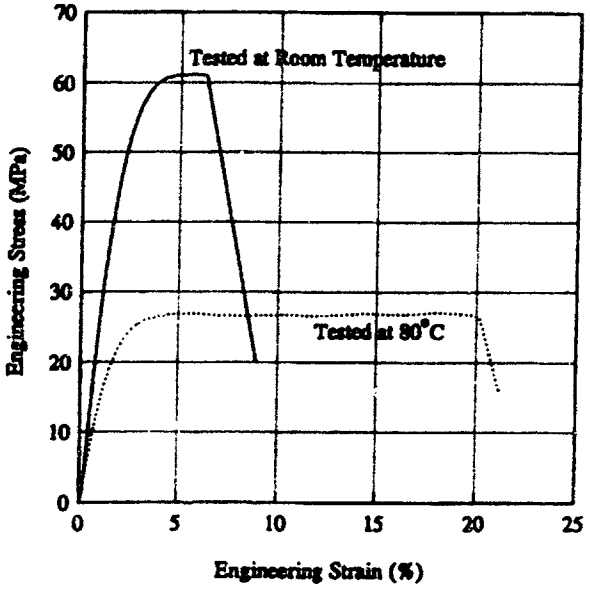

Figure 3.33: Typical tensile stress-strain curve of adhesive XD4600

3.3.1.5 Triggering

For the purpose of ensuring a desirable progressive folding mechanism and reducing the peak load as well, the specimens for axial crushing tests were pre-triggered at their top ends (Fig.3.34).

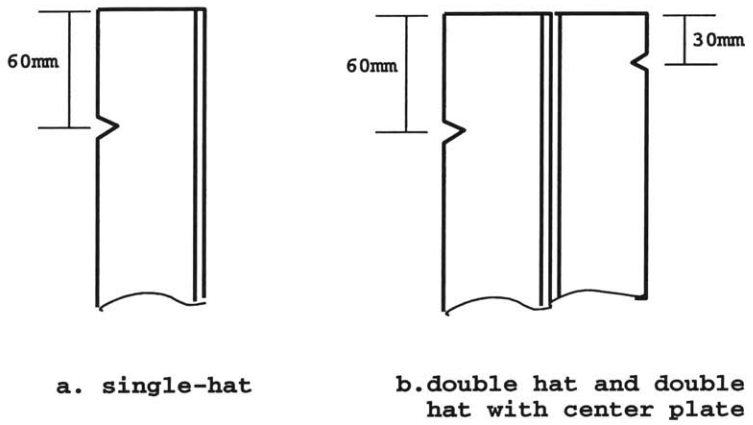

Figure 3.34: Triggers on the axial crushing members

As can be noted in Fig.3.34, two unsymmetrical triggers were introduced on the double-hat and double-hat with a center plate specimens. The above triggers helped to initiate a stable asymmetric crushing mode. A special trigger jig was designed and is shown in Fig.3.35.

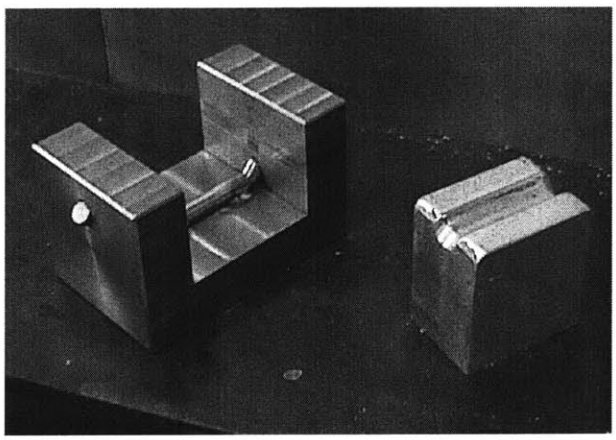

Figure 3.35: Trigger jig for axial crushing specimens

3.3.1.6 Axial Crushing Tests

Axial crushing tests were conducted on all 34 shorter specimens. Some of the pre-test specimens are shown in Fig.3.36. All tests were quasi-static with a cross-head displacement rate of $0.2 \backsim 0.3$ mm/s, performed on the ESH 300kN Testing Machine (Fig.3.37 left) at Alcan International, Banbury Laboratory, England and on the MTS 200kN universal long stroke Testing Machine at MIT (Fig.3.37 right). The force and displacement data were recorded at a frequency of 10Hz.

Figure 3.36: Some of the pre-test specimens

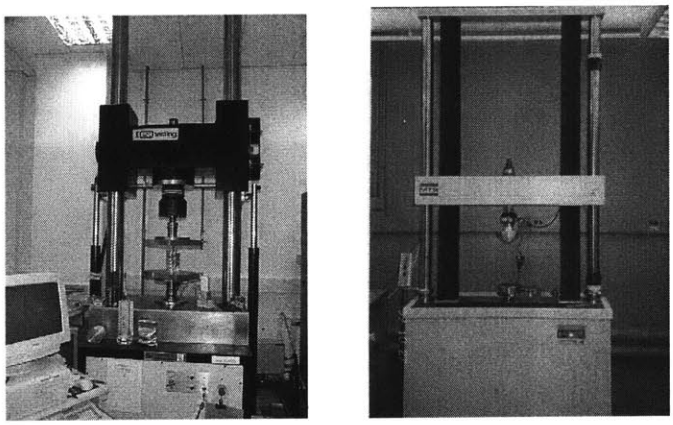

Figure 3.37: Testing machines

The test specimens were placed between the two platens of the testing machine without any additional fixing. The two ends of the specimens were carefully polished to ensure their flatness.

3.3.2 Test Results

3.3.2.1 Empty Profiles

In order to set up the reference basis for foam-filled columns, several empty columns were tested first. Table 3.3 lists the details of all the axial crushing specimens tested so far in this project.

Single-hat Profiles

All three tested empty single-hat specimens (sgl_ept1, sgl_ept2, and sgl_ept3) collapsed in a predictable, stable and progressive manner (Fig.3.38). The local collapse was initiated at the trigger and propagated from one end to the other to form an asymmetric folding mechanism with the hat part of the section folded asymmetrically and the back closing plate bending along stationary horizontal hinge lines.

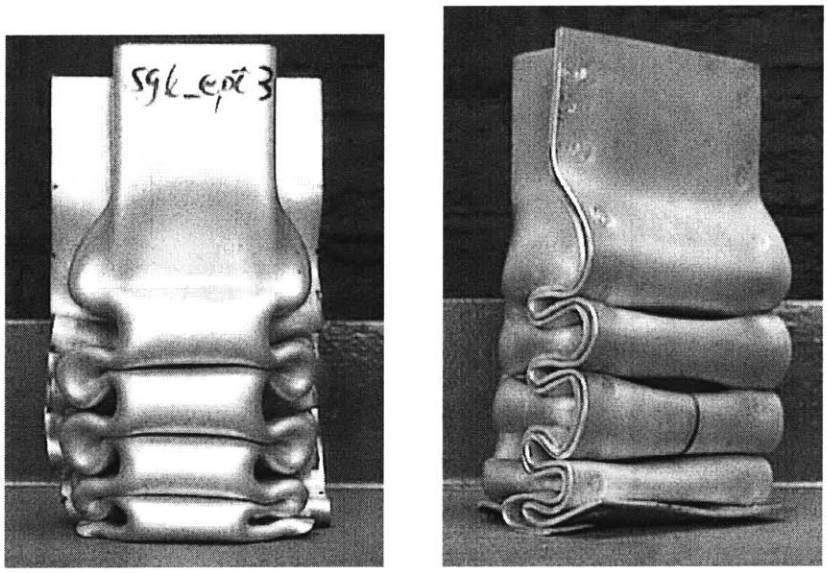

Figure 3.38: Asymmetric folding mechanism of a single hat empty column

Some failure of the spot welds was observed during the crushing tests, which is consistent with the results reported in [55, 56, 57]. The spot-welding strength in aluminum is about one half that in steel for equal gauges. The integrity of the welds in aluminum crash members become points of concern for the stability of the collapse and crash

energy management. In contrast, no spot welds failure occurred in the axial crushing tests of steel hat members and the structures can be considered as continuously joined, as reported in [59]. It was observed in the present tests that joint retention in the positions away from the crash zone of the specimens is very essential to maintain a stable progressive collapse. If the spot weld opens prior to the crash region, a subsequently "unzip" along the flange length will occur. An irregular collapse mode occurs almost inevitably resulting in a deficient amount of energy absorption.

In the present tests, a spot-welding pitch of 25 mm was used for all the empty specimens. The spot-welding failure was observed only in the crash zone during the rolling deformation of the flanges. Consequently, a stable progressive collapse mechanism was obtained, which indicates that such a spot-welding configuration is sufficiently strong for the empty hat members used in the tests. However, it is not the case for the foam-filled hat members, as revealed later on in the tests.

Fig.3.39 shows the crushing force responses of the empty single hat specimens. The mean crushing force, averaged for the three tests is 32kN.

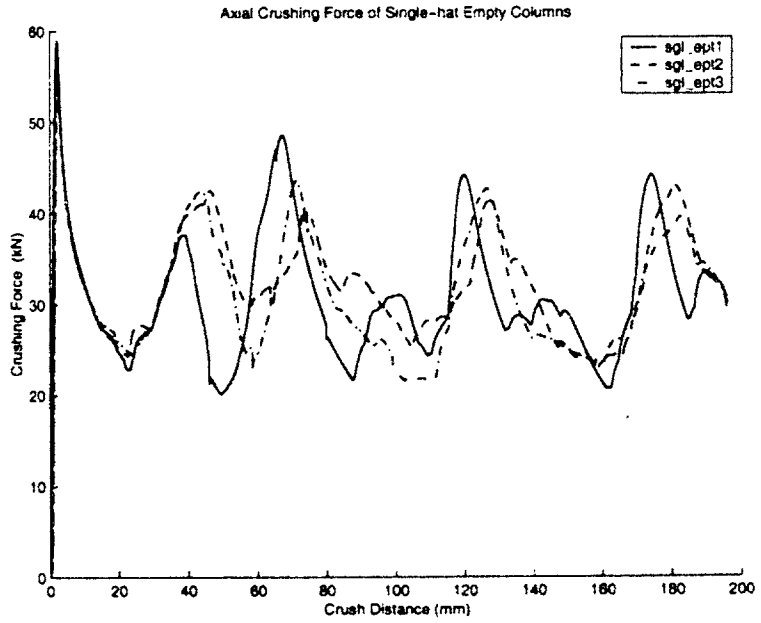

Figure 3.39: Crushing force response of empty single hat members

Table 3.3: Details of the specimens for axial crushing tests. a, b and s are referred to Fig.3.22, Fig.3.23 and Fig.3.24.

Specimen ID	Section Type	a (mm)	b (mm)	s (mm)	Joint	Fititng	δ (mm)	P_m (kN)
sgl_ept1	SH	52	52	21	sw25	no	200	30.9
sgl_ept2	SH	52	54	21	sw25	no	200	32.2
sgl_ept3	SH	52	54	21	sw25	no	200	31.4
dbl_ept1	DH	51	104	20.5	sw25	no	200	51.2
dbl_ept2	DH	52	103	21	sw25	no	200	47.4
dblc_ept1	DHC	52	105	21	sw25	no	200	66.0
dblc_ept2	DHC	52	105	21	sw25	no	200	63.7
dblc_ept3	DHC	52	105	21	sw25	no	200	63.7
S4	SH	52	54	21	sw75+ad	FM1	122	43.5
S3	SH	52	54	21	sw75+ad+rv2	FM1	175	52.5
S2	SH	52	54	21	sw25+rv1	FM1	200	51.0
S31	SH	51	54	21	sw25	FM2	141	39.7
S42	SH	51	54	21	sw25	FM3	200	49.8
S43	SH	51	54	21	sw25	FM3	200	49.8
S81	SH	52	53	21	sw75+ad+rv3	FM1	190	52.2
S6	DH	52	103	21	sw25	FM1	162	77.1
S10	DH	52	103	21	sw75+ad+rv2	FM1	193	81.6
S45	DH	51	104	20.5	sw25	FM3	77	78.2
S44	DH	51	104	21	sw25	FM3	127	83.7
S8	DH	51	104	21	sw75+ad+rv3	FM1	171	74.3
S13	DHC	52	105	21	sw25	FM1	175	85.5
S15	DHC	52	105	21	sw75+ad+rv2	FM1	200	121.5
S46	DHC	51	105	21	sw25	FM3	200	97.3
S14	DHC	52	105	21	sw75+ad+rv3	FM1	181	119.3

Note: SH=single-hat; DH=double-hat; DHC=Double-hat with a center plate; sw25=spot-welding with 25mm pitch; sw75+ad=weld-bond with 75mm pitch; rv1=1 rivet added each pitch of spot-welding; rv2=2 rivets added each pitch of spot-welding; rv3=3 rivets added each pitch of spot-welding; FM1= precisely fitting; FM2= pre-compression fitting; FM3= Adhesive bond fitting

Double-hat Members

Two empty double hat specimens tested (dbl_ept1 and dbl_ept2) showed similar collapse mode (Fig.3.41 left). In this crushing mode, instead of the flange undergoing a rolling deformation along the length of the specimen, as observed on single hat specimens, the flanges buckled inward and outward in its own plane. The process of axial crushing loses its stability at early stage, which is obviously undesirable for the crash energy management.

This irregular collapse mechanism is due to a large aspect ratio of the section (b/a=2.0). It's worth noting that a stable progressive folding deformation can still be obtained for an extruded rectangular member (without flanges) even with large aspect ratio, while it is not the case for closed hat sections with flanges. The flanges have large in-plane bending stiffness and therefore the side-plates with flanges can only develop folding with very large wavelength. The only progressive folding mode that a double hat member can undergo is the one with the rolling deformation of flanges, which can be anticipated in sections with small aspect ratio, or in the sections with strong filler, or a double-hat sections with center plates, where the in-plane movement of the flanges can be prevented.

Fig.3.40 shows the crushing force responses of empty double hat specimens. The mean crushing force of approximately 50kN was recorded.

Double hat with a center plate

A stable progressive asymmetric folding deformation was observed on double hat columns with center plates (Fig.3.41b)

Owing to the existence of the center plate, the in-plane buckling of the flanges were prevented and a rolling deformation of the flanges were developed. It can be noted that spot welds were not strong enough to hold three 2mm plates together. Many spot welds failed in the crush zone. However, similar to the case of single hat members, the failure happened in the crash zone and it did not affect significantly the crushing mechanism and energy absorption of the specimens.

Fig.3.42 shows the crushing force responses of double hat columns with center plates.

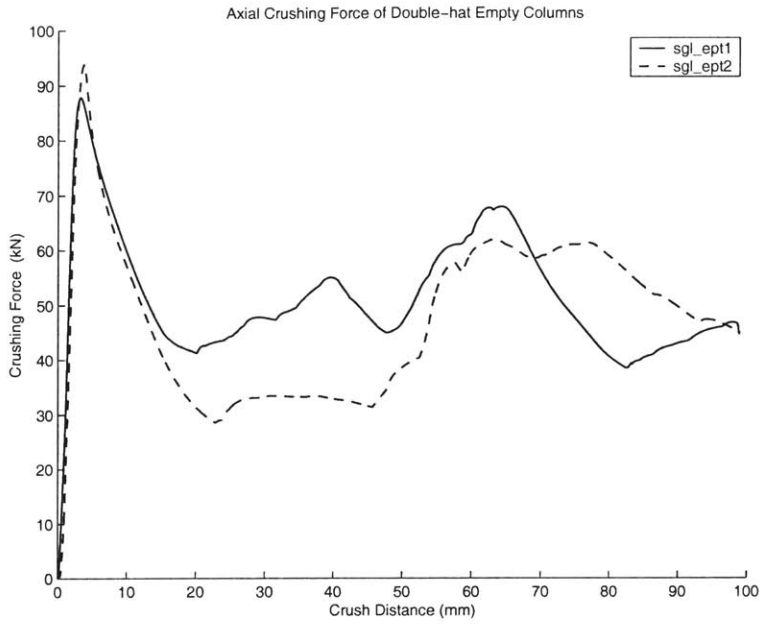

Figure 3.40: Crushing force response of empty double-hat members

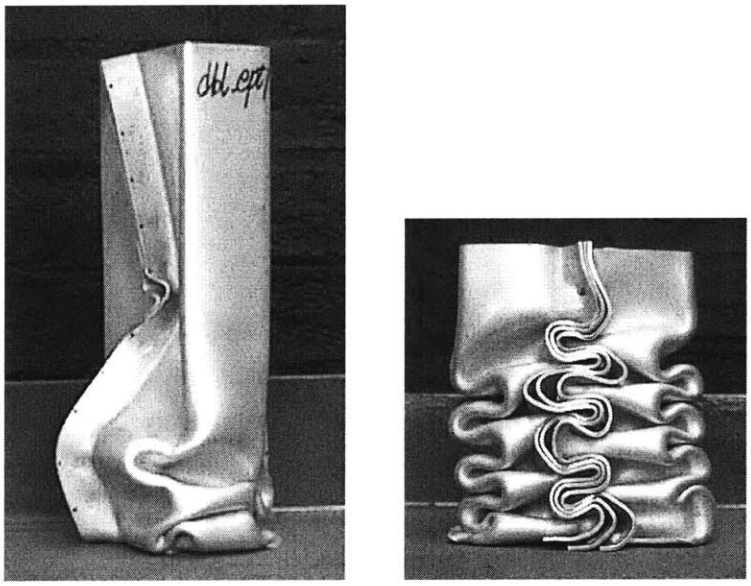

Figure 3.41: Crushing deformation of double hat columns. Left: double-hat w/o center plate. Right: double-hat w/ center plate

Comparing force-displacement diagrams for single and double hat sections one can see doubling of the mean crushing force (increase from 32kN to 64kN). This is to be

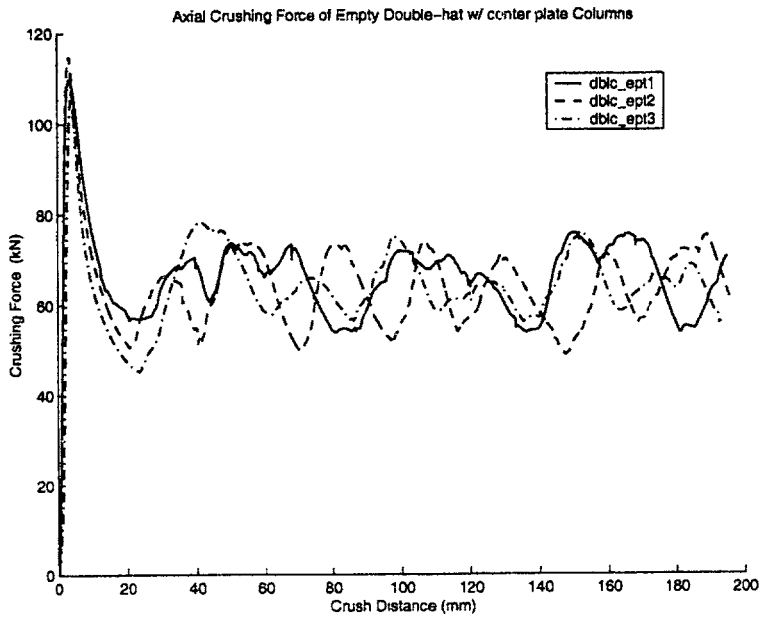

Figure 3.42: The crushing force of empty double-hat columns with center plates

expected because double hat sections have eight corners compared to only four for single hats.

3.3.2.2 Foam-filled Profiles

Sixteen quasi-static axial crushing tests have been carried out on the foam-filled columns. It was revealed in these tests that spot-welding, which appears to be sufficiently strong in empty columns, failed prematurely by tension/peeling in foam-filled columns. Rivets were therefore added to improve the joining strength and prevent the undesirable premature joint failure. This is still an on-going subject of research. Results obtained so far are summarized in the following.

Single-hat Profiles

Some interesting observations were made on the axial crushing behavior of the single hat foam-filled columns:

(i) The specimens filled with foam without bonding, and with the same joint method

as in empty columns (spot-welding with pitch 25 mm or welding-bonding with pitch 75 mm), exhibited premature joint separations during crush tests (Fig.3.43 specimen S4). The back closing plate was peeled off from the top hat and bent at stationary hinge lines and thus developed only two large folds, while a few folding lobes were formed on the top hat.

(ii) The columns fitted with foam by adhesive bonding showed a stable and progressive asymmetric collapse mode with little or no joint separation observed (Fig.3.43, Specimen S42, S43). The joint method used for the specimens is spot-welding with a pitch of 25 mm. No additional strengthening was made on the joint.

(iii) Two rivets were added between one pitch (75 mm) on a weld-bond specimen to improve the joint. Early-stage joint opening, similar to case (i), still happened (Fig.3.44, specimen S3).

(iv) Three rivets were added between one pitch (75mm) on a weld-bond specimen. The joint strength was improved and little premature joint separation was observed (Fig.3.44, Specimen S81). The specimen was not triggered at either end. The peak crushing force is thus much higher than other triggered specimens, as can be seen in Fig.3.46.

(v) One rivet was added between one pitch (25 mm) on a spot-welded column. The densely distributed rivets prevented developing a pure rolling deformation, which is essential for a progressive folding for a closed hat member. Only two large folds was formed at the closing plate. The large amount of out-of-phase deformation pattern between the top hat and the closing plate resulted in fracture at the flange corner of the top hat sheet metal (Fig.3.45, S2).

Fig.3.46 shows the crushing force responses of single hat foam-filled specimens (S4,S42, S43, S3, S81, and S2). Despite various irregular failure modes resulting from weld failure, the columns still developed considerable resistance of approximately 50kN as an average among all five tests.

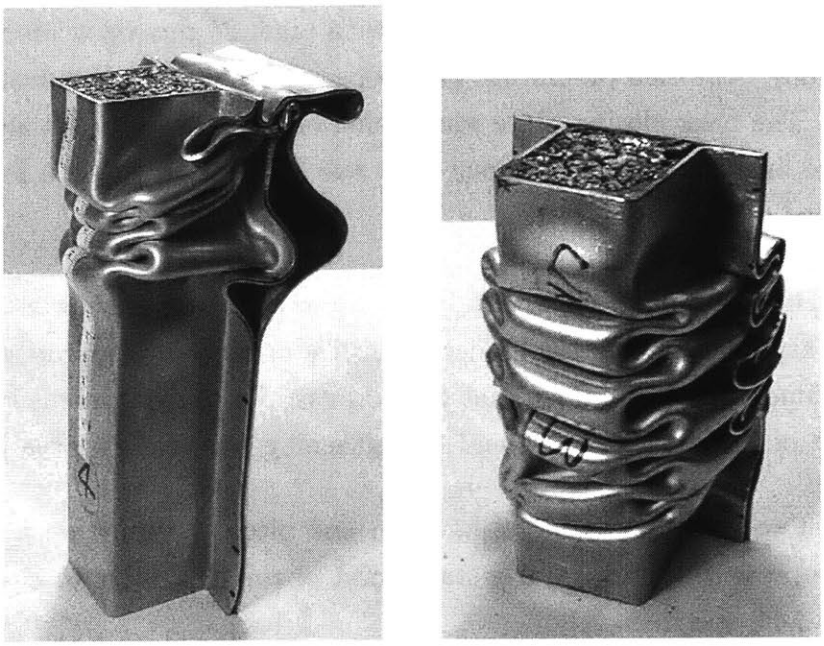

Figure 3.43: Crush deformation of single-hat foam-filled members. Left: specimen S4. Right: specimen S43

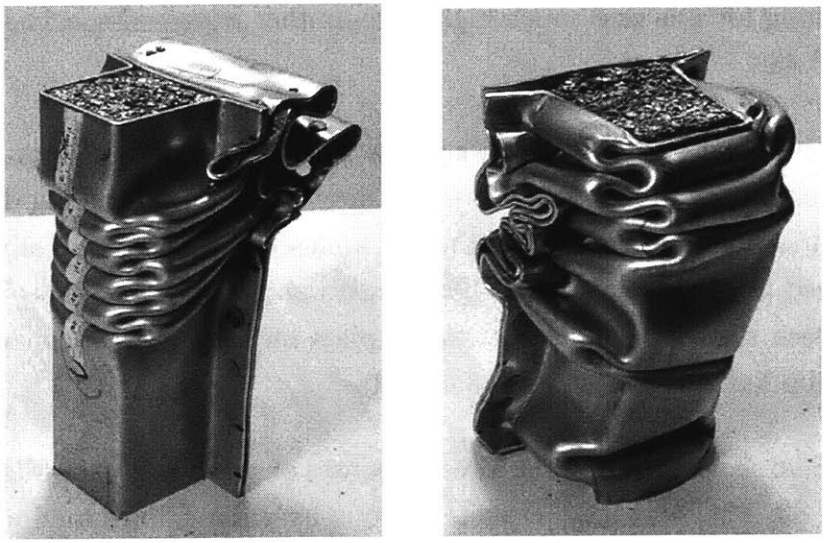

Figure 3.44: Crush deformation of single-hat foam-filled columns with rivets added. Left: specimen S3. Right: specimen S81

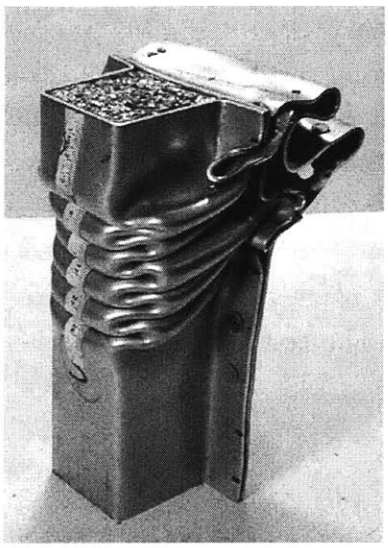

Figure 3.45: Crush deformation of single-hat foam-filled member (Specimen S2)

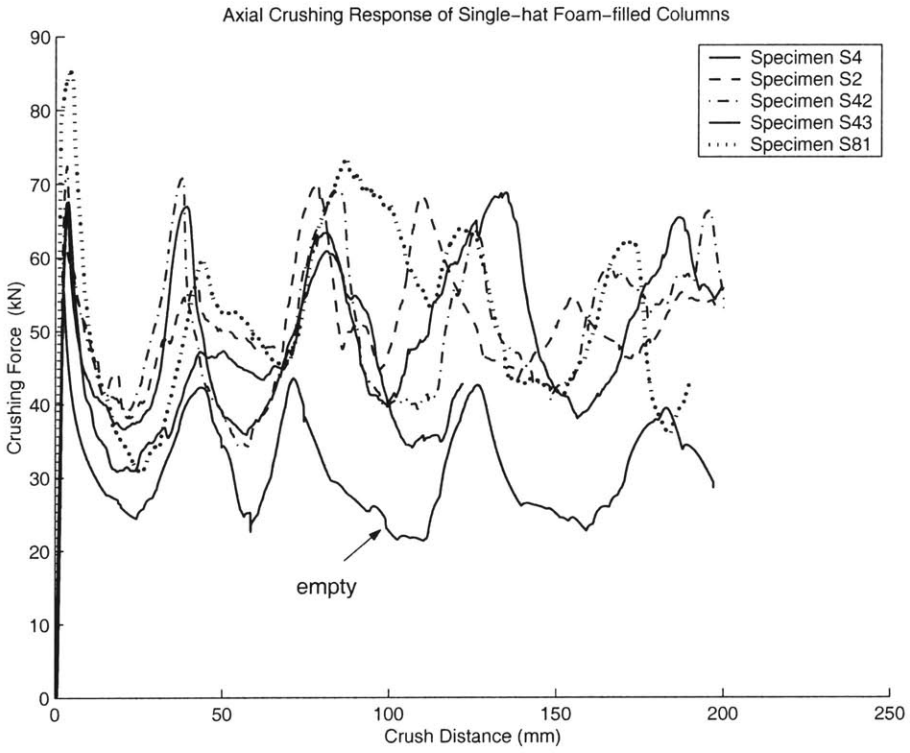

Figure 3.46: The crushing forces of single-hat foam-filled specimens

Double-hat Profiles

From five double-hat foam-filled columns which were tested, the following general observations can be made:

(i) A specimen with spot-welding of 25mm pitch and with unbonded foam filler underwent premature joint open-up. Instead of rolling deformation, the flanges developed in-plane movement. The test was stopped when the specimen tended to lose global stability (Fig.3.47).

Figure 3.47: Crush deformation of double-hat foam-filled column (Specimen S6)

(ii) Specimens with pitch 25mm spot-welding and with bonded foam filler lost global stability when two flanges underwent large and unsymmetrical in-plane deformation. The large in-plane deformation also resulted in the joint separation (Fig.3.48, Specimens S44 and S45).

(iii) Two rivets were added between one pitch (75mm) on a weld-bond specimen. Premature joint failure was greatly reduced. Flanges developed in-plane deformation (Fig.3.49, Specimen S10).

(iv) Finally, three rivets were added between one pitch (75mm) on a weld-bond specimen. No premature joint failure was observed. Flanges underwent in-plane buckling (Fig.3.49, S8).

Fig.3.50 shows the crushing forces of the double-hat foam-filled columns. It can

Figure 3.48: Crush deformation of double-hat foam-filled columns. Left: specimen S44. Right: specimen S45

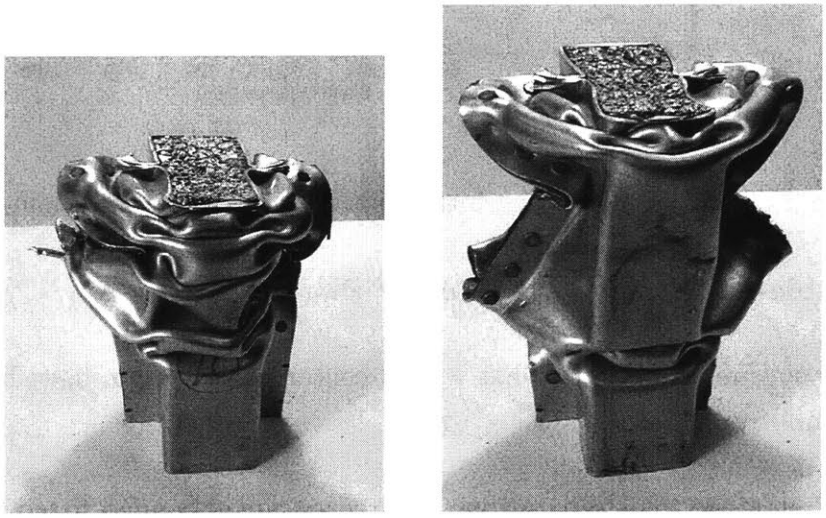

Figure 3.49: Crush deformation of double-hat foam-filled columns. Left: specimen S10. Right: specimen S8

be seen that the foam filler not only increase the crushing force level of double-hat columns, but also increase the stable crush distance of the columns. Therefore, the energy absorption can be significantly increased with the existence of the foam filler. The mean crushing force increased further to around 80kN, as an average among all five tests.

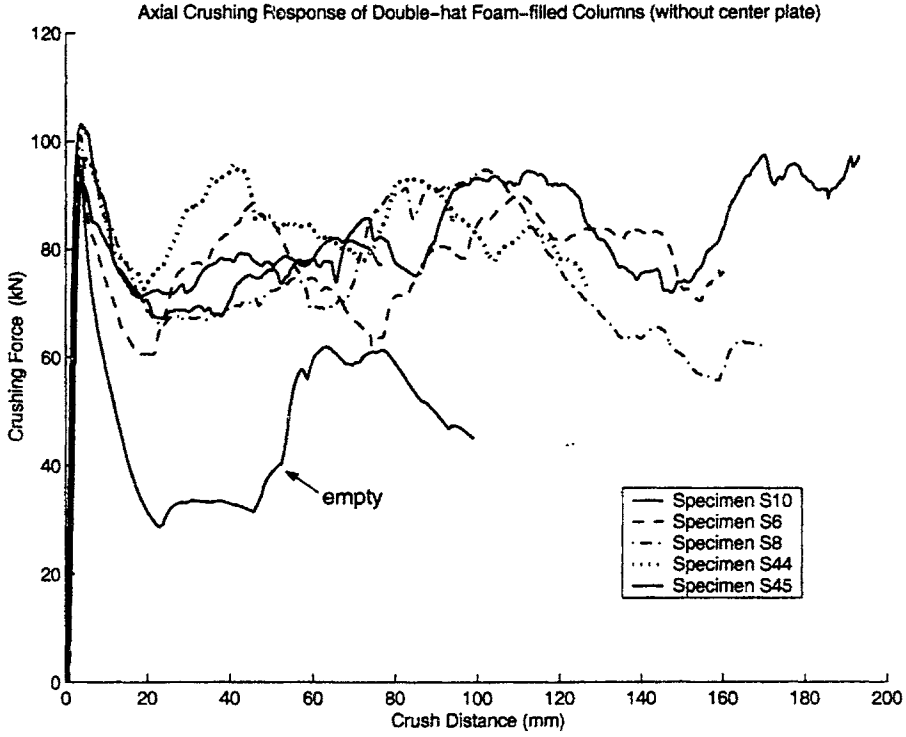

Figure 3.50: Crushing force responses of double-hat foam-filled columns

Double-hat Profiles with Center Plates

Four specimens of double hat with a center plate section have been tested so far. It was observed that:

(i) Premature joint separation occurred on an unbonded fitted specimen with pitch 25mm spot-welding (Fig.3.51, Specimen S13).

(ii) For a similar specimen to case (i), but the foam filler was bonded to the aluminum sheet, a stable and progressive asymmetric folding was developed (Fig.3.51, Specimen S46).

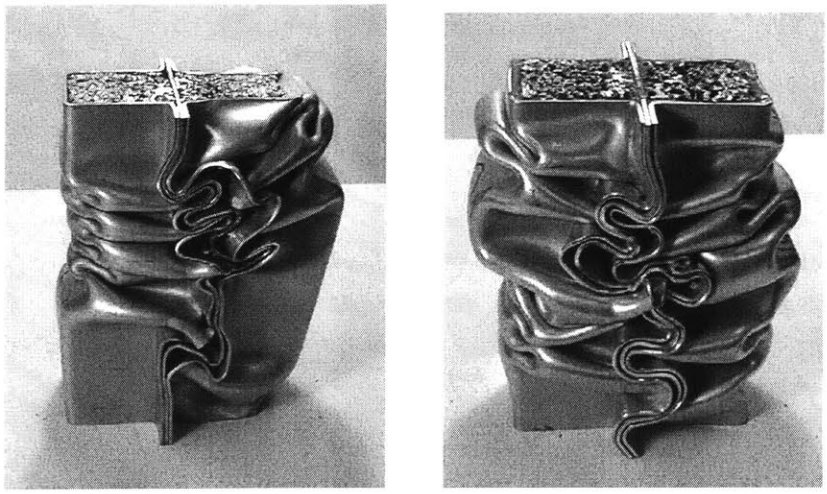

Figure 3.51: Crush deformation of double-hat foam-filled columns. Left: specimen S13. Right: specimen S46

(iii) For the specimen S15, which was weld-bonded with pitch 75mm, the foam was fitted without bonding. Two rivets were added between one pitch. A fairly stable folding was developed. But the flanges were too stiff to form regular rolling deformation. The out-of-phase deformation pattern between the top hat and the flanges resulted in small amount of fracture (Fig.3.52, Specimen S15).

(iv) Finally, 3 rivets each pitch were added to a specimen similar to the one in (iii). The flanges are even stiffer with more rivets added. No rolling deformation were developed on flanges. The testing was stopped when the specimen tended to lose global stability (Fig.3.52, Specimen S14).

Fig.3.53 shows the crushing forces of double-hat foam-filled columns with center plates. The mean crushing force for this group was even higher reaching 105kN, as an average between four tests.

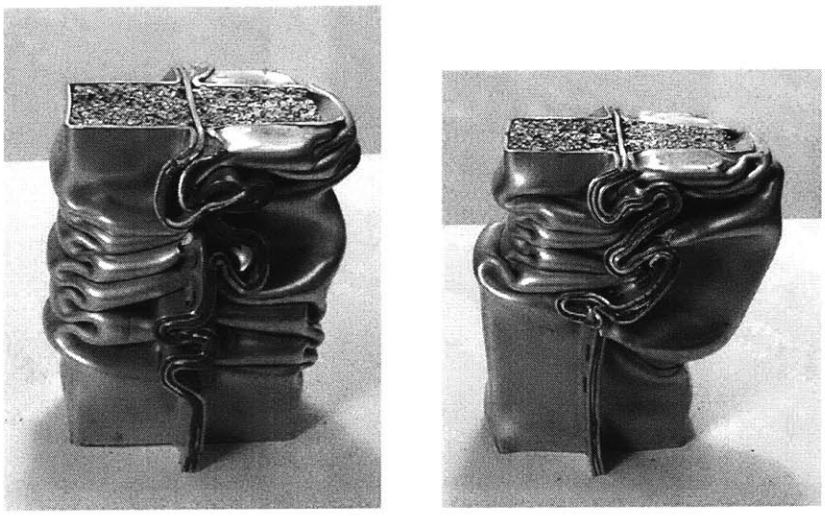

Figure 3.52: Crush deformation of double-hat foam-filled columns. Left: specimen S15. Right: specimen S14

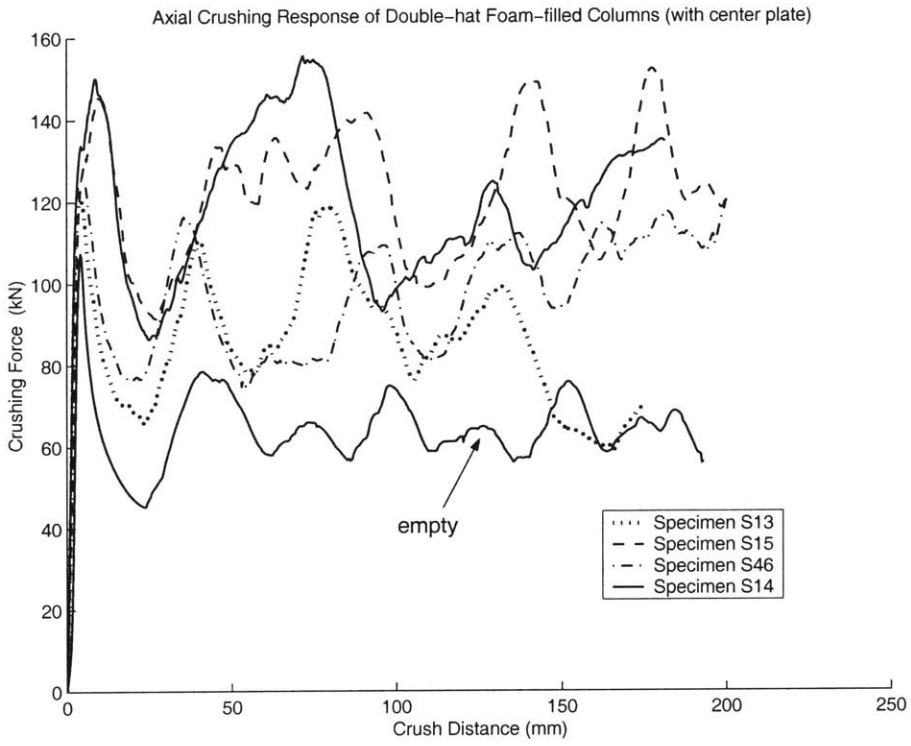

Figure 3.53: Crushing forces of double-hat foam-filled columns with center plates

3.3.3 Energy Absorption and Specific Energy Absorption

From the crushing force-displacement data, the energy absorption of the columns during axial crushing can be calculated according to

$$E_n = \int_0^{\delta} P d\delta = P_m \delta \tag{3.36}$$

where P_m is the mean crushing force and δ is the crush distance. In the above calculation, the contribution from the elastic deforamtion is neglected.

The specific energy absorption (SEA), which is defined as the energy absorption per unit mass of structural member, can then be calculated by Eq.(3.35).

Table 3.4 lists the average values of energy absorption and specific energy absorption of tested specimens with various sections for the same amount of axial crush (δ=200mm).

Table 3.4: Energy absorption and specific energy absorption of the specimens

Section Type	P_m (kN)	Energy En (kJ)	Mass of Column(kg)	Mass of Filler(kg)	SEA (kJ/kg)
Empty single-hat	31.5	6.3	0.541	0	11.5
Empty double-hat w/ closure	64.5	12.9	0.907	0	14.2
Filled single-hat	49.8	9.96	0.541	0.191	12.6
Filled double-hat w/ closure	109.0	21.8	0.907	0.382	16.9

From Table 3.4, one can see that

(i) Empty double-hat section with center plate can absorb crash energy 105% higher than empty single-hat section while the mass increases 68%. Therefore, the specific energy absorption gains of the double-hat is 24% increases when compared to single hat section;

(ii) Foam-filled single-hat section can absorb crash energy 58% higher than their empty counterpart with a 35% increasing in the total mass. Thus, the specific energy absorption of the foam-filled single-hat section is only 18% higher than that of empty one;

(iii) Foam-filled double-hat section with center plate can absorb energy 69% higher than its empty counterpart with a 42% increasing in the total mass. Hence, the specific energy absorption gains a 19% increasing for foam-filled sections compared to empty ones.

It should be noted that the above calculation is based on the current test results with the sheet metal gauge 2mm and foam density 0.27 g/cm3. Much higher gain in specific energy absorption is expected for foam-filled members if the dimensions, gauges and foam density are optimized. We shall address this in Chapter 6.

3.3.4 Discussions

Experimental study carried out so far have revealed some interesting points:

(i) The foam-filling methods of adhesive-bonding and pre-compression proposed in the current testing project could be conducive to high volume production of foam-filled closed-hat structural members;

(ii) Double-hat empty section with large aspect ratio may undergo unstable collapse deformation during axial crushing with flanges developing in-plane buckling, which is highly undesirable for crash energy management. To resolve this, a center plate or a ultralight metal filler can be introduced to suppress the in-plane movement of the flange and therefore obtain a stable folding mechanism;

(iii) Joint techniques should be the point of concern in the design of aluminum closed hat members. Spot-welding becomes more problematic in foam-filled members than empty ones. The spot-welding and weld-bond schemes, which appear sufficiently strong for empty hat members, are not strong enough for foam-filled members. The premature joint failure of foam-filled members to large extent jeopardizes their relative merit as weight-efficient crash members compared to the empty counterparts. More

research must be carried out to study various joint techniques to ensure the joint integrity of foam-filled member during a crash event;

(iv) Riveting can be applied together with spot-welding and weld-bond to improve the strength of joint. More experiments must be performed to investigate an appropriate joining scheme to obtain desirable regular rolling deformation of the flanges;

(v) With the same joining method, bonded-fitting members exhibited more desirable collapse characteristic and less premature joint failure than the unbonded-fitting members and therefore is favorable for crash energy management;

(vi) Foam-filled columns provided the specific energy absorption (SEA) around 20% higher than their empty counterparts during axial crushing for the sheet gauge and foam density used in the current study (2mm and 0.27 g/cm^3, respectively). The double-hat empty members with center plates exhibited higher energy absorption than single-hat empty members by about 25%.

(vii) As observed in the tests, the development of a regular rolling deformation of the flanges is essential for closed-hat members to undergo a stable and progressive collapse deformation in the axial crushing. However, the large bending stiffness due to the double thickness at the flanges somehow hinders the rolling deformation. Therefore, a thinner closing plate or center plate might be beneficial in obtaining desirable folding deformation and higher specific energy absorption as well. This will be addressed in the continuation of the study.

The experimental study on the same profiles subjected to large rotation bending will be addressed in the next chapter.

Chapter 4

Bending Collapse of Ultralight Structures

The problem of a deep bending collapse of thin-walled beams has received a great deal of attention over the past twenty years. A study on 81 real world vehicle crashes [63] showed that up to 90% involved structural members failed in bending collapse mode. A first comprehensive study of the bending collapse of prismatic members was made by Kecman [64]. The bending collapse behavior of rectangular and square section was studied theoretically and experimentally. Simple failure mechanisms involving stationary and moving plastic hinge lines were proposed in his analysis, and the moment-rotation characteristics was calculated in the post-failure range up to 40°. A similar approach was developed independently by Abramowicz [65]. Mahmood et al. [66] developed a bending collapse model which divides the thin-walled cross-section into a number of strips. Experiments for aluminum hat sections undergoing cantilever bending up to 20° were reported by McGregor et al. [55]. Wierzbicki et al. [67] extended the concept of *Superfolding Element*, developed originally for axially loaded columns, to the cases of bending and combined bending/compression loadings. Closed-form solutions were derived for the moment-rotation characteristics in the deep bending collapse range.

Usually, bending collapse of thin-walled members is localized at plastic hinges, with remaining parts of beam-columns rotating as rigid bodies. Only a small portion of the

structures is involved in plastic deformation. The plastic bending resistance drops significantly after local sectional collapse occurs at relatively small rotation angle, which results in a low energy absorption efficiency. From a practical point of view, a constant force or a "square wave" response seems to be ideal. With the constant collapse force, the energy absorption is maximized with respect to the deceleration rate that is applied to the passenger compartment [1]. In order to achieve higher weight efficiency in energy absorption and the desirable force response, the concept of introducing an ultralight metal filler, such as aluminum foam or aluminum honeycomb, into the thin-walled hollow structural members has received increasing interest. Santosa et al. [7, 8] studied the effect of foam filling on the bending crush resistance of thin-walled beam through quasi-static numerical simulations and physical experiments. It was found that the presence of the foam filler offers additional support from inside and suppresses the sectional collapse at the compressive flange, and therefore prevents the drop in load carrying capacity, thus maximizes the energy absorption.

The first part of this chapter is to study experimentally the crushing behavior of foam-filled aluminum hat profiles undergoing very deep bending collapse. Quasi-static bending tests are carried out on empty and foam-filled single and double hat sections. Because the bending angle of a specimen on a conventional three-point bending fixture is usually limited by the depth of the fixture, a new experimental approach is applied so that the specimen can undergo large bending angles up to 150°. In such an approach, the tests are conducted by two steps. First, bending tests are run on a conventional three-point bending fixture up to 40° rotation. Then, the bent specimens are loaded vertically in compression, and the specimens are bent further up to 150°. Some interesting features of the deep bending behavior of empty and filled hat members are revealed, and the strengthening effect of foam filling is quantified by the test results.

The finite element simulation on the deep bending of empty and foam-filled single-hat sections are also conducted using non-linear explicit code PAM-CRASH. Simulations are run in two steps similar to those in the experiment by utilizing time sensors. Numerical results are compared with the testing results showing good agreement.

In the second part of this chapter, the strengthening effects of the foam and honeycomb filler on the plastic resistance of thin-walled members in bending collapse are studied numerically. The increase in bending moment resulting from filling is quan-

tified based on the analytical solution, experimental data and numerical results. The densities of the fillers considered in the study are up to 20% relative density, which is of practical interest.

4.1 Experimental and Numerical Study on Foam-filled Hat Profiles

Experimental study were carried out on the hat profiles with the same cross-sections as those used in the axial crushing tests. Numerical simulation was then conducted, and results were compared to the experimental data.

4.1.1 Experimental Study

Quasi-static deep bending tests were conducted on empty and foam-filled hat sections. Three different sections were considered in the present study, which are single-hat, double-hat, and double-hat with closure. The specimens were manufactured at Alcan International, Banbury Laboratory, England. The bending tests were carried out on a 200kN MTS long stroke universal testing machine at Impact & Crashworthiness Laboratory at the Massachusetts Institute of Technology. A total of 12 specimens were tested.

4.1.1.1 Specimen Preparation

The specimens were prepared in the same way as those used in the axial crushing tests and described in the previous chapter. An open-hat section of $50mm \times 50mm$, $2.0mm$ gauge and $21mm$ flange(Fig.3.21) was used as a "standard" section to assemble with closing plate or center plate to form three different types of closed hat sections, i.e., single-hat, double-hat, and double-hat with a center flange (see Fig.3.22 $\backsim$ Fig.3.24).

The aluminum foam core was fitted into the open channel before the assemblage by

three different fitting methods: precise fitting, pre-compression fitting, and adhesive-bond fitting. See the description in Chapter 3.

The foam-filled hat members were assembled with closing plates by spot-welding of 25mm pitch. The length of specimens is 675mm.

4.1.1.2 Material Properties

The aluminum sheet used in the tests is HS5754. Typical uniaxial tensile stress-strain curves of this alloy, obtained from specimen cut from longitudinal, 45-degree and transverse directions, were shown in Fig.3.31. The mechanical properties were listed in Table 3.1.

The aluminum foam used in the tests was manufactured by CYMAT. The macroscopic mass density of the foam is $0.27g/cm^3$. Fig.3.32 shows the typical stress-strain curves obtained from quasi-static uni-axial compression crush tests on aluminum foam cubes in three different directions. The alignment of the foam core within the hat profiles are the same as those in the axial crushing tests: l direction of the foam aligning with the longitudinal direction of the beam and t direction aligning with the width direction of the hat section.

The adhesive applied in bonding foam to aluminum sheet is adhesive XD4600. The tensile properties of it are listed in Table 3.2.

4.1.1.3 Experimental Design

The bending tests involve two stages. First, the tests were run on a conventional three-point bending configuration, see Fig.4.1(a). The maximum punch displacement was set to be 99mm (the maximum travel distance available on the three-point bending fixture). The corresponding bending rotation angle is $30° \backsim 40°$, depending on the section type. The specimens were unloaded at the end of the first stage. Subsequently, the bent specimens were loaded vertically in compression for further bending, see Fig.4.1(b).

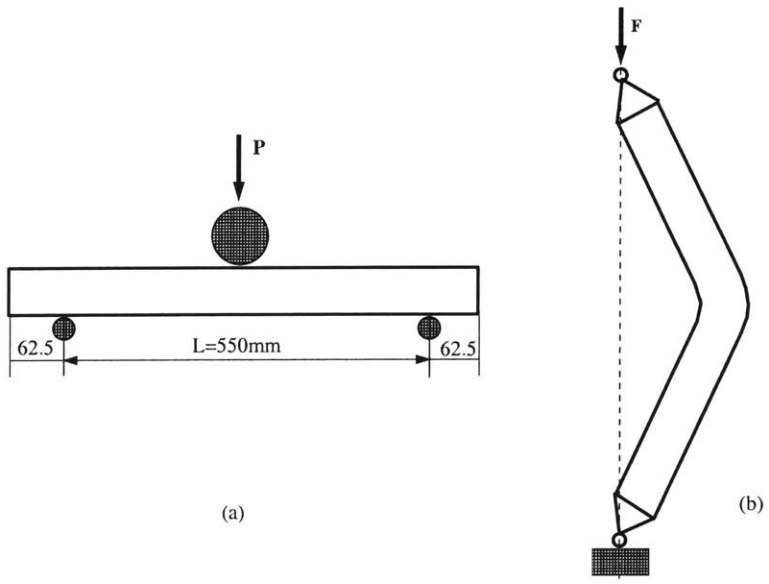

Figure 4.1: Experimental setup for the deep bending tests. (a) stage 1; (b) stage 2

A special end fixture was designed for installing the bent specimens vertically on the testing machine in such a way that one end of the specimen is pin-pin connected with the stroke with two degrees of freedom (vertical displacement and in-plane rotation), and the other end is pin-pin connected with the base of the testing machine with only one in-plane rotational degree of freedom. Fig.4.2 shows one such end fixture.

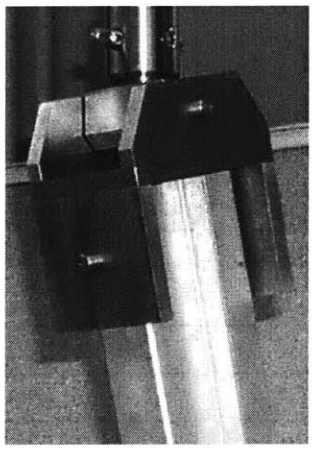

Figure 4.2: A specially designed end fixture

Via such connection, only forces are transmitted to the ends of specimens, and speci-

mens are bent further up to 150° by compressing the upper end down. All tests were run quasi-statically with a cross-head displacement rate 0.4mm/s. The vertical force and displacement were recorded at a frequency of 10Hz in both bending stages.

4.1.1.4 Stage I: Three-point Bending

Three-point bending tests were conducted on 12 specimens. The diameter of the punch was set to be 100mm (from our experience, a punch with the diameter comparable to the dimension of the cross-section of the specimen is a reasonable choice). The span of the beam between two supporting points was 550mm. The punch went down with a constant low rate of 0.2mm/s. The details of specimens are listed in Table 4.1. The following component test numbering system was applied, e.g. sgl_b1 means the following: sgl: single-hat (dbl for double-hat, and dblc for double-hat with a center flange); b: empty section under bending (bf for foam-filled); 1: repetition number. The post-test specimens are shown in Fig.4.3.

Table 4.1: Summary of specimens (SH=Single-hat; DH=Double-hat; DHC=Double-hat with closure). Parameters a, b, and s are referred to Fig.3.22 ∽ Fig.3.24

Specimen ID	Section type	a (mm)	b (mm)	s (mm)	Foam-filling	Punch travel(mm)
sgl_b1	SH	51.5	54	21.3	Empty	99
sgl_bf1	SH	53	53	20.5	Filled	99
sgl_bf2	SH	53	53.5	20.5	Filled	99
sgl_bf4	SH	53	53.5	20.5	Filled	99
dbl_b1	DH	51	104	20.5	Empty	99
dbl_bf1	DH	53	102.5	21.0	Filled	99
dbl_bf2	DH	52	103	20.5	Filled	99
dbl_bf3	DH	52.5	102.5	20.8	Filled	99
dblc_b1	DHC	51.5	105	20.8	Empty	99
dblc_bf1	DHC	52.5	105	20.8	Filled	99
dblc_bf2	DHC	52	105	20.5	Filled	99
dblc_bf3	DHC	53	104.5	20.5	Filled	99

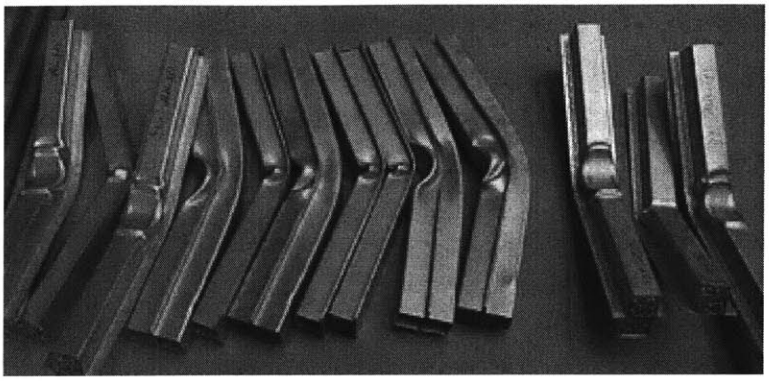

Figure 4.3: Post-test specimens of bending stage I

Some general observations can be made regarding the deformation patterns of both empty and foam-filled beams.

- No joint failure was observed at all the specimens tested, empty or foam-filled;
- One single inward fold was developed at the compression flange and two outward folds at the adjacent sides on single hat beams , both empty and foam-filled ones, see Fig.4.4;
- One large inward fold was developed on an empty double-hat beam. The shape of the fold more or less conforms that of the punch. It indicates that the crushing behavior is a combination of a localized indentation and a global bending collapse. In contrast, the inward folding deformation of foam-filled double-hat beam was suppressed by the lateral support of the foam, which resulted in higher bending resistance. The localized folding propagates to the adjacent sections, and more plastic hinge lines were formed, see Fig.4.5;
- The deformation patterns of double-hat with closure beams are more or less similar to their double-hat counterparts, see Fig.4.6.

The punch force-displacement curves of single-hat, double-hat and double-hat with closure sections are shown in Fig.4.7, 4.8, 4.9, respectively. As can bee seen, the punch forces, and thus the bending resistances are increased due to the foam filling. Among all tested specimens, specimen sgl_bf4 is the only filled beam with adhesive-bond filling. It is interesting to note that the punch force at the early stage of bending

is smaller than those of the other two filled beams, while in the advanced bending state, specimen sgl_bf4 shows higher bending resistance. The reason for this is that the supporting from foam filler in specimen sgl_bf4 is weak at small bending because the foam core is undersized with appreciable gap between the core and the skin.

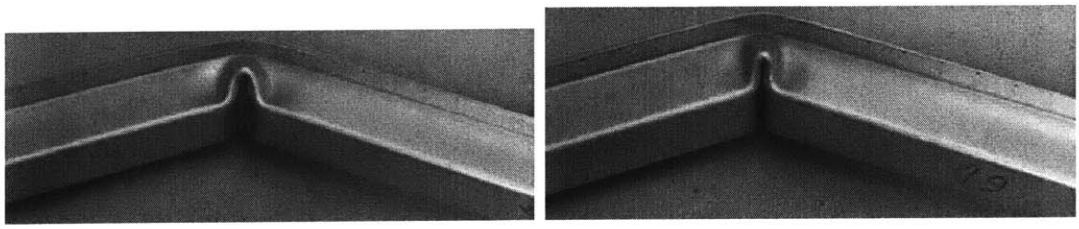

Figure 4.4: The deformation patterns of single-hat beams after three-point bending(left:empty; right:filled)

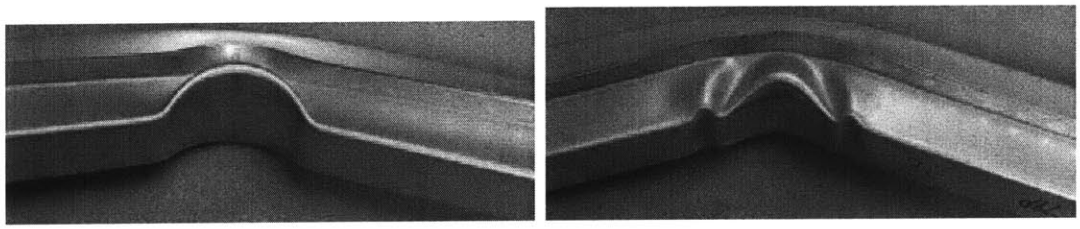

Figure 4.5: The deformation patterns of double-hat beams after three-point bending (left:empty; right:filled)

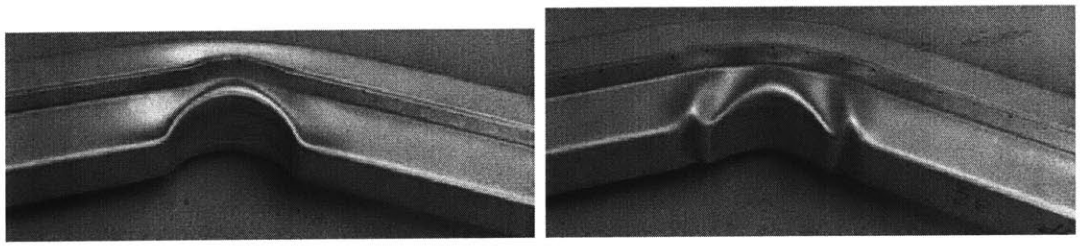

Figure 4.6: The deformation patterns of double-hat with closure beams after three-point bending (left:empty; right:filled)

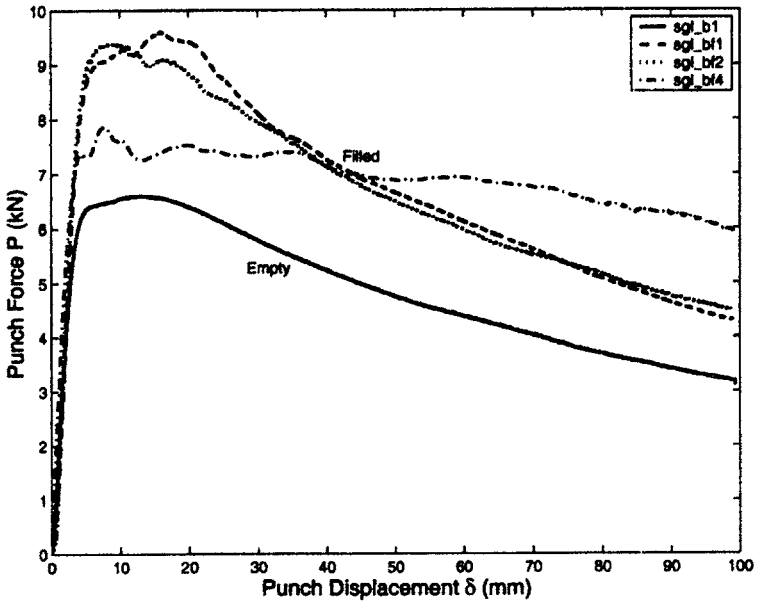

Figure 4.7: The punch force-displacement curves of single-hat beams

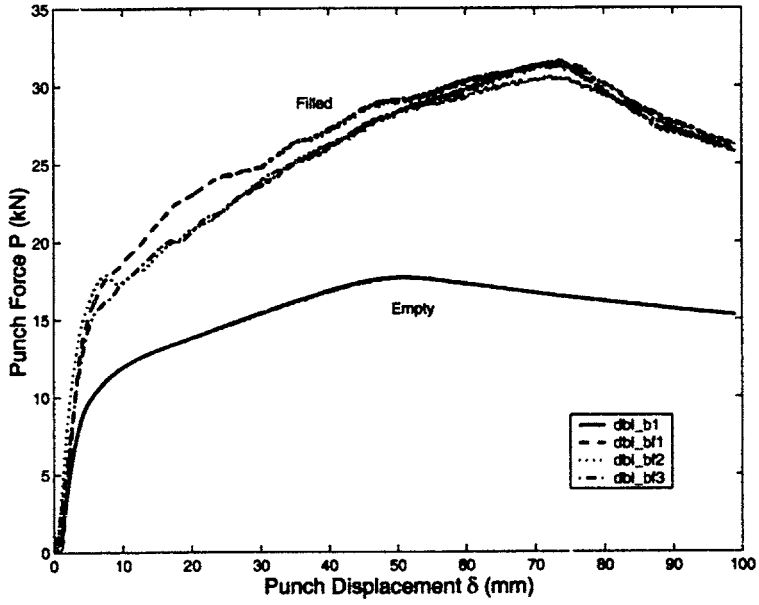

Figure 4.8: The punch force-displacement curves of double-hat beams

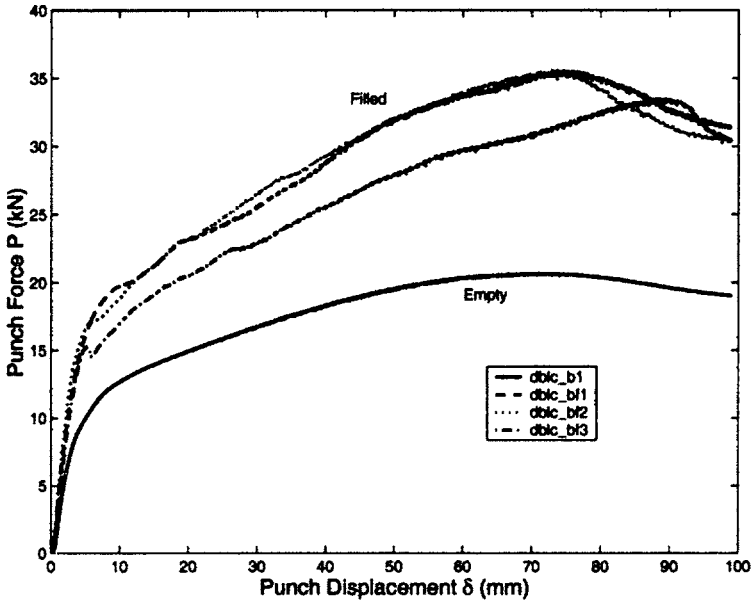

Figure 4.9: The punch force-displacement curves of double-hat with closure beams

4.1.1.5 Stage II: Vertical Compression

The second stage of the deep bending tests was conducted on the bent pieces of the first stage. After unloaded from the three-point bending mode, the bent specimens had small spring-back, which changed the rotation angles by about 1°. They were then vertically mounted and loaded in compression, as shown in Fig.4.10. Lengths R and e were measured before compressive loading, and are listed in Table 4.2.

In this stage, the specimens were bent by being compressed at the ends. The plastic deformation concentrated on the center portion of the beam-column. For simplicity in analysis, the plastic zone at the center portion of the beam-column (see Fig.4.10(a)) was treated as a generalized plastic hinge (see Fig.4.10(b)). The remaining parts of the beam-column were kept undeformed and rotated as rigid bodies.

The compressive force F and the vertical displacement Δ recorded in the quasi-static tests for single-hat, double-hat and double-hat with closure beams are shown in Fig.4.11, Fig.4.12 and Fig.4.13, respectively.

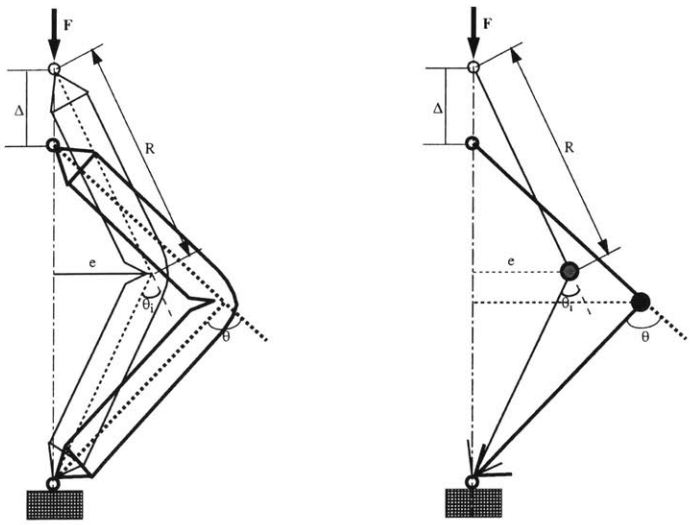

Figure 4.10: Vertical compression configuration for the second bending stage

Table 4.2: The summary of specimens in the bending stage II (SH=single-hat; DH=double-hat; DHC=double-hat with a center flange; E=empty; F=filled). Parameters R, e, θ_i, Δ and θ are referred to Fig.4.10

Specimen ID	Section type	R (mm)	e (mm)	θ_i (Deg)	Δ (mm)	θ (Deg)	Fracture
sgl_b1	SH,E	380.5	125	38.4	580	156	No
sgl_bf1	SH,F	380.5	138	42.5	550	153	No
sgl_bf2	SH,F	380.5	136	41.9	502	146	No
sgl_bf4	SH,F	380.5	136	41.9	546	151	No
dbl_b1	DH,E	380.5	95	28.9	548	151	No
dbl_bf1	DH,F	380.5	120	36.8	448	135	No
dbl_bf2	DH,F	380.5	118	36.1	550	152	No
dbl_bf3	DH,F	380.5	115	35.2	51	52	Yes
dblc_b1	DHC,E	380.5	95	28.9	549	151	No
dblc_bf1	DHC,F	380.5	111	33.9	39	48	Yes
dblc_bf2	DHC,F	380.5	112	34.2	46	50	Yes
dblc_bf3	DHC,F	380.5	110	33.6	529	149	No

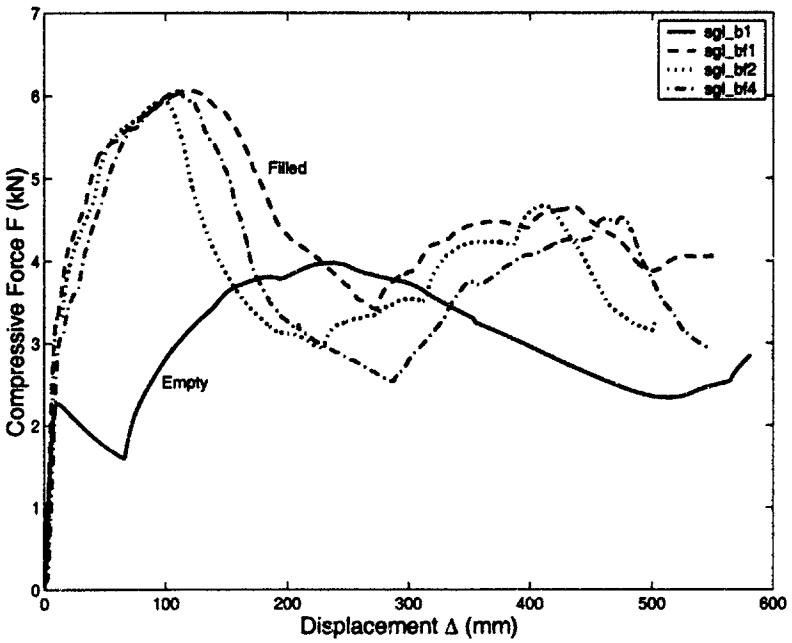

Figure 4.11: Compressive force-displacement responses of single-hat beams

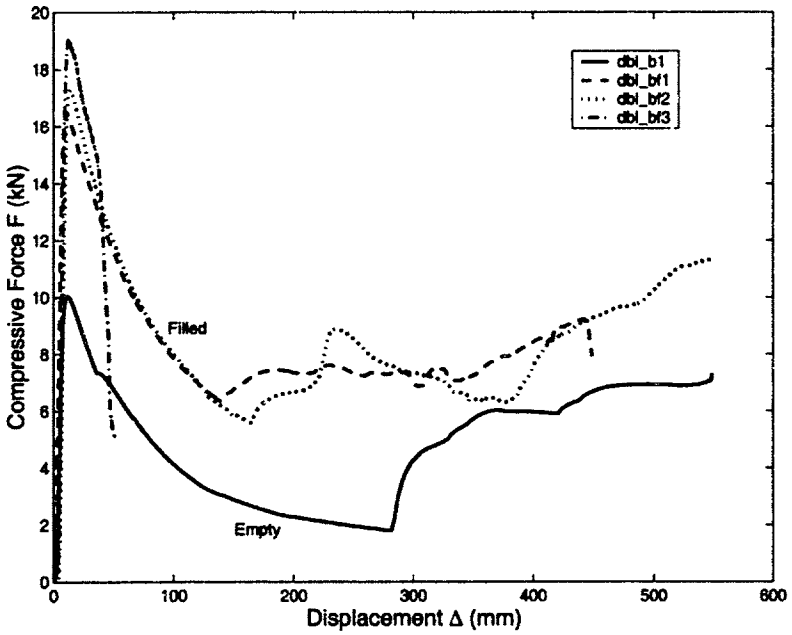

Figure 4.12: Compressive force-displacement responses of double-hat beams

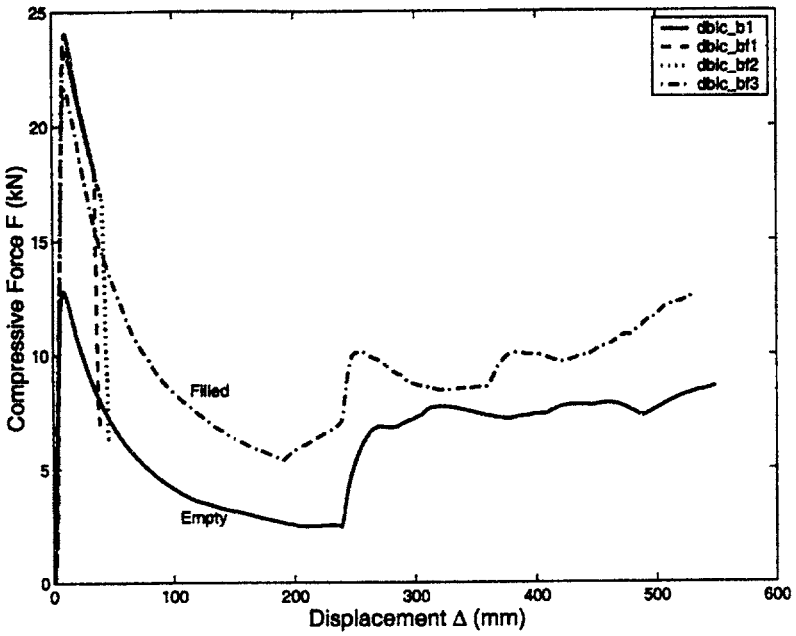

Figure 4.13: Compressive force-displacement responses of double-hat with closure beams

A few general observations can be made regarding the bending deformation of various sections.

Single-hat Sections

- For the empty single-hat section, the inward folding at the generalized plastic hinge develops with one inward fold at the beginning of the deformation process associated with decreasing of the compressive force, until the first jamming occurs (touching of two sides of the fold, see Fig.4.14). At that point, the compressive force started to increase and reached one peak (Fig.4.11 empty) when a second fold developed (Fig.4.14), and the force dropped accordingly. A second jamming started to develop at a large compression (thus large bending rotation), and the force increased again.

- For the foam-filled single-hat beam, the jamming of the first fold developed in the three-point bending stage occurred at the beginning of this bending stage (Fig.4.15), and accordingly the compressive force started to climb up to a peak (Fig.4.11, filled), where a second fold started (Fig.4.15). As a consequence, the

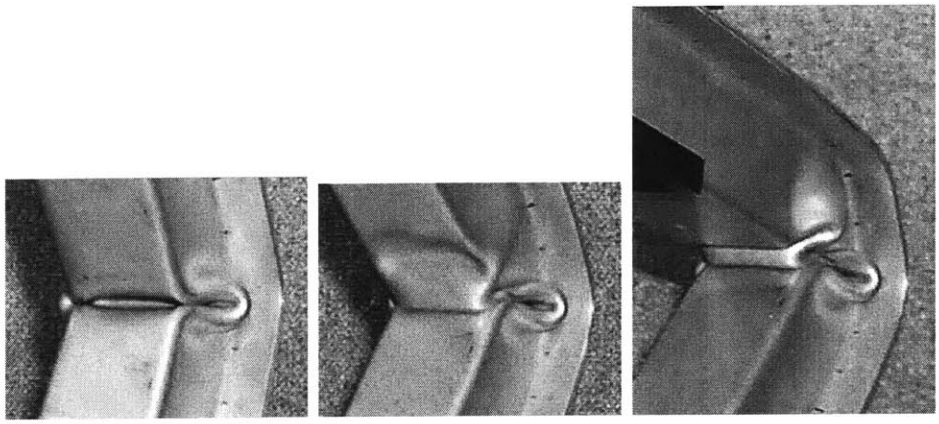

Figure 4.14: Bending deformations of empty single-hat beam (from left to right: first jamming, second fold, second jamming)

force dropped until a second jamming occurred (Fig4.15). At that time the force reached a second peak. After that, a third fold developed and force decreased again.

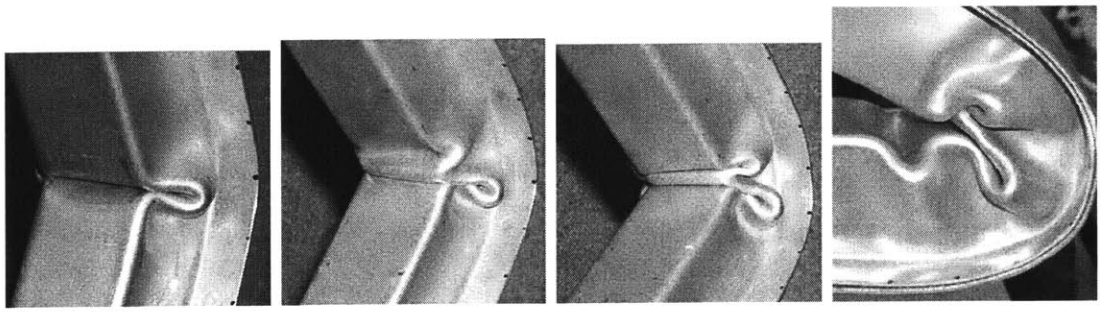

Figure 4.15: Bending deformations of filled single-hat beam (from left to right: first jamming, second fold, second jamming, third fold)

- The final deformed empty and filled single-hat beams are shown in Fig.4.16. Fig.4.17 shows a cut-through view of the generalized plastic hinge of two specimens. As can be noted, the foam provided the lateral support to the compressive flange of the beam, and therefore suppressed the sectional collapse deformation. Three folds were formed at the filled beam, while only two at the empty one. It can also be seen that the foam was subjected to bi-axial loading, with the compression in lateral direction being the dominant component. No appreciable fracture is observed in the foam material.

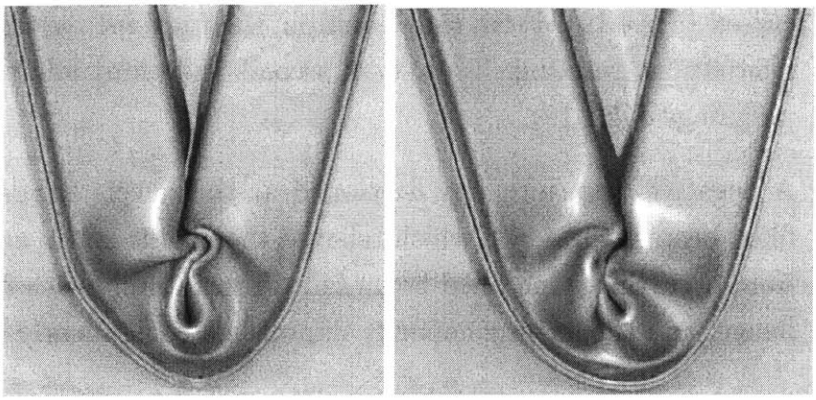

Figure 4.16: Bending deformations of empty and filled single-hat beams(left:empty; right: filled)

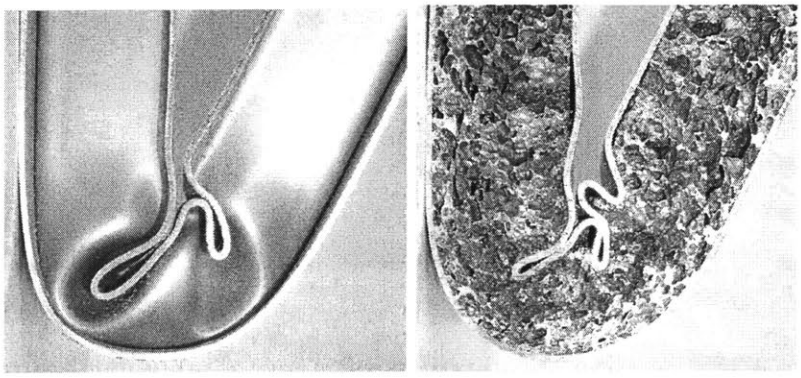

Figure 4.17: Cut-through of empty and filled single-hat beams(left:empty; right: filled)

Double-hat Section

- For the empty double-hat beam, the large inward fold developed in the bending stage I continued to grow in this stage (Fig.4.18), and the compressive force dropped rapidly(Fig.4.12, empty) until the jamming developed (Fig.4.18). After the jamming, the force increased, which indicates the increasing of the bending moment at the generalized plastic hinge.
- Similarly, the large inward fold on the filled double-hat beam continued to grow at the beginning of this bending stage (Fig.4.19), and the compressive force correspondingly dropped rapidly(Fig.4.12,filled), until the jamming oc-

curred (Fig.4.19). From that point on, the force increased generally, with small fluctuations resulting from small second and third folding and corresponding jammings(Fig.4.19).

- A negative curvature was developed at the tensile flange of both empty and filled beams (Fig.4.20), which relieved the plastic strain and prevented fracture from occurring. One filled beam failed prematurely with fracture at the tensile flange, and the loading capacity diminished consequently (Fig.4.12, dbl_bf3).

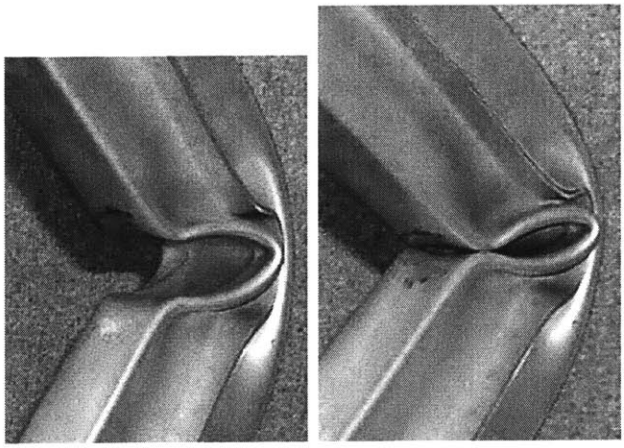

Figure 4.18: Bending deformations of empty double-hat beams(left:first fold; right: jamming)

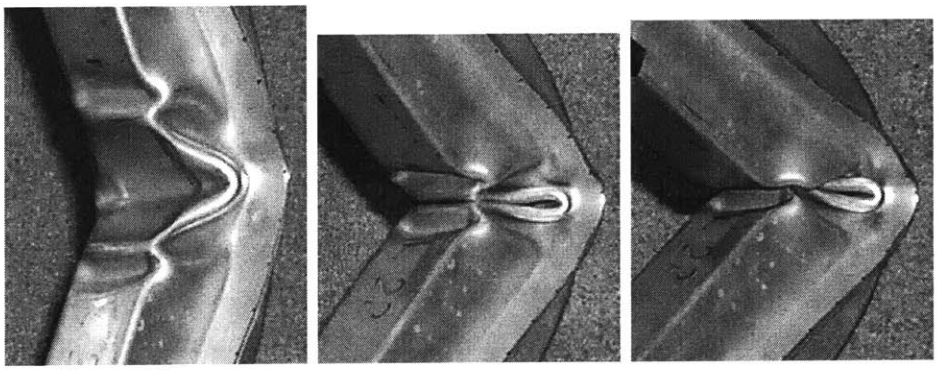

Figure 4.19: Bending deformations of filled double-hat beams(left to right: first fold, first jamming, subsequent folds and jammings)

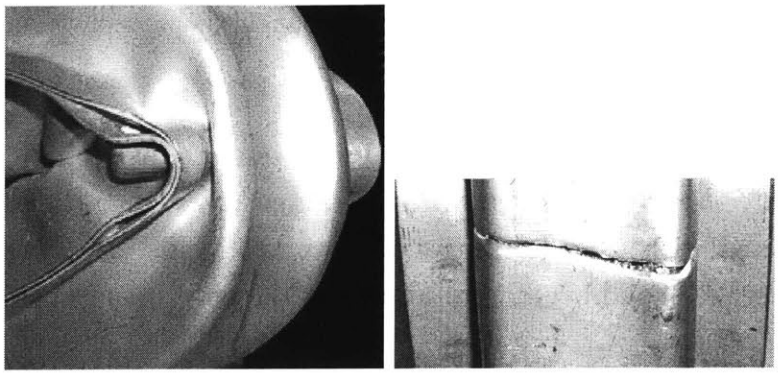

Figure 4.20: Negative curvature and fracture at the tensile flange of double-hat beam

Double-hat with Closure Section

- Similar deformation pattern and loading characteristics are observed in empty double-hat with closure beams, as in the case of empty double-hat without closure beams.
- Only one of three filled beams developed large bending rotation, with the deformation characteristics similar to the double-hat counterpart. The other two beams failed prematurely with fracture at the tensile flange. This underlines the importance of the consideration of fracture as a limiting factor of structural strengthening methods, such as foam filling.

4.1.1.6 Moment-rotation Characteristics

The moment-rotation characteristics of the generalized plastic hinges of various sections can be derived from force-displacement data. From the three-point bending configuration (Fig.4.1(a)), the bending moment and the rotation angle at the plastic hinge in the first bending stage can be calculated approximately from

$$M = \frac{PL}{4} \tag{4.1}$$

$$\theta = 2tan^{-1}(\frac{2\delta}{L}) \tag{4.2}$$

where P and δ are punch force and punch displacement in the bending stage I, respectively, and L is the beam span.

In the second bending stage(vertical compression), one can idealize the beam-column as a three-hinge mechanism, with the center hinge being the generalized plastic hinge connected with two end hinges via two rigid bars, see Fig.4.10(b). The bending moment $M(\theta)$ and bending rotation θ at the plastic hinge can then be approximated as

$$M(\theta) = F \cdot R sin\frac{\theta}{2} \tag{4.3}$$

$$\theta = 2cos^{-1}(cos\frac{\theta_i}{2} - \frac{\Delta}{2R}) \tag{4.4}$$

where F and Δ are the compressive force and vertical displacement, respectively. R is the length of the rigid bar shown in Fig.4.10. θ_i is the initial rotation angle at the beginning of this bending stage.

However, due to the spring-back during the unloading at the end of the first bending stage, the initial angle θ_i is not equal to the final angle θ_0 of the first bending stage. This discrepancy must be taken into account when combining the moment-rotation data of two bending stages into one continuous curve. Accordingly, Eq.(4.4) should be revised

$$\theta = 2cos^{-1}(cos\frac{\theta_0}{2} - \frac{\Delta - \Delta_0}{2R}) \tag{4.5}$$

where θ_0 is the final rotation angle of the first stage, and Δ_0 is a displacement correcting shift

$$\Delta_0 = 2R(cos\frac{\theta_i}{2} - cos\frac{\theta_0}{2}) \tag{4.6}$$

The calculated moment-rotation data in the deep bending range up to 150° rotation angle are plotted in Fig.4.21, 4.22, 4.23, respectively for single-hat , double-hat and

double-hat with closure sections. As can be seen, bending moments fluctuate with the bending angle in a way analogous to the axial folding behavior. The peaks and troughs on moment-rotation curves correspond respectively to the formation of subsequent folds and jamming. The bending moments of filled sections are elevated compared to non-filled sections due to the strengthening effect of filling. For those specimens in which fracture developed (dbl_bf3, dblc_bf1, dblc_bf2), the bending moments diminish rapidly.

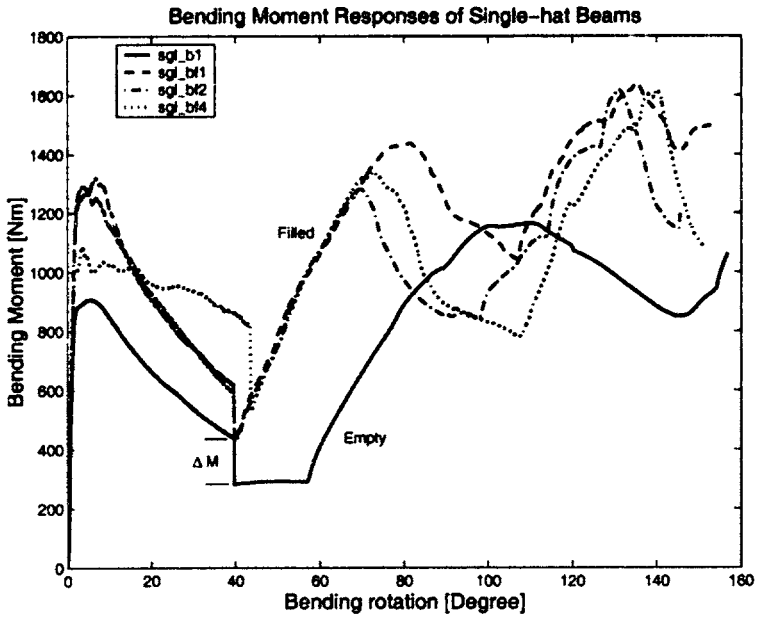

Figure 4.21: Moment-rotation responses of single-hat beams

It is also interesting to note that appreciable drop in bending moment is observed at the transition points of two bending stages. The moment drop is partly due to the change of loading condition. In the three-point bending stage, the plastic hinge is subjected to bending moment only (neglecting the shear force). When the first bending stage transits to the second stage, a compressive force N acts as well on the plastic hinge in addition to a bending moment M, see Fig.4.24.

Assuming that the failure condition of the plastic hinge can be expressed as

$$\left(\frac{M}{M_u}\right) + \left(\frac{N}{N_u}\right) = 1 \tag{4.7}$$

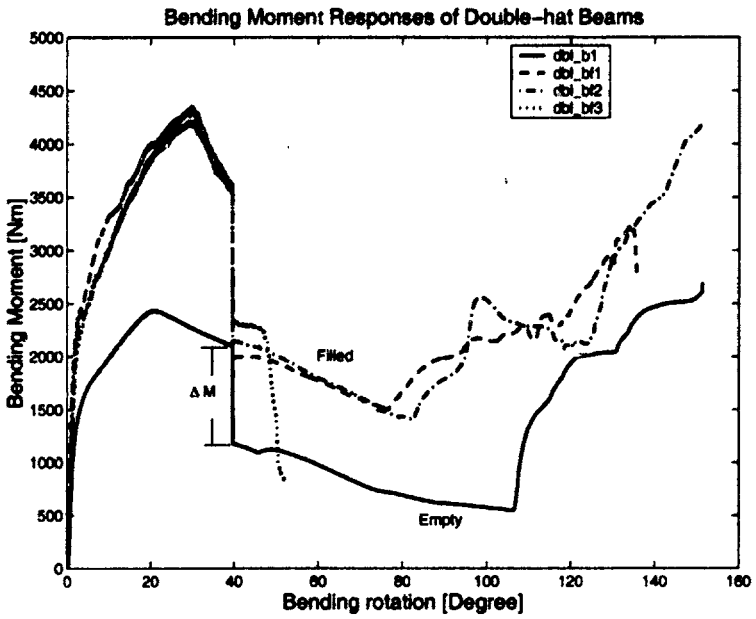

Figure 4.22: Moment-rotation responses of double-hat beams (Note a sudden drop in strength of fractured beam dbl_bf3)

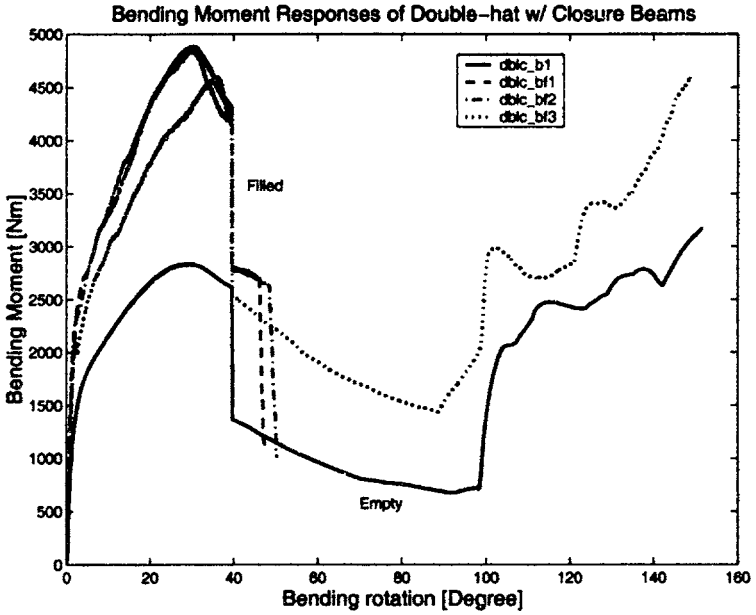

Figure 4.23: Moment-rotation responses of double-hat with closure beams (Note a sudden drop in strength of fractured beams dblc_bf1 and dblc_bf2)

Figure 4.24: The generalized plastic hinge subjected to bending moment and axial compression

M_u is the fully plastic bending moment of the section, and can be approximated by the bending moment developed on the section at the end of the first bending stage. N_u is the squash load of the section, and can be calculated

$$N_u = \sigma_0 A \tag{4.8}$$

where σ_0 is the plastic flow stress; A is the sectional area.

Rewriting Eq.(4.7) leads to the expression for the bending moment M at the beginning of stage II

$$M = (1 - \frac{N}{N_u})M_u \tag{4.9}$$

with

$$N = Fcos\frac{\theta_0}{2} \tag{4.10}$$

Therefore, the moment drop ΔM can be obtained

$$\Delta M = M_u - M = \frac{N}{N_u}M_u \tag{4.11}$$

The moment drops predicted by the above equation are listed in Table 4.3. The experimental results are also shown in the table. One can see that Eq.(4.11) generally under-predicts the moment drops compared to the experimental results. This could be attributed to several reasons including

(i) the approximate nature of Eq.(4.7);
(ii) the idealization of 3-hinge mechanism;
(iii) the wandering effect of the neutral axis.

Table 4.3: The moment drop at transition point of two bending stages

Specimen	moment drop predicted by Eq.(4.11) (Nm)	Moment drop obtained in experiment (Nm)
sgl_b1	23	148
sgl_bf1	51	168
sgl_bf2	54	185
sgl_bf4	68	289
dbl_b1	337	922
dbl_bf1	930	1563
dbl_bf2	979	1395
dbl_bf3	1083	1250
dblc_b1	464	1250
dblc_bf1	1400	1487
dblc_bf2	1354	1416
dblc_bf3	1250	1654

4.1.1.7 Energy Absorption and Specific Energy Absorption

From the moment-rotation data obtained above, the energy E_n absorbed by the specimens during the bending collapse can be calculated from the definition (neglecting the elastic deformation at the very beginning)

$$E_n = \int_0^{\theta_f} M(\theta) d\theta \tag{4.12}$$

where θ_f is the final rotation angle.

The specific energy absorption(SEA) can then be calculated by Eq.(3.35). Because bending deformations are localized in plastic hinges, only a small fraction of the beam participates in the process of energy absorption. Consequently the magnitude of SEA is relatively small for bent columns and beams.

Due to the localized nature of the bending collapse, filling beams with foam only at strategic locations, instead of the whole beam length, will still get high bending resistance, while the weight penalty from the filler is greatly reduced and thus the specific energy absorption will be much higher. This concept of partial filling was verified experimentally and numerically by Santosa et al. [7]. A simple formula to estimate the effective foam length L_f (see Fig.4.25) was proposed in [7]

$$L_f = L\left(\frac{\eta - 1}{\eta}\right) - 2H \tag{4.13}$$

where L is the beam length; η is a scaling parameter, $\eta = \frac{M_f}{M_0}$ with M_f being the ultimate bending moment of filled section and M_0 being the ultimate bending moment of empty section; H is the half folding wave length and can be calculated by (Wierzbicki et al. [67])

$$H = 1.276 b^{\frac{2}{3}} t^{\frac{1}{3}} \tag{4.14}$$

where b and t are sectional width and wall thickness, respectively.

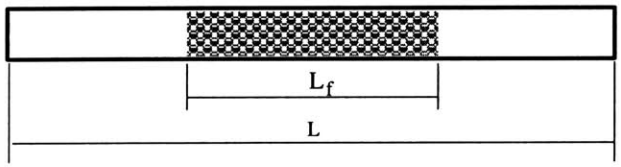

Figure 4.25: An illustration of partial filling

The energy absorption and the specific energy absorption of specimens with full filling and partial filling are calculated and listed in Table 4.4. One can see that by partial

filling, the SEAs of single-hat and double-hat beams can be increased by around 30% and 40%, respectively, compared to their non-filled counterparts. However, the capacity of energy absorption of some filled double-hat specimens are greatly reduced due to the premature fracture failure. The fracture on filled members should thus be a subject of further research.

It is also worth noting that the SEA will reach around 70% in bending collapse mode with smaller wall thickness and a medium foam density, according to the optimization study [68]. The parameters of the foam-filled sections must be optimized to achieve the most weight-efficient energy absorption.

Table 4.4: Energy absorption and specific energy absorption of specimens ($\theta_f = 150°$)

Specimen	E_n (kJ)	Gain in E_n	Full filling			Partial filling		
			mass (kg)	SEA (kJ/kg)	Gain in SEA	mass (kg)	SEA (kJ/kg)	Gain in SEA
sgl_b1	2.048	/	1.043	1.964	/	1.043	1.964	/
sgl_bf1	3.020	47%	1.400	2.157	10%	1.129	2.675	36%
sgl_bf2	2.620	28%	1.400	1.871	-4.7%	1.123	2.333	19%
sgl_bf4	2.767	35%	1.340	2.065	5%	1.075	2.574	31%
dbl_b1	3.920	/	1.407	2.786	/	1.407	2.786	/
dbl_bf1	6.381	63%	2.121	3.808	8%	1.666	3.829	37%
dbl_bf2	6.729	72%	2.121	3.173	14%	1.665	4.038	45%
dbl_bf3*	2.804	-2.8%	2.121	1.322	/	/	/	/
dblc_b1	4.795	/	1.750	2.740	/	1.750	2.740	/
dblc_bf1*	3.046	-36%	2.464	1.236	/	/	/	/
dblc_bf2*	3.165	-34%	2.464	1.284	/	/	/	/
dblc_bf3	7.225	51%	2.464	2.932	7%	1.972	3.663	34%

*Failed with premature fracture

4.1.2 Numerical Study

Numerical simulations are conducted using the explicit non-linear finite element code PAM-CRASH on the empty and foam-filled single-hat beams. Similarly as in the physical testing, numerical simulations are modeled as a quasi-static process, and consist of two bending stages: three-point bending(stage I) and a subsequent vertical compression (stage II). Details are discussed in the following.

4.1.2.1 Finite Element Modeling

Thin-walled single-hat beams with sectional geometry shown in Fig.3.22 and length 675mm is considered in the analysis. The outer skin of the beam is modeled with Belytschko-Tsay 4-node shell elements. Due to the localized nature of the bending deformation, the central portion where the bending collapse is expected is modeled with a fine mesh (2.5×5mm mesh size). The remaining parts of the beam, which rotate as rigid bodies during bending, are modeled with very coarse mesh to reduce computation time, see Fig.4.26. At the interface of fine mesh and coarse mesh, nodes are connected by rigid body mechanisms. The aluminum foam core is modeled with 8-node solid elements. The interaction between the foam core and the skin is simulated by a surface-to-surface sliding contact. Due to the expected symmetry of deformation, only a half of the beam is modeled in the analysis, and symmetry boundary conditions are applied at corresponding plane. Two rigid triangular plates are defined at two ends of the beam to model the end fixture where displacement boundary conditions are applied in the bending stage II.

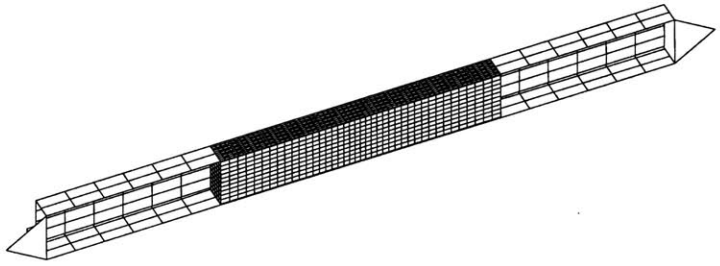

Figure 4.26: The finite element model of a single-hat beam

Two time sensors are defined in the analysis. Sensor I controls the punch and two supports, and sensor II controls the vertical compression process. At the beginning of the simulation, sensor I is activated, and the punch, which is modeled as a moving rigid cylinder with diameter 100mm, and two supports, which are modeled as stationary rigid cylinders with 550mm distance between, are active in the model. The velocity boundary condition is applied on the rigid punch with downward speed. When the punch displacement reaches 99mm, the sensor I is deactivated, and therefore the punch and two supports are removed from the model. Meanwhile, sensor II is activated, which triggers the displacement boundary conditions at two ends of the beam. All DOFs except the in-plane rotation of one end of the beam are fixed, while the other end has two DOFs, longitudinal movement and in-plane rotation. Velocity boundary condition is applied at the moving end. Consequently, the bending stage is transitted smoothly from three-point bending to vertical compression.

4.1.2.2 Material Modeling

The wall material of the beam is aluminum alloy HS5754, with Young's modulus $E = 70GPa$, initial yield stress $\sigma_y = 108MPa$, ultimate strength $\sigma_u = 237MPa$, and Poisson's ratio $\nu = 0.33$. The constitutive behavior is based on an elastic-plastic material model with Von Mises's isotropic plasticity algorithm with plastic hardening. The plastic hardening data is obtained by averaging three uniaxial tensile tests shown in Fig.3.31.

The mechanical behavior of aluminum foam is characterized by elastic modulus E_f, plastic collapse stress σ_f, shear modulus G_f, plastic shear strength τ_f, and densification strain ϵ_D, see Fig.2.7. The properties of the aluminum foam used in the experiments (CYMAT Al-SiC foam, 10% relative density) are obtained by calibrating the uniaxial compressive test data, see Fig.4.27, 4.28,4.29 for longitudinal, width and thickness directions, respectively. Being lack of experimental data, the plastic shear strength is taken to be a half of the plastic collapse stress, and the shear modulus G_f is set equal to elastic modulus E_f.

The maximum principal stress yielding model was applied for aluminum foam in the calculation.

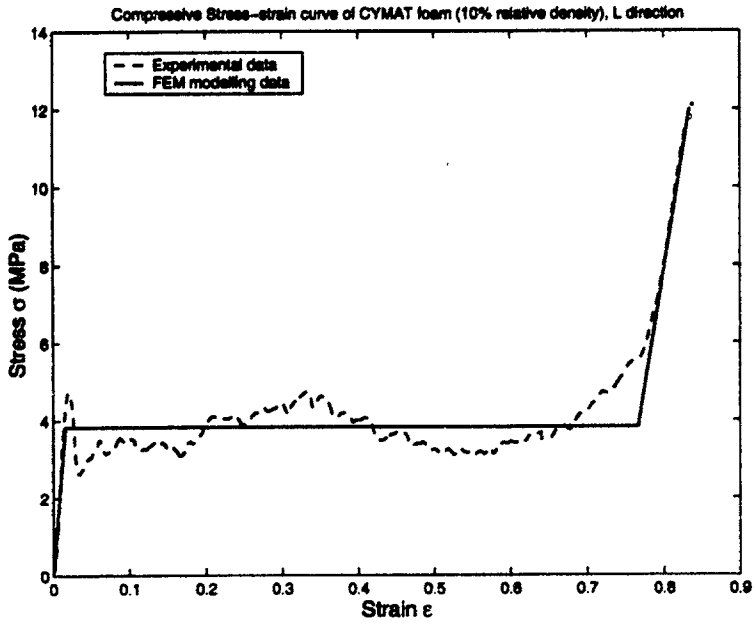

Figure 4.27: The material model for aluminum foam in L-direction

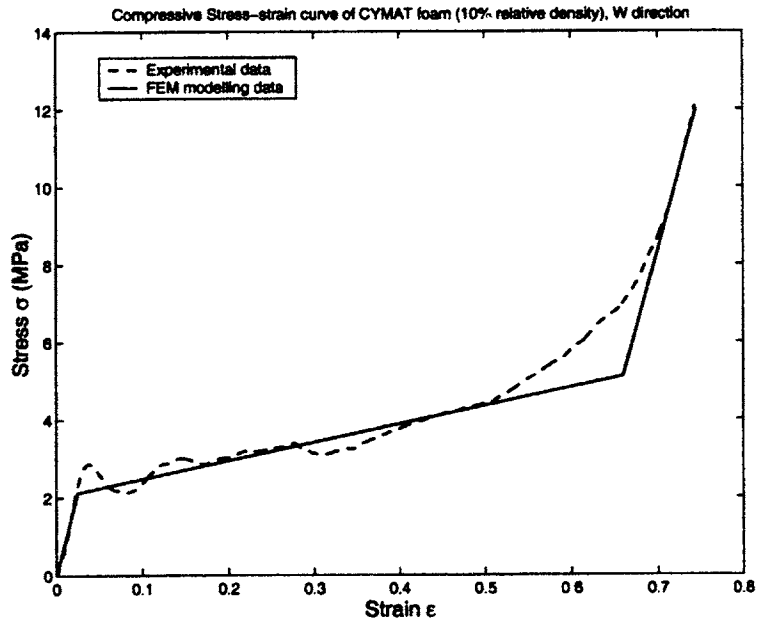

Figure 4.28: The material model for aluminum foam in W-direction

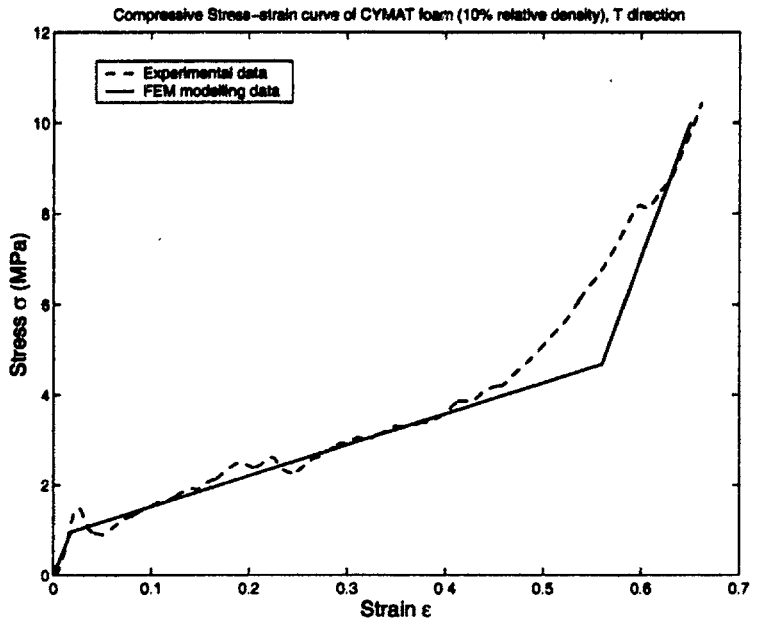

Figure 4.29: The material model for aluminum foam in T-direction

4.1.2.3 Numerical Results

The deformation modes of an empty and a foam-filled single-hat beam at the end of the bending stage I are shown in Fig.4.30 and Fig.4.31, respectively. A cut-through view of a foam-filled beam is shown in Fig.4.32. The corresponding post-test specimens are also shown in the same figures. One can see from these figures that the deformation patterns predicted by numerical simulations agree well with the experiments.

Fig.4.33 to Fig.4.36 show the deformation patterns of empty and filled beams at the end of bending stage II. Post-test specimens are also shown in the same figures for comparison. As can be seen, very good agreement is obtained between numerical simulations and physical testings in the light of bending collapse deformation.

The punch force-displacement responses in stage I and the compressive force-vertical displacement responses in stage II are shown in Fig.4.37 and Fig.4.38, respectively. As can be noted, the numerical results in bending stage I generally show good correlations with experimental results, except that numerical simulations over-predict the

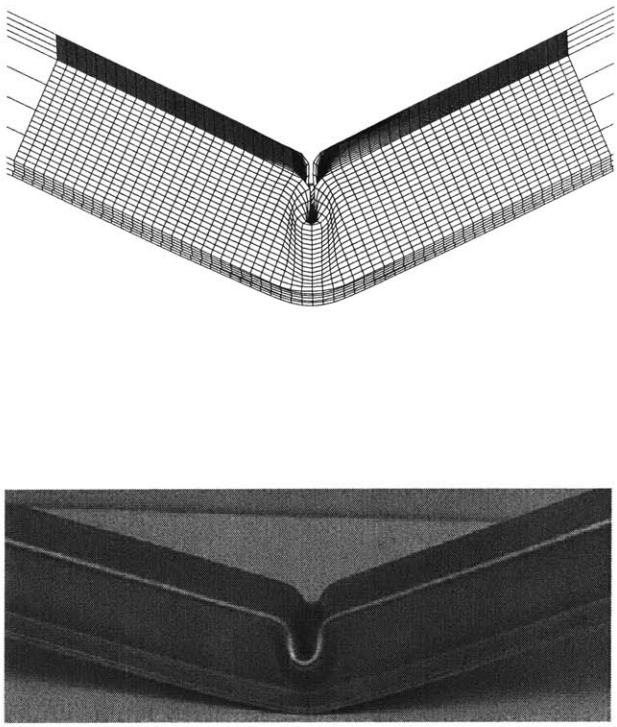

Figure 4.30: The deformation modes of empty single-hat beams at the end of bending stage I: numerical and experimental

peak loads. The reason for this is that the finite element model did not capture the initial geometrical imperfections and finite corner radius of sections inherent in real structures.

Two bending stages in numerical simulations are run continuously without unloading. Accordingly, a displacement shift Δ_0, as discussed in the previous section, must be taken into consideration in comparing the numerical and experimental results. One can see that the numerical results and experimental data of both empty and filled beams show reasonably good agreements.

The above comparisons between the numerical and experimental results validates the finite element modeling technique used in the present work. More numerical analyses are to be carried out in the next section with various sectional geometries and foam densities, for the purpose of studying and quantifying the strengthening effect of foam filling in the wide range of material parameters.

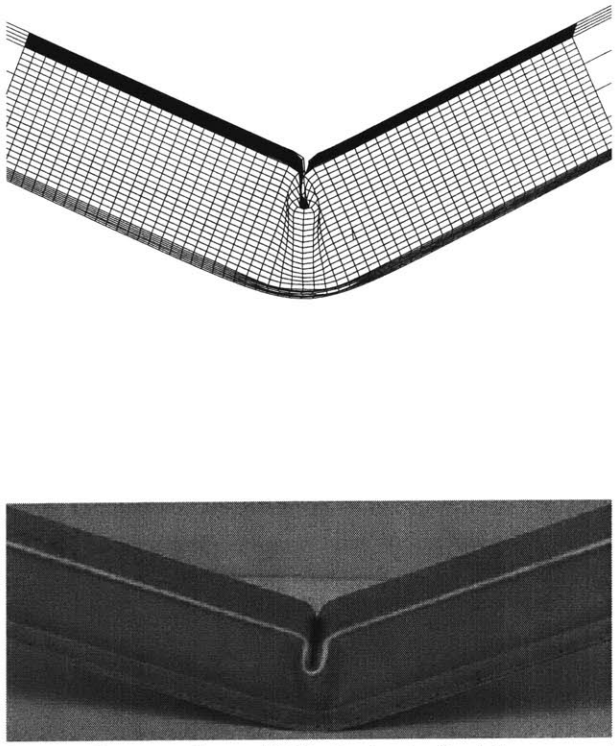

Figure 4.31: The deformation modes of filled single-hat beams at the end of bending stage I: numerical and experimental

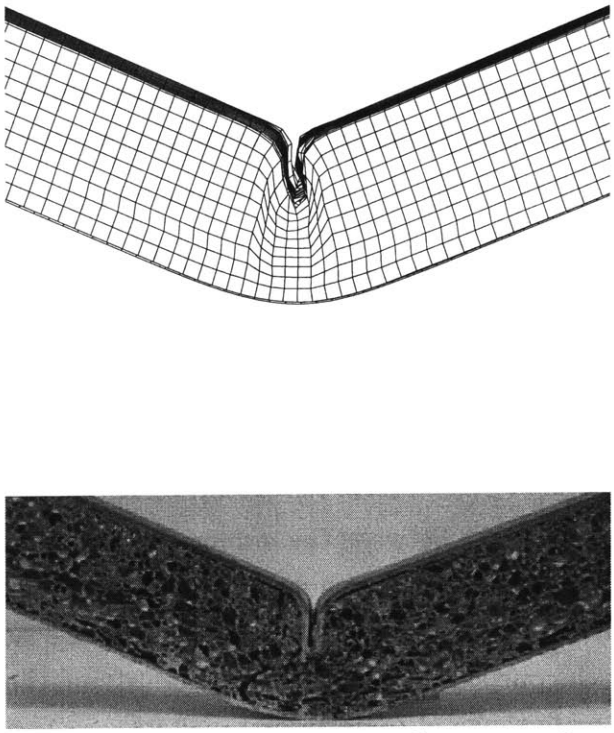

Figure 4.32: Cut-through view of filled single-hat beams at the end of bending stage I: numerical and experimental

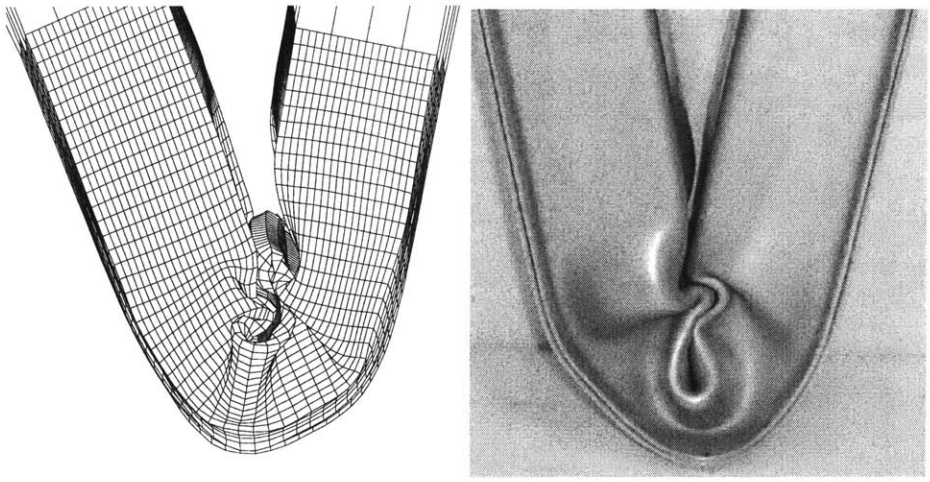

Figure 4.33: Bending collapse deformation of empty beams at the end of bending stage II: numerical and experimental

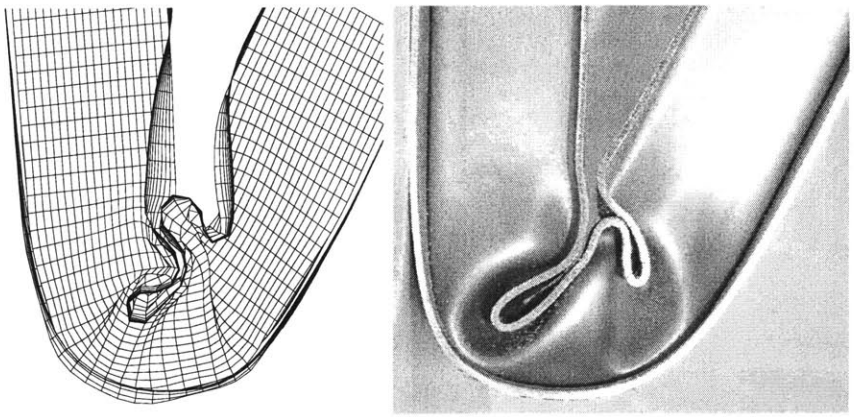

Figure 4.34: Cut-through view of empty beams at the end of bending stage II: numerical and experimental

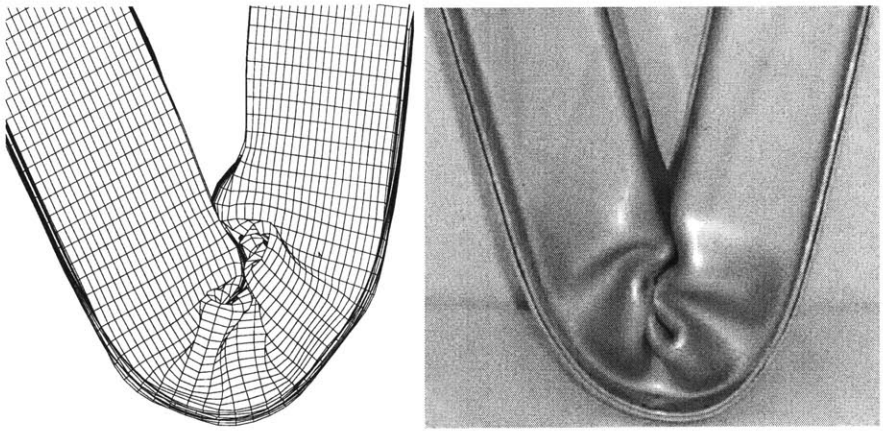

Figure 4.35: Bending collapse deformation of filled beams at the end of bending stage II: numerical and experimental

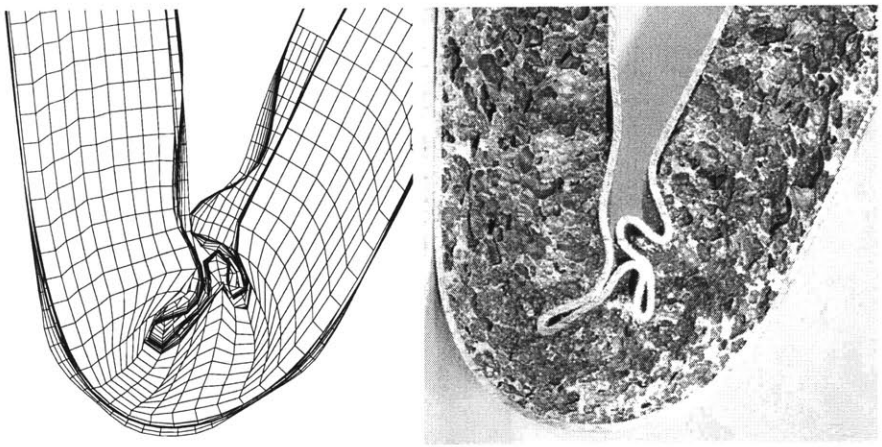

Figure 4.36: Cut-through of filled beams at the end of bending stage II: numerical and experimental

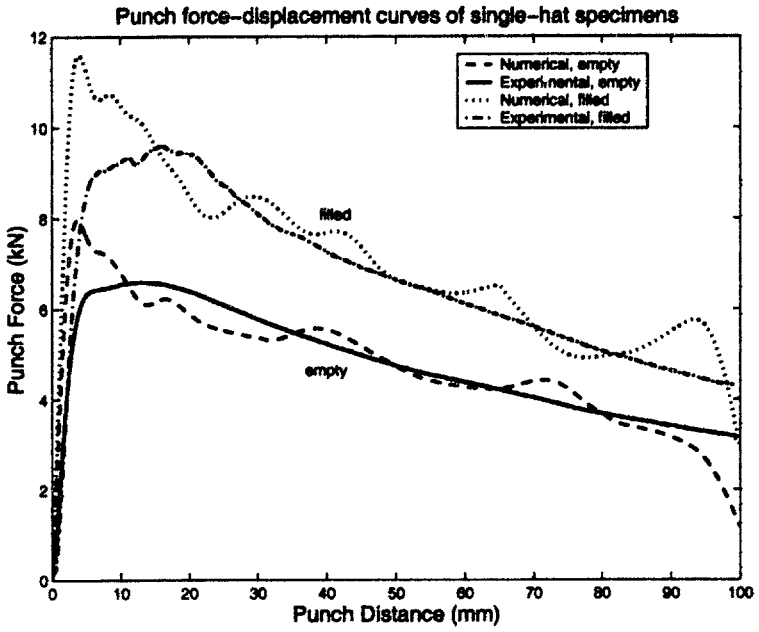

Figure 4.37: The punch force-displacement responses of beams in bending stage I

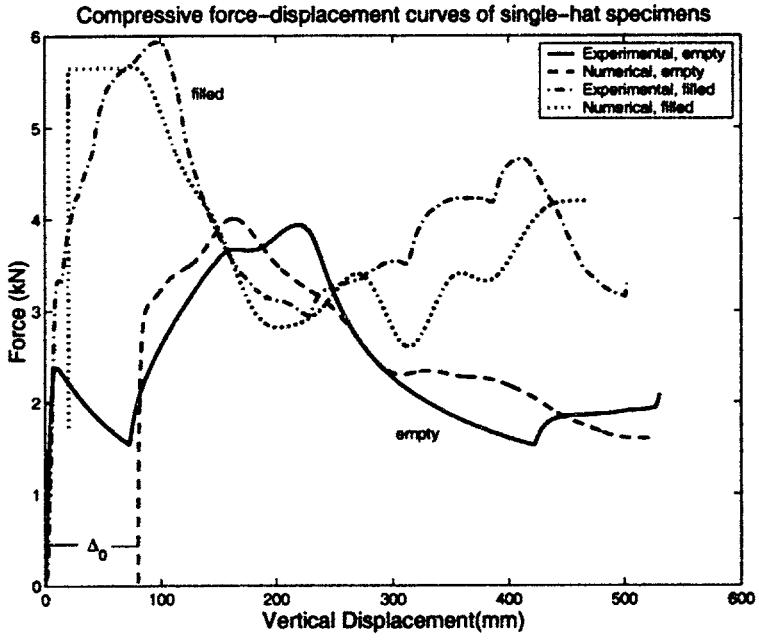

Figure 4.38: The compressive force-displacement responses of beams in bending stage II

4.1.3 Discussions

The deep bending collapse of thin-walled empty and foam-filled hat profiles were studied experimentally and numerically in this section. Three different hat profiles are considered, single-hat, double-hat and double-hat with a closure. The deep bending tests involve two steps. First, the beams are deformed in a conventional three-point bending mode up to approximately 40° rotation. Then, the bent specimens are loaded vertically in compression, and are bent further up to 150°.

Some important features of crushing behavior of empty and foam-filled hat members with large bending rotation are revealed, and differences in failure modes among three types of profiles are discussed. The moment-rotation characteristics are obtained experimentally for the generalized plastic hinges with the rotation angle up to 150°, and they are found to be similar to the case of axial folding of thin-walled members, with peaks and troughs on $M - \theta$ curves corresponding respectively to the initiation of buckles and formation of subsequent folds all the way to jamming.

It is found in the experimental study that foam-filled members with the current design of sectional geometry and foam density can achieve 30%-40% increase in the specific energy absorption, compared to traditional non-filled members. This proves great potentials of foam-filled structures as weight-efficient energy absorbers.

Some foam-filled double-hat specimens failed prematurely by developing necking and fractures at tensile flanges, which diminished energy absorption. This underlines the importance of fracture in filled structures as a subject of further research.

Numerical study using explicit nonlinear finite element method is also conducted. Quasi-static simulations of deep bending collapse of empty and foam-filled single-hat beams are carried out. A simple maximum principal stress yielding model is used for aluminum foam in the analysis. Numerical results are compared with the experimental results showing good agreement, which validates the finite element modeling techniques used in the analysis. More numerical analyses will thus be carried out in the next section with considerations of various sectional geometries and foam densities, for the purpose of studying and quantifying strengthening effect of foam filling.

4.2 Quantifying the Strengthening Effect of Ultralight Filler

Santosa [5] conducted numerical simulations on the bending collapse of empty square boxes and foam-filled ones with low density filler (relative density up to 2.7%) using nonlinear explicit finite element code PAM-CRASH. Based on the numerical results, the moment-rotation relations were derived, which are applicable for empty and filled sections with low density filler. The present work employs the same finite element modeling technique with the consideration of medium and high density foams (up to 20% relative density). The strengthening effect of the foam filling and honeycomb filling will be studied and quantified with the help of the numerical results and experimental data.

4.2.1 Plastic Bending Resistance of Empty Square Sections

Consider a square box beam with cross-section of $b \times b$ and thickness t undergoing bending rotation θ, see Fig.4.39. Bending collapse deformation is localized at the central portion of the beam and the plastic work is dissipated through the formation of hinge lines and membrane action zones. The localized nature of bending collapse deformation is characterized by the half folding length H, which is obtained from the postulate of minimum mean force [67], and was given in Eq.(4.14).

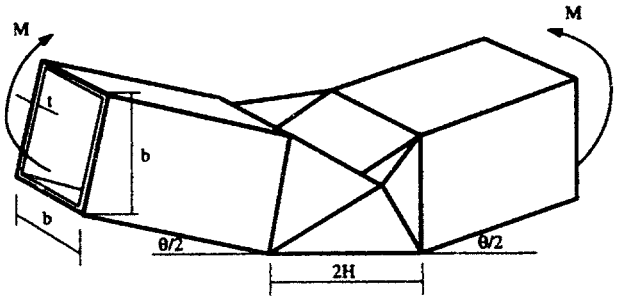

Figure 4.39: A simplified model of bending collapse of a thin-walled beam

The moment-rotation characteristic in post-buckling range was derived analytically

by Wierzbicki et al. [67] based on the concept of *Superfolding Element*

$$M(\theta) = 2P_m b(0.576 + \frac{1}{2\sqrt{\theta}}) \tag{4.15}$$

where

$$P_m = 2.76\sigma_0 b^{\frac{1}{3}} t^{\frac{5}{3}} \tag{4.16}$$

and σ_0 is the equivalent flow stress and is given in Eq.(3.10).

An approximate expression for the ultimate bending moment of the beam was derived by Santosa [5] based on his numerical analyses

$$M_u = 4.65\sigma_0 b^{\frac{5}{3}} t^{\frac{4}{3}} \tag{4.17}$$

By equating Eq.(4.15) with Eq.(4.17), the critical bending rotation θ_c for local sectional collapse can be obtained

$$\theta_c = \frac{1}{4}\left[\frac{1}{0.8(\frac{b}{t})^{\frac{1}{3}} - 0.576}\right]^2 \tag{4.18}$$

Therefore, the moment-rotation response of an empty thin-walled square section can be expressed as

$$M(\theta) = \begin{cases} 4.65\sigma_0 b^{\frac{5}{3}} t^{\frac{4}{3}} & 0 \leq \theta < \theta_c \\ \\ 2P_m b(0.576 + \frac{1}{2\sqrt{\theta}}) & \theta \geq \theta_c \end{cases} \tag{4.19}$$

Eq.(4.19) is valid for the bending rotation angle up to 30°. Figure 4.40 shows schematically the moment-rotation characteristics of the thin-walled beam.

4.2.2 Plastic Bending Resistance of Foam-filled Sections

The presence of the foam filler suppresses the local sectional collapse and therefore increases the plastic bending resistance of the thin-walled beams. It is assumed that the ultimate bending moment of a filled section is of the additive form of the ultimate bending moment of a non-filled section and a moment elevation resulting from filling, as illustrated schematically in Fig.4.40

$$M_{uf} = M_u + \Delta M \tag{4.20}$$

where M_{uf} denotes the ultimate bending moment of foam-filled section; M_u is the ultimate bending moment of empty section given in Eq.(4.17); ΔM is a moment elevation resulting from foam filling, which is a function of the foam properties and the sectional dimensions.

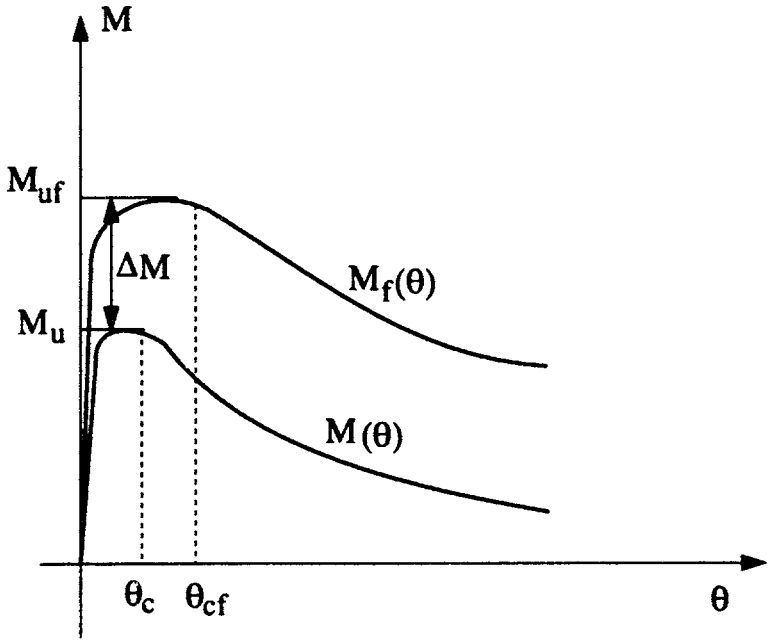

Figure 4.40: Schematical illustration of the moment increase resulting from foam filling

The bending moment of foam-filled section in the post-buckling range can also be evaluated by an horizontal and a vertical shifting of the moment-rotation charac-

teristic of corresponding empty section given in Eq.(4.15). The shifting constant is determined by setting the bending moment at the critical bending rotation $M(\theta_{cf})$, equal to the ultimate bending moment M_{uf} given in Eq.(4.20). The bending moment of foam-filled section is then

$$M_f(\theta) = \begin{cases} M_{uf} & 0 \leq \theta < \theta_{cf} \\ P_m b(\frac{1}{\sqrt{\theta}} - \frac{1}{\sqrt{\theta_{cf}}}) + M_{uf} & \theta_{cf} \leq \theta \leq \theta_0 \end{cases} \tag{4.21}$$

where $M_f(\theta)$ is the bending moment of foam-filled section at rotation angle θ; P_m and M_{uf} are given in Eq.(4.16) and Eq.(4.20), respectively; θ_0 is an upper limit for θ usually set by the jamming condition. θ_{cf} is the critical bending rotation for local sectional collapse of foam-filled section, and was determined by Santosa [5] based on the numerical simulation results

$$\theta_{cf} = \theta_c + 3.98\frac{\rho_f}{\rho_s} \tag{4.22}$$

where ρ_f denotes the macroscopic mass density of the foam, and ρ_s is the mass density of the skeleton material of the foam. Additional comparison with numerical results for larger relative densities confirmed the validity of this equation.

The moment-rotation characteristic of foam-filled section is illustrated in Fig.4.40. To obtain the full expression of bending moment $M_f(\theta)$, the moment elevation ΔM needs to be determined. One has to resort to numerical and experimental means for this.

4.2.3 Numerical Simulation of Bending Collapse of Foam-filled Beams

In order to quantify the bending moment elevation ΔM, numerical simulations using PAM-CRASH are conducted on a three-point bending configuration of thin-walled square beam. Under such a configuration, the shear force is a reaction in the beam

theory. If the Love-Kirchhoff hypothesis is adopted, then the shear strains vanish ($d\epsilon_{xz} = 0$) and there is no work done in the shear mode. The foam filler considered in the simulation is of relative density up to 20%.

4.2.3.1 Finite Element Modeling

A thin-walled square beam with sectional geometry 50 × 50 × 1.5mm and length 470mm is considered in the analysis. The beam is subject to three-point bending, see Fig.4.41.

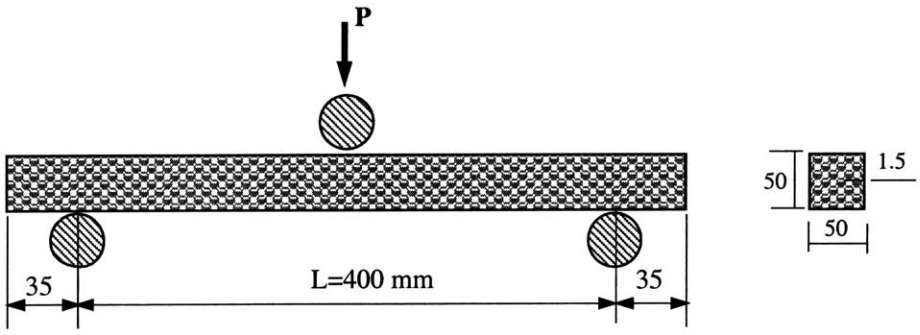

Figure 4.41: A foam-filled thin-walled square beam undergoing bending

The outer skin of the beam is modeled with Belytschko-Tsay 4-node shell elements. Due to the localized nature of the deformation, the central segment where the bending collapse is expected is modeled with finer mesh(2.5×2.5mm mesh size). The aluminum foam core is modeled with 8-node solid elements. The punch is modeled as a rigid cylinder with diameter 50mm. The velocity boundary condition is applied on the rigid punch. The two supports are spaced 400mm apart and are modeled as stationary rigid cylinders. The interaction between the foam core and the skin is simulated with a surface-to-surface sliding contact. The bending process is simulated quasi-statically.

4.2.3.2 Material Modeling

The wall material of the beam is stainless steel Cr18Ni8, with Young's modulus $E = 200$GPa, initial yield stress $\sigma_y = 507.6$MPa, ultimate strength $\sigma_u = 698.6$MPa,

Poisson's ratio $\nu = 0.3$. The reason for choosing this material is that some experimental data on the bending collapse of beams made of such material is available [8]. The constitutive behavior is based on an elastic-plastic material model with Von Mises's isotropic plasticity algorithm with multilinear plastic hardening. The plastic hardening data was obtained by averaging four uniaxial tensile tests. The stress-strain curves of the tensile tests are shown in Fig.4.42.

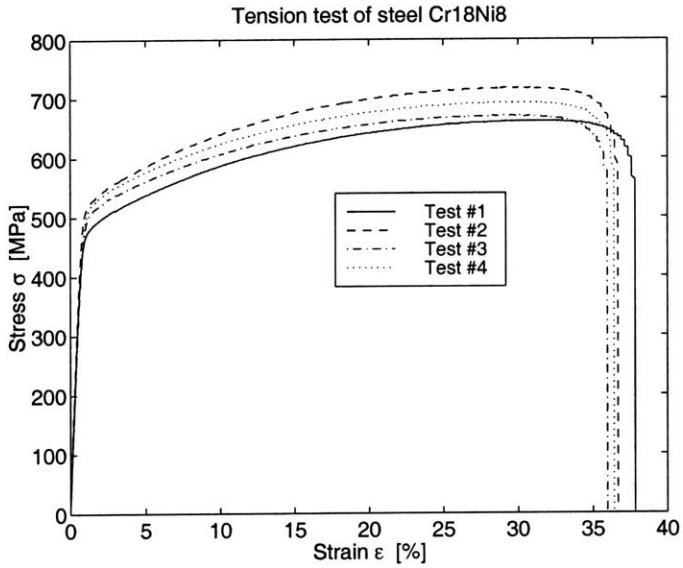

Figure 4.42: Stress-strain curves of stainless steel Cr18Ni8

The mechanical behavior of aluminum foam is characterized by elastic modulus E_f, plastic collapse stress σ_f, shear modulus G_f, plastic shear strength τ_f, and densification strain ϵ_D, see Fig.2.7. These parameters strongly depend on the aluminum foam density ρ_f, and were described in Chapter 2 via Eq.(2.1) $\backsim$ Eq.(2.6).

The IFAM aluminum foam is used in the present analysis, which has the plastic flow stress $\sigma_{0f} = 111.4$MPa and Young's modulus $E_s = 94.1$GPa, [8].

4.2.3.3 Numerical Results

Finite element simulations are conducted on the empty and foam-filled beams with foam density $\rho_f = 0.20, 0.35, 0.47, 0.54 g/cm^3$, respectively.

The deformation modes of an empty and a foam-filled beam($\rho_f = 0.47g/cm^3$) are shown in Fig.4.43 and Fig.4.44, respectively. The corresponding post-test specimens (obtained from reference [8]) are also shown in the same figures. One can see that the bending collapse of hollow beam consists of an inward fold at the compression flange and two outward folds at the adjacent flanges, while the localized crushing is retarded due to the presence of the foam filler and propagates to the adjacent sections in filled beams. More plastic hinge lines are formed, which results in higher energy dissipation and plastic bending resistance.

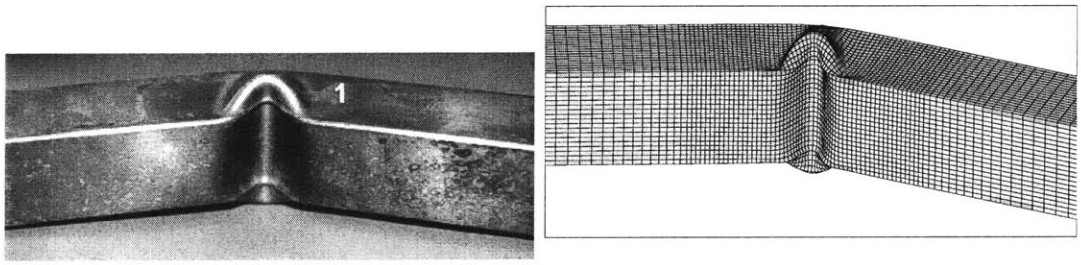

Figure 4.43: Deformation patterns of empty beam: experimental and numerical

Similar deformation patterns were also observed in the three-point bending test of foam-filled hat sections described in the previous section (see Fig.4.45).

The strengthening effect of the foam filling can be observed in Fig.4.46, which shows the punch force-displacement response of three-point bending of empty and foam filled beams($\rho_f = 0.2g/cm^3$). The bending moments and the bending rotation relationship can be derived approximately from the three-point bending configuration, and was given in Eq.(4.1) and Eq.(4.2).

The calculated $M - \theta$ responses are shown in Fig.4.47.

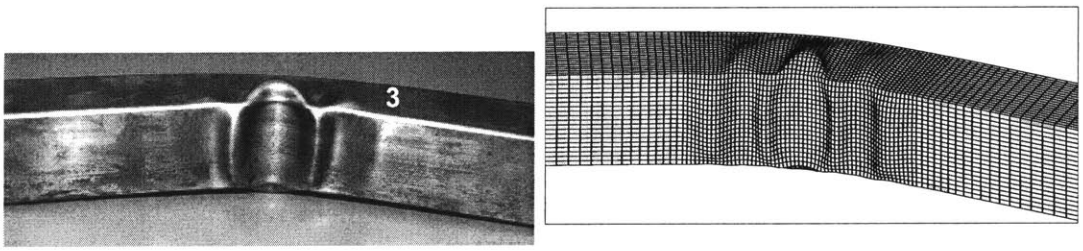

Figure 4.44: Deformation pattern of foam-filled beam: experimental and numerical

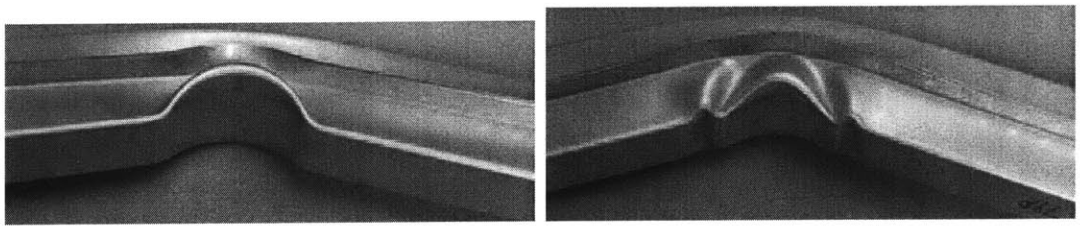

Figure 4.45: Deformation patterns of foam-filled hat sections(left:non-filled; right:foam-filled).

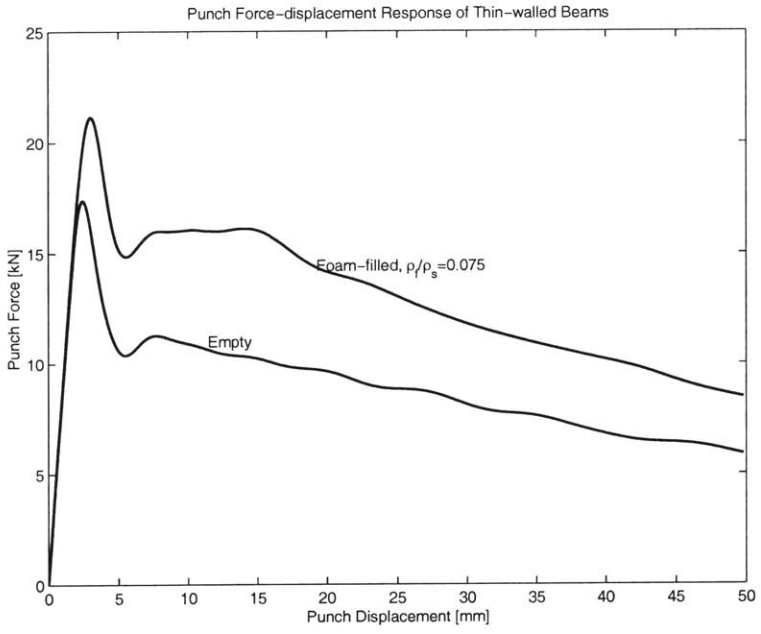

Figure 4.46: Punch force-displacement response of beams

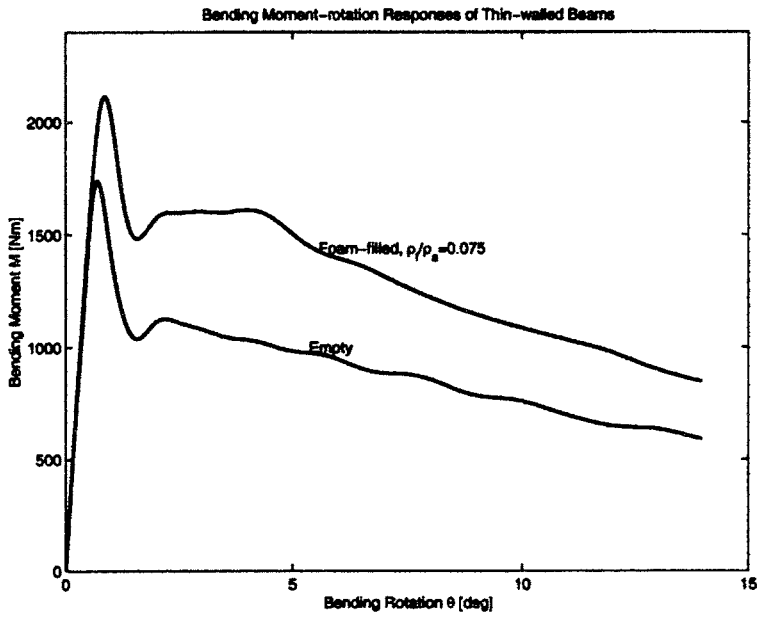

Figure 4.47: Bending moment-rotation response of beams

The bending moment elevations ΔM resulting from foam filling can be evaluated from the differences between the ultimate bending moment of filled beams and that of empty beams. The results for various foam densities are listed in Table 4.5. Some experimental data are also shown in the same table.

4.2.4 The Bending Moment Elevations due to Foam Filling

The bending moment elevations ΔM for various foam densities predicted by numerical simulations are listed in Table 4.5. The results for low density foam($\rho_f/\rho_s = 0.01 \backsim 0.027$) are taken from reference [5]. Experimental data obtained in the previous section, and by IFAM [8] and BMW are also listed in the same table. The plastic flow stress σ_{0f} of the skeleton material of different foams were obtained experimentally [5].

As discussed in Chapter 3, the mean crushing force elevation resulting from foam-filling in axial crushing mode of thin-walled square column is proportional to the crushing force of the foam core, i.e., $\Delta P_m \propto \sigma_f b^2$. Using a dimensional analysis, it is reasonable to assume that the bending moment elevation resulting from foam filling

can be approximated as

$$\Delta M = C\sigma_f b^3 \tag{4.23}$$

On employing the expression for σ_f (Eq.(2.4)), it yields

$$\frac{\Delta M}{\sigma_{0f} b^3} = C\left(\frac{\rho_f}{\rho_s}\right)^{\frac{3}{2}} \tag{4.24}$$

where C is the coefficient, and can be determined via least-square fitting of the numerical and experimental data in Table 4.5, which gives

$$C = 0.95 \tag{4.25}$$

Table 4.5: The predictions of bending moment elevation ΔM

	Numerical Results								Experimental Data			
									MIT	BMW	IFAM	
$\rho_f(g/cm^3)$	0.029	0.046	0.06	0.073	0.20	0.35	0.47	0.54	0.27	0.135	0.275	0.594
ρ_f/ρ_s	0.011	0.017	0.022	0.027	0.075	0.13	0.175	0.20	0.10	0.05	0.102	0.22
$\sigma_{0f}(MPa)$	150.4	150.4	150.4	150.4	111.4	111.4	111.4	111.4	98.3	150.4	150.4	111.4
b(mm)	51	51	51	51	50	50	50	50	50	*	*	50
t(mm)	1.6	1.6	1.6	1.6	1.5	1.5	1.5	1.5	2	1.4	1.4	1.5
ΔM(Nm)	58.8	82.8	99.3	113.5	307.5	985	1108	750	385	371	1449	1100
$\frac{\Delta M}{b^3\sigma_{0f}}$	0.003	0.004	0.005	0.006	0.022	0.071	0.08	0.054	0.031	0.007	0.027	0.079

**BMW testing was on a rectangular hat section. For such a section, b^3 term in normalizing ΔM is approximated as $bh(\frac{b+h}{2})$.*

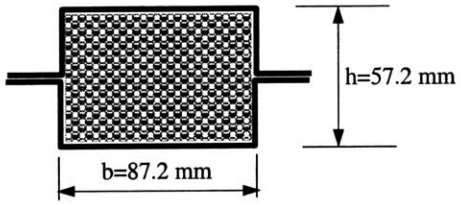

Figure 4.48: Rectangular hat section tested by BMW

It leads to the expression of the ultimate bending moment of foam-filled section

$$M_{uf} = M_u + 0.95\sigma_{0f}b^3\left(\frac{\rho_f}{\rho_s}\right)^{\frac{3}{2}} \tag{4.26}$$

where M_u is the ultimate bending moment of empty section given in Eq.(4.17).

Fig.4.2.4 shows the curve-fitting of the numerical and experimental data of bending moment elevation. One can see that Eq.(4.24) with $C = 0.95$ gives very good approximation compared to the numerical and experimental results.

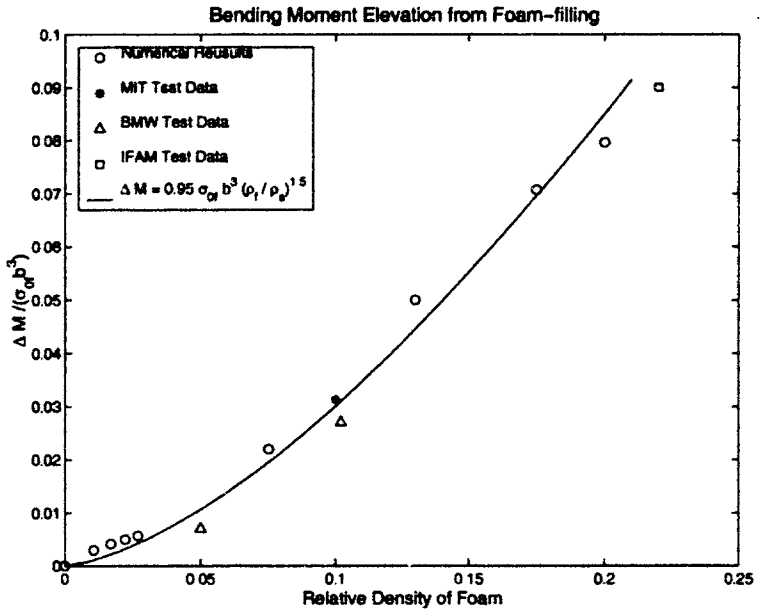

Figure 4.49: Bending moment elevation resulting from foam filling

4.2.5 The Bending Moment Elevations due to Honeycomb Filling

Another ultralight material which can be utilized to fill hollow structural members is aluminum honeycomb. Similar to the case of foam filling, numerical simulations were carried out to predict the plastic bending resistance of honeycomb-filled sections. The

relative density of the honeycomb filler is up to 20%. The same three point bending configuration and finite element modeling techniques are employed as in the case of foam filling. The strengthening effect of the honeycomb filling was quantified.

The material modeling of honeycomb is slightly different from that of foam. The mechanical properties of aluminum honeycomb are smeared in three orthogonal directions of T, L, and W as shown in Fig.2.11. The mechanical properties in each direction are defined in Table 2.1. The out of plane direction T is considered as the *strong axis*, while the in-plane directions L and W are *weak axes*. In the numerical analysis, 5256 Hexcel aluminum honeycomb is used. The *strong axis* of the honeycomb is aligned with the punching direction. Fig.4.50 shows a typical bending collapse deformation of honeycomb filled beam. As can be seen, the deformation pattern is similar to that of a foam-filled beam. The moment-rotation responses of the empty beam and a honeycomb-filled beam with $\rho_h/\rho_s = 0.15$ are depicted in Fig.4.51.

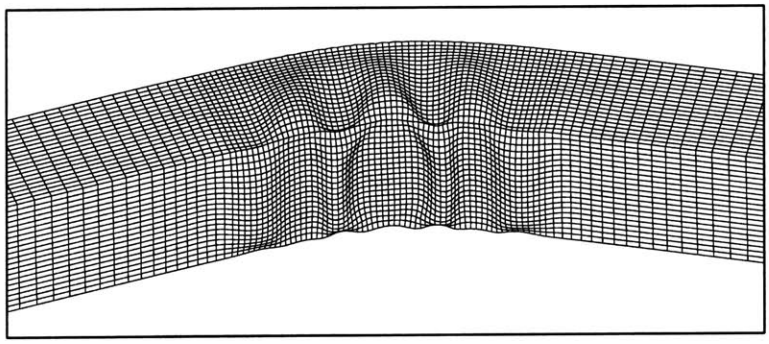

Figure 4.50: The deformation pattern of a honeycomb-filled beam (relative density 0.15)

The moment elevation ΔM resulting from honeycomb filling predicted by numerical analysis for various honeycomb densities are summarized in Table 4.6. With the same

argument as in the case of foam filling, ΔM can be expressed as

$$\Delta M = \alpha \sigma_{0h} b^3 \left(\frac{\rho_h}{\rho_s}\right)^{\beta} \tag{4.27}$$

where α and β are two coefficients to be determined by least square fitting of the numerical results.

Table 4.6: The numerical results for various of honeycomb densities

ρ_h/ρ_s	0	0.0125	0.025	0.05	0.10	0.15	0.20
b(mm)	50	50	50	50	50	50	50
σ_{0h} (MPa)	285	285	285	285	285	285	285
ΔM (Nm)	0	59.0	183.8	356.2	480.9	557.1	677.8
$\frac{\Delta M}{\sigma_{0h} b^3}$	0	0.0017	0.0052	0.010	0.0135	0.0156	0.0190

Fig.4.52 shows the curve-fitting of the numerical data of Table 4.6 using Eq.(4.27) with $\alpha = 0.06$ and $\beta = \frac{2}{3}$. With Eq.(4.27), the ultimate bending moment of honeycomb-filled section can be calculated

$$M_{uh} = M_u + 0.06 \sigma_{0h} b^3 \left(\frac{\rho_h}{\rho_s}\right)^{\frac{2}{3}} \tag{4.28}$$

where the ultimate bending moment of non-filled section M_u is given in Eq.(4.17).

Finally, the moment-rotation characteristic of honeycomb-filled beam can be obtained

$$M_h(\theta) = \begin{cases} M_{uh} & 0 \le \theta < \theta_{ch} \\ P_m b(\frac{1}{\sqrt{\theta}} - \frac{1}{\sqrt{\theta_{ch}}}) + M_{uh} & \theta \ge \theta_{ch} \end{cases} \tag{4.29}$$

where θ_{ch} is the critical bending rotation to sectional collapse and was given in [5] based on the numerical simulation results. Additional comparison with numerical results for larger relative densities confirmed the validity of this equation.

$$\theta_{ch} = \theta_c + 4.92 \frac{\rho_h}{\rho_s} \tag{4.30}$$

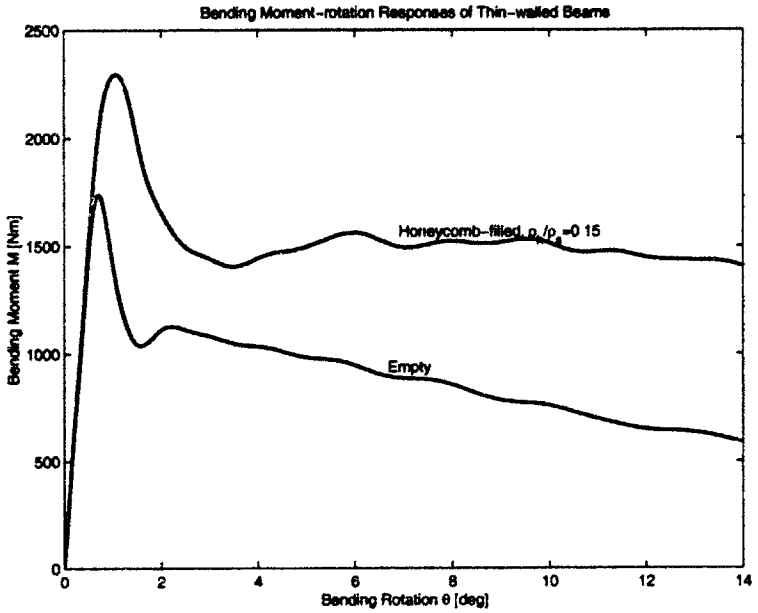

Figure 4.51: The moment-rotation responses of beams

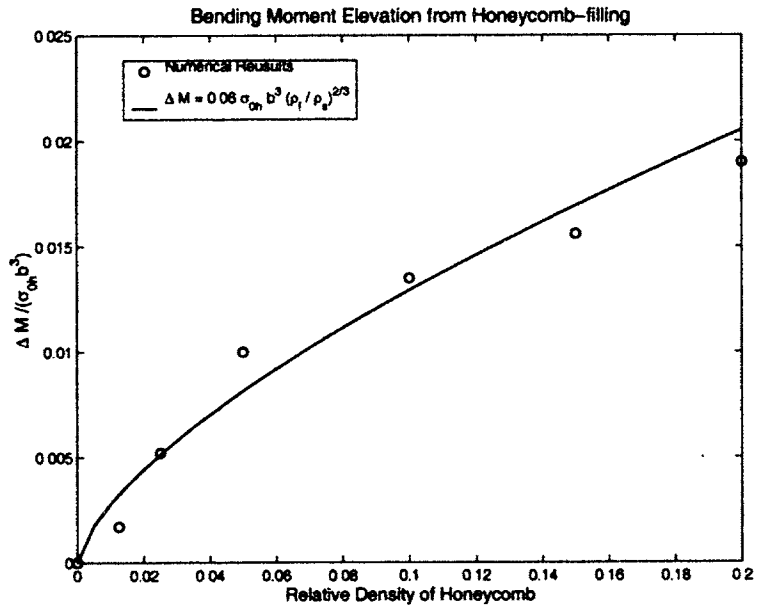

Figure 4.52: Bending moment elevation resulting from honeycomb filling

4.2.6 Comparison Between Foam and Honeycomb Fillings

Take Hydro aluminum foam and Hexcel aluminum honeycomb for comparison. One can see from Fig.4.53, the moment elevation resulting from honeycomb filling is larger than that from foam filling for the relative density of filler up to 8%.

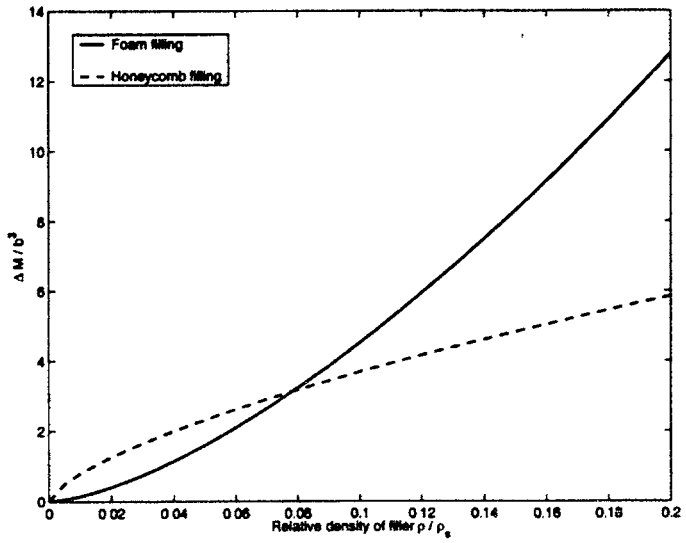

Figure 4.53: Comparison of strengthening effects of foam filling and honeycomb filling

It should be underlined that the strengthening effect of filling strongly depends on the mechanical properties of the filler (σ_{0f} and σ_{0h}, for instance). The above conclusion is only valid for the currently considered core materials (Hydro aluminum foam and Hexcel aluminum honeycomb).

Furthermore, honeycomb material shows strong orthogonality in three directions. It is assumed in the calculation that the strong axis T of honeycomb material is aligned normal to the compression flange of the beam. If the weak axis W or L is aligned in the bending direction, the strengthening effect of the honeycomb is almost negligible. Hence, the reinforcement provided by the honeycomb filler depends on the loading direction in bending mode. On the contrary, the aluminum foam shows more or less isotropy in its mechanical behavior.

Chapter 5

Torsional Crushing of Foam-filled Thin-walled Tubes

The load bearing capacity of prismatic tubes under torsion was given much less attention in the literature than the corresponding axial crushing and bending collapse cases. However, the torsional behavior of thin-walled beams or tubes well beyond the maximum torque is of interest in many applications. For example, in a side impact of a car, the bending collapse of the B-pillar may induce twisting deformation on the roof rail (see Fig.5.1, the space frame structure of Audi A8).

The maximum load under torsion or combined loading has been studied over the past several years. Baba [69] developed a finite element formulation for stress analysis of a twisting bar with a solid or a thin-walled section. The formulation can be applied to elastic-plastic pure-torsion or warping-torsion problems with small displacement. Murray [70] studied a single rectangular plate subjected to pure torsion, bending and compressive loading. The uncoupled solutions were later extended to combined loading in the case of compressive and torsional moment [71], and torsion and bending moment [72]. Grant [73] proposed a solution to the thin-walled sections undergoing uniform torsion. Ma [74] carried out an experimental study of the static and dynamic plastic buckling of circular cylindrical shells under impact torque using the Hopkinson torsional bar. The static and dynamic critical torque of the shells were determined experimentally. All the aforementioned theoretical analyses developed for the torsion

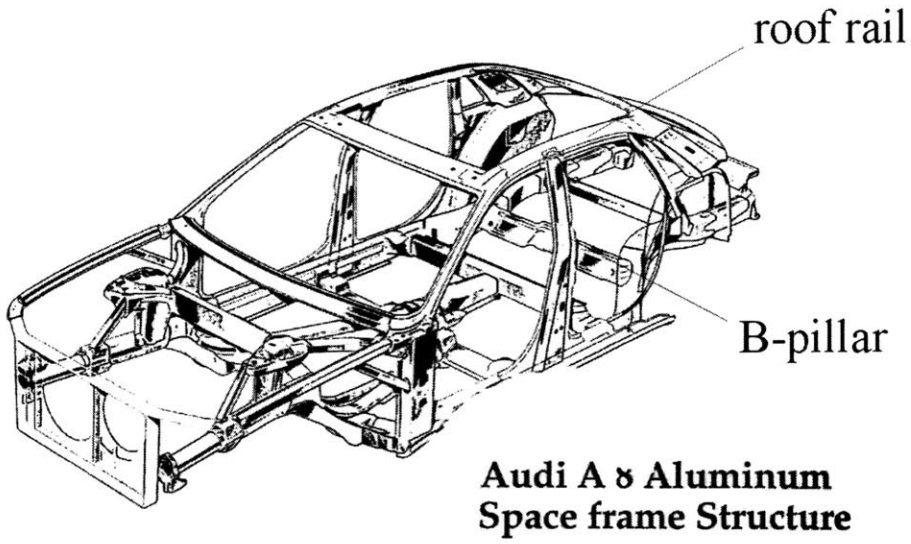

Figure 5.1: An illustration of Audi A8 space frame structure

problems were restricted to the onset of local buckling. Trahair [75] developed a method to analyze the plastic torsion behavior of monosymmetric I-sections, lipped and unlipped channels, and equal flange lipped angles, and of point-symmetric lipped and unlipped Z-sections. Recently, Santosa and Wierzbicki [9] conducted numerical simulations for empty boxes and the tubes with light metal filler using a nonlinear finite element code. Three parameters, which are initial crushing moment, the stabilized torsional crushing moment and the critical twisting rotation, were defined to characterize the torsional behavior of empty box tubes.

In the first part of this chapter, a theoretical solution is proposed for the torsional behavior of thin-walled square tubes in the range of large rotation up to 180°. Simple torsional cross-sectional buckling models are developed, which capture the basic torsional crushing mechanisms of thin-walled tubes. The pre-buckling, plastic buckling and post-buckling behavior of square tubes are predicted using kinematic approach. Approximate formulas for the torsional resistance are derived and the solutions are compared with the numerical results. The analytical solution for the square tubes is then extended to rectangular and hexagonal thin-walled tubes. Numerical simulations for rectangular and hexagonal tubes are also carried out and the results are presented for comparison with the analytical solutions.

Of particular interest in crashworthiness application is the effect of the lightweight metal filler on the resistance and energy absorption of a structural member. The torsional collapse behavior and plastic resistance of thin-walled tubes filled with aluminum foam are investigated theoretically and numerically in the second part of this chapter. It is found that the presence of the lightweight filler acting as elastic-plastic foundation to the skin changes the sectional collapse mode into higher ones, and hence increases the torsional resistance. The upper and lower bounds on the torsional resistance of filled tubes are established approximately. Numerical simulations are carried out. Based on the obtained numerical results, the strengthening effects of foam filling are investigated, and the twisting moment elevation due to filling is quantified.

Finally, torsional experiments on empty and foam-filled square tubes are performed and results are used to validate the theoretical and numerical solutions.

5.1 Thin-walled Empty Square Tubes

5.1.1 Numerical Solutions

The torsional crushing problem of thin-walled square tubes will be solved numerically in this section using the non-linear explicit finite element code PAM-CRASH. The twisting deformation pattern of the tube and the sectional buckling mode are illustrated. The torsional plastic resistance of tubes with various length-width ratios are revealed at large twisting rotations up to 180^0. Santosa and Wierzbicki [9] conducted numerical simulations for empty thin-walled box tubes undergoing torsion using non-linear explicit finite element code PAM-CRASH. The numerical study is continued in present research.

5.1.1.1 Finite Element Modeling

The considered tube has length l, width b and wall thickness t, with $l/b = 4 \backsim 6.5$ and $b/t = 50$. The end twisting rotation is denoted by θ_0 (see Fig.5.2). The tube wall was modeled with Belytschko-Tsay-4-node thin shell elements with one integration

point in element plane and three integration points over the thickness. See Fig.5.3 for FE model. Clamped boundary condition was applied at one end of the tube, while the other end was connected to a rigid body mechanism. The rigid body was allowed to rotate about the x-axis and move in x direction. By connecting to this rigid-body mechanism, warping at the end section was prevented. The velocity of twisting rotation was applied at the center of gravity of the rigid body. The torsion process was simulated under quasi-static condition.

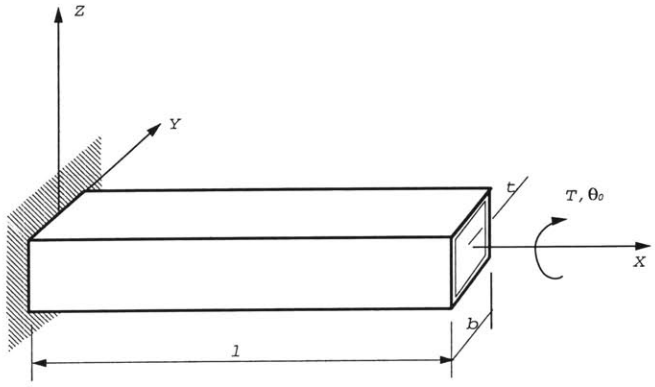

Figure 5.2: A thin-walled square tube under torsional loading

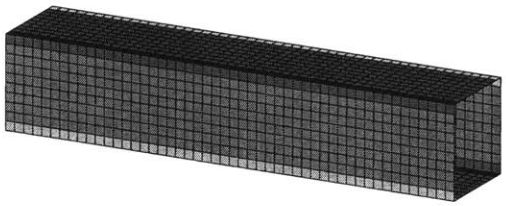

Figure 5.3: Finite Element Model of the tube

Self impact contact (type 36 in PAM-CRASH) was utilized to simulate the contact between walls of the tube during large twisting deformation.

The constitutive behavior of the thin shell element for the tube material was based on

Table 5.1: Strain hardening data for AA6063 T7

Plastic Strain	Plastic Stress [MPa]	Plastic Modulus [MPa]
0.00000	86.94	33390.0
0.00027	95.94	2913.0
0.00211	101.30	2200.0
0.00575	109.30	1959.0
0.01493	127.30	1460.0
0.02630	149.30	594.1
0.06939	169.50	18.0
0.15270	171.00	0.0

the elastic-plastic material model with Von-Mises isotropic plasticity algorithm. The transverse shear effect was also considered by this material model. Plastic hardening was described by a multi-linear curve, in which pairs of the plastic tangent modulus and the plastic stress were specified.

The material used in the calculation was the aluminum extrusion AA6063 T7, which is commonly used for automotive structures, with mechanical properties of Young's modulus $E = 69GPa$, initial yield strength $\sigma_y = 86.94MPa$, Poisson's ratio $\nu = 0.3$. The strain hardening data are given in Table 5.1. The engineering stress-strain data were converted to true stress-strain data for finite element calculation.

5.1.1.2 Deformation Pattern

Square tubes with wall thickness $t = 1mm$, width-thickness ratio $b/t = 50$, and length-width ratio $l/b = 4 \backsim 6.5$ were considered in the numerical calculation. The deformed shape of the tube with $l/b = 5$ at 45° rotation is illustrated in Fig.5.4. The evolution of the shape at the mostly deformed cross-section is shown in Fig.5.5. The following conclusions can be drawn from the analysis of the above figures.

(i) In the pre-buckling stage, all sections rotate without sectional buckling. The

resistance is derived from shear stresses that increase with the increasing rotation angle for an elastic-plastic material.

(ii) After buckling, the walls deform inwards with an increasing amplitude w_0 of the transverse displacement function $w(x_\alpha)$. This reduces shear stresses and changes the geometry so that the torsional resistance drops by a factor of 2 to 3 relative to the pre-buckling state.

(iii) At a certain deflection amplitude and rotation angle, internal touching occurs which locally stiffens a given cross-section. From this point on, torsional deformation spreads along the length of the tube causing a moderate increase of the torque.

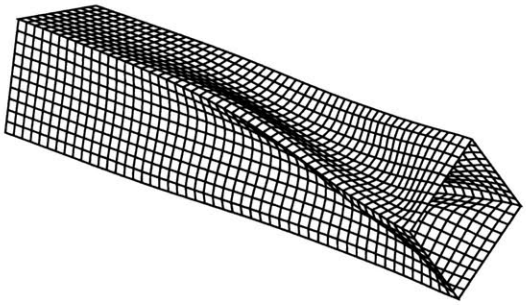

Figure 5.4: Deformed shape of the thin-walled square tube at 45° rotation (normalized rotation 0.0785)

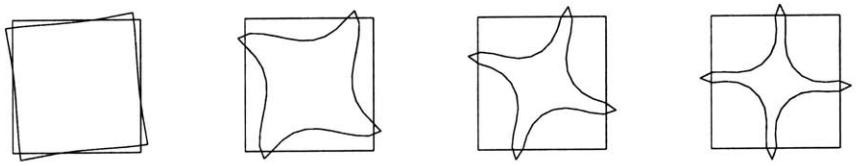

Figure 5.5: Evolution of the shape at the mostly deformed cross-section

5.1.1.3 Plastic Resistance

The torsional plastic resistances of tubes with $t = 1mm$, $b/t = 50$ and $l/b = 4 \backsim 6.5$ are plotted in Fig.5.6 at rotation angles up to 180°. It can be seen that the twisting moment reached an ultimate value approximately at a twisting rotation

of 10°. Subsequently, the torsional resistance dropped significantly with increasing twisting rotation due to the plastic sectional buckling of the tube. At large rotations, the twisting moment appeared to reach a constant asymptotic value.

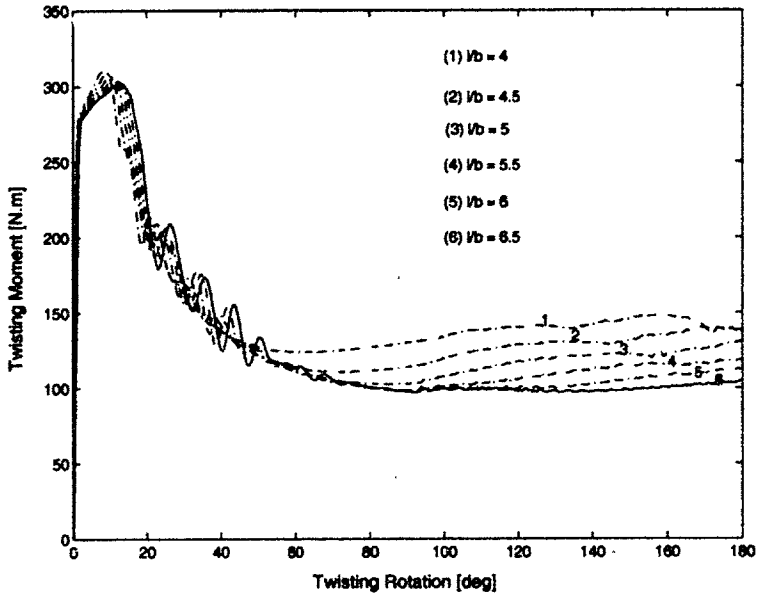

Figure 5.6: Torsional plastic resistance of thin-walled square tubes (To normalize, plot $\frac{T}{2\sigma_0 b^2 t}$ vs $\frac{b\theta_0}{l}$ with $\sigma_0 = 105.4MPa$, $t = 1mm$ and corresponding b and l)

5.1.2 Theoretical Solution

The torsional crushing of thin-walled square tubes will be modeled analytically in this section. A kinematic approach is utilized in the analysis based on the principle of virtual velocities. Pre-buckling, cross-section deforming and deformation-spreading mechanisms are proposed as three phases of torsional deformation. A kinematically admissible displacement field is established in each phase of deformation and a closed-form solution for torque is obtained. By considering the analogy between a square tube and a cylindrical shell, the critical twisting rotation to plastic buckling is estimated.

5.1.2.1 Theoretical Formulation

A kinematic approach is proposed in the present study based on assumed displacement fields and the principle of virtual velocities

$$T\dot{\theta}_0 = \int_S N_{\alpha\beta}\dot{\epsilon}_{\alpha\beta}dS \tag{5.1}$$

where T is the twisting moment applied at the end of the tube; $N_{\alpha\beta}$ and $\dot{\epsilon}_{\alpha\beta}$ are respectively components of the membrane stress tensor and strain rate tensor in the tube wall. The material is assumed to be rigid-perfectly plastic. The components of the strain rate tensor in the local in-plane coordinate system $\alpha, \beta = 1, 2$ are

$$\dot{\epsilon}_{\alpha\beta} = \begin{pmatrix} \dot{\epsilon}_{xx} & \dot{\epsilon}_{xy} \\ \dot{\epsilon}_{yx} & \dot{\epsilon}_{yy} \end{pmatrix} \tag{5.2}$$

where x is aligned with the longitudinal axis of the tube. Components $\dot{\epsilon}_{xx}$ and $\dot{\epsilon}_{xy}$ can be evaluated from the assumed deformation modes and are related to the twisting rotation $(\theta_0, \dot{\theta}_0)$. The tensor of membrane stress $N_{\alpha\beta}$ is determined from the associated flow rule. To take strain hardening effect into account in the rigid-perfectly plastic model, the work equivalent flow strength is used in the calculation. The expression for the equivalent flow stress σ_0 was given in Eq.(3.10).

The Von Mises yielding condition in a plane stress field is

$$F \equiv \sigma_{xx}^2 + \sigma_{yy}^2 - \sigma_{xx}\sigma_{yy} + 3\tau_{xy}^2 - \sigma_0^2 = 0 \tag{5.3}$$

The strain rate can be calculated from the associated flow rule

$$\dot{\epsilon}_{\alpha\beta} = \dot{\kappa}\frac{\partial F}{\partial \sigma_{\alpha\beta}} \tag{5.4}$$

where $\dot{\kappa}$ is a flow constant at a given point (Eq.(5.6)), but varies in space and time.

The components of stress tensor $\sigma_{\alpha\beta}$ can be expressed in terms of the proportionality constant $\dot{\kappa}$ and the strain rate tensor $\dot{\epsilon}_{\alpha\beta}$ by inverting Eq.(5.4)

$$\begin{aligned}
\sigma_{xx} &= \frac{1}{3\dot{\kappa}}(\dot{\epsilon}_{yy} + 2\dot{\epsilon}_{xx}) \\
\sigma_{yy} &= \frac{1}{3\dot{\kappa}}(\dot{\epsilon}_{xx} + 2\dot{\epsilon}_{yy}) \\
\tau_{xy} &= \frac{1}{3\dot{\kappa}}\dot{\epsilon}_{xy}
\end{aligned} \tag{5.5}$$

The constant $\dot{\kappa}$ can now be determined by substituting Eq.(5.5) into Eq.(5.3)

$$\dot{\kappa} = \frac{1}{\sqrt{3}\sigma_0}\sqrt{\dot{\epsilon}_{xx}^2 + \dot{\epsilon}_{yy}^2 + \dot{\epsilon}_{xx}\dot{\epsilon}_{yy} + \dot{\epsilon}_{xy}^2} \tag{5.6}$$

The rate of plastic work per unit volume is $\sigma_{\alpha\beta}\dot{\epsilon}_{\alpha\beta}$, which can be expanded into the following form

$$\sigma_{\alpha\beta}\dot{\epsilon}_{\alpha\beta} = \sigma_{xx}\dot{\epsilon}_{xx} + \sigma_{yy}\dot{\epsilon}_{yy} + 2\tau_{xy}\dot{\epsilon}_{xy} \tag{5.7}$$

Substituting Eq.(5.5) and Eq.(5.6) into Eq.(5.7) leads to

$$\sigma_{\alpha\beta}\dot{\epsilon}_{\alpha\beta} = \frac{2\sigma_0}{\sqrt{3}}\sqrt{\dot{\epsilon}_{xx}^2 + \dot{\epsilon}_{yy}^2 + \dot{\epsilon}_{xx}\dot{\epsilon}_{yy} + \dot{\epsilon}_{xy}^2} \tag{5.8}$$

Therefore, Eq.(5.1) can be re-written as

$$T\dot{\theta}_0 = \frac{2\sigma_0 t}{\sqrt{3}}\int_S \sqrt{\dot{\epsilon}_{xx}^2 + \dot{\epsilon}_{yy}^2 + \dot{\epsilon}_{xx}\dot{\epsilon}_{yy} + \dot{\epsilon}_{xy}^2}\, dS \tag{5.9}$$

where the integration is taken over the surfaces of the tube. It should be noted that bending and warping resistances are neglected in the current analysis.

5.1.2.2 The Deformation Modes

As observed in numerical simulations, sectional buckling occurs when the end rotation reaches a certain angle (critical twisting rotation) and an inward sectional deformation mode is developed in the tube (see Fig.5.5), which reduces stresses and changes the geometry so that the torsional resistance considerably drops. The amplitude of the sectional buckling deformation increases with the increase of twist. At a certain rotation angle, internal touching occurs at the most deformed cross-section which locally stiffens the section. As a result, a most-deformed section is formed. From that point on, this deformation will spread along the length of the tube and thus form a most-deformed area. With these physical understandings, a three-phase deformation mechanism is proposed in the current approximate analysis. The three phases are namely, pre-buckling, cross-section buckling and collapse-spreading. They will be described in the following.

In each phase, a velocity field is assumed and the principle of virtual velocities (Eq.(5.9)) is applied to evaluate the torsional resistance of the tube. The shell of the tube is assumed to be inextensible in the hoop direction. Thus, $\dot{\epsilon}_{yy} = 0$.

Pre-buckling

In this phase, all sections rotate as rigid bodies without sectional deformation. It is assumed that the rotation angles at sections from the fixed end to the free end are varying linearly from 0 to the end rotation angle θ_0. Therefore, the walls of the tube become spiral surfaces, as illustrated in Fig.5.7.

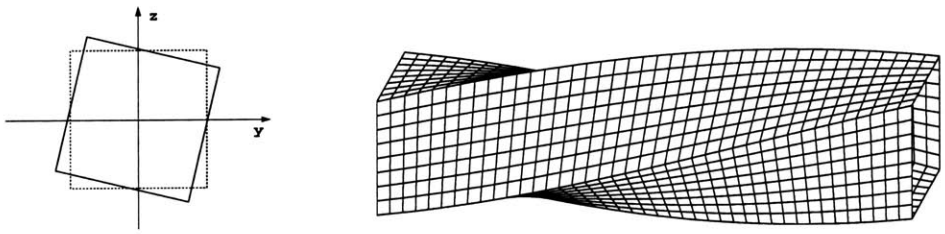

Figure 5.7: Theoretical pre-buckling deformation of a square tube under torsion

Consider the upper flange of the tube, the components of the displacement vector (u, v, w) at a cross-section with longitudinal coordinate x can be found from the assumption of the spiral-shape deformation

$$\begin{aligned} u &= 0 \\ v &= y\cos(\frac{\theta_0}{l}x) + \frac{b}{2}\sin(\frac{\theta_0}{l}x) - y \\ w &= \frac{b}{2}\cos(\frac{\theta_0}{l}x) - y\sin(\frac{\theta_0}{l}x) - \frac{b}{2} \end{aligned} \tag{5.10}$$

where θ_0 is the end twisting rotation; y denotes the coordinate in hoop direction.

The Lagrangian strain tensor can then be calculated

$$\begin{aligned} \epsilon_{xx} &= \frac{\partial u}{\partial x} + \frac{1}{2}[(\frac{\partial u}{\partial x})^2 + (\frac{\partial v}{\partial x})^2 + (\frac{\partial w}{\partial x})^2] = \frac{\theta_0^2 y^2}{2l^2} + \frac{b^2\theta_0^2}{8l^2} \\ \epsilon_{xy} &= \frac{1}{2}[\frac{\partial u}{\partial y} + \frac{\partial v}{\partial x} + (\frac{\partial u}{\partial x}\frac{\partial u}{\partial y} + \frac{\partial v}{\partial x}\frac{\partial v}{\partial y} + \frac{\partial w}{\partial x}\frac{\partial w}{\partial y})] = \frac{b\theta_0}{4l} \end{aligned} \tag{5.11}$$

and the strain rates

$$\begin{aligned} \dot{\epsilon}_{xx} &= [(\frac{y}{l})^2 + \frac{1}{4}(\frac{b}{l})^2]\theta_0\dot{\theta}_0 \\ \dot{\epsilon}_{xy} &= \frac{1}{4}(\frac{b}{l})\dot{\theta}_0 \end{aligned} \tag{5.12}$$

The other components of the strain and strain rate tensor are zero.

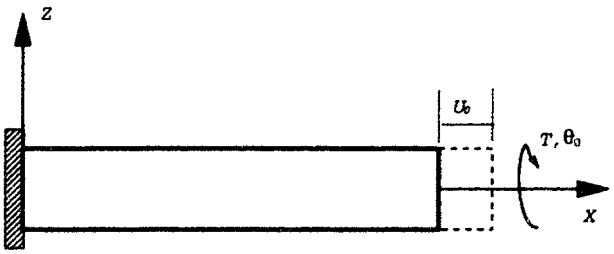

Figure 5.8: An axially free tube with displacement U_0

If the tube is axially free at the loaded end, there will be an axial displacement U_0, as shown in Fig.5.1.2.2. The strain and strain rate in X direction will become

$$\begin{aligned} \epsilon_{xx} &= \frac{\theta_0^2 y^2}{2l^2} + \frac{b^2\theta_0^2}{8l^2} - \frac{U_0}{l} \\ \dot{\epsilon}_{xx} &= [(\frac{y}{l})^2 + \frac{1}{4}(\frac{b}{l})^2]\theta_0 \cdot \dot{\theta}_0 - \frac{\dot{U}_0}{l} \end{aligned} \tag{5.13}$$

Applying the principle of virtual velocities and substituting the above expressions of strain rate into Eq.(5.9) finally results in the following expression for the torsional resistance. The algebraic details can be found in Appendix A of reference [76] and more details in reference [77].

$$\tau = 0.58 + 0.05r^2\theta_0^2 \tag{5.14}$$

where θ_0 is the end twisting rotation angle; r is the width-length ratio of the tube,

$$r = \frac{b}{l} \tag{5.15}$$

and τ is the dimensionless twisting moment defined by

$$\tau = \frac{T}{2\sigma_0 b^2 t} \tag{5.16}$$

where T is the physical twisting moment; σ_0 denotes the plastic flow stress of the material; b and t are width and wall thickness of the tube, respectively.

Cross-section Buckling

Sectional buckling will begin when the twisting rotation reaches a certain angle (critical twisting rotation). During buckling, the walls deform inward. This relieves the membrane strains and reduces the load-carrying capacity of the tube. In the present analysis, a sinusoidal sectional buckling mode is assumed (see Fig.5.9) and a sinusoidal-spiral deformation is developed in the tube(see Fig.5.10 and Fig.5.11). The sectional distortion is the largest at the mid-section of the tube and it decreases to zero at the two ends. Meanwhile, the collapsing sections rotate with angles assumed to vary linearly from one end to the other. The amplitude of the sectional deformation at each section is related to the rotation angle via the geometry of the problem and an assumption of inextensibility in the hoop direction of the wall.

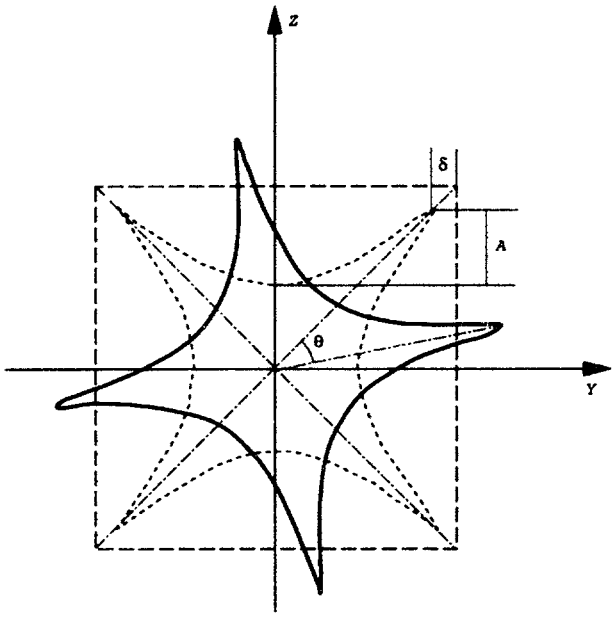

Figure 5.9: Theoretical buckling deformation of the cross-section under torsion

Consider a buckling section shown in Fig.5.9. The dotted lines denote a virtually deformed section before twisting rotation. The solid lines represent the buckling section with a rotation angle θ. From the geometry, the displacement of the upper flange at this section can be obtained

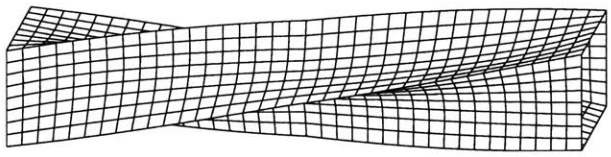

Figure 5.10: Buckling deformation of a square tube under torsion

$$
\begin{aligned}
v &= (y - \delta \sin\frac{\pi y}{b})\cos\theta + (\frac{b}{2} - A\cos\frac{\pi y}{b} - \delta)\sin\theta - y \\
w &= (\frac{b}{2} - A\cos\frac{\pi y}{b})\cos\theta - (y - \delta\sin\frac{\pi y}{b})\sin\theta - \frac{b}{2}
\end{aligned}
\tag{5.17}
$$

where θ is the rotation angle at current section, $\theta = \frac{x}{l}\theta_0$; A and δ are two parameters which can be calculated by considering the geometry of the section and the deformation characteristics (see reference [77] for details):

$$
\begin{aligned}
\delta &= \frac{b}{4}(1 - \frac{\sqrt{2}}{2})\frac{4}{\pi}\theta, \qquad (0 \le x \le \frac{l}{2}) \\
\delta &= \frac{b}{4}(1 - \frac{\sqrt{2}}{2})\frac{4}{\pi}(\theta_0 - \theta), \qquad (\frac{l}{2} \le x \le l)
\end{aligned}
\tag{5.18}
$$

and the amplitude A can be approximated by the expression (details can be found in reference [77]):

$$
\frac{A}{b} = 0.24(1 - e^{-40\frac{\delta}{b}}) \tag{5.19}
$$

The expressions for Lagrangian strain and strain rate tensor can be derived in the same manner as in the pre-buckling phase.

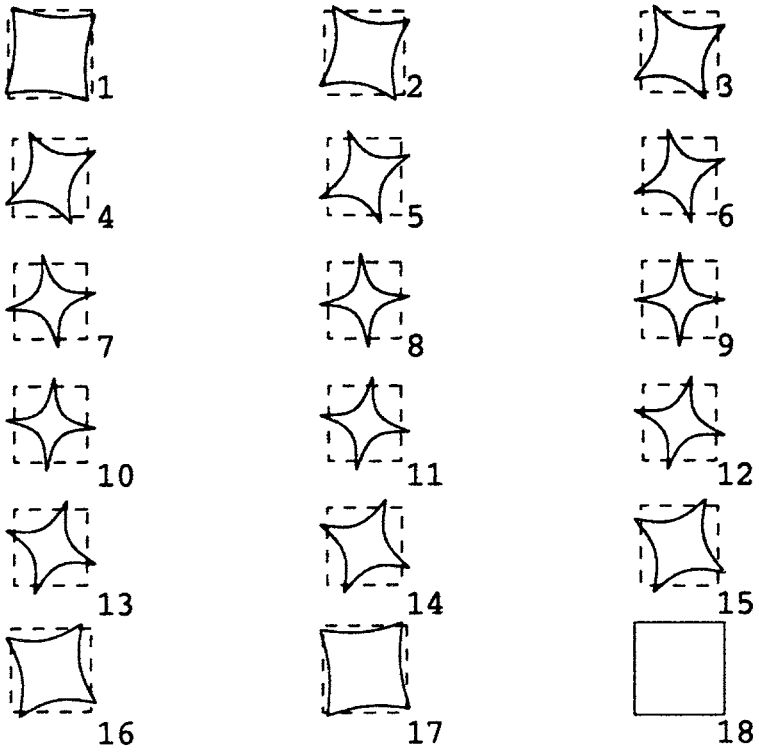

Figure 5.11: Deformed sections along the tube

By employing Eq.(5.9), the torsional resistance in the buckling phase can be found as a function of the twisting rotation θ_0(algebraic details can be found in reference [77]):

$$\tau = 0.58 - 0.21r^{-0.22}\theta_0^{0.34} \tag{5.20}$$

where r is width-length ratio of the tube.

Collapse-spreading

At a certain transverse deflection amplitude and corresponding twisting rotation angle (transitional twisting rotation), internal touching occurs at the mid-section of the tube, which is the most-deformed section in this theoretical model. It is hypothesized that the most-deformed section is formed when the twisting rotation $\theta_0 = \frac{\pi}{2}$, i.e.,the transitional twisting rotation $\theta_m = \frac{\pi}{2}$. Fig.5.12 shows the most-deformed section.

From this point on, the most-deformed section will spread towards two ends from the mid-section and a most-deformed area will be formed centering at the mid-section with length 2ξ (see Fig.5.13).

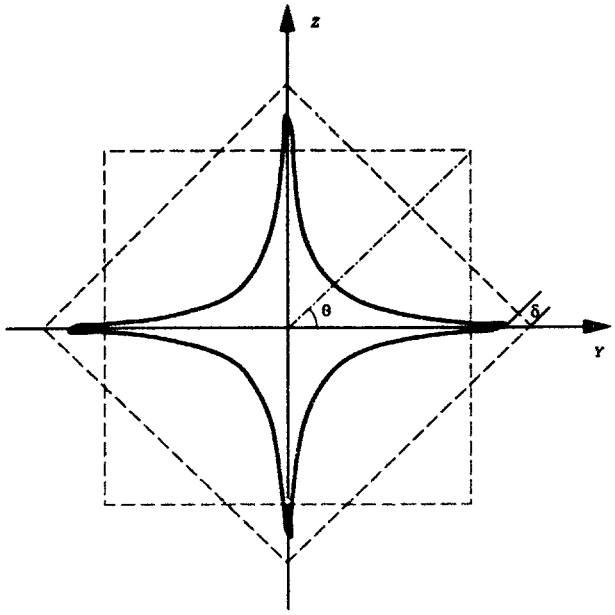

Figure 5.12: Most-deformed section

From the point of view of energy, the tube in this phase is equivalent to a tube with twisting rotation θ_m and a most-deformed area 2ξ. With the increase of twisting rotation, additional work is done by spreading the most-deformed area, the effect of which is equivalent to the reduction of the length of the tube and thus the growth of the width-length ratio r. Therefore, the effect of deformation spreading can be considered by introducing an equivalent width-length ratio R

$$R = \frac{L_0}{L_0 - \xi} r = \frac{\theta_0}{\theta_m} r \tag{5.21}$$

Hence the torsional resistance in the deformation-spreading phase can be evaluated by replacing the original width-length ratio r in Eq.(5.20) with the above-defined equivalent width-length ratio R

$$\tau = 0.58 - 0.21 R^{-0.22} \theta_m^{0.34} = 0.58 - 0.21 \frac{\theta_m^{0.56}}{\theta_0^{0.22}} r^{-0.22} \tag{5.22}$$

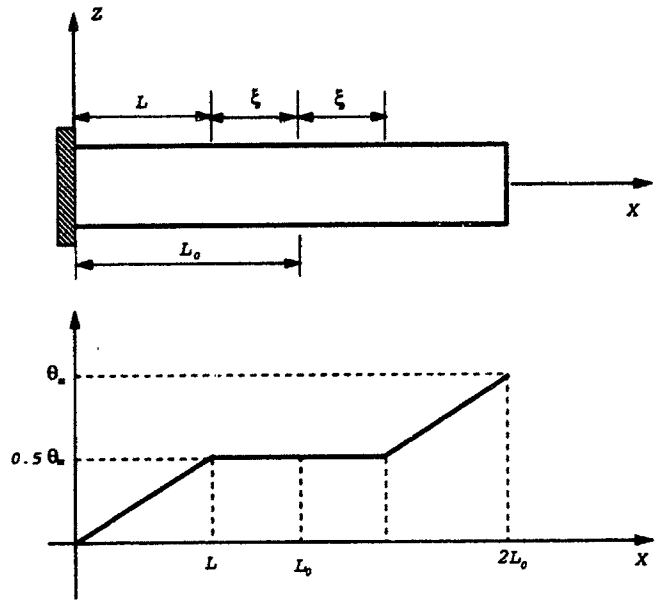

Figure 5.13: Equivalent tube with spreaded most-deformed area when $\theta_0 > \theta_m$

5.1.3 Critical Twisting Rotation for Plastic Buckling

The critical twisting rotation θ_c can be estimated by using an analogy of the current problem to the buckling problem of a cylindrical shell undergoing torsion, the governing equation of which is [78]

$$D\nabla^8 w + \frac{1-\nu^2}{a^2} C w_{,xxxx} - \frac{2}{a} N_{x\theta} \nabla^4 w_{,x\theta} = 0 \tag{5.23}$$

where w is the deflection function; D and C are, respectively the bending and axial rigidity of the shell;a denotes the radius of the cylinder; $N_{x\theta}$ is the pre-buckling shear force.

Under torsional loading, the buckling deformation of a cylindrical shell consists of a number of circumferential waves that spiral around the cylinder from one end to the other (nodal lines of helical form). Such waves can be represented by a radial

deflection function of the form

$$w = C_1 sin(\bar{m}x - n\theta) \tag{5.24}$$

where C_1 is a constant and $\bar{m} = m\pi a/L$.

Substituting Eq.(5.24) into Eq.(5.23) yields the following expression

$$N_{x\theta} = \frac{(\bar{m}^2 + n^2)^2}{2\bar{m}n}\frac{D}{a^2} + \frac{\bar{m}^3}{2(\bar{m}^2 + n^2)^2 n}(1 - \nu^2)C \tag{5.25}$$

where $C = Et/(1 - \nu^2); D = Et^3/12(1 - \nu^2)$.

For long cylinders, the shell buckles in two circumferential waves; i.e., the smallest values of $N_{x\theta_0}$ corresponds to $n = 2$ (Fig.5.14).

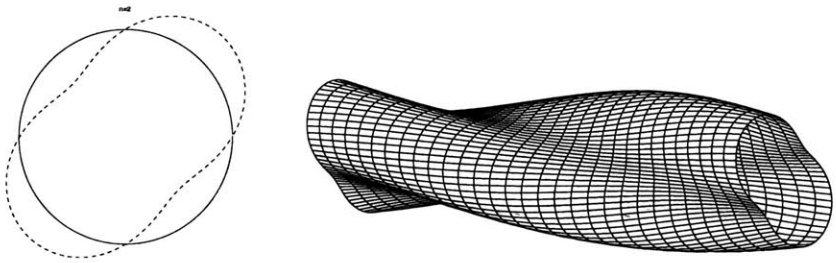

Figure 5.14: Torsional buckling of a cylindrical shell (n=2)

In the case of a thin-walled square tube, the presence of four right corners will induce a different torsional buckling mode from that of a cylindrical shell. A reasonable assumption is that the tube will buckle in the way as shown in Fig.5.15. This corresponds to $n = 4$.

On employing Eq.(5.25), introduction of $n = 4$ gives

$$N_{x\theta} = \frac{32Et^3}{12(1 - \nu^2)\bar{m}a^2} + \frac{\bar{m}^3 Et}{2048} \tag{5.26}$$

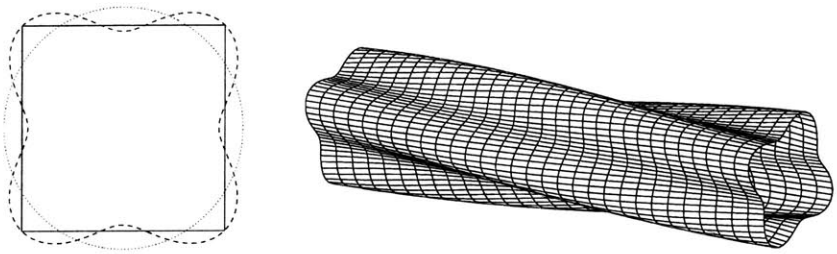

Figure 5.15: Torsional buckling mode of a cylindrical shell (n=4)

as long as the analogy between the square and circular tube holds.

The value of $\bar{m}$ for which $N_{x\theta_0}$ is a minimum may be determined by analytical minimization of $N_{x\theta_0}$ with respect to $\bar{m}$. It leads to

$$\bar{m} = 6.53(\frac{t^2}{(1-\nu^2)a^2})^{0.25} \tag{5.27}$$

Introduction into the expression for $N_{x\theta}$ and rearrangement now yields

$$\tau_{cr} = \frac{0.55E}{(1-\nu^2)^{0.75}}(\frac{t}{a})^{1.5} \tag{5.28}$$

Accordingly, the critical shear strain to buckling is

$$\varepsilon_{cr} = \frac{\tau_{cr}}{2G} = \frac{0.55(1+\nu)}{(1-\nu^2)^{0.75}}(\frac{t}{a})^{1.5} \tag{5.29}$$

It was suggested by Rhodes [79] that the strain to buckling is the same in the plastic and elastic range. The shear strain in pre-buckling phase of thin-walled square tube undergoing pure torsion is related to the rotation angle θ_0 by Eq.(5.11)

$$\varepsilon_{xy} = \frac{\theta_0 b}{4l} \tag{5.30}$$

where θ_0 is the end twisting rotation; b and l denote the width and length of the tube, respectively.

Equating Eq.(5.29) and Eq.(5.30) results in the critical twisting rotation θ_c for torsional plastic buckling of a square tube

$$\theta_c = \frac{2.2(1+\nu)}{(1-\nu^2)^{0.75}} \left(\frac{t}{a}\right)^{1.5} \frac{l}{b} \tag{5.31}$$

For a square tube with Poisson ratio $\nu = 0.3$ and geometrical parameters $\frac{l}{b} = 5 \backsim 6$ and $\frac{b}{t} = 50$, if a is taken approximately as $b/2$ (inscribed circle inside a square), Eq.(5.31) gives the critical twisting rotation $\theta_c = 7° \backsim 8°$. It is quite close to the angle predicted numerically in Ref.[9] and predicted analytically in Ref.[80], which both give $\theta_c \approx 10°$.

5.1.4 Comparison Between Theoretical Solution and Finite element Solution

In the previous section, analytical expression for the torque in three successive phases were obtained:

$$\begin{aligned} \tau &= 0.58 + 0.05 r^2 \theta_0^2 && (0 \le \theta_0 \le \theta_c) \\ \tau &= 0.58 - 0.21 r^{-0.22} \theta_0^{0.34} && (\theta_c < \theta_0 \le \theta_m) \\ \tau &= 0.58 - 0.21 R^{-0.22} \theta_m^{0.34} && (\theta_0 > \theta_m) \end{aligned} \tag{5.32}$$

where θ_0 is the twisting rotation(in radian); $\theta_m = \frac{\pi}{2}$; R is defined in Eq.(5.21); r denotes the width-length ratio, $r = b/l$.

The critical twisting rotation for plastic sectional buckling can be evaluated by Eq.(5.31). The physical twisting moment is related to the dimensionless twisting moment by

$$T = 2\sigma_0 b^2 t \tau \tag{5.33}$$

Taking, for instance, that the tube material is AA6063 T7 with plastic flow stress of $\sigma_0 = 105.4 N/mm^2$, and taking $b = 50mm$, $\frac{b}{t} = 50$, the twisting moment in

pre-buckling, post-buckling and collapse-spreading phase are plotted in Fig.5.16(solid lines) for tubes with length-width ratio varying from 4 to 6.5. The results of finite element analysis are also shown in the figure for comparison (dashed lines).

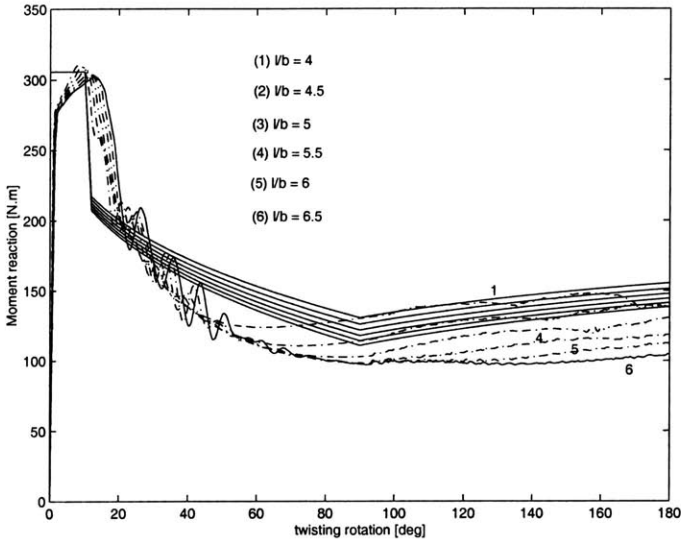

Figure 5.16: Plastic resistance of square tubes of alloy AA6063 T7 (Solid lines:analytical model; dotted lines: FEM results. To normalize, plot $\frac{T}{2\sigma_0 b^2 t}$ vs $\frac{b\theta_0}{l}$ with $\sigma_0 = 105.4MPa$, $t = 1mm$ and corresponding b and l)

As can be seen in the figure, the analytical solutions agree well with the numerical results. The torsional resistance reaches the ultimate value at approximately 10° at which point the sectional buckling initiates. After that, crushing mechanism take place at sections and the loading resistance drops considerably due to the plastic sectional buckling. At large rotations, the twisting moments appear to assume constant values, which correspond to a stabilized crushing.

5.2 Plastic Resistance of Thin-walled Rectangular and Hexagonal Tubes

The analytical solution obtained in the previous section for a square tube will be extended to rectangular and hexagonal tubes. Numerical simulations will be conducted for rectangular and hexagonal tubes and results will be compared with theoretical solutions.

5.2.1 Theoretical Solution

Now consider the torsional crushing of rectangular and hexagonal tubes (shown in Fig.5.17). Due to the similarity in the geometry, we can expect that the torsional behavior of these two tubes will be similar to that of a square tube. Thus, we can assume for simplicity that the dimensionless twisting moments and the critical twisting rotation of rectangular and hexagonal tubes are the same as those of square tube. Therefore, Eq.(5.31) and Eq.(5.32) can be readily applied to the cases of rectangular and hexagonal tubes, with a new width-length ratio r defined as $\frac{b+h}{2l}$ for rectangular tubes.

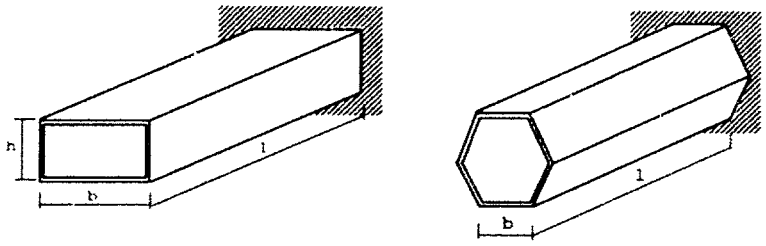

Figure 5.17: Rectangular and hexagonal tubes subjected to torsion

However, Eq.(5.33) should be revised to calculate the physical twisting moment of non-square tubes. One can note that the b^2 term in Eq.(5.33) represents the area enclosed by the cross-section of a square tube [81]. Employing the counterparts of this in rectangular and hexagonal tubes, we can obtain the torsional resistance of a

rectangular tube

$$T = 2\tau\sigma_0 bht \tag{5.34}$$

and hexagonal tube

$$T = 3\sqrt{3}\tau\sigma_0 b^2 t \tag{5.35}$$

where τ denotes the dimensionless twisting moment expressed in Eq.(5.32) for pre-buckling, cross-section buckling and collapse-spreading phases.

More generally, the torsional resistance of a prismatic tube can be calculated

$$T = 2\tau\sigma_0 At \tag{5.36}$$

where A is the area enclosed by the cross-section of the tube.

The foregoing analytical solutions of rectangular and hexagonal tubes with material AA6063 T7 are plotted in Fig.5.20 and Fig.5.21, respectively. Numerical study was conducted for comparison.

5.2.2 Numerical Study

Rectangular tubes of $b = 50mm$, $l = 250mm$ and $t = 1mm$ with three different aspect ratios $b/h = 2; 1.5$ and 1.25 were analyzed numerically using the PAM-CRASH. Numerical simulations were also carried out for hexagonal tubes of $l = 250mm$ and $t = 1mm$ with three different width of flanges, $b = 30mm, 40mm$ and $50mm$ respectively. In all cases, a clamped boundary condition is applied at one end of the tube, while the other end is connected to a rigid body mechanism (therefore no warping at the end section). which is allowed to move axially. The twisting rotation is applied quasi-statically at the center of the rigid section. The tube material is aluminum extrusion

AA6063 T7, with tensile parameters of Young's modulus $E = 6.9 \times 10^4 N/mm^2$ and initial yield stress $\sigma_y = 86.94 N/mm^2$.

The plastic deformation of rectangular and hexagonal tubes at 90° twisting rotation are illustrated in Figs.5.18 and 5.19 respectively. It can be seen that, similar to the case of square tubes, inward sectional buckling mode is developed and propagated along the length of the tubes. The moment responses are shown in Fig.5.20 and Fig.5.21, together with the analytical solutions derived above.

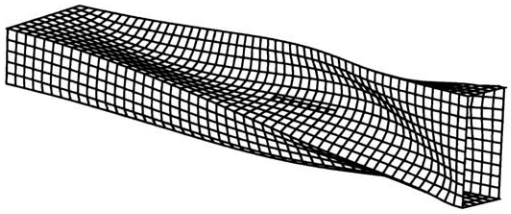

Figure 5.18: Plastic deformation of a rectangular tube at 90° rotation

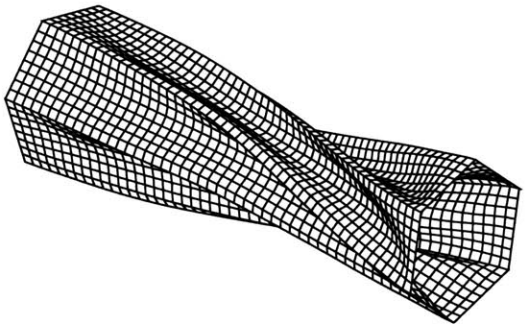

Figure 5.19: Plastic deformation of a hexagonal tube at 90° rotation

As can be seen from the figures, the torsional behavior of thin-walled rectangular and hexagonal tubes can also be characterized by three distinct phases, as in the case of square square tubes, namely pre-buckling, buckling and collapse-spreading

phases. In the pre-buckling phase, the tubes show high load resistance which drops significantly when tubes buckle and appears to assume a nearly constant value in the collapse-spreading phase.

The analytical solution for rectangular tubes compares very well with the numerical results, as can be seen from Fig.5.20, while for hexagonal tubes, it predicts smaller pre-buckling response and critical twisting rotation than numerical results give. It is due to the fact that the analytical solution is based on the geometry of a square tube. The rectangular tube deforms in a similar way as the square tube and the deformation mode of a hexagonal tube is differed.

It should also be noted that, because a hexagonal section has larger corner angles(120°) than a square section(90°), it can deform inward more than a square section can. Consequently, the collapse-spreading will be delayed in the hexagonal tube and the transition angle θ_m (which defines a kink in the stabilized phase of response) will be larger than $\pi/2$. This can be observed in the numerical results shown in Fig.5.13 but this property has not been taken into account in the present analytical solution.

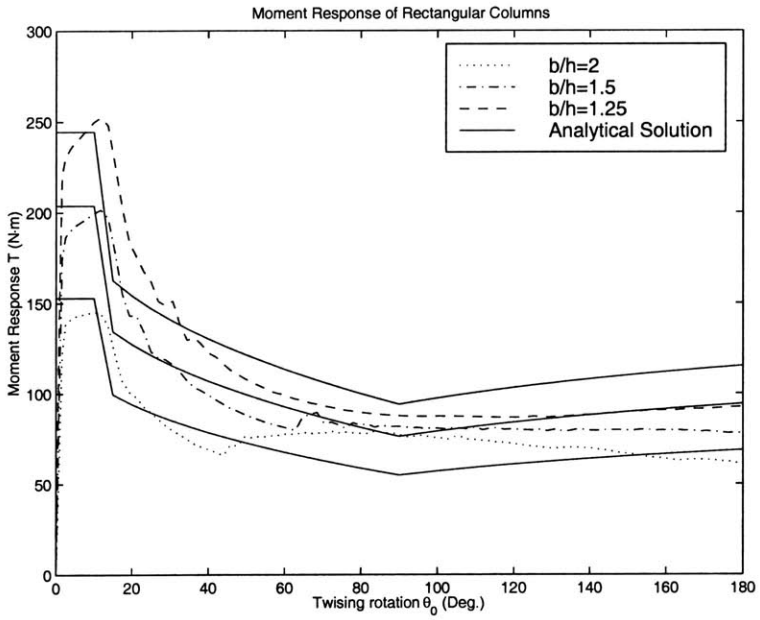

Figure 5.20: Torsional resistance of rectangular tubes($l/b = 5, b/t = 50$)

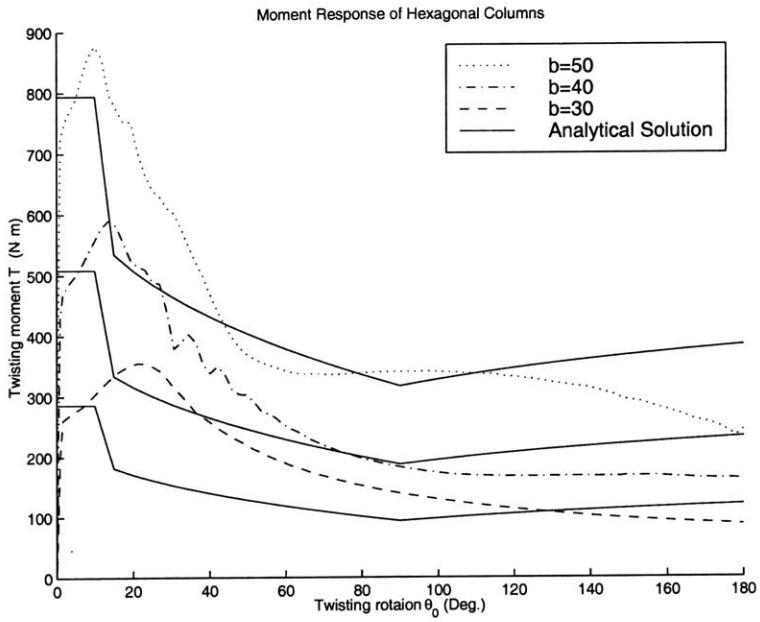

Figure 5.21: Torsional resistance of hexagonal tubes($l = 250mm, t = 1mm$; The unit for b in figure is also mm)

5.3 Foam-filled Thin-walled Tubes

From the viewpoint of weight-efficient crashworthy structural design, it is of interest to study the torsional behavior and plastic resistance of thin-walled columns filled with ultralight crushable metal core. An earlier numerical study [9] showed that the light metal filler has the significant effect on the torsional resistance and is preferable, in terms of specific energy absorption, to the conventional way of strengthening by means of increasing the wall thickness.

We shall consider in the following the torsional crushing behavior of square tubes filled with aluminum foam. It is expected that the foam will provide lateral support to the flanges of the column and therefore change the collapse mechanism of the column. The mechanics of the process involves the collapse of the flanges, the crushing of the foam and the interactions between the outer skin and the filler. It is very difficult to take into account all these complicated factors in a simple analytical model, even though the mechanics behind them are well understood. However, we still can, by reasonable assumptions and simple analysis, obtain some useful results.

5.3.1 Upper Bound of Torsional Resistance

Consider a thin-walled square tube with width b, thickness t and length l undergoing torsion. The tube material is assumed to satisfy the Von Mises yielding condition. The equivalent plastic stress $\bar{\sigma}$ is defined by

$$\bar{\sigma}^2 = \sigma_x^2 + \sigma_y^2 - \sigma_x\sigma_y + 3\tau_{xy}^2 \tag{5.37}$$

Noting that the shear stress τ_{xy} resulting from torsion is the main component of the stress tensor in a tube undergoing pure torsion, Eq.(5.37) can be reasonably approximated as

$$\tau_{xy} = \frac{\bar{\sigma}}{\sqrt{3}} \tag{5.38}$$

It is assumed that the strain hardening of the material obeys the power law

$$\bar{\sigma} = C\bar{\varepsilon}^n \tag{5.39}$$

where C and n are material constants. Denoting by $\bar{\varepsilon}$ the equivalent plastic strain, Eq.(5.39) gives

$$\tau_{xy} = \frac{C}{\sqrt{3}}\varepsilon_{xy}^n \tag{5.40}$$

In previous sections, a pre-buckling configuration of square tube subjected to torsion was studied and the shear strain in tube was given by Eq.(5.30).

Substituting Eq.(5.30) into Eq.(5.40) yields the following expression for τ_{xy} along the entire tube before sectional buckling

$$\tau_{xy} = \frac{C}{\sqrt{3}}\left(\frac{b\theta_0}{4l}\right)^n \tag{5.41}$$

It is straightforward then to get the twisting moment T on the sections [81](Fig.5.22).

$$T = 2\tau_{xy} b^2 t = \frac{2Cb^2 t}{\sqrt{3}} \left(\frac{b\theta_0}{4l}\right)^n \tag{5.42}$$

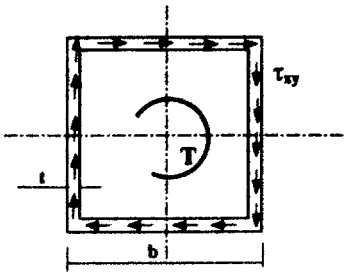

Figure 5.22: Shear stress distribution on a square section

It should be noted that the above solution applies to empty tubes with rigidly rotating cross-sections or for the tubes with infinite strong filler inside. Therefore, Eq.(5.42) establishes approximately an upper bound for the torsional resistance of the tube.

5.3.2 Lower Bound on Torsional Resistance

As pointed out earlier, the foam filler can provide lateral support to the tube sections and thus changes the torsional collapse mechanism of the tube. Further investigation shows that, rather than buckling inward as in empty tubes, the foam-filled sections may buckle outward due to the presence of the foam functioning as elastic-plastic foundation. This higher order deformation mode will increase the torsional rigidity and hence lead to a higher twisting resistance.

Assuming an inward sectional collapse mode (observed in empty tubes) and introducing the power law stress-strain relationship into the torsional resistance formulation, with Eq.(5.20), (5.33), we can get the following equation for the torsional resistance, which should form a lower bound of the twisting resistance of foam-filled tubes.

$$T = 2\left[0.58 - 0.21\left(\frac{l}{b}\right)^{0.22} \theta_0^{0.34}\right] C \left(\frac{b\theta_0}{4l}\right)^n b^2 t \tag{5.43}$$

5.3.3 Torsional Resistance of the Foam Core

So far, we have established the upper and lower bounds on the torsional resistance which foam-filled tubes can provide without taking into account the load carrying capacity of the foam core itself, which also contributes to the total torsional resistance of the tube.

The numerical analysis shows that aluminum foam inside tubes is subjected only to a limited crushing. This suggests that the resistance of the foam filler can be decoupled from the resistance of the column. For simplicity, we shall consider an equivalent solid cylinder with the same radius of gyration as the solid foam core, which gives $R = 0.57b$, where R is the radius of the equivalent cylinder (Fig.5.23).

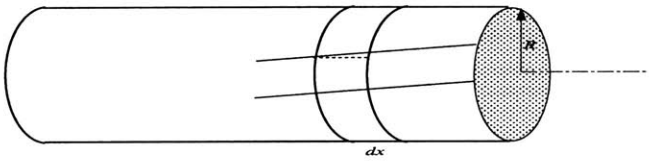

Figure 5.23: An equivalent foam cylinder subjected to torsion

The shear strain $\varepsilon_{x\theta}$ at current radius r in the cylinder is

$$\varepsilon_{x\theta} = \frac{r}{l}\theta_0 \tag{5.44}$$

where θ_0 is the end twisting rotation.

and the rate of shear strain

$$\dot{\varepsilon_{x\theta}} = \frac{r}{l}\dot{\theta_0} \tag{5.45}$$

Denoting by τ_f the flow stress of the foam in shear and applying the principle of virtual velocities to calculate the twisting moment

$$T\dot{\theta_0} = \frac{2\tau_f}{\sqrt{3}}\int_V \dot{\varepsilon_{x\theta}} dV \tag{5.46}$$

where T is the twisting moment and the integration is over the whole volume.

Substituting Eq.(5.45) into Eq.(5.46) and performing the integration result in the following equation

$$T = 0.225\tau_f b^3 \tag{5.47}$$

It is evident that T depends only on the plastic shear stress τ_f of the foam and the sectional dimension b.

Finally, we can set forth the upper and lower bounds of the torsional resistance of a foam-filled tube including the contribution from the shear resistance of the foam. The upper bound is obtained by assuming no sectional collapse and adding the contribution of Eq.(5.47) to Eq.(5.42)

$$T_u = \frac{2Cb^2t}{\sqrt{3}}\left(\frac{b\theta_0}{4l}\right)^n + 0.225\tau_f b^3 \tag{5.48}$$

Similarly, the lower bound is calculated taking into account the "inward" sectional collapse.

$$T_l = 2\left[0.58 - 0.21\left(\frac{l}{b}\right)^{0.22}\theta_0^{0.34}\right] C\left(\frac{b\theta_0}{4l}\right)^n b^2t + 0.225\tau_f b^3 \tag{5.49}$$

It should be noted that the strength contribution from the shear of the foam is relatively small, usually of an oder of less than 10%. Corresponding plots of lower and upper bound solutions are given in Fig.5.30.

We have thus far established the lower and upper bounds of the torsional crushing resistance of foam-filled tubes. Due to the complexity of the problem, one must resort to numerical method for more detail and accurate solutions. We shall present some numerical results in the next section.

5.3.4 Numerical Simulations

Santosa and Wierzbicki [9] have conducted non-linear finite element analysis on foam-filled square tubes subjected to large twisting rotation. Chen and Wierzbicki [82] later on continued the analysis and carried out more detail studies on this problem. Both unbonded and bonded filling were considered and different aluminum foam, with strength from 50psi(0.345MPa) to 250psi(1.723MPa) were used to analyze the effect of foam filler. The results of the above analyses are summarized in the following.

5.3.4.1 Finite Element Modeling

Square box tubes of 50x50mm cross section with thickness 1mm, length 250mm are considered in the numerical simulation. The column wall was modeled with 4-node shell element using material type 103 of the PAM-CRASH material library. The foam core was modeled with 8-node solid element using material type 41. Clamped boundary conditions are applied at one end of the column, while the other end is connected to a rigid body mechanism, which is allowed to move in two-degree of freedom so that it can perform rigid rotations and axial displacements. By connecting to this rigid body mechanism, warping at the end section was not allowed. The twisting rotation is applied at the center of the rigid body. See Fig.5.24.

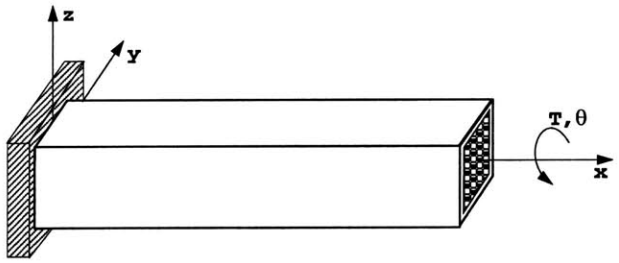

Figure 5.24: A foam-filled tube subjected to torsion

The column material is aluminum extrusion AA6063 T7, with mechanical properties of Young's modulus $E = 69GPa$, yield stress $\sigma_y = 86.94MPa$. The foam core is Hydro Aluminum foam. A simplified foam model is used in the current study based on an uncoupled compressive and shear strength of the foam (σ_f, τ_f), see Fig.2.7.

Mechanical properties of aluminum foam for various relative densities were given in Chapter 2 via Eq.(2.1) $\backsim$ Eq.(2.6).

5.3.4.2 Failure Modes

Examples of deformed square tubes at 45° rotation calculated using the above model are shown in Fig.5.25 to Fig.5.27 corresponding to the empty, unbonded foam-filled and bonded foam-filled columns, respectively. Cross-sectional deformation of the same tubes in the mostly deformed sections are shown in Fig.5.28. The following conclusions can be drawn from the numerical analysis:

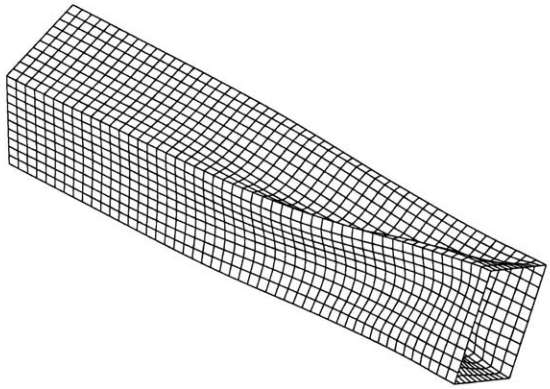

Figure 5.25: Deformed shapes of square tubes at 45°: empty

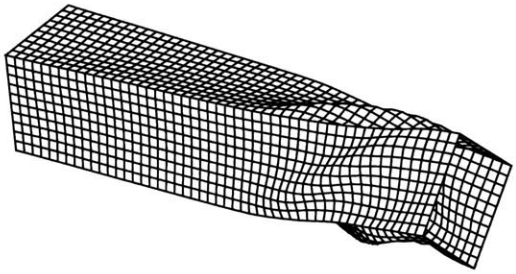

Figure 5.26: Deformed shapes of square tubes at 45°: unbonded foam filling ($\sigma_f = 0.689MPa$)

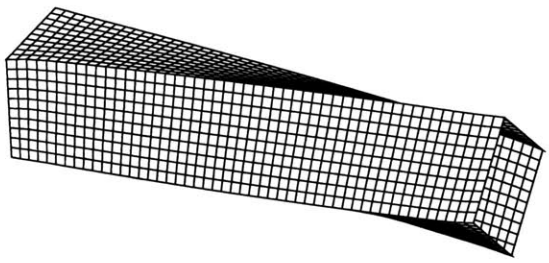

Figure 5.27: Deformed shapes of square tubes at 45°: Bonded foam-filling(σ_f = $0.689MPa$)

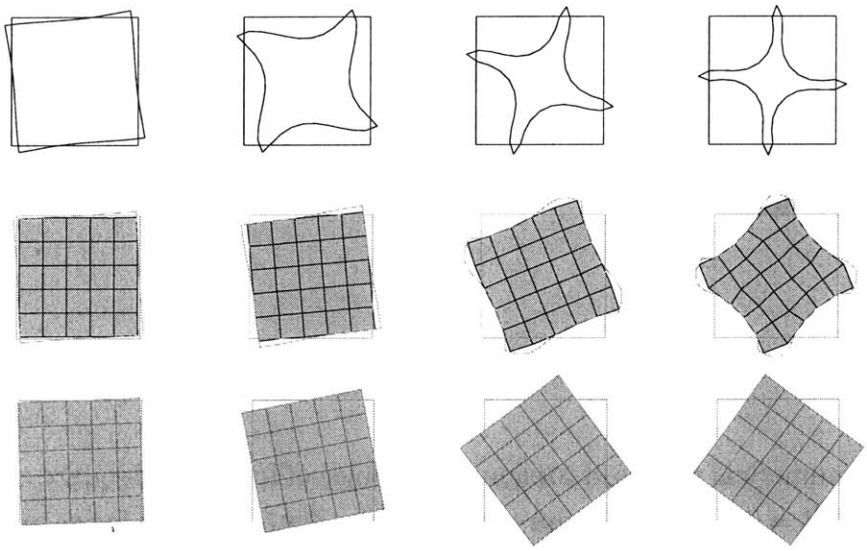

Figure 5.28: Evolution of shapes at the mostly deformed cross-sections. Upper row empty tube; Middle row unbonded filling; Lower row bonded filling

(i) In the pre-buckling stage, all sections rotate as rigid bodies. The resistance is derived from shear stresses that increases with the rotation angle because of strain-hardening;

(ii) After an onset of buckling, the walls collapse inwards with an increasing amplitude

of the transverse displacement function. This reduces both shear strains and stresses so that the torsional resistance considerably drops relative to the pre-buckling state;

(iii) Unbonded filler provides one-sided crushable foundation to the side plates causing them to buckle in the second or higher modes (Fig.5.29). Higher buckling modes are generated in tubes filled with more dense foams. The foam restricts the inward collapse thus keeping the torque high;

(iv) Bonded filler provides a double-sided crushable foundation which for relatively low dense foam retards the cross-section deformation.

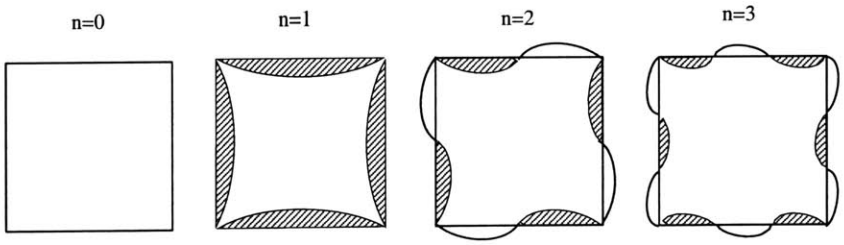

Figure 5.29: Possible modes of cross-sectional deformation. Shaded areas denote the crushed foam.

5.3.4.3 Plastic Resistance

The numerical results of torsional resistance of foam-filled square columns with $l/b = 5$ and $b/t = 50$ ant $t = 1mm$ are shown in Fig.5.30. The lower and upper bounds on torsional resistance established earlier are also plotted in the same figure. One can see that the two bounding curves bracket the actual resistance of the columns, as predicted by numerical solutions.

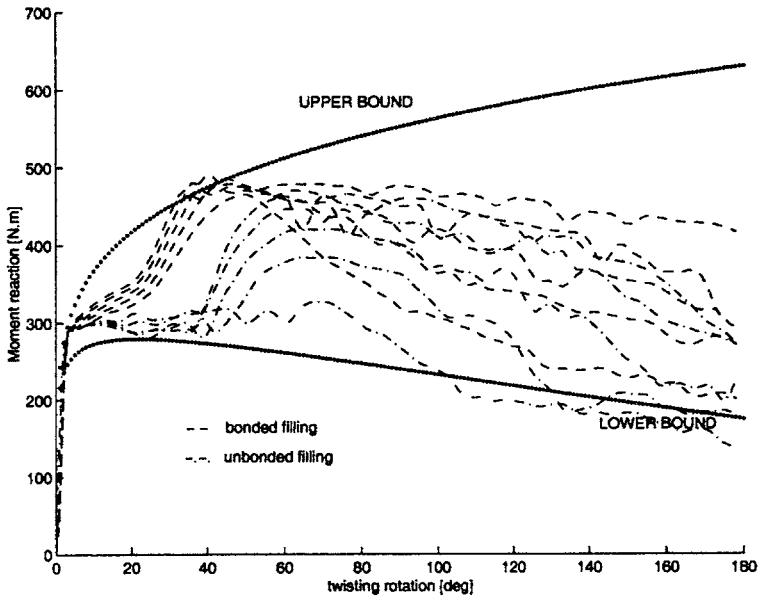

Figure 5.30: Torsional resistance of foam-filled square tubes

5.3.5 Strengthening Effect of Foam Filling

In order to quantify the strengthening effect of foam filling on the plastic resistance of thin-walled tubes undergoing torsion, a series of numerical simulations were carried out with a wide range of foam density (1% $\backsim$ 20% relative density). A simple strengthening model was proposed, and the solutions to twisting moment and critical twisting rotation of foam-filled tubes were derived based on the numerical results.

5.3.5.1 Twisting Moment Elevation due to Foam Filling

The presence of the foam filler provides the support from within to the tube wall and thus retards the inward sectional collapse. As a result, the critical twisting rotations to sectional buckling will be increased for foam-filled tubes compared to the non-filled ones. In the post-buckling state, the foam filler functions as an elastic-plastic foundation. It induces higher buckling mode (see Fig.5.29), and therefore results in a higher torsional resistance.

It is assumed accordingly that the torsional resistance of a foam-filled tube in the pre-buckling phase is the same as that of a non-filled tube, while its critical twisting rotation angle is increased. In the post-buckling phase, the torsional resistance of a foam-filled tube is elevated, and is of the additive form of the resistance of a non-filled tube and a torque elevation resulting from filling, which is in turn a function of the cross-sectional dimension and foam properties. Thus, the twisting moments and critical twisting rotation take the following form

$$T_{if} = T_i \tag{5.50}$$

$$T_{pf} = \bar{T}_p + \Delta T(b, \sigma_{0f}, \frac{\rho_f}{\rho_s}) \tag{5.51}$$

$$\theta_{cf} = \theta_c + \Delta\theta(\frac{\rho_f}{\rho_s}) \tag{5.52}$$

where T_{if} and T_{pf} are the torsional resistance of foam-filled tubes in pre-buckling and post-buckling phase, respectively; T_i is the torsional resistance of empty tube in pre-buckling phase, and was given by Eq.(5.32) and Eq.(5.33)

$$T_i = 2\sigma_0 b^2 t(0.58 + 0.05 r^2 \theta_0^2) \tag{5.53}$$

$\bar{T}_p$ is the mean twisting moment in the post-buckling phase calculated by averaging the torque in the range of $[\theta_c, \theta_m]$

$$\bar{T}_p = 2\sigma_0 b^2 t \left(0.58 - 0.16 r^{-0.22} \frac{\theta_m^{1.34} - \theta_c^{1.34}}{\theta_m - \theta_c}\right) \tag{5.54}$$

ΔT is the twisting moment elevation due to the filling; θ_{cf} is the critical twisting rotation to buckling for filled tubes; $\Delta\theta$ is an angle shift in critical twisting rotation due to filling. Such a strengthening behavior is illustrated in Fig.5.31

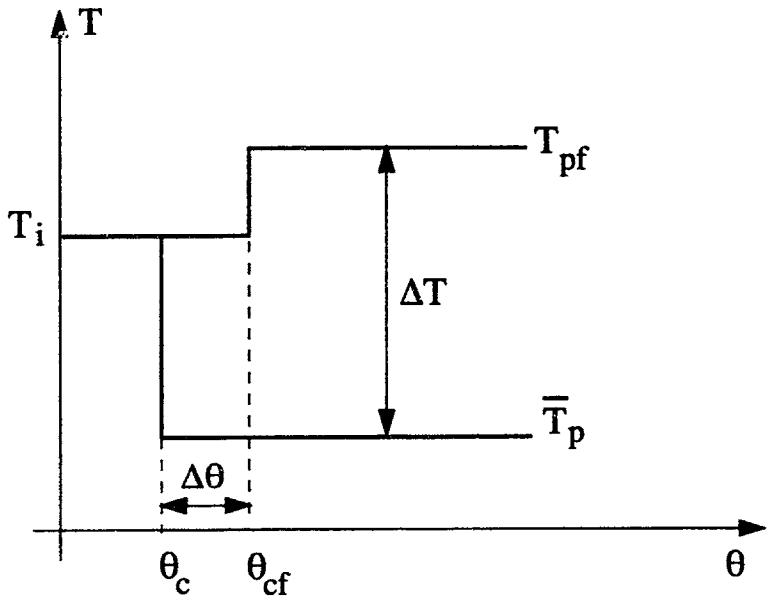

Figure 5.31: Strengthening effect of foam filling

5.3.5.2 Quantifying the Strengthening Effect

In order to quantify the twisting moment elevation ΔT and critical rotation shift $\Delta\theta$, numerical simulations were conducted using PAM-CRASH. The same finite element model as that described in section 5.3.4.1 is used. The tube wall material was aluminum extrusion AA6063 T7, with mechanical properties of Young's modulus $E = 69$GPa, yield strength $\sigma_y = 86.9$MPa, and Poisson's ratio $\nu = 0.3$. The strain hardening data from tensile test are given in Table 5.1. The constitutive behavior of the thin shell element was based on an elastic-plastic material model with Von Mises isotropic plasticity algorithm with piecewise linear plastic hardening. The mechanical properties of the foam material are related to its density via Eq.(2.1)$\backsim$ Eq.(2.6). Its constitutive behavior is based on the maximum principal stress yielding model described in the Chapter 2. The foam material used in the analysis is CYMAT aluminum foam, which has the plastic flow stress $\sigma_{0f} = 98.3$MPa, and Young's modulus $E_s = 70$GPa.

The twisting moment-twisting rotation responses of the empty tube and the tubes filled with foams of various densities are shown in Fig.5.32. One can see that two

strengthening effects exist due to the foam filling: a delayed sectional collapse, and a higher plastic resistance in post-buckling range.

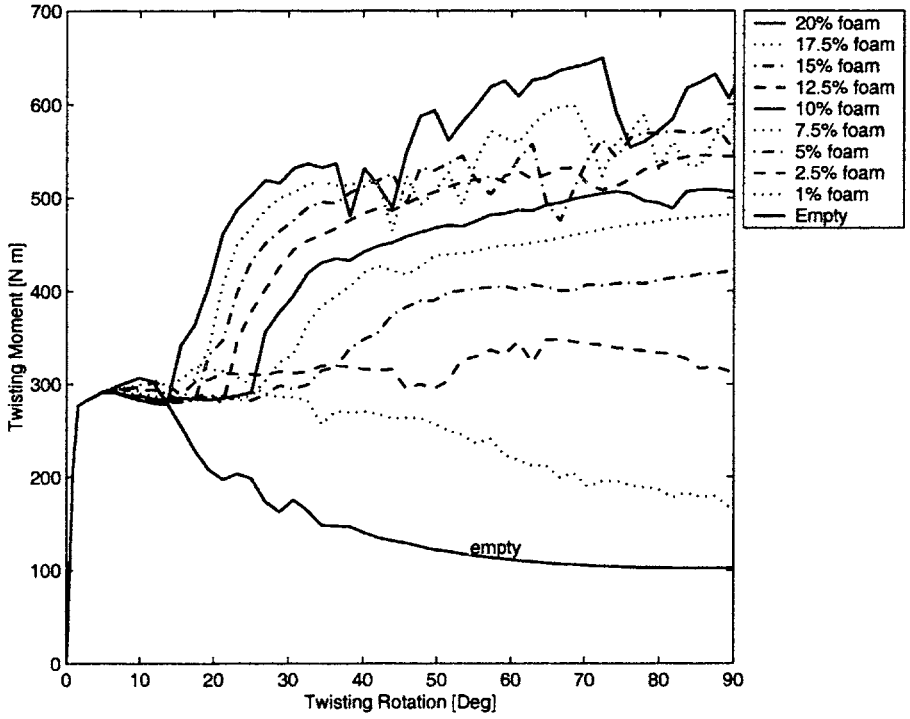

Figure 5.32: Torque responses of empty and filled tubes up to 90° twisting rotation

As discussed earlier in this chapter, the torsional plastic resistance of a foam-alone bar can be approximated by

$$T = 0.225\tau_f b^3 \tag{5.55}$$

It is evident that T only depends on the shear strength τ_f of the foam and the sectional width b. Following the same procedure as in the cases of compression and bending addressed in Chapter 3 and Chapter 4, the strengthening effect of the foam filling in torsion is assumed to be related to the contribution from foam alone with a coupling (interaction) factor. Because the shear strength τ_f is in turn a function of the foam density, the twisting moment elevation ΔT can therefore be written in the form of

$$\Delta T = \alpha\sigma_{0f} b^3 \left(\frac{\rho_f}{\rho_s}\right)^{\beta} \tag{5.56}$$

where α and β are two coefficients to be determined by fitting the numerical results obtained above, which gives

$$\begin{aligned} \alpha &= 0.06 \\ \beta &= 0.45 \end{aligned} \tag{5.57}$$

Figure 5.33 shows that the ΔT predicted by the finite element analysis and by Eq.(5.57) are very close, indeed.

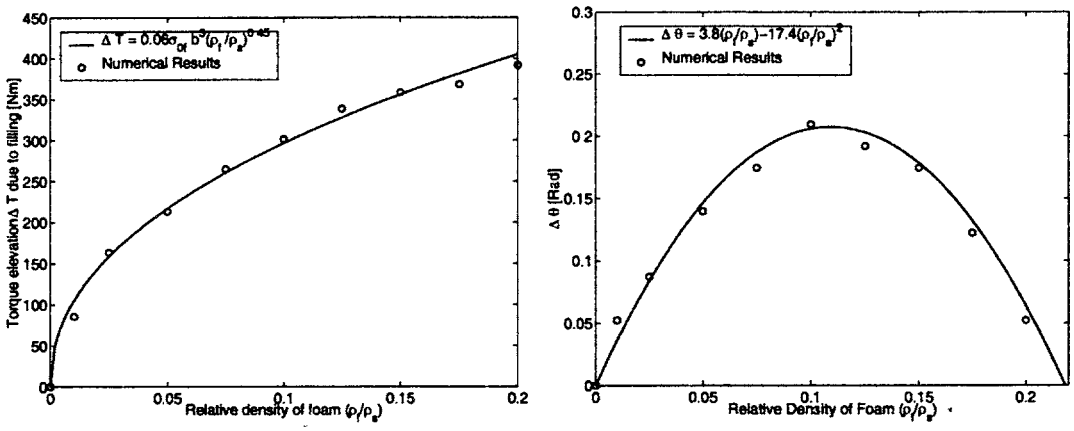

Figure 5.33: Curve-fitted ΔT and $\Delta\theta$

In a similar manner, the angle shift $\Delta\theta$ predicted by numerical simulations is fitted as a function of the relative density of the foam filler (see Fig.5.33)

$$\Delta\theta = 3.8\left(\frac{\rho_f}{\rho_s}\right) - 17.4\left(\frac{\rho_f}{\rho_s}\right)^2 \tag{5.58}$$

One can see that the $\Delta\theta$ is an increasing function of $\frac{\rho_f}{\rho_s}$ initially, because the sectional collapse was delayed due to the presence of the filler. However, when the foam density increases and the foam is strong enough, higher sectional buckling modes readily develop, which leads to decreasing critical rotation angles as foam density increases.

5.4 Experimental Study

Torsional experiments on empty and foam-filled thin-walled square tubes have been performed to validate the analytical and numerical solutions discussed earlier in this chapter. The specimens used in the test were provided by Norsk Hydro ASA, Norway. The experiments were carried out at University der Bundeswehr Munchen, Germany.

5.4.1 Experimental Design

Pilot tests were conducted with a torsional actuator with maximum capacity of $2kNm$. But calculations of peak twisting moments showed that such a torsional actuator was not sufficient for the current testing program. In addition, there was not enough axial displacement available on the torsional actuator which is necessary to compensate the shortening of specimen during twisting. Therefore, a completely new testing rig was designed and manufactured, which uses a linear actuator.

Figures 5.34 and 5.35 show the testing apparatus. A simple lever arm design is applied allowing an axial DOF of the loading end of the specimen using a ball bearing. On the other end of the specimen, a clamped fixture represents the loading boundary condition. The linear actuator is connected with the top of a cardan joint and thereby has all necessary DOFs for the kinematics. The lever arm itself is hinged with the actuator. Care was taken to release any axial force that might have developed during the process of large rotation.

The force and displacement associated with the linear actuator are recorded by force sensor and displacement sensor, respectively. From the kinematics of the system, these data can be easily converted to twisting moment acting on the specimen and the corresponding twisting angle. The testing rig is integrated into a stiff frame. The fixture of the specimen is mounted on a stiff plate horizontally. The linear actuator is displacement-controlled and powered by a hydraulic supply. The maximum stroke of the actuator is 600mm and its maximum loading capacity is $40kN$. Fig.5.35 shows the details of the lever arm. The range of the twisting angle of the lever arm is $-30° \sim +30°$.

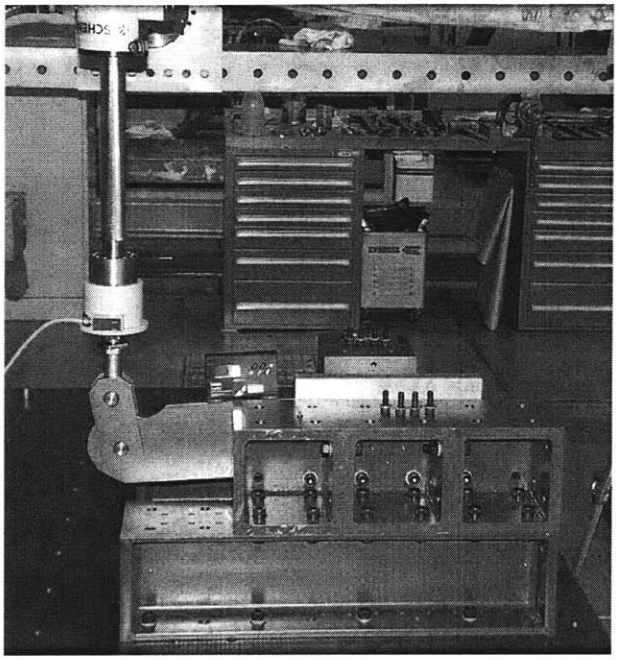

Figure 5.34: Testing rig design

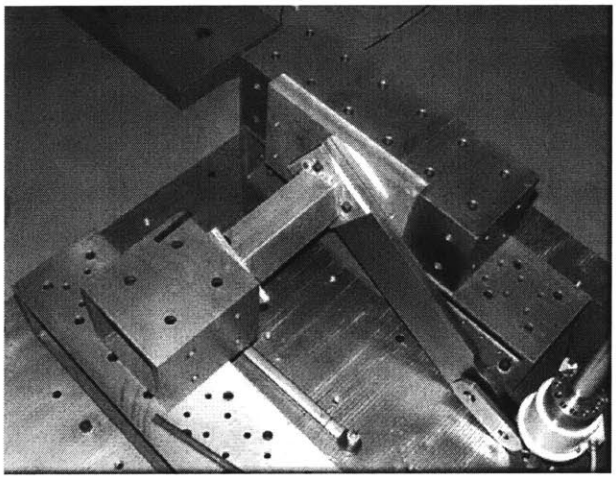

Figure 5.35: Design details of the lever arm

The tests were run quasi-statically with an actuator velocity at about $0.8mm/s$. The data sampling frequency is $1Hz$.

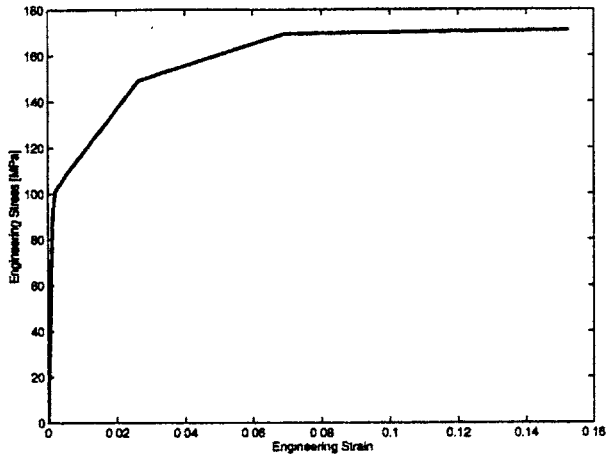

Figure 5.36: Engineering stress-strain curve of AA6063 T7

5.4.2 Specimens

The aluminum extrusions and aluminum foams were provided by Norsk Hydro ASA, Norway. The extrusions are square sections with dimension $80mm \times 80mm$, thickness $3mm$ and length $270mm$. The material is AA6063 T7. An engineering stress-strain curve of this material is shown in Fig.5.36.

The aluminum foam has geometry $270 \times 77 \times 77mm$ and were filled into the extrusion sections. Four different foam densities were tested. Table 5.2 summarizes the specimen information.

5.4.3 Testing Results

The tests were run quasi-statistically. One end of the tube was clamped while the other end was axially free and was subjected to twisting rotation up to 32°. Some interesting observations were made from the experiment:

(i) The twisting deformation and sectional deformation pattern of empty tube agree generally with the numerical predictions and the analytical model(see Fig.5.37 and Fig.5.38);

Table 5.2: Specimen summary

Specimen No.	Type	Foam Weight $[g]$	Foam Density $[g/cm^3]$	Foam Crushing Strength $[MPa]$
S1	empty	0	0	0
S2	empty	0	0	0
S3	filled	220	0.14	1.78
S4	filled	240	0.15	1.97
S5	filled	300	0.19	2.81
S6	filled	300	0.19	2.81
S7	filled	380	0.24	3.99
S8	filled	380	0.24	3.99

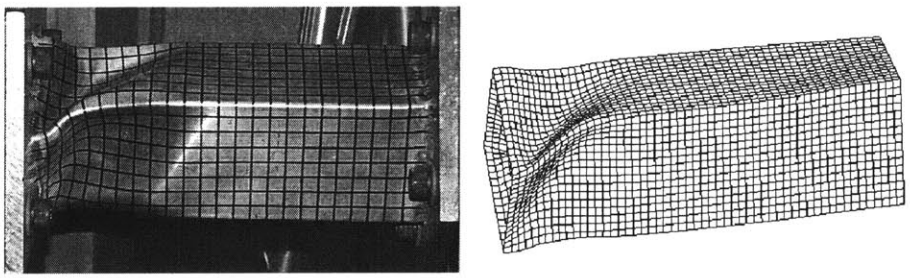

Figure 5.37: Torsional deformation shapes: experimental and numerical

(ii) The torsional resistance responses of an empty tube obtained in the test is shown Fig.5.39. The resistances predicted by numerical simulation and analytical solution are shown in the same figure for comparison. It can be noted that the numerical result and analytical solution have reasonably good agreement while the experimental result gives much smaller twisting resistance after the peak moment. This is due to an improper design of the end fixture plate of the specimen, which resulted in an unexpected welding failure under large torque, as shown in Fig.5.44. The welding crack, developed in all but one specimen, diminishes significantly the twisting resistance of the specimen after the peak moment.

(iii) The sectional transverse deflection was retarded by the foam-filler, which resulted

Figure 5.38: Sectional deformation: experimental, numerical and model

in a smaller deflection amplitude. The sectional deformations of foam-filled tubes are more localized than that of empty tube. Fig.5.40 and Fig.5.41 show the deformation shape and sectional deformation pattern of one foam-filled tube observed in experiment and predicted numerically. It is evident that the numerical simulation gave fairly good prediction on the deformation;

(iv) Numerical simulations were carried out on two foam-filled tubes with foam filler of density $0.14g/cm^3$ and $0.24g/cm^3$, respectively. The moment responses are shown in Fig.5.42 together with testing results for comparison. As can be seen, two sets of results agree fairly well up to the angle of the peak moment. After that, numerical results predict an increasing resistance while the experiments were stopped because of the fixture failure.

(v) Torsional resistance of all tested tubes vs. twisting rotation are plotted in Fig.5.43. Although the tubes lost much of their twisting capacity due to a premature weldment failure during experiment, substantial increase in the energy absorption are still achieved for the foam-filled tubes. This bears an important implication of the attractive potential of the foam-filled thin-walled members as weight-efficient energy-absorbing and force-maintaining structures in collision of a vehicle.

(vi) There are welding failures occurring at the end fixture plate of specimens (Fig.5.44), which resulted in a considerable loss of post-buckling torque of the tubes. A careful re-design of the end fixture for specimens is needed in later experiments of this kind.

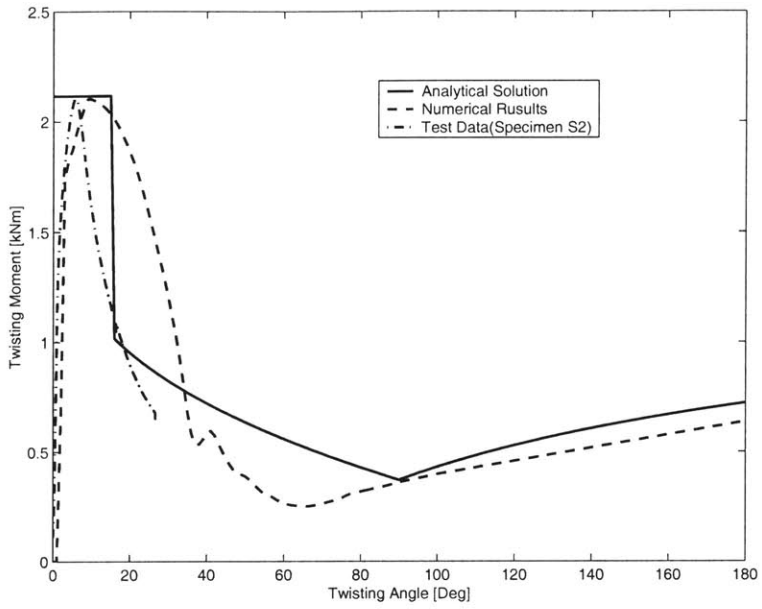

Figure 5.39: Torsional resistance of empty tube:analytical, numerical and experimental (To normalize, plot $\frac{T}{2\sigma_0 b^2 t}$ vs $\frac{b\theta_0}{l}$ with corresponding b, t, l and σ_0)

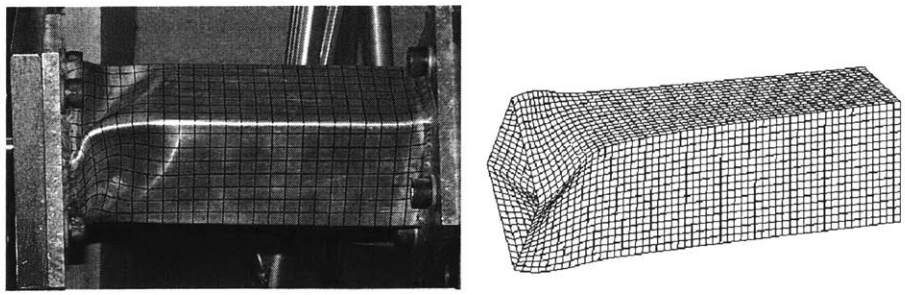

Figure 5.40: Deformation shapes of a foam-filled tube: experimental and numerical

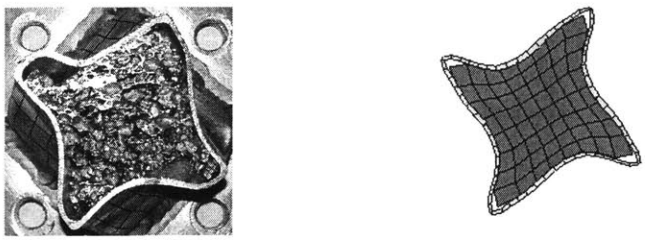

Figure 5.41: Sectional deformation of foam-filled tubes: experimental and numerical

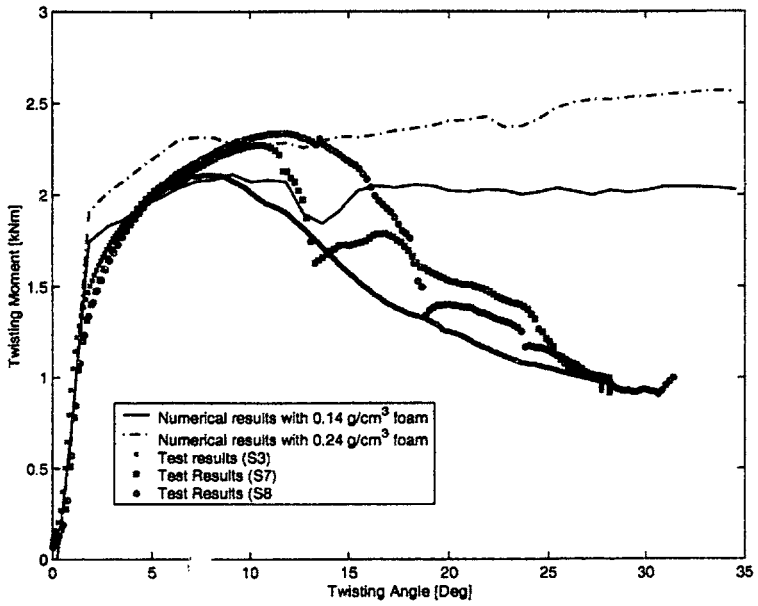

Figure 5.42: Torsional resistance of foam-filled tube: experimental and numerical

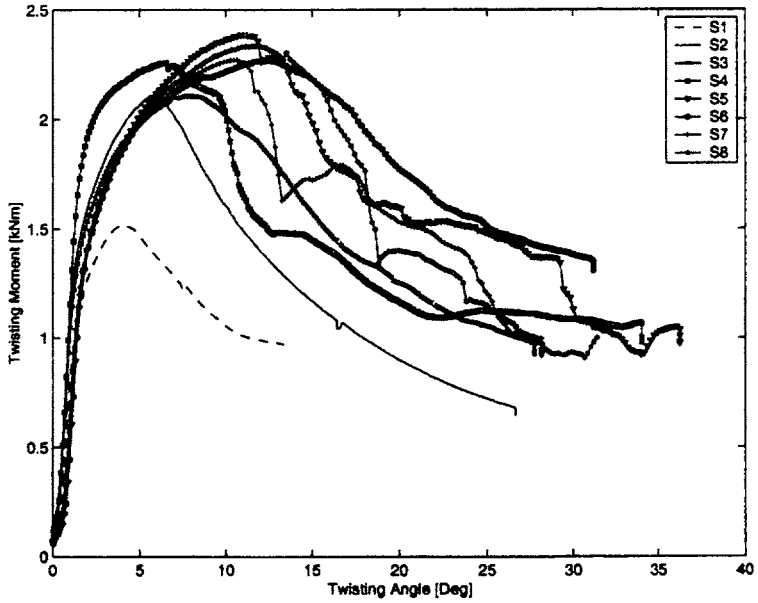

Figure 5.43: Torque-twist curves for tested specimens(S1 and S2 are empty tubes; the others are foam filled ones)

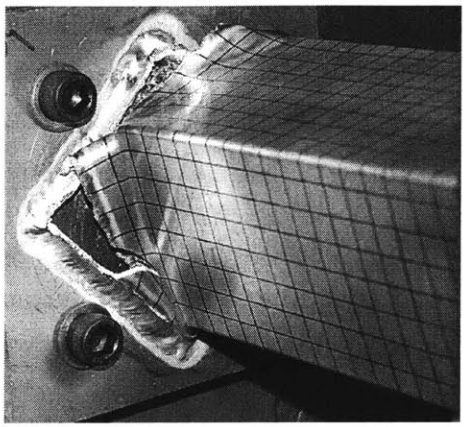

Figure 5.44: Welding failure of the end fixture of a tube

5.5 Summary

An analysis by applying the principle of virtual velocities to assumed displacement fields was used to predict the torsional behavior of thin-walled square tubes with large plastic deformations. Three successive deformation phases, namely pre-buckling, cross-section buckling and collapse-spreading phase were identified based on the physical understanding of the torsional behavior of thin-walled prismatic tubes. The analytical model was then extended to the cases of thin-walled rectangular and hexagonal tubes. Numerical simulations were carried out and the results are compared with the analytical solutions, giving good agreement.

The torsional crushing behavior of foam-filled square tubes under large rotation was studied in the second part of this chapter. The upper and lower bounds on the torsional resistance were established approximately and compared with the numerical results. It was noted that the presence of the core material changes the collapse mechanism and gives rise to higher sectional collapse modes and therefore increases the plastic resistance of the tube. The analysis also showed that, there are two basic mechanisms through which the core material is increasing the energy absorption of thin-walled tubes. The main mechanism is to prevent or reduce the inward sectional collapse of the cross-section and ensure the full membrane stress to be developed in the wall. The second mechanism for increasing the energy absorption is a direct contribution from the torsion of the core material, which is proved to be a small fraction

compared with the aforementioned main mechanism. Based on the numerical results within a wide range of foam densities (1% $\backsim$ 20% relative density), the strengthening effects of foam filling were quantified. The solutions will be used in the optimization study in the next chapter.

Torsional experiments on empty and foam-filled square tubes were carried out and results were compared with finite element solutions, and analytical models. A new testing rig was designed, which was able to convert the force on linear actuator to twisting moment on specimen by a specially designed lever arm. Although the end platens of specimens were not properly designed and unexpected welding failure occurred on those fixtures in testing, which diminished significantly the twisting moment of the tubes, the deformation shape and sectional deformation pattern of empty tubes revealed in the experiment agree well with the numerical predictions and analytical models. The experimental results show increase in plastic resistance and energy absorption for foam-filled tubes compared to empty ones, thus offering potential for thin-walled members with ultralight metal filler as weight-efficient energy-absorbing structures.

In the simple analytical model, the sectional buckling was assumed to initiate at the center of tube and then propagate towards two ends. The most-deformed section was also developed at the center of the tube (see Fig.5.10 and Fig.5.11). In contrast, the finite element solution (see Fig.5.4) and experimental result (see Fig.5.37) exhibit different deformation patterns, in which the initiation of sectional buckling and the most-deformed section are shifted from the center of tube towards one end. Such an assumption on the deformation mode in the approximate model simplified the analysis while sacrificing to some extent the accuracy of the solution.

More experiments are needed with re-designed end platens to ensure its integrity under large twisting moment. Furthermore, the present model is restricted to the cases of torsional deformations without warping. In addition to the deformation considered so far, a nonuniform axial displacement may give rise to a warping of the cross-section.

In real applications, torsion seldom acts alone. Usually it is combined with compression and/or bending. The interaction of torsion with compression and bending should be considered in the continuation of the present research.

Chapter 6

Design Optimization of Ultralight Structures

In the previous chapters, we studied the crushing behavior of thin-walled structures filled with the ultralight metal filler. This fundamental work is of great importance in achieving a clear physical understanding of the crushing mechanics of ultralight structures. The strengthening effect and interaction effect between the filler and the metal skin under compression, bending and torsional loadings were revealed and quantified, which led to some simple design formula for predicting the crush resistance and energy absorption of the ultralight core filled structures. With a full understanding of the crushing mechanics of filled members, it is possible to select among all feasible options an optimum design of structural geometry and material properties for the minimum weight while satisfying the requirements of structural integrity and crashworthiness.

Structural optimization has been a topic of interest for many years and is now a reasonably mature technology for weight efficient or cost efficient structural design. However, not much work has been directed toward problems of vehicle crashworthiness. This is primarily because of the inherent and significant nonlinearity due to large deformation, material plasticity and the presence of contact during a crash event. In an early attempt at structural optimization with crashworthiness constraints, Bennett, et al [83] used a lumped parameter structural model to find feasible designs. Song [84] created a direct link between the thickness of a rectangular member and the safety in-

dex in the nonlinear force-deformation curve of the spring-mass model, which allowed the determination of the component dimensions for minimum mass while meeting given safety criteria. Lust [85] combined this approach with linear elastic structural optimization to produce an integrated structural design system. DeVries et al [86] presented a methodology to incorporate the concept modeling, structural optimization, and the beam section analysis code SECOLLAPSE for the automated structural optimization of thin-walled beam sections for minimum weight design. Bennett et al [87] reviewed some optimal design strategies in crashworthiness and occupant protection and examples were given addressing the idea of creating approximate design problems based on a small number of system analyses. Other attempts of structural optimization for crashworthiness problem involved the direct coupling of optimization techniques with the discretized field models such as nonlinear finite element method [88, 89, 90]. The issue relating to this approach is that it is usually computationally intensive. Regarding the thin-walled component with lightweight filler, few attempts have been made on the sizing optimization of foam-filled sections for minimum weight with crashworthiness constraints. In a study which involves optimizing the component geometries and the polyurethane foam density, Lampinen and Jeryan [4] found that the range of wall thickness for which foam reinforcement is weight effective if of no practical use. Recently, Hanssen et al [91] investigated the optimum design for energy absorption of aluminum foam filled square colu[illegible] and indicated that significant mass, length and volume reductions are possible by utilizing aluminum foam filler.

In this chapter, a methodology was proposed which combined structural optimization techniques with the recent achievements in the crushing mechanics of ultralight structures. The optimization formulations were constructed on a component level for the minimum weight with the constraints of crashworthinss and elastic bending stiffness. Design optimization of various sections were carried out using proposed methodology to decide the most weight efficient design for crash energy management in axial crushing, bending collapse and torsional crushing loadings. The proposed methodology is suitable for early-stage design of crash members with very little computational effort.

6.1 General Formulation

Optimum design of a structural system like a car is a complex task. It involves many factors which often lead to conflicting needs and make the optimization procedure hard and seemingly insurmountable. However, we can start this broad project by addressing a relatively simple problem, such as sizing and shape optimization of the cross-section of one structural component subjected to a given type of crush loading. The above simple problem will provide a much needed understanding of the crashworthiness optimization process. This in turn will help to move on into multi-component subsystem optimization and system optimization considering combined load sets and finally achieve a computer-based knowledge system for optimum design with regarding to mass, stiffness, safety, manufacturability, NVH, and many other factors.

In the present study, we consider the optimization problems of ultralight structures on a component level for minimum weight under structural integrity and crashworthiness constraints. A general problem of structural optimization for minimum weight can be stated: find the set of design variables, $\mathbf{X}$, that will,

Minimize $m(\mathbf{X})$
subject to

$$\begin{aligned} g_j(\mathbf{X}) &\leq 0, \qquad j = 1, m \\ X_i^L &\leq X_i \leq X_i^U, \qquad i = 1, n \end{aligned} \tag{6.1}$$

The function $m(\mathbf{X})$, which is referred to as the objective or merit function, is the mass of the structural member. The $g_j(\mathbf{X})$ are referred to as constraints, and they provide bounds on various response quantities. The region of search for the optimum is limited by the side constraints $X_i^L \leq X_i \leq X_i^U$.

For a proper crash energy management, a crash member is usually required to absorb during a crash event certain amount of kinetic energy (target energy absorption), that is,

$$E_n \geq \widetilde{E_n} \tag{6.2}$$

where E_n is the actual energy absorption of the crash member during the crash deformation; $\widetilde{E_n}$ is the target value.

On the other hand, the cross-section of the structural member must provide enough elastic bending stiffness for normal loading condition and for ensuring the global stability in axial crush loading as well. Thus, a lower bound of the sectional bending stiffness must be set

$$EI \geq \widetilde{EI} \tag{6.3}$$

where E is the Young's modulus; I denotes the second moment of inertia of the cross-section. $\widetilde{EI}$ is a target value.

Therefore, the optimization problem of a structural component for minimum weight under crashworthiness and bending stiffness constraints can be formulated in the following way

Minimize $m(\mathbf{X})$
subject to

$$\begin{aligned} g_1(\mathbf{X}) &= -E_n + \widetilde{E_n} \leq 0 \\ g_2(\mathbf{X}) &= -EI + \widetilde{EI} \leq 0 \\ X_i^L &\leq X_i \leq X_i^U, \qquad i = 1, n \end{aligned} \tag{6.4}$$

We shall in the following solve such optimization problems under various crash loading conditions.

6.2 Solution Algorithms

The problem formulated above is a constrained optimization problem with both objective function and constraints being nonlinear. A solution of the nonlinear optimization problem generally requires an iterative procedure to establish a direction of

search at each major iteration. This is usually achieved by the solution of a Linear Programming (LP), a Quadratic Programming (QP), or an unconstrained subproblem.

6.2.1 Graphical Approach

A two-variable design problem can be solved using the graphical optimization approach [92]. In this approach, each constraint function is plotted on a graph. This gives a curve that divides the design space into two parts. One side of the curve represents all the design points that satisfy the constraint (feasible design) and the other side represents the design that violate the constraint (infeasible designs). The feasible region represents a set of designs that satisfy all the constraints of the problem.

Next is to locate the best possible design in the feasible region. A few iso-cost curves are drawn through the feasible region and a point that gives least value to the cost function (objective function) is identified as the optimum solution. The coordinates for the optimum point are read directly from the graph. The constraints that govern this design are called *active* or *critical*, whereas others are called *inactive* or *noncritical*. We shall use the graphical approach to solve some simple two-variable problems in this chapter.

6.2.2 Sequential Quadratic Programming

Closed form analytical and/or graphical solutions for practical optimization problems are difficult to obtain if the number of design variables is more than two and/or the constraint expressions are complex. Therefore numerical methods must be used to solve most optimization problems. In these methods, an initial design for the system is selected which is iteratively improved until no further improvements are possible without violating any of the constraints.

In the present study, a Sequential Quadratic Programming(SQP) method was used to solve the optimization problem. Given the general nonlinear problem, the principle idea of SQP is the sequential linearization and formulation of a quadratic program-

ming sub-problem based on a quadratic approximation of the Lagrangian function. This quadratic subproblem is then solved to find a search direction so that a sufficient decrease in a merit function is obtained. For details readers are referred to reference [93].

The SQP algorithm was implemented in the present study using Matlab Script Language [94].

6.3 Optimization for Axial Crushing

6.3.1 Formulation

A foam-filled square column subjected axial crushing is investigated first. The column has length l, width b and wall thickness t. The material properties of the tube are mass density ρ_0, Young's modulus E and plastic flow stress σ_0. The filler inside the tube is aluminum foam with density ρ_f(see Fig.6.1).

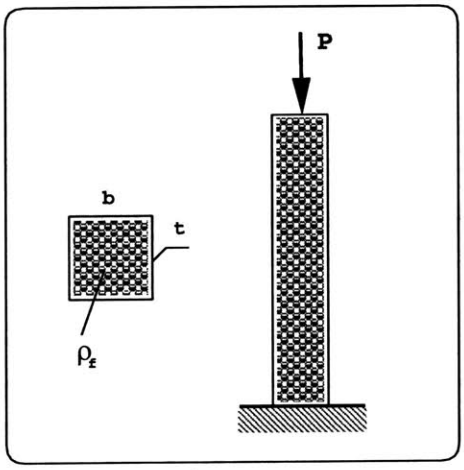

Figure 6.1: A foam-filled thin-walled column subject to axial crushing

The axial crushing behavior of the column were extensively studied, as summarized in Chapter 3. Useful design formula were derived to predict the mean crushing force and energy absorption with sufficient accuracy in the neighborhood of realistic designs.

Fig.6.2 is a schematic of a force-deflection curve which shows the essential behavior exhibited by thin-walled columns. The energy absorption during the crushing can be evaluated

$$E_n = P_m d \tag{6.5}$$

where P_m is the mean crushing force and d is the crush distance.

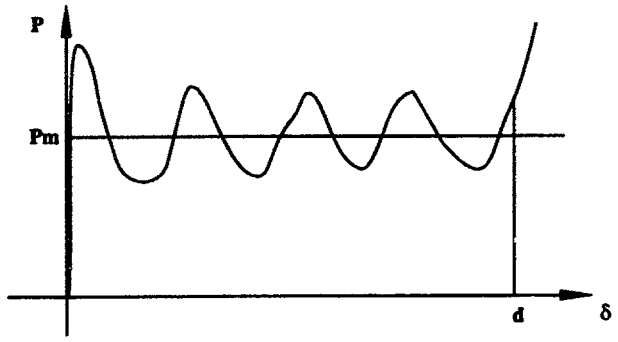

Figure 6.2: An illustration of crushing force response

If we assume that the crush distance d or the so called stroke efficiency d/l doesn't change much within the range of tube and foam parameters we select, we can neglect the effect of length and simplify our task to the cross-sectional optimization. Hence the energy absorption capacity of the column is equivalent to considering the mean crushing force level P_m. Therefore, a requirement for the column to absorb the kinetic energy during a crash event can be satisfied by setting a target mean crushing force level $\widetilde{P_m}$ which must be provided by the column

$$P_m \geq \widetilde{P_m} \tag{6.6}$$

Additionally, the peak impact force P_u is usually restricted to ensure the structural integrity of the passenger compartment. Then, a constraint should be set on the maximum crushing force

$$P_u \leq \widetilde{P_u} \tag{6.7}$$

Four design variables are identified: the width b, the wall thickness t, the plastic flow stress σ_0 of the tube material, and the foam density ρ_f, that is,

$$\mathbf{X}^T = \{b, t, \sigma_0, \rho_f\} \tag{6.8}$$

where these design variables are allowed to vary within prescribed limits

$$\begin{aligned} b^L &\leq b \leq b^U \\ t^L &\leq t \leq t^U \\ \sigma_0^L &\leq \sigma_0 \leq \sigma_0^U \\ \rho_f^L &\leq \rho_f \leq \rho_f^U \end{aligned} \tag{6.9}$$

The sectional mass (mass per unit length) of the column can be expressed by design variables

$$m(\mathbf{X}) = 4bt\rho_0 + b^2\rho_f \tag{6.10}$$

The formulation of Eq.(6.4) can then be re-stated in the following for foam-filled square sections undergoing axial crushing

Minimize $m(\mathbf{X})$
subject to

$$\begin{aligned} g_1(\mathbf{X}) &= -P_m + \widetilde{P_m} \leq 0 \\ g_2(\mathbf{X}) &= -EI + \widetilde{EI} \leq 0 \\ g_3(\mathbf{X}) &= P_u - \widetilde{P_u} \leq 0 \\ X_i^L &\leq X_i \leq X_i^U, \qquad i = 1, 4 \end{aligned} \tag{6.11}$$

Obviously, this formulation can also be applied to other sections with different geometry, such as hexagonal, double-hat rectangular, double-hat hexagonal and double-walled sandwich (Fig.6.3).

An accurate prediction of the response functions used in the optimization formulation is essential for a successful optimization calculation. The prediction of the mean crushing force and peak impact load of various sections will be addressed in the following.

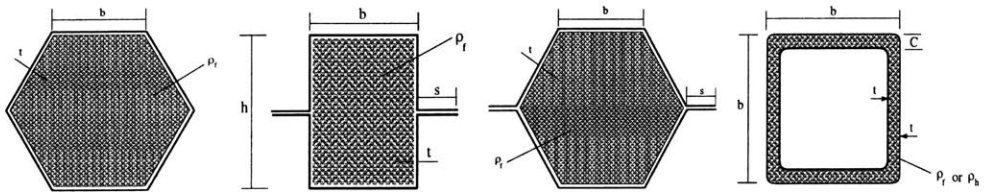

Figure 6.3: Various foam-filled sections

6.3.2 Summary of Crush Resistance of Thin-walled Columns with Ultralight Filler

A successful optimization heavily relies on the accurate prediction of the crushing behavior of structural members. The axial crushing behavior of thin-walled metal tubes has been studied extensively for several decades. The folding deformation of the tubes are known to be an efficient energy absorbing mechanism. Wierzbicki and Abramowicz [53] derived theoretically a solution of the mean crushing force of a thin-walled square column, see Section 3.1.

$$P_m = 13.06\sigma_0 b^{\frac{1}{3}} t^{\frac{5}{3}} \tag{6.12}$$

where b and t are width and wall thickness of the tube, respectively; σ_0 is referred to as the energy equivalent flow stress of column material and was given in Eq.(3.10).

The theory was improved later leading to the *Superfolding Element* theory which can be applied for arbitrary multi-corner sheet metal columns [54]. For instance, the mean crushing force of a hexagonal column (Fig.6.4(i)) can be calculated

$$P_m = 20.23\sigma_0 t^{1.6} b^{0.4} \tag{6.13}$$

and a double-hat rectangular (Fig.6.4(ii))

$$P_m = 13.06\sigma_0 t^{\frac{5}{3}} (C_1^{\frac{1}{3}} + C_2^{\frac{1}{3}}) \tag{6.14}$$

where $C_1 = s + \frac{1}{4}h$; $C_2 = \frac{1}{2}b + \frac{1}{4}h$

and a double-hat hexagonal(Fig.6.4(iii))

$$P_m = 13.49\sigma_0 t^{1.6}(C_1^{0.4} + C_2^{0.4}) \tag{6.15}$$

where $C_1 = s + \frac{1}{2}b$; $C_2 = b$

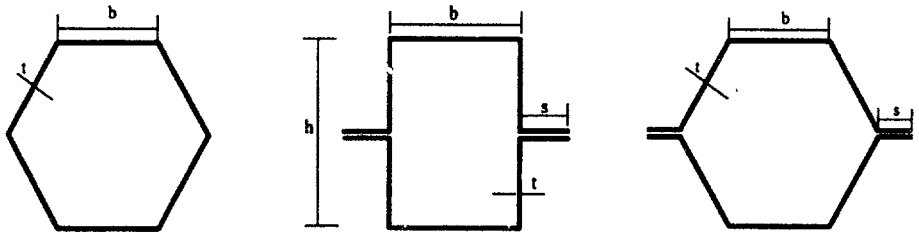

(i) (ii) (iii)

Figure 6.4: Empty thin-walled sections (i) hexagonal; (ii) double-hat rectangular; (iii) double-hat hexagonal

Extensive studies have been carried out by Santosa and Wierzbicki [39, 95, 5, 10] to investigate the crushing behavior of thin-walled structures with an ultralight filler. Based upon their theoretical solutions and numerical results, they developed practical design formulas to predict the mean crushing forces of various foam-filled sections. Summing up in the following are the formulas which will be used for current optimization calculation.

Foam-filled square section (Fig.6.5)

$$P_m = 13.06\sigma_0 b^{\frac{1}{3}} t^{\frac{5}{3}} + 1.8\sigma_f b^2 \tag{6.16}$$

Foam-filled hexagonal section(Fig.6.5)

$$P_m = 20.23\sigma_0 t^{1.6} b^{0.4} + 4.68\sigma_f b^2 \tag{6.17}$$

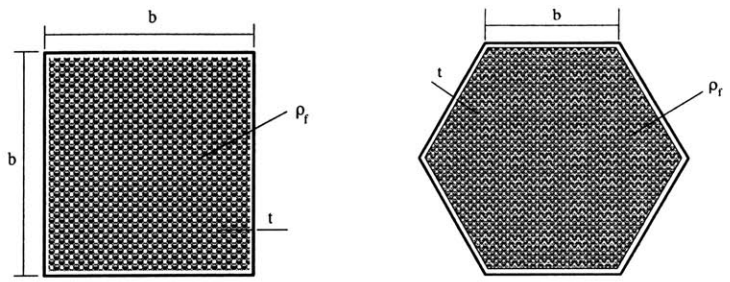

Figure 6.5: Geometry of foam-filled square and hexagonal section

Foam-filled double-hat rectangular section(Fig.6.6)

$$P_m = 13.06\sigma_0 t^{\frac{5}{3}}(C_1^{\frac{1}{3}} + C_2^{\frac{1}{3}}) + 1.8\sigma_f bh \tag{6.18}$$

where $C_1 = s + \frac{1}{4}h$; $C_2 = \frac{1}{2}b + \frac{1}{4}h$.

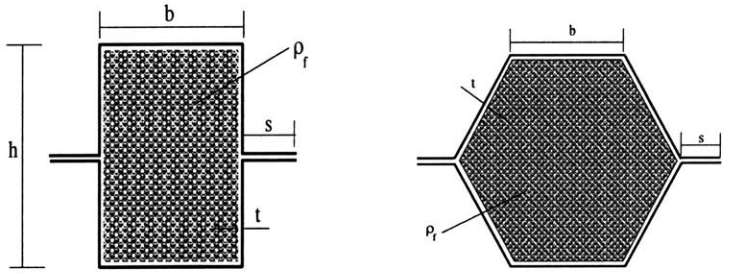

Figure 6.6: Geometry of foam-filled double-hat rectangular section

Foam-filled double-hat hexagonal section(Fig.6.6)

$$P_m = 13.49\sigma_0 t^{1.6}(C_1^{0.4} + C_2^{0.4}) + 4.68\sigma_f b^2 \tag{6.19}$$

where $C_1 = s + \frac{1}{2}b$; $C_2 = b$

In the above equations, b, t,s and h are geometrical parameters of sections defined in the figures. The plastic flow stress of the foam filler which is related to its mass density is denoted by σ_f

More recently, a concept of a double-walled sandwich column to be used as a weight efficient crashworthy structure was proposed by Santosa and Wierzbicki [6]. The mean crushing force of double-walled honeycomb sandwich and aluminum foam sandwich can be predicted by the following formulas.

Double-walled honeycomb sandwich(Fig.6.7)

$$P_m = 13.06\sigma_0(2t_i)^{\frac{5}{3}}b^{\frac{1}{3}} + 60.48C^{\frac{7}{4}}b^{\frac{1}{4}}\sigma_h \tag{6.20}$$

where σ_h is the flow stress of the honeycomb core; t_i denotes the thickness of inner and outer wall; C is the core height.

Double-walled foam sandwich(Fig.6.7)

$$P_m = 13.06\sigma_0(2t_i)^{\frac{5}{3}}b^{\frac{1}{3}} + 20.57C^{\frac{5}{4}}b^{\frac{3}{4}}\sigma_f \tag{6.21}$$

where σ_f is the flow stress of the aluminum foam core.

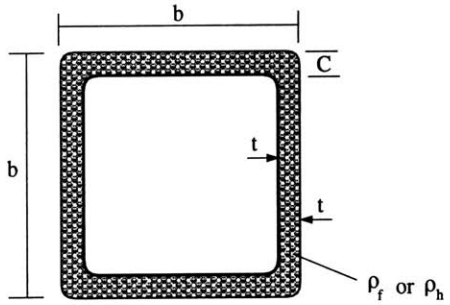

Figure 6.7: Geometry of double-walled sandwich section

The mechanical properties of aluminum foam and aluminum honeycomb were discussed in Chapter 2. They are related to their mass densities via Eq.(2.1)∽ Eq.(2.6) and Table 2.1. For instance, the mechanical properties of Hydro aluminum foam are as follows: E_{sf}=69GPa; σ_{0f}=150.4MPa; $\rho_{sf} = 2.7g/cm^3$. For the 5056 Hexcel aluminum honeycomb, the parameters are: E_{sh}=69GPa; σ_{0h}=285MPa; $\rho_{sh} = 2.7g/cm^3$.

6.3.3 Optimization of Foam-filled Square Section

For one-variable objective functions and some multi-variable linear objective functions, it is mathematically straightforward to carry out an optimization (maximization or minimization) procedure. However, the crashworthiness optimization involves highly non-linear objective functions and constraints, which makes analytical optimization enormously difficult, if not impossible. Therefore we have to resort to some numerical optimization techniques for our task. The graphical approach is one of these methods which is very useful and easy to interpret for a two-variable optimization problem. In this section, the simplest case of an empty thin-walled square section will be investigated analytically. Then the graphical approach is used to study the reduced problem of foam-filled section with some variables fixed. Finally, a general foam-filled square section problem is solved by Sequential Quadratic Programming and results are discussed.

6.3.3.1 Empty Square Section

1. Constraint on Peak Impact Load

For the simple case of an empty square section, the objective is to minimize the sectional mass

$$m = 4bt\rho_0 \tag{6.22}$$

where b and t are width and wall thickness, respectively; ρ_0 is the mass density of the column material.

The constraint on the mean crushing force is

$$g_1 = 13.06\sigma_0 b^{\frac{1}{3}} t^{\frac{5}{3}} - \widetilde{P_m} = 0 \tag{6.23}$$

where $\widetilde{P_m}$ denotes the target mean crushing force.

If we take into consideration as well the constraint on the peak impact load P_u, then the second constraint is introduced

$$g_2 = P_u - \widetilde{P_u} \leq 0 \tag{6.24}$$

where $\widetilde{P_u}$ is the maximum allowable peak load.

The peak impact load P_u of an empty thin-walled square column can be well approximated by Von Karman effective width theory [96]

$$P_u = 7.6t^2\sqrt{E_0\sigma_0} \tag{6.25}$$

where E_0 and σ_0 are the Young's Modulus and plastic flow stress of the column material, respectively.

It is evident that a limit on the peak load actually imposes a restriction on the maximum wall thickness given the column material constants E_0 and σ_0. On the other hand, a higher plastic flow stress σ_0 will lead to smaller width b and thickness t and thus is always favorable for minimum weight. For given material property of σ_0 and E_0, the optimum b and t can be obtained through simple derivation considering the constraints g_1 and g_2. Eliminating b in Eq.(6.22) results in

$$m = \frac{\widetilde{P_m}^3}{549.3\sigma_0^3 t^4} \tag{6.26}$$

One can see that a largest feasible wall thickness t, which should be determined by Eq.(6.25), will result in a minimum sectional mass. Therefore, an optimum thickness t^* is decided by

$$t^* = \sqrt{\frac{\widetilde{P_u}}{7.6\sqrt{E_0\sigma_0}}} \tag{6.27}$$

The optimum width b^* can then be found from Eq.(6.23)

$$b^* = \frac{\widetilde{P_m}^3}{(13.06\sigma_0)^3 t^{*\,5}} \tag{6.28}$$

Take, for instance, a square column made of aluminum extrusion AA6060 T4. The material properties are: yield stress $\sigma_y = 80\ MPa$; ultimate stress $\sigma_u = 173\ MPa$; Young's Modulus $E_0 = 6.82 \times 10^4 MPa$; power law index $n = 0.23$.The energy equivalent flow stress can be found to be σ_0=106.1 MPa by Eq.(3.10).

Assuming that the target mean crushing force is $10kN$ and the highest allowable peak load is $20kN$, the optimum design of width and thickness can be calculated as

$$\{b^*, t^*\} = \{380mm, 1mm\} \tag{6.29}$$

As can be seen, the value of selected width is well beyond the practical range of interest. Practically, a high peak impact force can be eliminated by introducing a trigger on the top of the crash member, as described in the experimental study in Chapter 3. Therefore, we shall not consider the peak load constraint in the following analysis. Instead, a constraint on bending stiffness will be imposed.

2. Constraint on Bending Stiffness

In order to ensure enough elastic sectional stiffness and prevent global buckling of the column during axial crushing, a constraint on the bending stiffness should be imposed

$$EI \geq \widetilde{EI} \tag{6.30}$$

where $\widetilde{EI}$ is the target bending stiffness.

The bending stiffness EI of a thin-walled non-filled square section can be expressed by design variables (neglecting 3rd order term of t)

$$EI = \frac{2}{3} E_0 b^3 t \tag{6.31}$$

From Eq.(6.22), Eq.(6.23), Eq.(6.30) and Eq.(6.31), the optimum solution of b and t can be obtained through simple derivation

$$\begin{aligned} b^* &= \left(\frac{13.06\sigma_0}{\widetilde{P_m}}\right)^{\frac{3}{14}} \left(\frac{3\widetilde{EI}}{2E_0}\right)^{\frac{5}{14}} \\ t^* &= \left(\frac{\widetilde{P_m}}{13.06\sigma_0}\right)^{\frac{9}{14}} \left(\frac{2E_0}{3\widetilde{EI}}\right)^{\frac{1}{14}} \end{aligned} \tag{6.32}$$

Take, for instance, the mechanical properties of the column material are: σ_0=106.1MPa, E_0=68.2GPa, $\rho_0 = 2700kg/m^3$. The target values are taken as: $\widetilde{P_m}$=60kN, $\widetilde{EI} = 25kNm^2$. Solving Eq.(6.32) yields

$$\{b^*, t^*\} = \{50.1mm, 4.4mm\} \tag{6.33}$$

which is more reasonable for real application than the previous result from peak load consideration.

6.3.3.2 Foam-filled Square Sections

1. graphical approach

An optimization problem with only two design variables can usually be solved by graphical method. The graphical method is helpful to gain a physical understanding and to properly interpret the optimization procedure. In the following, three different cases will be considered. In each case, two of the design variables $\mathbf{X}^T = \{b, t, \sigma_0, \rho_f\}$ are fixed and the other two are left active. In all cases, the mass density of the column material ρ_0 is taken as $2700kg/m^3$. The filler is assumed to be Hydro Aluminum foam. The bending stiffness of a foam-filled section can be expressed by design variables as

$$EI = \frac{2}{3}E_0 b^3 t + \frac{1}{12}E_f(b-2t)^4 \tag{6.34}$$

where Young's Modulus of the foam E_f is related to the foam density ρ_f via Eq.(2.1).

Case 1: b and σ_0 fixed, t and ρ_f variable

Figure 6.8 shows the solutions to the optimization problem of a foam-filled column having a cross section width b=84mm and plastic flow stress σ_0=106.1MPa (AA6060 T4). In the figure, the contours of mean crushing force, bending stiffness and the sectional mass are plotted as functions of foam density ρ_f and wall thickness t. Straight lines represent the combinations of foam density and wall thickness that give constant values of sectional mass while the circle-like contours represent the combinations of ρ_f and t that yield constant values of P_m. Two contours of $EI = 25kNm^2$ and $EI = 50kNm^2$ are also plotted. One can see that, with the increase of foam density and wall thickness(moving from lower left corner of the figure to upper right), the mean crushing force and sectional mass are increasing as well. Some important features of the optimization problem can be discovered based on this figure.

Firstly, if a target mean crushing force is set, for example, 60kN, we can find in the figure the 60kN P_m contour, curve ECF. It can be observed that point F, which represents a foam alone column($t = 0$), gives a value of mass around 1.5 kg/m. Meanwhile, point E, which corresponds to an empty column($\rho_f = 0$) gives a value of mass around $3.5kg/m$, higher than point F. Due to the convex shape of the P_m contour and linearity of the mass contour, all other points on the 60kN contour give mass higher than point F. Therefore, it can be concluded that, for columns with given width and material property, a column made of foam alone will exhibit, among all possible combinations of wall thickness and foam density, the highest Specific Energy Absorption (SEA, energy absorption per unit mass).

However, a foam-alone column is not practically feasible because the column usually functions as a structural member which must provide strength and stiffness under normal working condition. Therefore, a constraint on the bending stiffness EI is introduced. Take, for instance, $EI \geq 25kNm^2$, an optimum point S can then be found at the intersection of P_m=60 contour and EI=25 contour, which gives the minimum weight design while satisfying both mean crushing force and bending stiffness requirements.

It is also interesting to note in the figure that, from point E to point C on 60kN

contour ($0 < \rho_f < 0.16$, correspondingly), foam-filled columns have larger mass therefore lower specific energy absorption than that of non-filled column (point E). Only if the density of the foam filler is larger than a critical value (point C), foam-filled columns will be superior to non-filled column in terms of specific energy absorption.

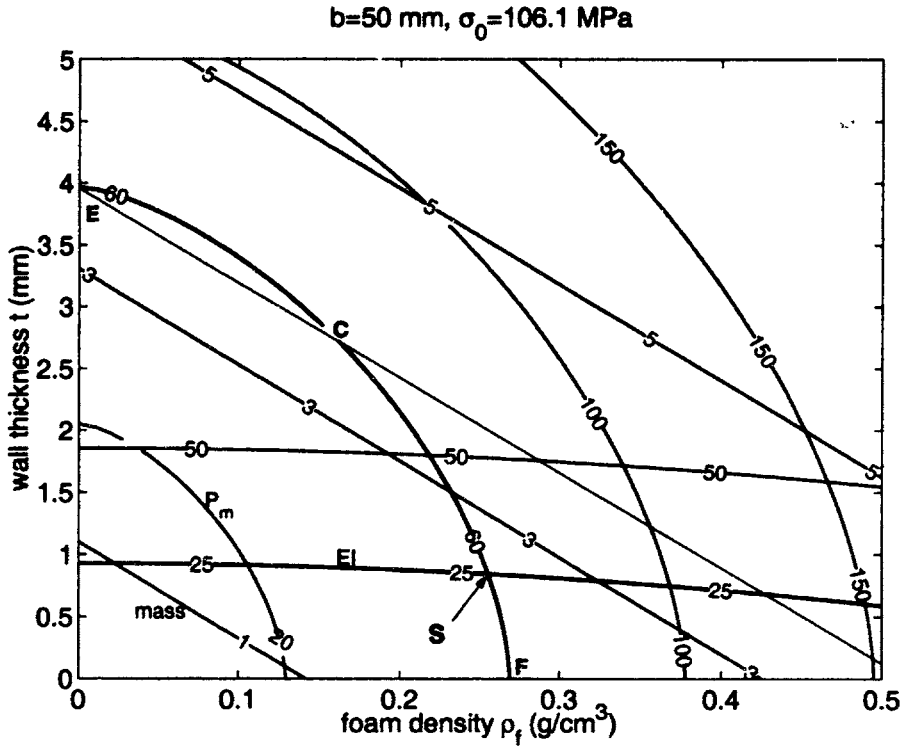

Figure 6.8: Graphical approach for optimization with fixed b and σ_0

Case 2: t and σ_0 fixed, b and ρ_f variable

Figure 6.9 shows the optimization solution of columns with given wall thickness t=0.8mm and flow stress σ_0=106.1MPa. The width of columns is varying from 50 to 100 mm and the range of foam density is $0\sim0.5g/cm^3$. In the same manner as in the previous figure, the contours of constant values of mass, P_m and EI are plotted as functions of the combinations of width and foam density. As can be seen, for a given target force P_m=60kN, point A, which is corresponding to the highest possible foam density, yields the smallest mass hence highest SEA. However, the constraint on bending stiffness $EI \geq 25$ rules out this choice and results in the optimum solution at point S.

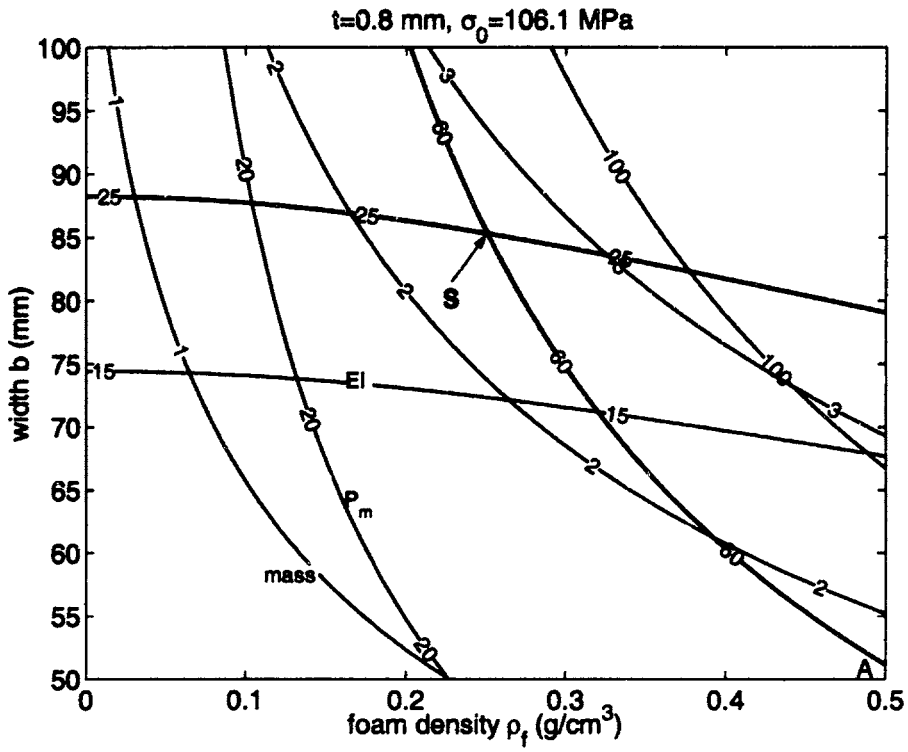

Figure 6.9: Graphical approach for optimization with $\sigma_0 = 106.1$ MPa and t=0.8mm

Case 3: b and t fixed, σ_0 and ρ_f variable

It is obvious that the mean crushing force will increase with the increase of the flow stress σ_0 without any additional weight penalty. Therefore, a high flow stress σ_0 is always favorable for crash member design, assuming the failure mode remains the same and without taking the material cost into consideration.

2. Numerical Optimization of Foam-filled Square Section with Prescribed Material

As indicated in above discussion, within a material group of same mass density, the one with the highest flow stress σ_0 is always the choice for weight efficient crashworthy design. Therefore, the flow stress σ_0 will not be considered as a design variable in the following analysis. The optimization formulation of foam-filled square sections can then be re-stated as

Find a set of design variable $\mathbf{X} = \{b, t, \rho_f\}$ to

Minimize $m(\mathbf{X}) = 4bt\rho_0 + b^2\rho_f$
Subject to

$$\begin{aligned} g_1(\mathbf{X}) &= -(13.06\sigma_0 b^{\frac{1}{3}} t^{\frac{5}{3}} + 1.8\sigma_f b^2) + \widetilde{P_m} \leq 0 \\ g_2(\mathbf{X}) &= -(\frac{2}{3}E_0 b^3 t + \frac{1}{12}E_f(b-2t)^4) + \widetilde{EI} \leq 0 \\ X_i^L &\leq X_i \leq X_i^U, \qquad i = 1,3 \end{aligned} \tag{6.35}$$

where σ_f and E_f are related to foam density ρ_f via Eq.(2.4) and Eq.(2.1), respectively.

The above problem has only three design variables and two constraint functions. It can be solved by numerical method such as Sequential Quadratic Programming with only limited computations required.

The column material is assumed to be aluminum alloy AA6060 T4 with mass density $2700kg/m^3$ and plastic flow stress σ_0=106.1MPa. The filler is Hydro Aluminum foam.

Several levels of target mean crushing force are specified with a constant target bending stiffness $\widetilde{EI} = 25kNm^2$. For the purpose of investigating the effect of wall thickness on the specific energy absorption (SEA), different feasible ranges of thickness t are specified. The optimized results are listed in the following tables. Similarly, optimization problems of non-filled square sections are also solved and optimum solutions are listed in same tables for comparison.

A few observations can be made based upon the above optimization results:

- The optimized specific energy absorption (SEA) of non-filled square section is generally lower than that of foam-filled section, unless the wall thickness of the non-filled section can reach un-practically large values. In that case, the SEA of empty section is about 8% higher than that of filled one while the wall thickness of empty section reach as large as $5 \backsim 6$mm;

- Due to the manufacturability, the largest allowable wall thickness t_{max} of thin-walled members is usually limited. If t_{max} is set to be 4mm, the SEA of filled section is 34% higher than that of non-filled section for a medium target force

Table 6.1: Optimization solutions with t unconstrained

Variables	Constraints							
t (mm)	no constraint							
b (mm)	no constraint							
ρ_f (g/cm^3)	0∽0.5							
$\widetilde{EI}$ (kNm^2)	25							
$\widetilde{P_m}$ (kN)	50		60		70		80	
Optimized Solutions	filled	empty	filled	empty	filled	empty	filled	empty
b^* (mm)	87.9	52	83.8	50	80.5	48.4	77.9	47
t^* (mm)	0.7	3.9	0.8	4.4	0.9	4.8	1.0	5.3
ρ_f^* (g/cm^3)	0.213	0	0.256	0	0.299	0	0.342	0
m^* (kg/m)	2.35	2.19	2.56	2.37	2.76	2.53	2.93	2.68
Specific energy absorption (kJ/kg)	21.3	22.8	23.4	25.3	25.4	27.7	27.3	29.9

Table 6.2: Optimization solutions with $t = [0, 4]$

Variables	Constraints							
t (mm)	0∽4							
b (mm)	no constraint							
ρ_f (g/cm^3)	0∽0.5							
$\widetilde{EI}$ (kNm^2)	25							
$\widetilde{P_m}$ (kN)	50		60		70		80	
Optimized Solutions	filled	empty	filled	empty	filled	empty	filled	empty
b^* (mm)	87.9	52	83.8	79.3	80.5	125.9	77.9	187.9
t^* (mm)	0.7	3.9	0.8	4	0.9	4	1.0	4
ρ_f^* (g/cm^3)	0.213	0	0.256	0	0.299	0	0.342	0
m^* (kg/m)	2.35	2.19	2.56	3.43	2.76	5.44	2.93	8.12
Specific energy absorption (kJ/kg)	21.3	22.8	23.4	17.5	25.4	12.9	27.3	9.9

Table 6.3: Optimization solutions with $t = [0, 3]$

Variables	Constraints							
t (mm)	0∽3							
b (mm)	no constraint							
ρ_f (g/cm^3)	0∽0.5							
$\widetilde{EI}$ (kNm^2)	25							
$\widetilde{P_m}$ (kN)	50		60		70		80	
Optimized Solutions	filled	empty	filled	empty	filled	empty	filled	empty
b^* (mm)	87.9	193.3	83.8	334.1	80.5	530.5	77.9	791.9
t^* (mm)	0.7	3	0.8	3	0.9	3	1.0	3
ρ_f^* (g/cm^3)	0.213	0	0.256	0	0.299	0	0.342	0
m^* (kg/m)	2.35	6.26	2.56	10.83	2.76	17.19	2.93	25.66
Specific energy absorption (kJ/kg)	21.3	8.0	23.4	5.5	25.4	4.1	27.3	3.1

Table 6.4: Optimization solutions with $t = [0, 2]$

Variables	Constraints							
t (mm)	0∽2							
b (mm)	no constraint							
ρ_f (g/cm^3)	0∽0.5							
$\widetilde{EI}$ (kNm^2)	25							
$\widetilde{P_m}$ (kN)	50		60		70		80	
Optimized Solutions	filled	empty	filled	empty	filled	empty	filled	empty
b^* (mm)	87.9	1468.2	83.8	2537.0	80.5	4028.7	77.9	6013.7
t^* (mm)	0.7	2	0.8	2	0.9	2	1.0	2
ρ_f^* (g/cm^3)	0.213	0	0.256	0	0.299	0	0.342	0
m^* (kg/m)	2.35	31.71	2.56	54.8	2.76	87.02	2.93	129.90
Specific energy absorption (kJ/kg)	21.3	1.6	23.4	1.1	25.4	0.8	27.3	0.6

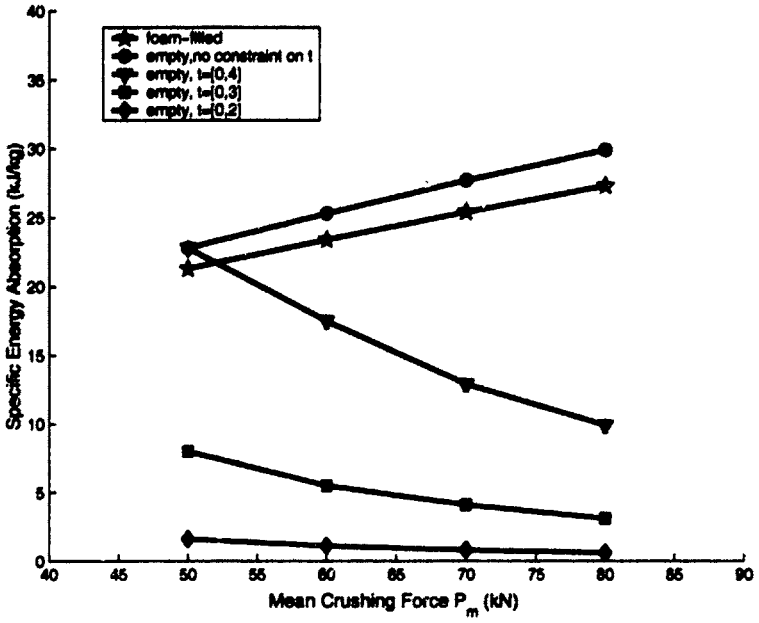

Figure 6.10: Specific energy absorption under various conditions

(60kN). This gain of SEA for filled section compared to non-filled one will reach as high as 175% for a larger target force (80kN);

- When the feasible range of wall thickness shrinks, the SEA of non-filled section drops significantly, which consequently results in an increasing high superiority for filled sections in specific energy absorption, as can be seen in Fig.6.10. For instance, the SEA of filled section is four times higher than that of non-filled section for $\widetilde{P_m}$=60kN and t in the range of $0 \backsim 3$mm;

- With the increase of the target force level, the SEA of filled section increases as well while the SEA of empty section is decreasing;

- For the target force levels specified in calculation, the optimized solution of filled section usually yields relatively small wall thickness ($0.6 \backsim 1.0$mm), a medium foam density ($0.2 \backsim 0.3 g/cm^3$), and a width $80 \backsim 90$mm. In comparison, the optimum design of a non-filled section will take a relatively large wall thickness. If the selection of large wall thickness is restrained, a large width will be consequently resulted in to meet the target force requirement. For example, in the case of $t = 0 \backsim 3$mm and $\widetilde{P_m}$=60kN, the optimized width of empty section is 334.1mm, which is four times larger than the width of filled section (83.8mm).

Therefore, in addition to significant weight saving, dramatic volume reduction can also be achieved by utilizing aluminum foam filler;

- It can be concluded that the wall thickness is the most sensitive variable in the design of square-section crash members;
- It should be underlined that some optimization results for empty sections with 2mm wall thickness (Table 6.4) give huge values in width. The design formula of the mean crushing force used in the current optimization formulation may not be valid any more for such sections. Hence, the optimization results for those sections might not be sufficiently accurate. However, the trend revealed in above analysis should be still valid;

Table 6.5: Optimization solutions with $\widetilde{EI}$ varying

Variables	Constraints							
t (mm)	0∽3							
b (mm)	no constraint							
ρ_f (g/cm^3)	0∽0.5							
$\widetilde{P_m}$ (kN)	60							
$\widetilde{EI}(kNm^2)$	10		20		30		40	
Optimized Solutions	filled	empty	filled	empty	filled	empty	filled	empty
b^* (mm)	59.4	334.1	77.0	334.1	89.8	334.1	100.2	334.1
t^* (mm)	0.9	3.0	0.9	3.0	0.8	3.0	0.8	3.0
ρ_f^* (g/cm^3)	0.405	0	0.286	0	0.233	0	0.202	0
m^* (kg/m)	2.01	10.83	2.42	10.83	2.69	10.83	2.90	10.83
Specific energy absorption (kJ/kg)	29.9	5.5	24.8	5.5	22.3	5.5	20.7	5.5

Let us set the target mean crushing force at a specified value, for example, 60kN, and make the target bending stiffness vary in a certain range. The corresponding optimization results are shown in Table 6.5. The feasible range of wall thickness is set in the calculation to be 0 ∽ 3mm, as commonly used in real applications. Fig.6.11 shows the optimized specific energy absorption of filled and non-filled sections.

As can be noted in the Fig.6.11, the specific energy absorption of foam-filled section is a decreasing function of the target bending stiffness. The constraint on the bending stiffness retarded the selection of high density foam. The higher the requirement of bending stiffness is, the lower the resulted foam density is. This is consistent with what was observed in graphical approach discussed earlier.

The SEA of the non-filled section is a horizontal line in Fig.6.11. It indicates that the bending stiffness constraint is not active in the optimization process of empty sections.

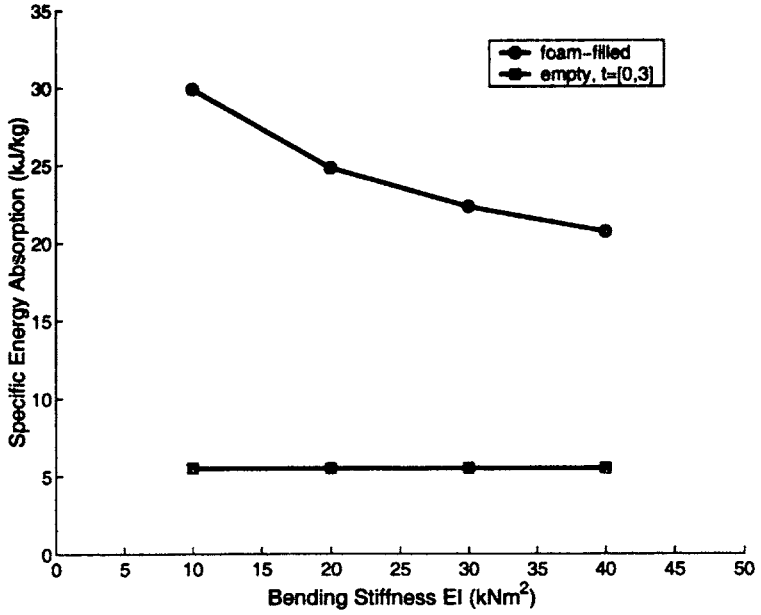

Figure 6.11: Specific energy absorption vs. target bending stiffness

6.3.4 Optimization of Other Sections

Similarly as in the case of foam-filled square sections, other types of cross-sections, such as hexagonal, double-hat rectangular, double-hat hexagonal and double-walled sandwich sections, can also be optimized for minimum weight using the proposed methodology. We shall consider these cases in the following. In call cases, the wall material is assumed to be Aluminum alloy AA6060 T4 with plastic flow stress σ_0=106.1Mpa and mass density $\rho_0 = 2700kg/m^3$. A practically feasible range of wall

thickness $t = 0 \backsim 3$mm is specified for all sections except for double-walled sandwich sections. The foam filler is Hydro Aluminum foam. The honeycomb core in double-walled honeycomb sandwich is 5060 Hexcel Honeycomb. The mechanical properties of these two ultralight core material can be found in Chapter 2.

6.3.4.1 Foam-filled Hexagonal Section

A foam-filled hexagonal section with width b, wall thickness t and foam density ρ_f is considered (Fig.6.12).

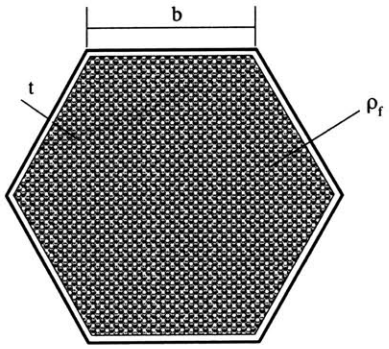

Figure 6.12: Geometry of a foam-filled hexagonal section

The optimization formulation can be constructed by applying the corresponding expressions of mass, mean crushing force and bending stiffness into the general formulation with crashworthiness and stiffness constraints:

Find a set of design variable $\mathbf{X} = \{b, t, \rho_f\}$ to
Minimize $m(\mathbf{X}) = 6bt\rho_0 + \frac{3\sqrt{3}}{2}b^2\rho_f$
Subject to:

$$\begin{aligned} g_1(\mathbf{X}) &= -(20.23\sigma_0 b^{1.6}t^{0.4} + 4.68\sigma_f b^2) + \widetilde{P_m} \leq 0 \\ g_2(\mathbf{X}) &= -[E_0(\frac{5}{2}b^3t + \frac{1}{4}bt^3) + \frac{5\sqrt{3}}{16}b^4E_f] + \widetilde{EI} \leq 0 \\ X_i^L &\leq X_i \leq X_i^U, \qquad i = 1, 3 \end{aligned} \tag{6.36}$$

where σ_f and E_f are related to foam density ρ_f via Eq.(2.4) and Eq.(2.1).

An optimization problem of non-filled hexagonal section can be solved by setting ρ_f=0 in Eq.(6.36). Results of both filled and non-filled sections are listed in Table 6.6 for comparison. Fig.6.13 shows the specific energy absorption vs. target force levels.

Table 6.6: Optimization solutions of hexagonal sections

Variables	Constraints							
t (mm)	$0 \backsim 3$							
b (mm)	no constraint							
ρ_f (g/cm^3)	$0 \backsim 0.5$							
$\widetilde{EI}$ (kNm^2)	25							
$\widetilde{P_m}$ (kN)	50		60		70		80	
Optimized Solutions	filled	empty	filled	empty	filled	empty	filled	empty
b^* (mm)	37.0	37.0	36.5	51.0	36.4	75.0	36.3	104.7
t^* (mm)	2.9	2.9	3.0	3.0	3.0	3.0	3.0	3.0
ρ_f^* (g/cm^3)	0	0	0.108	0	0.191	0	0.260	0
m^* (kg/m)	1.74	1.74	2.15	2.48	2.43	3.64	2.65	5.09
Specific energy absorption (kJ/kg)	28.7	28.7	27.9	24.2	28.8	19.2	30.2	15.7

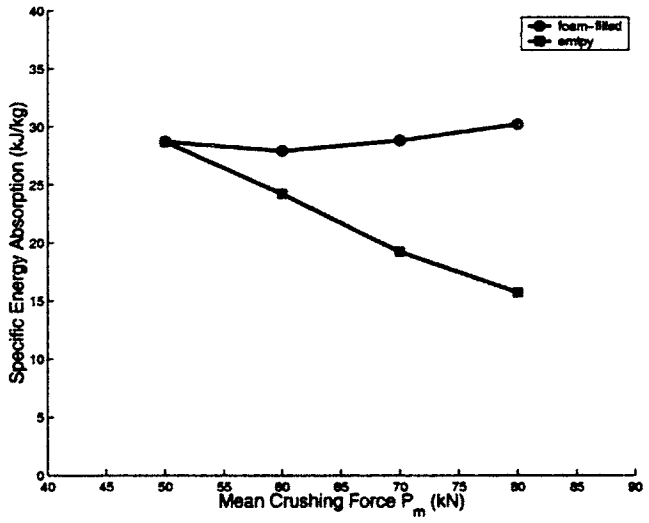

Figure 6.13: Specific energy absorptions of hexagonal sections

One can note from the optimum solutions that the foam-filled hexagonal section exhibits up to 100% higher specific energy absorption than non-filled one at a high target force level(80kN). The dimensions of filled section are much smaller than empty section, which leads to significant volume reduction of structural members, which is beneficial from the packaging point of view.

6.3.4.2 Foam-filled Double-hat Rectangular Section

Similarly, the weight optimization problem of foam-filled double-hat rectangular section with width b, wall thickness t, height h, flange s and foam density ρ_f (see Fig.6.14) can be formulated as follows with design variables $\mathbf{X} = \{b, t, h, s, \rho_f\}$. To ensure a stable progressive folding mechanism in axial crushing of double-hat rectangular sections, a constraint on height h is imposed as $h \leq 1.5b$ defined as $g_3(\mathbf{X})$.

Minimize $m(\mathbf{X}) = \rho_0(4s + 2h + 2b) + \rho_f bh$
Subject to:

$$\begin{aligned} g_1(\mathbf{X}) &= -\{13.06\sigma_0 t^{\frac{5}{3}}[(s+\frac{1}{4}h)^{\frac{1}{3}} + (\frac{1}{2}b+\frac{1}{4}h)^{\frac{1}{3}}] + 1.8\sigma_f bh\} + \widetilde{P_m} \leq 0 \\ g_2(\mathbf{X}) &= -[E_0(\frac{4}{3}st^3 + \frac{1}{6}th^3 + \frac{1}{2}bth^2) + \frac{1}{12}bh^3E_f] + \widetilde{EI} \leq 0 \\ g_3(\mathbf{X}) &= h - 1.5b \leq 0 \\ X_i^L &\leq X_i \leq X_i^U, \qquad i = 1,5 \end{aligned} \tag{6.37}$$

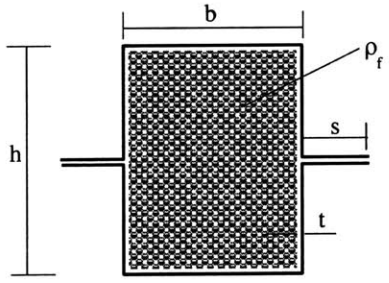

Figure 6.14: Geometry of a foam-filled double-hat rectangular section

Again, the problem was reduced to a non-filled one by setting ρ_f=0 in Eq.(6.37). Optimized solutions are shown in Table 6.7 and Fig.6.15.

Table 6.7: Optimization solutions of double-hat rectangular sections

Variables	Constraints							
t (mm)	$0 \backsim 3$							
b (mm)	no constraint							
h (mm)	$\leq 1.5b$							
s (mm)	$20 \backsim 30$							
ρ_f (g/cm^3)	$0 \backsim 0.5$							
$\widetilde{EI}$ (kNm^2)	25							
$\widetilde{P_m}$ (kN)	50		60		70		80	
Optimized Solutions	filled	empty	filled	empty	filled	empty	filled	empty
b^* (mm)	66.7	42.8	66.7	49.8	65.6	82.4	63.6	136.3
t^* (mm)	0.7	2.8	0.6	3.0	0.6	3.0	0.7	3.0
h^* (mm)	100.0	64.3	100.0	67.4	98.4	123.5	95.4	204.5
s^* (mm)	20	20	20	24.9	20	30	20	30
ρ_f^* (g/cm^3)	0.230	0	0.264	0	0.302	0	0.344	0
m^* (kg/m)	2.26	2.19	2.46	2.71	2.64	4.31	2.81	6.49
SEA (kJ/kg)	22.1	22.8	24.4	22.1	26.5	16.2	28.5	12.3

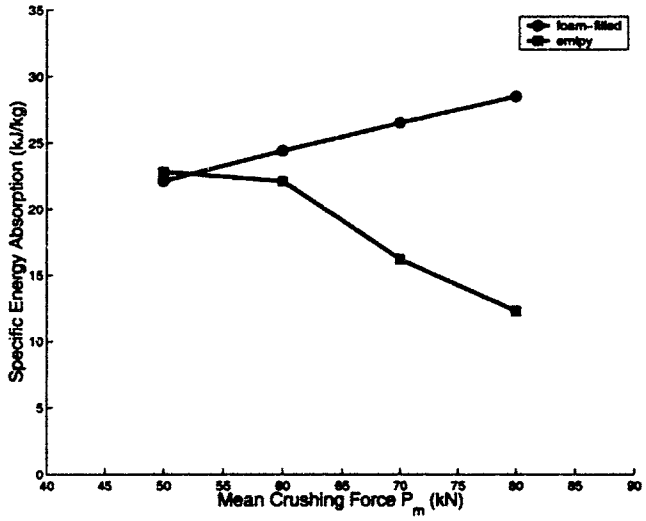

Figure 6.15: Specific energy absorption of double-hat rectangular sections

As can be seen, significant weight and volume savings can be achieved by introducing foam filler into thin-walled double-hat rectangular sections.

6.3.4.3 Foam-filled Double-hat Hexagonal Section

Optimization formulation of foam-filled double-hat hexagonal section with width b, wall thickness t, flange s and foam density ρ_f (see Fig.6.16) can be constructed by applying the corresponding expressions for mean crushing force and bending stiffness and identifying the design variables $\mathbf{X} = \{b, t, s, \rho_f\}$:

Minimize $m(\mathbf{X}) = \rho_0 t(4s + 6b) + \frac{3\sqrt{3}}{2}\rho_f b^2$
Subject to:

$$\begin{aligned} g_1(\mathbf{X}) &= -\{13.49\sigma_0 t^{1.6}[(s + \frac{1}{2}b)^{0.4} + b^{0.4}] + 4.68\sigma_f b^2\} + \widetilde{P_m} \leq 0 \\ g_2(\mathbf{X}) &= -[E_0(\frac{5}{2}b^3 t + \frac{1}{4}bt^3 + \frac{4}{3}st^3) + \frac{5\sqrt{3}}{16}b^4 E_f] + \widetilde{EI} \leq 0 \\ X_i^L &\leq X_i \leq X_i^U, \qquad i = 1, 4 \end{aligned} \tag{6.38}$$

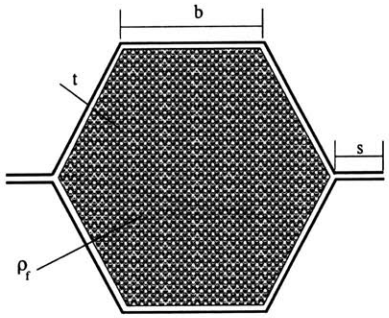

Figure 6.16: Geometry of a foam-filled double-hat hexagonal section

Table 6.8 and Fig.6.17 show the optimization solutions for filled and non-filled sections. It is interesting to note that foam-filled sections provide specific energy absorption about 15% lower than the non-filled sections, except at a high target force level of 80kN. The reason for this is, the double-hat hexagonal section itself is a weight efficient energy absorber due to its multi-corner features in geometry. The foam-filler can not improve the specific energy absorption unless at high target force levels.

Table 6.8: Optimization solutions of double-hat hexagonal sections

Variables	Constraints							
t (mm)	$0 \backsim 3$							
b (mm)	no constraint							
s (mm)	$20 \backsim 30$							
ρ_f (g/cm^3)	$0 \backsim 0.5$							
$\widetilde{EI}$ (kNm^2)	25							
$\widetilde{P_m}$ (kN)	50		60		70		80	
Optimized Solutions	filled	empty	filled	empty	filled	empty	filled	empty
b^* (mm)	53.9	39.5	52.4	37.9	51.1	36.6	50.0	51.0
t^* (mm)	0.9	2.4	0.9	2.7	1.0	3.0	1.0	3.0
s^* (mm)	20	20	20	20	20	20	20	25.5
ρ_f^* (g/cm^3)	0.192	0	0.229	0	0.266	0	0.302	0
m^* (kg/m)	2.41	2.04	2.63	2.23	2.84	2.41	3.03	3.30
Specific energy absorption (kJ/kg)	20.7	24.5	22.8	26.9	24.6	29.0	26.4	24.2

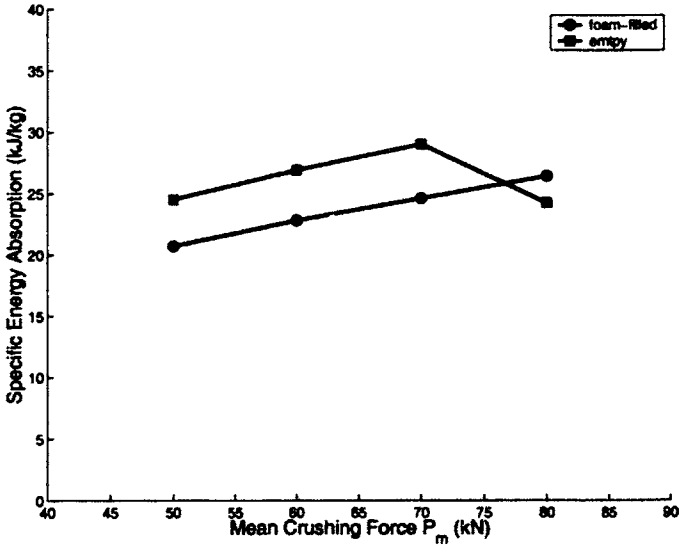

Figure 6.17: Specific energy absorptions of double-hat hexagonal sections

6.3.4.4 Double-walled Sandwich

The weight optimization problem of double-walled sandwich section with width b, inner and outer wall thickness t, core height C, honeycomb density ρ_h or foam density ρ_f(see Fig.6.18) can be formulated by introducing the corresponding expressions of mean crushing force and bending stiffness into the general optimization formulation. The results of this optimization problem should be considered tentative because the formula for the mean crushing force was obtained only from a limited number of computer runs and was restricted to a limited range of design parameters.

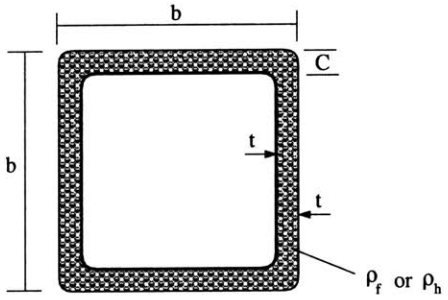

Figure 6.18: Geometry of double-walled sandwich section

Aluminum Honeycomb Sandwich

Minimize $m(\mathbf{X}) = \rho_0 t[4b + 4(b-2C)] + \rho_h C[2b + 2(b-2C)]$
Subject to:

$$\begin{aligned} g_1(\mathbf{X}) &= -[13.06\sigma_0(2t)^{\frac{5}{3}}b^{\frac{1}{3}} + 60.48C^{\frac{7}{4}}b^{\frac{1}{4}}\sigma_h] + \widetilde{P_m} \leq 0 \\ g_2(\mathbf{X}) &= -EI + \widetilde{EI} \leq 0 \\ X_i^L &\leq X_i \leq X_i^U, \qquad i = 1,4 \end{aligned} \tag{6.39}$$

where bending stiffness EI can be expressed as

$$\begin{aligned} EI = \; & 2E_0 t[\tfrac{2}{3}(\tfrac{b}{2}-C)^3 + \tfrac{2}{3}(\tfrac{b}{2})^3 + \tfrac{1}{12}(b-2C)t^2 + (b-2C)(\tfrac{b}{2}-C)^2 + \tfrac{1}{12}bt^2 + \tfrac{1}{4}b^3] \\ & +2E_h C[\tfrac{2}{3}(\tfrac{b}{2})^3 + (b-2C)(\tfrac{b}{2}-\tfrac{C}{2})^2 + \tfrac{1}{12}(b-2C)C^2] \end{aligned} \tag{6.40}$$

The formula for the function g_1 were developed by Santosa [6].

Design variables in this problem are $\mathbf{X} = \{b, t, C, \rho_h\}$; σ_h and E_h are related to honeycomb density in Table 2.1.

aluminum Foam Sandwich

To find a set of $\mathbf{X} = \{b, t, C, \rho_f\}$ to
Minimize $m(\mathbf{X}) = \rho_0 t[4b + 4(b - 2C)] + \rho_f C[2b + 2(b - 2C)]$
Subject to:

$$\begin{aligned} g_1(\mathbf{X}) &= -[13.06\sigma_0(2t)^{\frac{5}{3}}b^{\frac{1}{3}} + 20.57C^{\frac{5}{4}}b^{\frac{3}{4}}\sigma_f] + \widetilde{P_m} \leq 0 \\ g_2(\mathbf{X}) &= -EI + \widetilde{EI} \leq 0 \\ X_i^L &\leq X_i \leq X_i^U, \qquad i = 1, 4 \end{aligned} \tag{6.41}$$

where EI can be evaluated by Eq.(6.40) with E_h being replaced by E_f;

The problems are solved for the specified target bending stiffness and target force levels. Results are shown in Table 6.9 and Fig.6.19. The optimum solutions of non-filled square sections are also shown in Fig.6.19 for comparison. One can see that compared to the traditional non-filled square section, the double-walled aluminum foam sandwich section can provide 5-10 times higher specific energy absorption. Even higher is the double-walled honeycomb sandwich section. Significant volume reductions are achieved as well by these double-walled sandwich sections. The dramatic weight saving and volume reduction potentials of double-walled sandwich section justify its promising future as efficient crash structural members.

However, it should be noted that the formula for the mean crushing force used in the optimization formulation was obtained only from a limited number of analyses and assuming that the core is not crushed. It was observed in the experiments [52] that the core generally crushed in a transverse shear or in an in-plane failure mode. Therefore, the optimization results might overpredict the energy absorption capacity and the gain in specific energy absorption of the double-walled sandwich sections.

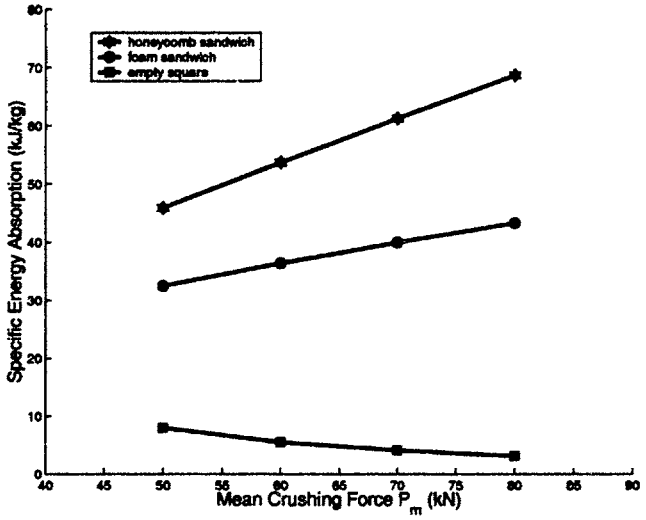

Figure 6.19: Specific energy absorptions of double-walled sandwich sections

Table 6.9: Optimization solutions of double-walled sandwich sections (H:honeycomb; F: foam)

Variables	Constraints							
t (mm)	$0.5 \backsim 3$							
b (mm)	no constraint							
C (mm)	$0 \backsim 10$							
ρ_h (g/cm^3)	$0 \backsim 0.8$							
ρ_f (g/cm^3)	$0 \backsim 0.5$							
$\widetilde{EI}$ (kNm^2)	25							
$\widetilde{P_m}$ (kN)	50		60		70		80	
Optimized Solutions	H	F	H	F	H	F	H	F
b^* (mm)	82.0	82.4	81.1	82.5	80.3	82.6	79.6	82.7
t^* (mm)	0.5	0.5	0.5	0.5	0.5	0.5	0.5	0.5
C^* (mm)	10.0	4.5	10.0	5.3	10.0	6.0	10.0	6.8
ρ_h^* or ρ_f^* (g/cm^3)	0.108	0.5	0.122	0.5	0.136	0.5	0.148	0.5
m^* (kg/m)	1.09	1.54	1.12	1.65	1.14	1.75	1.17	1.85
Specific energy absorption (kJ/kg)	45.9	32.5	53.7	36.4	61.3	40.0	68.7	43.3

6.3.5 Discussions

A study on optimization for minimum weight of foam-filled sections and double-walled sandwich section of crash members undergoing axial crushing was carried out in this section. A methodology was proposed which combined the structural optimization technique with the recent achievements in crushing mechanics of ultralight structures. The optimization problems of foam-filled square, hexagonal, double-hat rectangular, double-hat hexagonal sections and double-walled sandwich sections were formulated and solved with crashworthiness and bending stiffness constraints. The proposed methodology requires relatively simple computations and is suitable for early stage of crash member design. Some conclusions can be made based upon the optimization results of above mentioned cross-sections:

- Significant weight saving and volume reduction can be achieved by introducing ultralight metal filler into thin-walled crash members, especially when a large energy absorption level is required;
- The specific energy absorption (energy absorption per unit mass) of foam-filled sections are generally 50% to five times higher than that of non-filled sections, depending on the sectional geometry and target crushing force level;
- Among all studied sections, double-walled sandwich sections exhibit the highest specific energy absorption, see Fig.6.20.

Crash optimization for bending collapse will be addressed in the next section.

6.4 Optimization for Bending Collapse

The bending collapse behavior of thin-walled foam-filled or honeycomb-filled beams were studied in Chapter 4. The strengthening effects of foam filling and honeycomb filling were quantified, and design formula were derived to predict the bending resistances of thin-walled beams filled with ultralight filler. Structural optimization

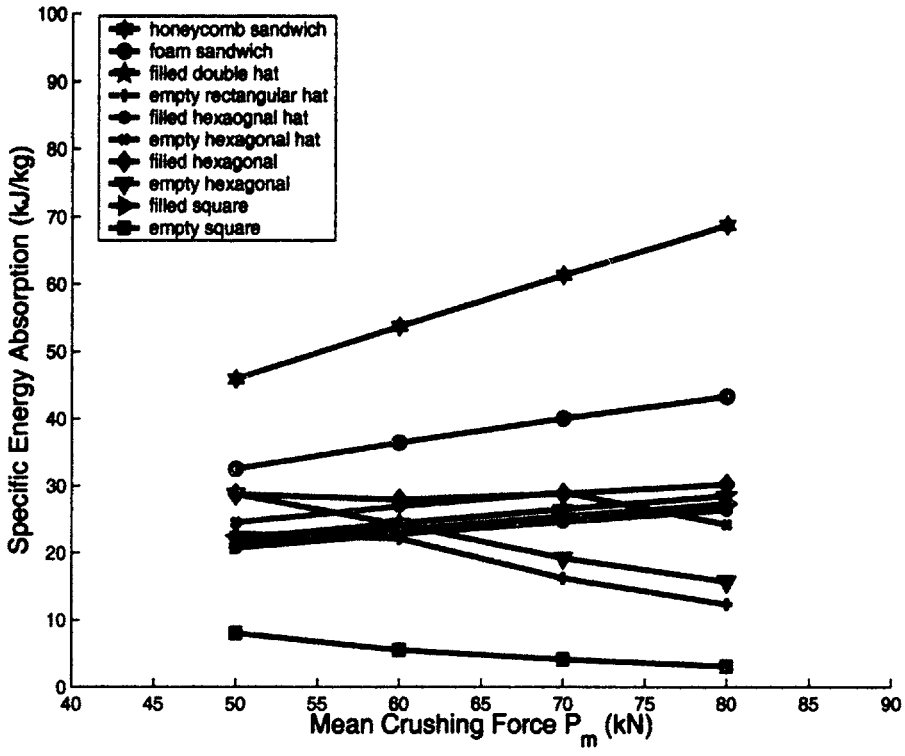

Figure 6.20: Specific energy absorption vs. target force level for various sections

technique can now be employed to select the most weight efficient design for crash energy management.

A general problem of structural optimization for minimum weight was stated in Eq.(6.4). In the case of sizing optimization of a filled square section, three design variables can be identified: the width b, the wall thickness t, and the mass density of filler ρ_f(for foam filling) or ρ_h(for honeycomb filling), that is,

$$\mathbf{X} = \{b, t, \rho_f \text{ or } \rho_h\} \tag{6.42}$$

The constraints considered in the present study are the requirement of energy absorption(target energy absorption) for proper crash energy management, and the requirement of cross-sectional elastic bending stiffness(EI) for integrity in normal loading condition.

The optimization problems of foam-filled and honeycomb-filled sections are solved in the following.

6.4.1 Optimization of Foam-filled Sections

The optimization problem of a foam-filled section for minimum weight with target energy absorption in bending collapse mode can be formulated in the following way

Find a set of design variables $\mathbf{X} = \{b, t, \rho_f\}$ to
Minimize $m(\mathbf{X}) = 4btL\rho_0 + (b-t)^2\rho_f L_f$
Subject to

$$\begin{aligned} g_1(\mathbf{X}) &= -E_n + \widetilde{E_n} \leq 0 \\ g_2(\mathbf{X}) &= -EI + \widetilde{EI} \leq 0 \\ X_i^L &\leq X_i \leq X_i^U, \qquad i = 1,3 \end{aligned} \tag{6.43}$$

where L is the beam length; L_f is the effective filling length given in Eq.(4.13); ρ_0 is the mass density of the wall material; $\widetilde{E_n}$ and $\widetilde{EI}$ denote the target energy absorption and bending stiffness, respectively; E_n is the actual energy absorption during bending collapse up to bending rotation θ_0 (smaller than the jamming angle), defined by (neglecting the small contribution from elastic deformation)

$$E_n = \int_0^{\theta_0} M_f(\theta) d\theta \tag{6.44}$$

with bending moment $M_f(\theta)$ given in Eq.(4.21).

and EI is the elastic bending stiffness of the cross-section

$$EI = E_0(\frac{2}{3}b^3t + \frac{1}{6}bt^3) + \frac{1}{12}(b-t)^4 E_f \tag{6.45}$$

where E_0 is the Young's modulus of the wall material; E_f is the elastic modulus of foam material and is related to the foam density ρ_f via Eq.(2.1).

The above optimization problem has only three design variables and two constraint functions. Both objective and constraint functions are continuous and differentiable in the design domain. With $\rho_f = 0$, the problem reduces to a non-filled one.

As a case study, let us consider an extruded square foam-filled beam, with length $L = 400$mm, wall material being aluminum alloy AA6060 T4($\rho_0 = 2.7g/cm^3, E_0 = 69GPa, \sigma_0 = 106.1MPa$) and the foam material being Hydro aluminum foam($\rho_s = 2.7g/cm^3, E_s = 69GPa, \sigma_{0f} = 150.4MPa$). Several values of target energy absorption are specified, while the target bending stiffness remains constant $\widetilde{EI} = 25kNm^2$. The feasible range of the wall thickness t is [0.5, 3], which is practical for aluminum automotive structures. The foam density is within the range of $\rho_f = (2.5\% \backsim 20\%)\rho_s$. The optimum solutions are listed in Table 6.10. The optimization problems of non-filled square sections are also solved and results are shown in the same table. In all cases, the bending collapse is assumed to stop at $\theta_0 = 30°$.

Table 6.10: Optimum solutions for foam-filled and empty sections

Variables	Constraints									
b (mm)	no constraint									
t (mm)	$0.5 \backsim 3$									
ρ_f (g/cm^3)	$0.0675 \backsim 0.54$									
$\widetilde{EI}$ (kNm^2)	25									
$\widetilde{E_n}$ (J)	1000		1500		2000		2500		3000	
Solutions	F	E	F	E	F	E	F	E	F	E
b^* (mm)	95.8	73.3	89.8	98.1	98.6	120.7	100.4	141.9	100.0	162.0
t^* (mm)	0.97	3.0	1.31	3.0	1.32	3.0	1.74	3.0	1.92	3.0
ρ_f^* (g/cm^3)	0.109	0	0.169	0	0.179	0	0.184	0	0.215	0
m^* (kg)	0.606	0.950	0.812	1.271	0.986	1.564	1.151	1.839	1.310	2.099
SEA(kJ/kg)	1.651	1.053	1.846	1.180	2.028	1.279	2.173	1.359	2.290	1.429

Note: F=Filled; E=Empty

A few observations can be made based upon the above optimization results

- The optimized specific energy absorption(SEA, energy absorption per unit mass) of foam-filled beams is about 60% higher than that of non-filled beam for the

specified target energy absorption levels, see Fig.6.21. This substantiates the argument that the foam-filled members are superior to non-filled ones in the light of weight-effective energy absorption.

- The optimum wall thickness of a filled section is generally smaller than that of a non-filled section (0.97$\backsim$ 1.92mm vs. 3mm). It indicates that the wall thickness of the foam-filled section has to be reduced compared with traditionally designed non-filled section if increase of specific energy absorption is to be achieved.

- Another consequence of foam filling is the reduced sectional width compared to non-filled sections. The reduction in width is 18% at a medium energy absorption level(2kJ), and it reaches as high as 62% at a higher level of energy absorption(3kJ). Therefore, in addition to the significant weight saving, considerable volume reduction can also be achieved by utilizing aluminum foam filler.

- For the target energy absorption levels considered in calculation, the optimum solutions of filled section yield relatively low foam density ($0.11 \backsim 0.22 g/cm^3$).

- For bent angles larger than $\theta_0 = 30°$, touching occurs and second fold develops. Results of the optimization process might be different.

6.4.2 Optimization of Honeycomb-filled Sections

Same methodology can be applied to optimize the honeycomb-filled sections for minimum weight. The formulation is stated in Eq.(6.43), with the mass density of foam ρ_f being replaced with the mass density of honeycomb ρ_h.

The energy absorption E_n can be calculated by (neglecting the small contribution from elastic deformation)

$$E_n = \int_0^{\theta_0} M_h(\theta) d\theta \tag{6.46}$$

with bending moment $M_h(\theta)$ given in Eq.(4.29).

The expression of EI is given in Eq.(6.45), with E_f being replaced with E_h formulated in Table 2.1.

Take, for instance, honeycomb-filled square beam with length $L = 400$mm, the wall material being AA6060 T4, and the honeycomb material being 5256 Hexcel aluminum honeycomb ($E_s = 69GPa, \sigma_{0h} = 285MPa, \rho_s = 2.7g/cm^3$). The bending collapse stops at $\theta_0 = 30°$. With $\rho_h = 0$, the problem reduces to a non-filled one. The optimized results at specified energy absorption levels are shown in Table 6.11.

Table 6.11: Optimum solutions for honeycomb-filled and empty sections

Variables	Constraints									
b (mm)	no constraint									
t (mm)	$0.5 \backsim 3$									
ρ_h (g/cm^3)	$0.0675 \backsim 0.54$									
$\widetilde{EI}$ (kNm^2)	25									
$\widetilde{E_n}$ (J)	1000		1500		2000		2500		3000	
Solutions	F	E	F	E	F	E	F	E	F	E
b^* (mm)	99.8	73.3	100.0	98.1	100.0	120.7	100.1	141.9	100.2	162.0
t^* (mm)	0.55	3.0	1.0	3.0	1.49	3.0	1.94	3.0	2.36	3.0
ρ_h^* (g/cm^3)	0.068	0	0.096	0	0.113	0	0.130	0	0.145	0
m^* (kg)	0.441	0.950	0.675	1.271	0.886	1.564	1.081	1.839	1.265	2.099
SEA(kJ/kg)	2.267	1.053	2.222	1.180	2.259	1.279	2.314	1.359	2.371	1.429

The specific energy absorption of optimized honeycomb-filled beams at specified levels of energy absorption are shown in Fig.6.21. The SEA of filled section is 66% $\backsim$ 115% higher than that of non-filled section, depending on the energy absorption level. Similar to the case of foam filling, the optimum solutions of honeycomb-filled section usually yield, compared to the non-filled case, smaller wall thickness(0.55 $\backsim$ 2.36mm vs. 3mm), smaller width, and relatively low density honeycomb(0.068 $\backsim$ 0.145g/cm^3). Therefore, significant weight saving and volume reduction can also be achieved by honeycomb filling.

As can be noted in Fig.6.21, the honeycomb-filled section offers the highest specific energy absorption, compared to the foam-filled section and traditional non-filled sec-

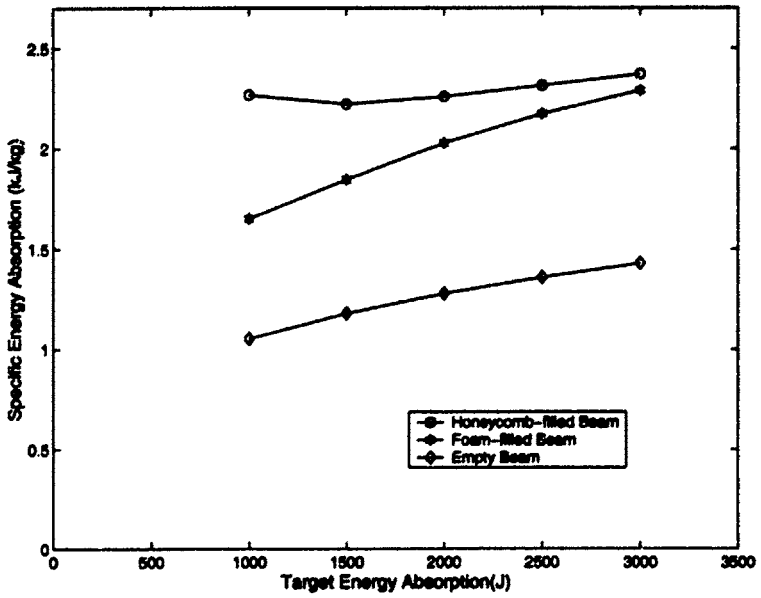

Figure 6.21: Specific energy absorptions at various energy absorption levels

tion. This is also evident if we study the strengthening effect of two filling methods, see Fig.4.53. The moment elevation resulting from honeycomb filling is larger than that from foam filling for the relative density of filler up to 8%, which is the range that optimum solutions of both foam and honeycomb fall in.

6.5 Optimization for Combined Compression/Bending Loading

The axial crushing behavior of thin-walled metal tubes has been studied extensively over the past twenty years. The axial folding deformation of the tubes are known to be an efficient energy absorbing mechanism. However, the truth is that axial progressive folding is easily reproducible only in laboratory experiments, and it seldom acts alone in real crash events. The progressive buckling of crash members will almost inevitably transit to a global bending collapse mode in the advanced stage of crash, as illustrated in Fig.6.22. This transition is also called "stability of progressive collapse" and has been studied only by few authors [97, 98].

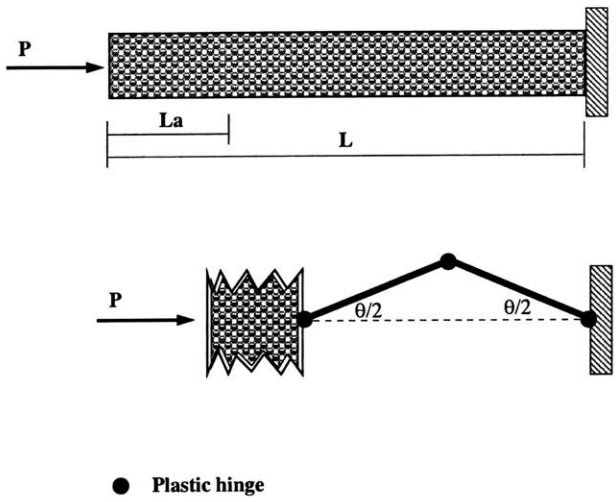

Figure 6.22: Transition from axial progressive crushing to global bending collapse

An important parameter is the ratio $\xi = \frac{L_a}{L}$, with L_a being the length of tube undergoing axial crushing, and L being the total length of the crash member. The transition parameter ξ depends on the initial inclination of the member, boundary conditions, the bending stiffness and the opening characteristics of the collapse section, and so on.

The optimization problem for minimum weight of foam-filled beam-column undergoing such combined loading is formulated, with constraints on energy absorption and elastic bending stiffness. The optimization study is performed with various values of transition parameter ξ, and the optimized results are discussed in this section.

6.5.1 Optimization Formulation

Consider a foam-filled square tube with sectional width b, wall thickness t, length L. The mass density of wall material is ρ_0, and the mass density of foam filler is ρ_f. The tube undergoes axial progressive collapse at the incipient stage of the crash. The length of the axial crushing part of the tube is L_a

$$L_a = \xi L \tag{6.47}$$

Following the progressive crushing is a global bending collapse with three plastic hinges formed at the center and two ends of the otherwise intact part of the tube, see Fig.6.22. Accordingly, the optimization formulation can be stated by Eq.(6.43), with E_n being the actual energy absorption during the crash, which can be calculated by the following equation (neglecting the small contribution from elastic deformation)

$$E_n = P_m\delta + 2\int_0^{\theta_0/2} M_f(\theta)d\theta + \int_0^{\theta_0} M_f(\theta)d\theta \tag{6.48}$$

The first term in Eq.(6.48) is the energy absorption during the axial progressive collapse at the incipient stage of the crash. The second and third terms are the energy absorption during the subsequent global bending collapse, with the second term corresponding to the two end plastic hinges and the third term corresponding to the center plastic hinge (see Fig.6.22).

The P_m in Eq.(6.48) is the mean crushing force of axial crushing and was given in Eq.(6.16). The δ is the effective crushing distance

$$\delta = L_a S_E \tag{6.49}$$

where S_E is the so-called "stroke efficiency", and it varies from 0.7 to 0.75 for thin-walled square tubes [54, 99].

$M_f(\theta)$ in Eq.(6.48) is the plastic bending resistance of the foam-filled section, and was given in Eq.(4.21). θ_0 denotes the bending rotation at the end of crash. The upper limit of the θ_0 is the jamming angle of the generalized plastic hinges.

With $\rho_f = 0$, the problem reduces to a non-filled one.

6.5.2 Optimum Solutions

Take, for example, a foam-filled beam with length $L = 400$mm. The wall material and foam material are the same as those used in the example for bending collapse.

The stroke efficiency S_E is assumed to be 0.7, and the transition parameter ξ is taken to be 0.2. The target energy absorption levels $\widetilde{E_n}$ are set to be $6 \backsim 10$kJ. $\theta_0 = 30°$. The optimized results are shown in Table 6.12.

Table 6.12: Optimum results ($S_E = 0.7, \xi = 0.2, \theta_0 = 30°$)

Variables	Constraints									
b (mm)	no constraint									
t (mm)	$0.5 \backsim 3$									
ρ_f (g/cm^3)	$0.0675 \backsim 0.54$									
$\widetilde{EI}$ (kNm^2)	25									
$\widetilde{E_n}$ (kJ)	6		7		8		9		10	
Solutions	F	E	F	E	F	E	F	E	F	E
b^* (mm)	99.5	106.4	95.0	123.9	93.1	140.8	88.0	157.4	85.0	174.7
t^* (mm)	0.50	3.0	0.56	3.0	0.58	3.0	0.68	3.0	0.73	3.0
ρ_f^* (g/cm^3)	0.188	0	0.225	0	0.256	0	0.304	0	0.346	0
m^* (kg)	0.951	1.380	1.035	1.606	1.112	1.825	1.184	2.038	1.252	2.250
SEA(kJ/kg)	6.311	4.349	6.766	4.358	7.196	4.384	7.601	4.416	7.990	4.445

A few observations can be made based upon the above optimum solutions

- The optimized SEA of a filled section is $45\% \backsim 80\%$ higher than that of a non-filled section, depending on the energy absorption level, see Fig.6.23. The gain in SEA in such a combined loading is similar to that in pure bending case, where the SEA gains about 60% increase by foam filling.
- Width b is reduced by foam filling, especially at high energy absorption levels, which results in significant volume reduction for crash members.
- The wall thickness of non-filled section takes the upper bound(3mm) as the optimum solution, while the filled section has much thinner one ($0.50 \backsim 0.73$mm).
- Medium density foams($\rho_f = 0.188 \backsim 0.346 g/cm^3$) are selected as optimum solutions at energy levels considered in the calculation.

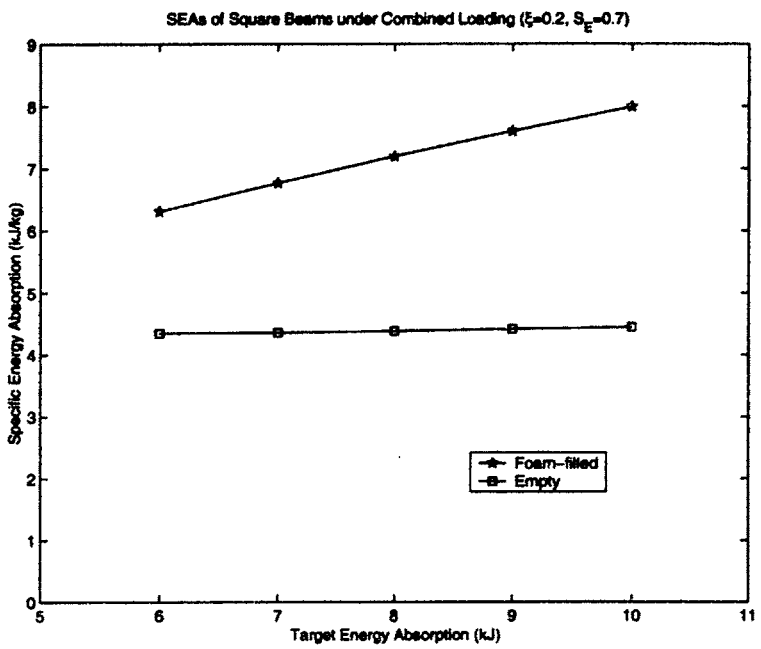

Figure 6.23: Specific energy absorption at various energy absorption levels

- From the optimization results of the pure bending, the combined loading, and the pure axial crushing, a general tendency can be observed: compared to traditionally designed non-filled section, filled section yields a significant increase in specific energy absorption, a smaller sectional width, a thinner wall, and a medium dense foam (of about 10% relative density).

Let us now consider the effect of transition parameter ξ. Set the target energy absorption at a specified value, for example, $\widetilde{E_n} = 8$kJ, and make ξ vary in the range of $0.1 \backsim 0.5$. The corresponding optimum solutions are shown in Table 6.13. Fig.6.24 shows the optimized specific energy absorption of filled and non-filled sections.

As can be noted in Table 6.13 and Fig.6.24, the SEAs of both filled and non-filled members are increasing functions of transition parameter ξ. The reason for this is that the axial progressive crushing is more efficient in energy absorption than bending collapse. With the increase of ξ, more material is involved in axial crushing, and thus higher specific energy absorption is achieved. This again emphasizes the importance of proper design of crash members to get the maximum advantage of weight efficiency of axial progressive crushing.

Table 6.13: Optimum results ($S_E = 0.7, \widetilde{E_n} = 8kJ, \theta_0 = 30°$)

Variables	Constraints									
b (mm)	no constraint									
t (mm)	$0.5 \backsim 3$									
ρ_f (g/cm^3)	$0.0675 \backsim 0.54$									
$\widetilde{EI}$ (kNm^2)	25									
ξ	0.1		0.2		0.3		0.4		0.5	
Solutions	F	E	F	E	F	E	F	E	F	E
b^* (mm)	93.0	162.4	93.1	140.8	95.0	120.9	97.5	101.8	98.5	84.7
t^* (mm)	0.53	3.0	0.58	3.0	0.57	3.0	0.54	3.0	0.54	3.0
ρ_f^* (g/cm^3)	0.318	0	0.256	0	0.211	0	0.179	0	0.158	0
m^* (kg)	1.301	2.104	1.112	1.825	0.989	1.564	0.901	1.319	0.834	1.097
SEA(kJ/kg)	6.151	3.803	7.196	4.384	8.091	5.114	8.883	6.065	9.598	7.289

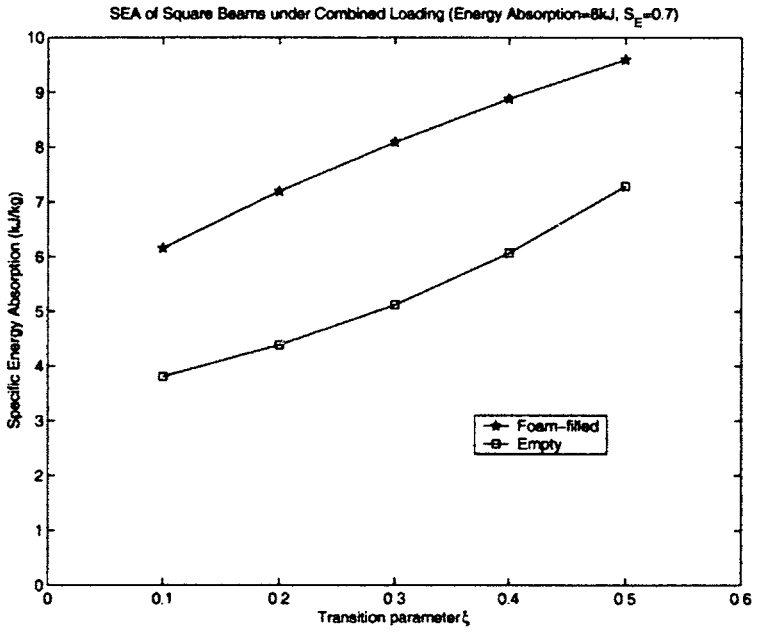

Figure 6.24: Specific energy absorption at various transition ratio

6.6 Optimization for Torsional Crushing

Based on the results obtained in Chapter 5, structural optimization technique can be similarly employed to select the most weight efficient design for crash energy management of foam-filled thin-walled square members in torsional loading. Three design variables can be identified: the width b, the wall thickness t, and the mass density of filler ρ_f, that is,

$$\mathbf{X} = \{b, t, \rho_f\} \tag{6.50}$$

The optimization formulation is the same as that in the bending case (Eq.(6.43)), with E_n being the actual energy absorption during torsional collapse up to twisting rotation θ_m, and is defined by

$$E_n = \int_0^{\theta_{cf}} T_{if} d\theta + \int_{\theta_{cf}}^{\theta_m} T_{pf} d\theta \tag{6.51}$$

with twisting moments T_{if} and T_{pf} given in Eq.(5.50) and Eq.(5.51), respectively, and θ_{cf} given in Eq.(5.52).

As a case study, let us consider a square foam-filled beam, with length $L = 250$mm, tube wall material being aluminum alloy AA6060 T4($\rho_0 = 2.7g/cm^3, E_0 = 69GPa, \sigma_0 = 106.1MPa$) and the foam material being Hydro aluminum foam($\rho_s = 2.7g/cm^3, E_s = 69GPa, \sigma_{0f} = 150.4MPa$). Take $\theta_m = 90°$.

First, let us assume that the width b is fixed and leave ρ_f and t as active design variables, Take $b = 80mm$, for instance. Since there are only two active design variables, we can use a graphical approach to solve the optimization problem. In Fig.6.25, the contours of energy absorption E_n (1000, 2000, 3000, 4000 J), bending stiffness EI (25, 50 kNm^2) and the structural mass (0.4, 0.6 0.8 1.0 kg) are plotted as functions of foam density ρ_f and wall thickness t. When a design point moves from lower left corner of the figure to upper right corner, both the energy absorption and the mass are increasing. If a target energy absorption value is set, for instance, 3000J, and the target bending stiffness is set to be 25 kNm^2, we can find in the figure

the 3000 E_n contour. It is evident that point S on this contour gives the smallest value of the mass (point S also satisfies the bending stiffness requirement). Point S represents a design of $\rho_f = 0.11g/cm^3$ and $t = 1.9mm$.

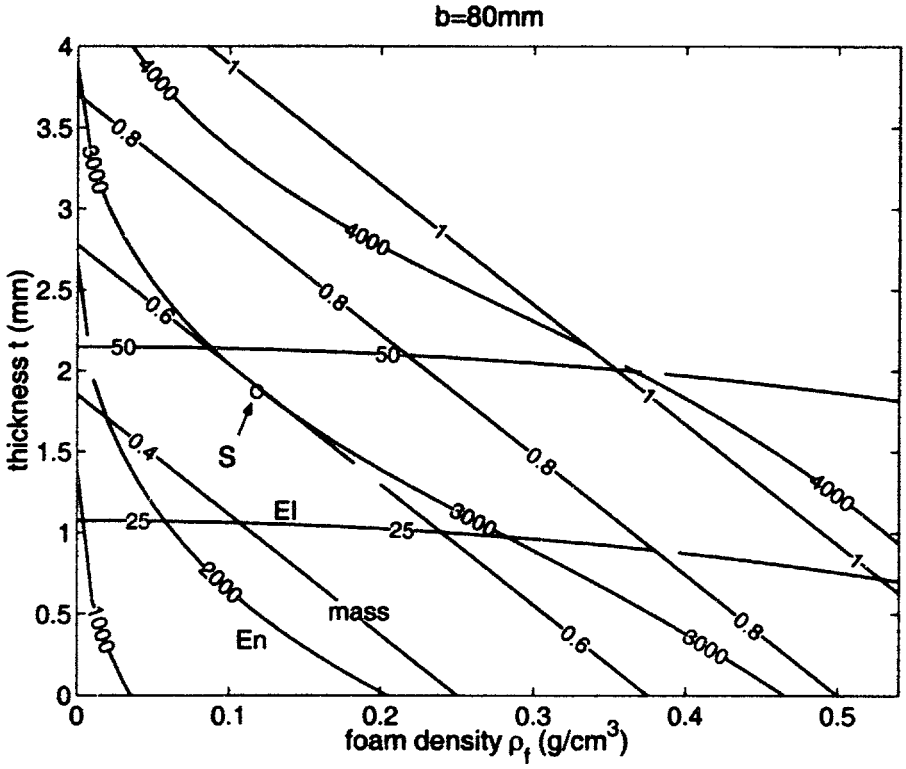

Figure 6.25: Graphical approach to solve the optimization problem with two active design variables

If a target bending stiffness is set, for example, $25kNm^2$, one can see that only when the energy absorption requirement is low (2000J, for example) is the bending stiffness constraint active. The EI constraint is not active any more when the E_n requirement gets higher. Because of the very demanding requirement of crash, it is thus plausible that the crush criteria will dominate structural design of a car body. Well designed crashworthy structures will generally meet the general stiffness criteria set by other requirements such as NVH.

Now let us consider a general case, with all three design variables active in optimization procedure. The side constraints are set as $b \in [40, 80]mm$, $t \in [0.5, 5]mm$ and $\rho_f \in [0.054, 0.54]g/cm^3$. The optimum solutions of foam-filled and non-filled sections

are listed in Table 6.14 for various target energy absorption levels. The corresponding Specific Energy Absorptions (SEA, energy absorption per unit mass) are also listed in the table and shown in Fig.6.26 as well. Note that the kink in the SEA curve of the filled sections is due to the transition of the bending stiffness constraint from active to inactive with the increasing target energy absorption.

Table 6.14: Optimum solutions for foam-filled and empty sections

Variables	Constraints									
b (mm)	40 $\backsim$80									
t (mm)	0.5 $\backsim$ 5									
ρ_f (g/cm^3)	0.054$\backsim$0.54									
$\widetilde{EI}$ (kNm^2)	25									
$\widetilde{E_n}$ (J)	1500		2000		2500		3000		3500	
Solutions	F	E	F	E	F	E	F	E	F	E
b^* (mm)	80	80	80	80	80	80	80	80	80	80
t^* (mm)	1.07	1.94	1.07	2.58	1.05	3.20	1.90	3.79	2.50	4.35
ρ_f^* (g/cm^3)	0.054	0	0.058	0	0.139	0	0.110	0	0.136	0
m^* (kg)	0.315	0.419	0.321	0.558	0.444	0.692	0.578	0.819	0.744	0.940
SEA(kJ/kg)	4.757	3.583	6.230	3.584	5.630	3.614	5.190	3.662	4.703	3.722

Note: F=Filled; E=Empty

A few observations can be made based upon the above optimization results

- The SEA of foam-filled sections is up to 70% higher than that of non-filled section. This substantiates the argument that the foam-filled members are superior to non-filled ones in the light of weight-effective energy absorption.
- The maximum allowable width ($b = 80mm$) is selected as optimum solution in all studied cases.
- The optimum wall thickness of a filled section is generally smaller than that of a non-filled section. It indicates that the wall thickness of the foam-filled section has to be reduced compared with traditionally designed non-filled section if increase of specific energy absorption is to be achieved.

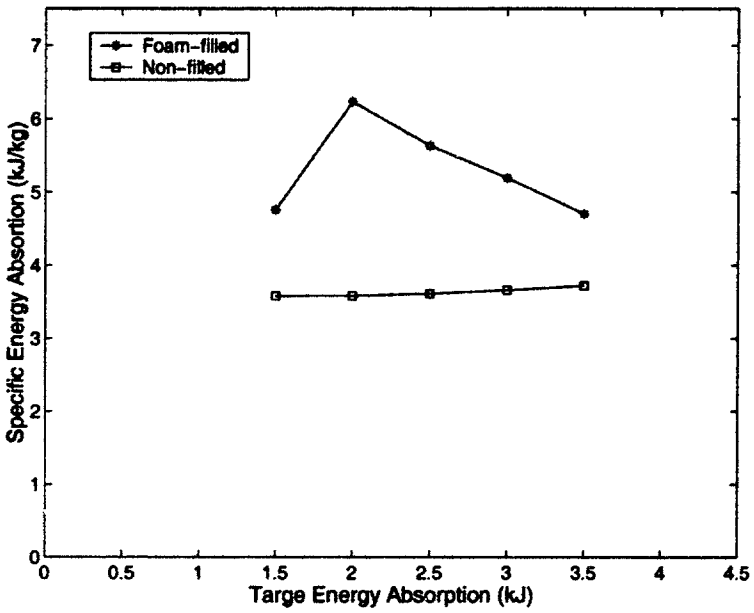

Figure 6.26: Specific energy absorption of filled and non-filled tubes

- For the target energy absorption levels considered in the calculation, the optimum solutions of filled section yield low foam density (2% $\backsim$ 5% relative density).

6.7 Discussions

A study on optimization for minimum weight of ultralight crash members undergoing various loading conditions was carried out in this chapter. A methodology was proposed which integrates the fundamental results of crushing mechanics of ultralight structures discussed in the previous chapters with the numerical optimization techniques to minimize the weight of the crash members with crashworthiness and elastic bending stiffness constraints. The proposed methodology requires relatively simple computations and is suitable for early stage of crash member design.

From the results of the case studies performed in this chapter for axial crushing, pure bending, combined compression/bending, and torsional loadings, a general tendency can be observed: compared to traditionally design non-filled sections, filled section

yields a significant increase in specific energy absorption, a smaller sectional width and a thinner wall (the resulting width-to-thickness ratio of the filled section is generally larger than that of non-filled section), and a low to medium dense filler (5% $\backsim$ 10% relative density).

The gains in the Specific Energy Absorption for the filled sections compared to non-filled sections vary depending on the loading conditions. A highest gain is expected in the axial crushing deformation where the SEA of foam-filled sections is on average 300% higher than that of non-filled sections, while in the bending collapse and combined axial crushing and bending collapse deformation, the gains in SEA are respectively 60% and 80%. The SEA gains would be as high as 70% under torsional loading. It is clear therefore that the foam-filled structures provide potentials of significant weight savings.

The present work focused on the crushing behavior and the reinforcement effects of foam filling on a single component subject to a simple type of loading. As more application-oriented cases, the reinforcement effects and potential weight savings of filled structures should be studied on a subsystem and system level.

Chapter 7

Conclusions and Recommendations

7.1 Conclusions

Extensive theoretical, numerical and experimental studies were carried out on the axial crushing, bending collapse and torsional deformation of thin-walled structures filled with lightweight metal core materials–ultralight structures. The weight effectiveness of such ultralight structures in crash energy management was discussed. The strengthening effects of the filling were revealed and quantitatively assessed, closed-form solutions were developed to predict the strengthening effects. With this, an optimization methodology was developed, which combines the above results with numerical optimization techniques, to minimize the weight of ultralight structures while satisfying crashworthiness and structural integrity requirements.

Axial Crushing of Empty and Foam-filled Multi-cell Extrusions

The axial crushing of hollow multi-cell columns were addressed first in the thesis by analytical and numerical approaches. Based on the *Superfolding Element* theory, an analytical solution for the mean crushing force of multi-cell section was derived, and the solution was compared very well with the numerical predictions. The gain in the specific energy absorption of the double cell and triple cell is about 15% compared to the single cell. Numerical studies were also carried out on the axial crushing of

foam-filled double-cell and triple-cell columns. From dimensional analysis, numerical results and analytical solutions, closed-form expressions were developed to predict the mean crushing strength of the foam-filled multi-cell sections. It was found that the interaction effects between the foam core and the column wall contribute to the total crushing resistance by the amounts equal to 140% and 180% of the direct foam resistance for double cell and triple cell, respectively. The foam-filled sections generally exhibit higher specific energy absorption values and thus higher weight efficiency in energy absorption, while the triple cell is no better than the double cell in terms of SEA, either filled or non-filled.

Tests on Foam-filled Hat Profiles subjected to Axial Crushing

An experimental study was carried out on aluminum hat profiles filled with aluminum foam and subjected to axial crushing loading. The foam fitting methods of adhesive-bonding and pre-compression investigated in the study could be conducive to high volume production of foam-filled closed-hat structural members. Joint techniques should be the point of concern in the design of aluminum closed-hat members. Spot-welding becomes more problematic in foam-filled members than in empty ones. The premature joint failure of foam-filled members to large extent jeopardizes their relative merit as weight-efficient crash members compared to empty ones. Riveting can be applied together with spot-welding and weld-bond to improve the strength of joint. The experiments indicate an 20% increase in specific energy absorption for foam-filled columns compared to non-filled ones.

Bending Collapse of Filled Structures

The deep bending collapse of thin-walled empty and foam-filled hat profiles were studied experimentally and numerically. Salient features of crushing behavior of empty and foam-filled hat members with large bending rotation were revealed. The moment-rotation characteristics for the generalized plastic hinges with the rotation angle up to 150° were found to be similar to the case of axial folding of thin-walled members, with peaks and troughs corresponding respectively to the initiation of buckles and formation of subsequent folds all the way to jamming. It was found in the experimental study that foam-filled members with the current design of sectional geometry and material properties can achieve 30–40% increase in the specific energy absorption, compared to non-filled members. Numerical results were compared with the experi-

mental results showing good agreement in terms of force responses and deformation patterns, which validates the finite element modeling techniques used in the analysis. Subsequently, series of numerical analysis were conducted with a wide range of fillers densities to study and quantify the reinforcement effects of foam filling and honeycomb filling. The lightweight filler prevents or reduces the bending moment drop after the local buckling, and the closed-form expressions for the bending moment elevation due to filling were developed based on the numerical results, experimental data and theoretical considerations.

Torsional Crushing of Empty and Filled Tubes

The torsional crushing behavior of empty and foam-filled square tubes under large rotations was studied theoretically, numerically and experimentally. An analytical solution for empty square tubes was derived using a kinematic approach. Three successive deformation phases, namely pre-buckling, cross-section buckling, and collapse-spreading phase were identified. The analytical model was then extended to the cases of thin-walled rectangular and hexagonal tubes. Numerical simulations were carried out and results were compared with the analytical solutions giving good agreement. It was noted that the presence of the core material changes the collapse mechanism and gives rise to higher sectional buckling modes and therefore increases the plastic resistance of the tube. The analysis showed that there are two basic mechanisms through which the core material is increasing the energy absorption of thin-walled tubes. The main mechanism is to prevent or reduce the inward sectional collapse of the cross-section and ensure a full membrane stress to be developed in the wall. The second mechanism for increasing the energy absorption is a direct contribution from the torsion of the core material, which was proved to be a small fraction compared with the aforementioned main mechanism. Based on the analytical solution and numerical results, the twisting moment elevation due to foam filling was quantified, and the closed-form expressions was to be incorporated into the optimization methodology developed in the next chapter.

The results of torsional experiments on empty and foam-filled square tubes were compared with finite element solutions and analytical models. Although the end platens of specimens were not properly designed and unexpected welding failure occurred on those fixtures during testing, which diminished significantly the twisting moment of the tubes, the deformation shape and sectional deformation pattern of

tubes observed in the experiments agree fairly well with the numerical predictions and analytical models. The experimental results show increase in plastic resistance and energy absorption for foam-filled tubes compared to non-filled ones.

Optimization Study

With the above results, an optimization methodology was proposed, which combines the closed-form solutions of crush resistances of ultralight structures developed in the previous chapters with numerical optimization techniques, to minimize the structural weight with crashworthiness and bending stiffness constraints. Because all the objective and constraint functions are explicitly expressed, continuous and differentiable, the proposed methodology requires relatively simple computations and is suitable for early-stage component design.

From the results of case studies of the optimization problems in axial crushing, pure bending, combined compression/bending, and torsional loading, a general tendency was observed: compared to traditionally non-filled section, filled section yields a significant increase in specific energy absorption, a smaller sectional width and a thinner wall, and a low to medium dense filler (5–10% relative density). The gain in the SEA for the filled sections compared to non-filled ones vary depending on the loading conditions. A highest gain is expected in the axial crushing deformation where the SEA of foam-filled sections is on average 300% higher than that of non-filled sections, while in the bending collapse and combined axial crushing and bending collapse deformation, the gains in SEA are respectively 60% and 80%. The SEA gains would be as high as 70% under torsional loading. It is clear therefore that the ultralight structures provide potentials of significant weight savings.

7.2 Future Research

It is suggested that further research should be conducted on the following issues:

- The axial crushing behavior of multi-cell columns were studied analytically and numerically in the present research. Experiments need to be conducted on multi-cell members to validate the analytical and numerical models.

- Joint techniques are vital for aluminum foam-filled closed-hat members. Various joining techniques should be further investigated to ensure the joint integrity during the crushing deformation.

- It was observed in the experiments that some foam-filled specimens failed prematurely by developing necking and fracture during crash deformation, which diminished energy absorption. This underlines the importance of fracture in filled structure as subject of further research.

- More torsional experiments should be carried out with properly designed end platens to ensure their integrity under large twisting moment.

- The present work focused on the crushing behavior and the reinforcement effects of foam filling on a single component subject to a simple type of loading. As more application-oriented cases, the reinforcement effects and potential weight savings of filled structures should be studied on a subsystem and system level.

- Structural energy absorption is only one portion of overall vehicle crash performance. Weight, packaging, and other factors should be assessed in any trade-off decision. Therefore, the discussions presented in this thesis apply to design only in a very restricted way. Design for crash energy management is of necessity a multi-faced process involving very close interaction of many diverse engineering disciplines.

Bibliography

[1] Paluszny, A. State-of-the-art review of automobile structural crashworthiness. American Iron and Steel Institute, Technical Report, 1992.

[2] Thornton, P.H. Energy absorption by foam filled structures. SAE paper 800081, 1980.

[3] Thornton, P.H., Mahmood, H.F., and Magee, C.L. Energy absorption by structural collapse. In Jones, N. and Wierzbicki, T., editors, *Structural Crashworthiness.* Butterworths, 1983.

[4] Lampinen, P. and Jeryan, R. Effectiveness of polyurethane foam in energy absorbing structures. SAE paper 820494, 1982.

[5] Santosa, S. *Crashworthiness Analysis of Ultralight Metal Structures.* PhD thesis, Massachusetts Institute of Technology, 1999.

[6] Santosa, S. The concept of double-walled sandwich columns for energy absorption. In Chirwa, E. and Viano, D, editors, *International Crashworthiness Conference.* Woodhead Publishing, 1999.

[7] Santosa, S., Banhart, J., and Wierzbicki, T. Bending crush resistance of partially foam-filled sections. Presented at the International Conference on Metal Foams and Porous Metal Structures, Bremen, Germany, June 14-16, 1999.

[8] Santosa, S., Banhart, J., and Wierzbicki, T. Experimental and numerical analysis of bending of foam-filled sections. *Acta Mechanica, in press*, 2000.

[9] Santosa, S. and Wierzbicki, T. Effect of an ultralight metal filler on the torsional crushing behavior of thin-walled prismatic columns. *International Journal of Crashworthiness*, 2(4):305–332, 1998.

[10] Santosa, S. and Wierzbicki, T. Crash behavior of box column filled with aluminum honeycomb or foam. *Computers and Structures*, 68(4):343–368, 1999.

[11] Santosa, S. and Wierzbicki, T. Effect of an ultralight metal filler on the bending collapse behavior of thin-walled prismatic columns. *International Journal of Mechanical Sciences*, 41(8):995–1019, 2000.

[12] Seitzberger, M., Rammerstorfer, F.G., Degischer, H.P., and Gradinger, R. Crushing of axially compressed steel tubes filled with aluminum foam. *Acta Mechanica*, 125:93–105, 1997.

[13] Seitzberger, M., Rammerstorfer, F.G., Gradinger, R., Degischer, H.P., Blaimschein, M., and Walch, C. Experimental studies on the quasi-static axial crushing of steel columns filled with aluminum foam. *International Journal of Solids and Structures*, 37:4125–4147, 2000.

[14] Hanssen, A.G., Langseth, M., and Hopperstad, O.S. Static crushing of square aluminum extrusions with aluminum foam filler. *International Journal of Mechanical Sciences*, 41:967–993, 1999.

[15] Hanssen, A.G., Langseth, M., and Hopperstad, O.S. Static and dynamic crushing of circular aluminum extrusions with aluminum foam filler. *International Journal of Impact Engineering*, 24:475–507, 2000.

[16] Hanssen, A.G., Langseth, M., and Hopperstad, O.S. Static and dynamic crushing of square aluminum extrusions with aluminum foam filler. *International Journal of Impact Engineering*, 24:347–383, 2000.

[17] Gibson, L. and Ashby, M. *Cellular Solids: Structure and Properties.* Cambridge University Press, Cambridge, UK, 1997.

[18] Doyoyo, M. and Wierzbicki, T. Fracture of aluminum honeycomb and foams under hemispherical-punch indentation. *Submitted to International Journal of Mechanical Sciences*, 2000.

[19] Christensen, R.M. Mechanics of low density materials. *Journal of Mechanics and Physics of Solids*, 34, 1986.

[20] Thornton, P.H. and Magee, C.L. Metallurgy Transaction, 6A, 1253, 1975.

[21] Thornton, P.H. and Magee, C.L. Metallurgy Transaction, 6A, 1801, 1975.

[22] McFarland, R. Hexagonal cell structure under post buckling axial load. *AIAA Journal*, 1:1380–1385, 1963.

[23] Wierzbicki, T. Crushing analysis of metal honeycombs. *International Journal of Impact Engineering*, 1:157–174, 1983.

[24] Markaki, A.E. *Mechanical Behavior of Layered Metal Foam/Ceramic Composites.* PhD thesis, University of Cambridge, 2000.

[25] Prakash, O., Sang, H., and Embury, J. Structure and properties of al-sic foam. *Materials Science and Engineering A*, 199:195–203, 1995.

[26] Akiyama, S., Imagawa, K., Kitahara, A., Nagata, S., Morimoto, K., T., T. N., and Itoh, M. Foam metal and method of producing same. U.S. patent No.4713277, 1987.

[27] Santosa, S. and Wierzbicki, T. On the modeling of crush behavior of closed-cell aluminum foam structure. *Journal of the Mechanics and Physics of Solids*, 46(4):645–669, 1998.

[28] Hanssen, A.G. *Validation of Constitutive models applied to aluminum foam.* PhD thesis, The Norwegian University of Science and Technology, 2000.

[29] Harte, A.M., Fleck, N.A., and Ashby, M.F. Fatigue failure of an open cell and a closed cell aluminum alloy foam. *Acta Metallurgica et Materialia*, 47(8), 1999.

[30] Doyoyo, M. and Wierzbicki, T. Tests on combined normal and shear loading of cellular solids. Impact & Crashworthiness Laboratory, Report No.40, MIT,2000.

[31] Sugimura, Y., Meyer, J., Bart-Smith, H., Grenstedt, J., and Evans, A.G. On the mechanical performance of closed cell al alloy foams. *Acta Metallurgica*, 45(2):5245–5259, 1997.

[32] Gibson, L.J., Ashby, M.F., Zhang, J., and Triantafillou, T.C. Failure surfaces for cellular materials under multiaxial loads i: Modeling. *International Journal of Mechanical Sciences*, 31(9):635–663, 1989.

[33] Drucker, D.C. and Prager, W. Soil mechanics and plastic analysis or limit design. *Quarterly Journal of Applied Mathematics*, 10, 1952.

[34] Miller, R.E. A continuum plasticity model of the constitutive and indentation behavior of foam metals. *International Journal of Mechanical Sciences, in press.*

[35] Deshpande, V.S. and Fleck, N.A. Isotropic constitutive models for metallic foams. *Journal of the Mechanics and Physics of Solids*, 48:1253–1283, 2000.

[36] Gioux, G., McCormack, T.M., and Gibson, L.J. Failure of aluminum foams under multiaxial loads. *International Journal of Mechanical Sciences*, 42, 2000.

[37] Doyoyo, M. and Wierzbicki, T. Tests on combined normal and shear loading of cellular solids, 2000. Impact & Crashworthiness Laboratory, Report No.40, MIT.

[38] Shaw, M.C. and Sata, T. The plastic behavior of cellular materials. *International Journal of Mechanical Sciences*, 8:469–478, 1966.

[39] Santosa, S., Wierzbicki, T., Hanssen, A.G., and Langseth, M. Experimental and numerical studies of foam-filled sections. *International Journal of Impact Engineering*, 24:509–534, 2000.

[40] Chen, W. Experimental and numerical studies on the deep bending collapse of foam-filled profiles. *Submitted to International Journal of Solids and Structures*, 2000.

[41] Chen, W. amd Wierzbicki, T., Breuer, O., and Kristiansen, K. Torsional crushing of foam-filled thin-walled square columns. *Accepted by International Journal of Mechanical Sciences*, 2000.

[42] Doyoyo, M. Bao, Y., Kim, H.S. and Wierzbicki, T. Spherical punch indentations on brittle aluminum foam, fem models and experiments, 2001. In preparation for publication.

[43] Deshpande, V.S. and Fleck, N.A. High strain rate compressive behavior of aluminum alloy foams. *International Journal of Impact Engineering*, 24:277–298, 2000.

[44] Hxcel. Hexweb honeycomb attributes and properties, 2000. http://www.hexcel.com.

[45] Hxcel. Mechanical properties of hexcel honeycomb materials, 1992. Technical Report, Hexcel Structural Division, Dublin, CA 94568, USA.

[46] Wierzbicki, T. Experimental, numerical, and analytical study of honeycomb material, 1997. Impact & Crashworthiness Lab, Report #1, Massachusetts Institute of Technology.

[47] Baker, W.E., Togami, T.C., and Weyder, J.C. Static and dynamic properties of high-density metal honeycombs. *International Journal of Impact Engineering*, 21(3), 1998.

[48] Wu, E. and Jiang, W-S. Axial crush of metallic honeycombs. *International Journal of Impact Engineering*, 19(5–6), 1997.

[49] Zhao, H. and Gary, G. Crushing behavior of aluminum honeycombs under impact loading. *International Journal of Impact Engineering*, 21(10), 1998.

[50] Wierzbicki, T. Ultralight aluminum products: Process development, modeling, applications, and costs, 1999. Research Proposal to U.S. Department of Energy.

[51] Barrera, J., Santosa, S., and Wierzbicki, T. Analytical, numerical, and experimental study of double-walled sandwich columns. Impact & Crashworthiness Laboratory, Report No.25, MIT,1999.

[52] Mohr, D. and Meyer, J. Crushing of double-walled sandwich profiles with honeycomb core. Impact & Crashworthiness Laboratory, Report No.37, MIT,2000.

[53] Wierzbicki, T. and Abramowicz, W. On the crushing mechanics of thin-walled structures. *Journal of Applied Mechanics*, 50:727–739, 1983.

[54] Abramowicz, W. and Wierzbicki, T. Axial crushing of multicorner sheet metal columns. *Journal of Applied Mechanics*, 56:113–120, 1989.

[55] McGregor, I.J, Meadows, D.J., Scott, C.E., and Seeds, A.D. Impact performance of aluminum structures. In Jones, N. and Wierzbicki, T., editors, *Structural Crashworthiness and Failure*. Elsevier, 1993.

[56] Barhat, S.D., Mahmood, H.F., and Prasad, P.P. Aluminum intensive vehicle crashworthiness design approach. AMD-Vol.225/BED-Vol.38, Crashworthiness, Occupant Protection and Biomechanics in Transportation Systems, ASME 1997.

[57] Mahmood, H.F., Baccouche, M.R., and Barthelemy B. Design of extruded aluminum space frame front end structures for crash energy management-part i.

AMD-Vol.225/BED-Vol.38, Crashworthiness, Occupant Protection and Biomechanics in Transportation Systems, ASME 1997.

[58] Baccouche, M.R. and Mahmood, H.F. Design of extruded aluminum space frame front end structures for crash energy management-part ii. AMD-Vol.230/BED-Vol.41, Crashworthiness, Occupant Protection and Biomechanics in Transportation Systems, ASME 1998.

[59] White, M.D. and Jones, N. Experimental quasi-static axial crushing of top-hat and double-hat thin-walled sections. *International Journal of Mechanical Sciences*, 41:179–208, 1999.

[60] White, M.D., Jones, N., and Abramowicz, W. A theoretical analysis for the quasi-static axial crushing of top-hat and double-hat thin-walled sections. *International Journal of Mechanical Sciences*, 41:209–233, 1999.

[61] Wierzbicki, T. Lecture notes on structural mechanics, 1998. Massachusetts Institute of Technology.

[62] Ulm, F. Dimensional Analysis, Lecture notes, Civil Engineering, MIT, 2000.

[63] Kallina, I., Zeidler, F., Baumann, K.H., and Scheunest, D. The offset crash against a deformable barrier, a more realistic frontal impact. Proceedings to the 14th International Technical Conference on Enhanced Safety of Vehicles, Munich, Germany, May 23-26, 1994, Vol.2, pp1300-1304.

[64] Kecman, D. Bending collapse of rectangular and square section tubes. *International Journal of Mechanical Sciences*, 25(9-10):623–636, 1983.

[65] Abramowicz, W. Simplified crushing analysis of thin-walled columns and beams. *Engineering Transactions*, 29:3–27, 1983.

[66] Mahmood, H.F., Paluszny, A., and Lin, Y.S. Bending deep collapse of automotive type components. SAE Paper 885044.

[67] Wierzbicki, T., Recke, L., Abramowicz, W., Gholami, T., and Huang, J. Stress profiles in thin-walled prismatic columns subjected to crush loading-i, compression. *Computers and Structures*, 51(6):611–623, 1994.

[68] Chen, W., Wierzbicki, T., and Santosa, S. Bending collapse of thin-walled beams with ultralight filler: Numerical simulation and weight optimization. Accepted by Acta Mechanica, 2000.

[69] Baba, S. and Kajita, T. Plastic analysis of torsion of a prismatic beam. *International Journal for Numerical Methods in Engineering*, 18(6):927–944, 1982.

[70] Murray, N.W. *Introduction to the Theory of Thin-walled Structures.* Clarendon Press, Oxford Engineering Science Series, UK, 1983.

[71] Mahendran, M. and Murray, N.W. Ultimate load behavior of box-columns under combined loading of axial compression and torsion. *Thin-walled Structures*, 9:91–120, 1990.

[72] White, G.J., Grzebieta, R.H., and Murray, N.W. Maximum strength of square thin-walled sections subjected to combined loading of torsion and bending. *International Journal of Impact Engineering*, 13(2):203–214, 1993.

[73] Grant, C. Network analysis of thin-walled sections in uniform torsion. *Proceedings of the Institute of Mechanical Engineers, Part C, Mechanical Engineering Science*, 209(2):133–140, 1995.

[74] Ma, H., Zhang, S., and Yang. G. Impact torsional buckling of plastic circular cylindrical shells: Experimental study. *International Journal of Impact Engineering*, 22:531–542, 1999.

[75] Trahair, N.S. Plastic torsion analysis of monosymmetric and point-symmetric beams. *Journal of Structural Engineering-ASCE*, 125(2):175–182, 1999.

[76] Chen, W. Plastic resistance of thin-walled tubes undergoing large twisting rotations. Master Thesis, MIT, 2000.

[77] Chen, W. and Wierzbicki, T. *Simplified analysis of torsional crushing behavior of thin-walled square columns.* Impact & Crashworthiness Laboratory, Technical Report 8, Massachusetts Institute of Technology, 1998.

[78] Brush, Don O. and Almroth, B.O. *Buckling of Bars, Plates, and Shells.* McGraw Hill, New York, 1975.

[79] Rhodes, James. Manual of crashworthiness engineering-vol.iv: Ultimate strength of thin-walled components. Center for Transportation Studies, Massachusetts Institute of Technology, 1989.

[80] W. Chen and T. Wierzbicki. Torsional collapse of thin-walled prismatic columns. *Thin-walled Structures*, 36(3), 2000.

[81] I.H. Shames. *Introduction to Solid Mechanics.* Prentice Hall, New Jersey, 1989.

[82] W. Chen and T. Wierzbicki. Torsional collapse of foam-filled columns. Technical report, No. 19, Impact and Crashworthiness Laboratory, Massachusetts Institute of Technology, 1999.

[83] Bennett, J.A., Lin, K.H., and Nelson, M.F. The application of optimization techniques to problems of automotive crashworthiness. *SAE Transactions*, 86:2255–2262, 1977.

[84] Song, J.O. An optimization method for crashworthiness design. Proceedings of the Sixth International SAE Conference on Vehicle Structural Mechanics, Detroit, MI, 1986.

[85] R.V. Lust. Structural optimization with crashworthiness constraints. Proceedings of the Third Air Force/NASA Symposium on Recent Advances in Multidisciplinary Analysis and Optimization, San Francisco, CA, 1990.

[86] DeVries, R.I., Saha, N.K., Surulinarayanasami, P., and Zebrowski, M.P. Structural optimization of beam sections for minimum weight subject to inertial and crash strength constraints. Proceedings of the Sixth International Conference on Vehicle Structural Mechanics, Detroit, Michigan, 1986.

[87] Bennett, J.A., Lust, R.V., and Wang, J.T. Optimal design strategies in crashworthiness and occupant protection. AME-Vol.126/BED-Vol.19, Crashworthiness and Occupant Protection in Transportation System, ASME, 1991.

[88] Pickett, A.K. et al. Optimization of the crashworthiness of a passenger car using iterative simulations. SAE paper 931977, 1993.

[89] Yang, R.J. et al. A numerical study of crash optimization. Proceedings of DETC99, ASME Design Engineering Technical Conference, Las Vagas, Nevada, 1999.

[90] Yamazaki, K. and Han, J. Maximization of the crushing energy absorption of tubes. *Structural Optimization*, 16:37–46, 1998.

[91] A.G. Hanssen, M. Langseth, and O.S. Hopperstad. Optimum design for energy absorption of square aluminum columns with aluminum foam filler. *International Journal of Mechanical Sciences*, 2000.

[92] Arora, J.S. *Guide to Structural Optimization.* ASCE Manuals and Reports on Engineering Practice No.90, ASCE, 1997.

[93] Haftka, R.T. and Gurdal, Z. *Elements of Structural Optimization.* Kluwer Academic Publishers, New York, 1992.

[94] Matlab optimization toolbox,user's manual. Mathworks,1999.

[95] Santosa, S. Crash behavior of box columns filled with aluminum honeycomb or foam. Master's Thesis, Department of Mechanical Engineering, Massachusetts Institute of Technology, 1997.

[96] Von Karman, T., Sechler, E.E., and Donnel, L.H. The strength of thin plates in compression. *Transaction SME, Applied Mechanics*, 54(2), 1932.

[97] Wierzbicki, T. and Abramowicz, W. Manual of crashworthiness engineering, vol.iii: Stability of progressive collapse, 1988. Center for Transportation Study, MIT.

[98] Abramowicz, W. and Jones, N. Transition from initial bending to progressive buckling of tubes loaded statically and dynamically. *International Journal of Impact Engineering*, 19(5-6):415–437, 1997.

[99] Abramowicz, W. The effective crushing distance in axially compressed thin-walled metal columns. *International Journal of Impact Engineering*, 1:309–317, 1983.